Probing Nuclear Effects in Neutrino Induced Pion Production

David Coplowe

Lady Margaret Hall

University of Oxford

A thesis submitted in fulfilment of the requirements

for the degree of

Doctor of Philosophy

Trinity Term, 2018

Probing Nuclear Effects in Neutrino Induced Pion Production

David Coplowe

Lady Margaret Hall, University of Oxford

A thesis submitted in fulfilment of the requirements for the degree of Doctor of Philosophy

Trinity Term, 2018

Abstract

The discovery of neutrino oscillations has opened the door to searches for matter-antimatter asymmetries in the lepton sector. Current accelerator-based long-baseline neutrino oscillation experiments, like T2K and NOνA, probing this phenomenon are moving into the realm of high statistics but systematically limited measurements. As a result work in reducing the dominant uncertainties in neutrino oscillations has become crucial in developing our understanding of leptonic $\mathcal{CP}$ Violation.

One of the dominant uncertainties lies in our understanding of neutrino-nucleus interactions. These affect our ability to determine the selection efficiencies for the respective signal and backgrounds, and the reconstruction of the neutrino energy spectra. This is due to our limited knowledge of nuclear effects and has renewed interest in neutrino-nucleus scattering measurements.

This thesis presents work on a novel method of isolating nuclear effects which can be applied to isolate interactions on hydrogen. Using Double Transverse Momentum — a kinematic imbalance of the final state hadronic system transverse to the neutrino direction and muon momentum plane, phenomenological studies are performed into its ability to probe nuclear effects.

We assess the feasibility of isolating neutrino-interactions on hydrogen in composite nuclear targets using the T2K near detector, ND280. This work is extended on to the MINERνA Experiment where work is undertaken in order to understand the heavy nuclear background. The first differential δp_{TT} cross section measurement for final states containing at least one proton and π^0 using the MINERνA detector is reported.

Statement of Originality

This thesis and the work presented in it are my own and were produced by me as a result of my own original research. Results and figures from published works by others have been clearly attributed, and this work has not been submitted for another qualification at this or any other university.

The thesis begins by introducing the reader to neutrinos in Chapters one and two, providing a background to the relevant theoretical and experimental components motivating this research. Chapter four outlines both the T2K and MINERvA experiments whose Monte Carlo and Data are discussed heavily in this work. These three chapters are a broad summary of work by others and have been referenced clearly.

Chapter three introduces the variable Double Transverse Momentum, developed by Xianguo Lu (Oxford University) and I to probe nuclear effects. Xianguo developed the kinematic framework and I assessed the kinematics ability to probe nuclear effects. Here a detailed study of the various theoretical predictions made in this variable is given. This work is my own unless stated otherwise.

The analysis Chapters, namely, five through eight, present work from the T2K and MINERvA experiments. These chapters use Monte Carlo to model how the data is expected to behave and is written by others. Each experiment has its own analysis framework to analyse both datasets that have been developed by various collaborators. Their contributions have been referenced in chapter four.

Chapter five introduces the T2K analysis which investigates the current experimental capabilities of measuring neutrino interactions on hydrogen and is entirely my own work. The work undertaken on the MINERvA experiment in chapters six, seven and eight started with a selection written by Ozgur Altinok whilst at Tufts University. My work is an extension to his analysis where I first redefine the signal definition before applying the analysis variable described in chapter three. The resultant background constraints, signal extraction and finally the cross section result is solely my work. Again, I clearly reference all work undertaken by Ozgur and others in this chapter.

Dedicated To

Donald Challen
(1927-2017)

Strawberry Kingpin, Historian and Grandfather.

Acknowledgements

The work presented in this thesis would not have been possible without the research and development made by many other people. To those of you behind this - I thank you. I would however like to make specific thanks to my supervisor, Giles Barr, his support throughout my DPhil, from funding applications to fruitful analysis discussions have made this work possible.

During my time at Oxford I had the pleasure of sharing an office with fellow students Raj, Kirsty, Stephen and honorary member Luke. Thank you for the interesting discussions and numerous Ski trips over the past four years. I would also like to thank Trever, Alfons, Dave and Xianguo for their advice and collaboration. Whilst not in the department I met many great people in Oxford; Caleb, Ning, Simon and Kris our trips were incredible but feel lucky to have had that SatNav. Jack, thank you for being such a great friend and flexible landlord, you made the many long term trips abroad much less hassle. I would also like to thank Ant and our infrequent visits to Plush. Amy, I really appreciate introducing me to pottery and miss our regular throw downs together. Perhaps one day one of my pieces will turn out okay!

I would also like to thank Fermilab for their financial support which allowed me to work on-site with my MINERνA collaborators. My frequent nagging of Trung, Dan and Phil made getting to grips with MINERνA's analysis framework much more manageable. You guys put up with me and can't thank you enough. The past and present spokes people of the MINERνA experiment: Laura, Debbie and Kevin shared their in depth knowledge of the field and could not have gone with out a mention here. It was great getting to know Roger, Nataly and Merheen whilst living in the village; if only the Frontier was open later.

Finally, to Ellis and Chloe; the many hours of Battlefield will never be forgotten, nor our regular sessions at the Rose and Crown. You two as well as Steve made my time at Oxford special in so many ways, from adventures around the UK to College balls. Muchas gracias.

Contents

List of Figures

List of Tables

Chapter 1

Neutrinos: From hypothesis to discovery

In a time where much of the western world was lit by candlelight, an accidental discovery made by Henri Becquerel opened the door to a field that today is known as Particle Physics. During his experimental searches in 1896 into understanding phosphorescence he discovered radioactivity [1]. Unbeknown to him at the time he also began a quest in trying to understand perhaps the most mysterious particle known to man – the neutrino.

The neutrino's queer behaviour started to present itself when James Chadwick was measuring the energy spectra of electrons in beta decay [2]. Unlike other forms of radioactivity being measured at the time, electrons produced from beta decay had a continuous energy spectrum [3]. An early explanation of this phenomenon and preferred by Neils Bohr was that beta decay violated conservation of energy. This was later rebutted by Wolfgang Pauli in his letter to Lise Meitner and the participants of a radioactivity conference in Tubingen, 1930 [4].

Pauli postulated that a new, neutral spin-half particle may exist with negligible mass compared to the proton. He also suggested that, given the lack of

observation at the time, it should interact weakly with matter [5]. Building on these properties, Enrico Fermi published his theory of weak interactions in 1934 to describe β-decay [6]. Fermi later coined the neutral little the neutrino.

It was not until 1953 when this ghostly particle began to present itself. Initial results presented by Reines and Cowan provided evidence of the neutrino's existence albeit tentative [7]. After a further four years of research, the two finally published confirmation of the electron anti-neutrino's existence [8]. Details of how they discovered the $\bar{\nu}_e$ is presented in Section 1.1 and in Section 1.2 the hypothesis and observation of two more generations of neutrino is reviewed.

So what makes neutrinos so strange? At this point the only apparent difference between neutrinos and other forms of matter is their low interaction probability. The neutrinos most peculiar feature lies in a phenomenon known as neutrino oscillations and took almost four decades to resolve. Shortly after the little neutral one's discovery, measurements of neutrinos originating from the sun by Ray Davis indicated large discrepancies between experimental results and Standard Solar Model predictions [9, 10]. The Standard Solar Model provides as a theoretical framework of the nuclear interactions in the core of the sun. Davis' studies seemed to indicate a deficit in the number of observed neutrinos compared to what was expected from various Solar Models. This became known as the 'solar neutrino problem'.

The nature of the solar neutrino problem was finally solved through work undertaken by Super-Kamiokande in 1998 and SNO in 2002 of the discovery of neutrino oscillations [11,12]. Their Nobel Prize winning work found that neutrinos transform from one generation to another due to mass differences. This implied that neutrinos have mass albeit small – something contradictory to Fermi's massless neutrino hypothesis and that of the Standard Model of Particle Physics. Today efforts are now working to probe deeper into this oscillatory phenomenon as it may provide an insight into the origins of the matter-antimatter asymmetry

observed in the universe. This is discussed in Section 1.3.

One such effect which is crucial in understanding the oscillatory phenomenon of neutrinos and forms the basis of this thesis, is in improving our knowledge of neutrino interactions with matter. We shall see later in Section 1.3 that studying neutrino oscillations is dependent on measuring the event rates and energies of detected neutrinos. These need to be constrained in order to probe any matter-antimatter asymmetry or $\mathcal{CP}$ Violation in neutrinos. Neutrino interactions will therefore be introduced in Chapter 2 before moving on to describing a means of probing one of the dominant uncertainties in neutrino oscillations, namely nuclear effects, in Chapter 3. The reader will then be introduced to the experiments used in this work in Chapter 4 and the respective analyses in Chapter 5 for T2K and Chapters 6-8 for MINERνA.

1.1 The Cowan and Reines Experiment

Brought on by World War Two, research into exploiting the vast amount of energy trapped inside the nucleus led to Cowan and Reines being able to discover the neutrino. Given the weak interaction strength predicted by Fermi, an intense source of neutrinos would be required. To do this Cowan and Reines exploited the Fission processes occuring inside reactors. By searching for the reaction

$$\bar{\nu}_e + \mathrm{p} \rightarrow n + e^+, \tag{1.1}$$

the two devised a means of identifying the interaction via the coincidence of electron-positron annihilation followed shortly after by neutron capture. The experiment used a water based Cadmium-Chloride ($CdCl_2$) solution which was surrounded by two liquid scintillators as shown figure Figure 1.1. The two used the scintillators to first identify two 511 keV photons produced in the annihilation process, then as the neutron is captured by Cd, a few micro-seconds later a

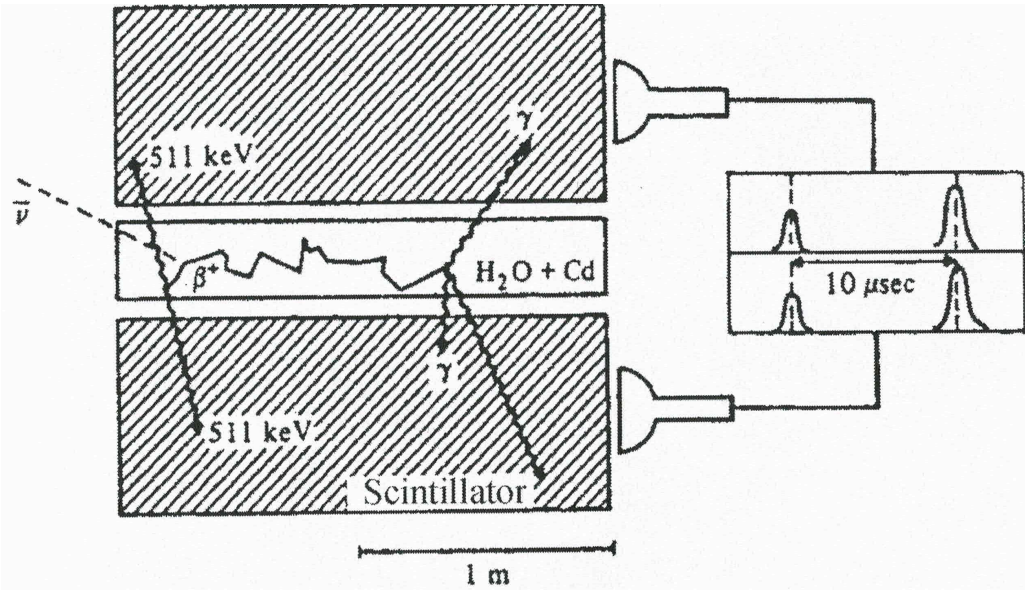

Figure 1.1: A schematic of the experimental set-up used by Cowan and Reines to detect $\bar{\nu}_e$ neutrinos. Source [4].

second burst of photons are detected from the de-excitation of Cd.

Cowan and Reines initial measurement in 1953 at the US based Hanford reactor lead to the observation of a vague signal. This however suffered from a large cosmic ray background due to poor shielding and there was insubstantial evidence to reliably say neutrinos had been observed. Undeterred, in 1956 the two repeated their measurement using 14 times more scintillator (4200 litres) placed at the Savannah River reactor. This reactor provided better shielding from cosmic rays as the detector could be placed underground. In order to improve the signal to background separation they also refined their experimental technique by using a more segmented configuration resulting in the first cross section measurement of

$$\bar{\sigma} = (11.0 \pm 2.6) \times 10^{-44} \text{ cm}^2. \tag{1.2}$$

This measurement taken from [8] agreed with Fermi's V-A theory leading to the discovery of the electron anti-neutrino.

1.2 Two More Flavours

Like the electron, the muon and tau were discovered before their neutral counterparts. The muon was discovered in 1936 and subsequent measurements of its properties implied that two neutrinos must be present in muon decay.

This observation was made when considering the branching ratio

$$\rho = \frac{R(\mu \to e + \gamma)}{R(\mu \to e + \nu + \bar{\nu})}, \tag{1.3}$$

for muon decay which was expected to have a value of order 10^{-4} unless neutrinos associated with muons are different from those associated to electrons. In February 1962 the branching ratio was measured to be $\leq 10^{-8}$ implying a second, muon-like neutrino might exist [13]. Just five months later experimental evidence of the muon neutrino, ν_μ, was observed by a team lead by L. Lederman, M. Schwartz and J. Steinberger (see later in this chapter) [14].

By this point a pattern was emerging, for each electron-like particle or charged lepton there existed an associated neutral equivalent. This led to many asking whether more pairs of leptons existed and if so how many. The idea of charge-neutral lepton pairs was incorporated into a theoretical framework which expanded on Fermi's four-point model [15]. This not only said that leptons are produced in pairs but that the weak interaction is prescribed via three force carrying mediators, namely, the $W^\pm$ and Z^0 bosons. During the development of this theory another even heavier charged lepton was discovered, the tau, at SLAC, an e^+e^- collider in 1975 [16]. It took another 25 years before its associated neutrino was discovered at Fermilab in 2000.

So how many pairs of leptons? This question was answered by the ALEPH, DELPHI, L3 and OPAL experiments based at CERN's LEP e^+e^- collider. They studied properties of the Z^0-boson resonance measuring both the total decay width and partial decay widths into charged fermions. This information was

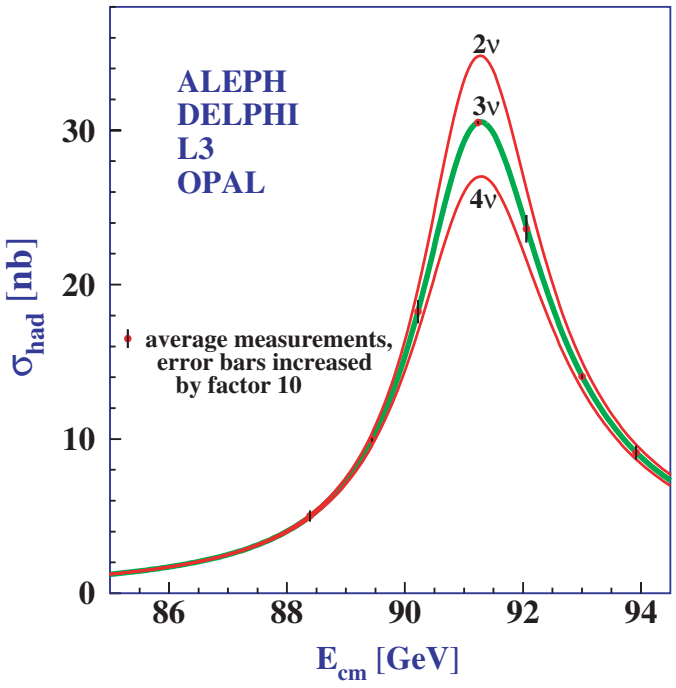

Figure 1.2: Combined measurements of the hadron production cross-section near the Z^0 mass using data from ALEPH, DELPHI, L3 and OPAL. The Standard Model prediction is overlaid for a two, three and four neutrino flavour hypothesis. Source [17].

used to compare the total decay width with the partial decay widths in order to measure the 'invisible' decay width. The 'invisible' width was then used to determine the number of light neutrinos by assuming lepton universality. From Figure 1.2, the number of light neutrinos whose mass are less then $m_{Z^0}/2$ was found to be 2.9840 ± 0.0082 [17], placing a limit on the number of neutrinos to be three.

1.2.1 First Muon Neutrino Observation

L. Lederman, M. Schwartz, J. Steinberger and collaborators built an experiment to test the hypothesis that if only one type of neutrino existed then, when neutrinos interact with nucleons, they should produce just as many electrons as muons. If on the other hand two distinct types of neutrino exist, for a beam of neutrinos produced via the decay, $\pi^{\pm} \rightarrow \mu^{\pm} + \nu/\bar{\nu}$, no electrons should be observed.

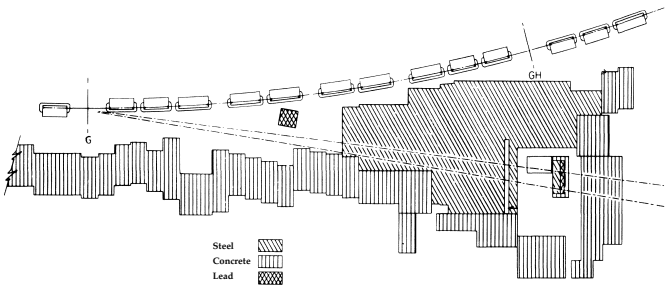

(a) Accelarator and absorber complex used to produce a neutrino beam and remove beam backgrounds before detection in experimental hall.

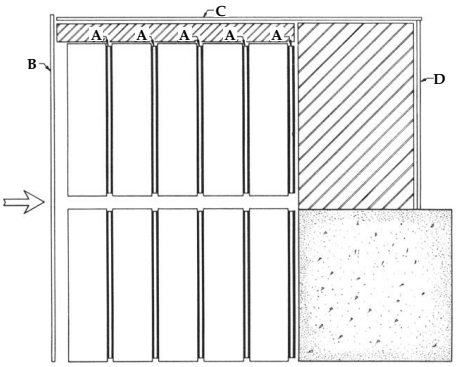

(b) Side on view of spark chamber and counter system. The white rectangles are modules which are separated by triggering slabs (A). Anti-coincidence slabs are defined by B, C and D.

Figure 1.3: Experimental set-up used to discover muon neutrinos at Brookhaven's AGS. Source [14].

To test these hypotheses they produced an intense beam of neutrinos by colliding 15 GeV protons onto a beryllium target which produced predominantly charged pions. These pions would decay leaving muons and neutrinos travelling towards the direction of the detector. In order to reduce backgrounds arising in the neutrino production process a 13.5 metre thick steel absorber was placed 3 metres downstream of the target as shown in Figure 1.3a. This helped to remove charged particles, specifically muons, entering the detector complex.

The group searched for both neutrino and anti-neutrino interactions of the form

$$\nu + n \to p + e^-, \qquad \bar{\nu} + p \to n + e^+,$$
$$\nu + n \to p + \mu^-, \qquad \bar{\nu} + p \to n + \mu^+.$$

To do this they used a spark chamber as seen in Figure 1.3b to detect neutrino interactions. This was formed using an array of ten one-ton modules; each made from nine aluminium 2.54 cm thick, 1.12 $\times$ 1.12 m^2 sheets separated by 1.9 cm plastic spacers. Every module contained high-pressure spark gaps which ionise

a gas as charged particles traverse through the detector.

A number of trigger systems were used to capture neutrino interactions within the detector by a camera. The trigger arrangement presented in Figure 1.3b firstly contained trigger counters downstream of each module to identify possible candidate interactions within a module. These were used in conjunction with anti-coincidence triggers to enable background-like events originating outside of the detector to be vetoed. The backgrounds consisted of remnant beam candidates as well as cosmic rays.

The experiment observed 113 events which were classified into four samples. The first contained 49 single short tracks whose visible momentum was less than 300 MeV/c. The second, a single muon sample consisted of 34 events where the track had more than 300 MeV/c and no more than two extraneous sparks. Twenty-two vertex events formed the third sample characterised by having more than one track originating from a single point. Finally, the fourth sample, named 'showers' saw 8 events whose structure was too irregular to be muon-like but more typical of electron interactions.

The final analysis rejected two samples in the discovery of the muon neutrino. These were the short tracks and vertex events. The former was ignored as they were believed to be low energy neutrino events or backgrounds which could not have their lepton type well determined. The vertex events were not used because they were believed to be dominated by backgrounds and not reliable due to large uncertainties in the knowledge of other scattering processes.

The remaining samples were further refined. The shower sample had events whose visible momentum was less than 300 MeV/c removed in order to ensure that each sample's kinematics were the same. Additional analysis of the single muon events identified five cosmic rays within the sample. This lead to 29 muon-like events and 6 electron-like events in the final analysis. The latter were found to be a result of beam contamination proving that neutrinos produced

with muons are distinct from those produced with electrons. This was the first observation of the muon neutrino. Later results made by various experiments at CERN confirmed L. Lederman, M. Schwartz and J. Steinberger's measurement and awarded them the 1988 Nobel Prize for the discovery [18, 19].

1.2.2 Discovery of the Tau Neutrino

It was not until the millennium when the DONuT Experiment discovered the tau neutrino [20]. The main purpose of this experiment was to study ν_τ induced charged-current events of the form

$$\nu_\tau + N \rightarrow \tau^- + X, \qquad \bar{\nu}_\tau + N \rightarrow \tau^+ + X.$$

It also recorded interactions produced from all neutrino flavours [21]. Like in the discovery of the ν_μ and much of what will be discussed in this thesis it relied upon an accelerator to produce the neutrino beam. The large mass of the tau (1.777 GeV/c^2 [22]) required the accelerated beam to be much more energetic in order to produce a non-negligable ν_τ component. The collaboration therefore used 800 GeV protons accelerated by the Tevatron that impinged on a solid tungsten alloy target. This produced a hadron shower which then went on to decay into predominantly ν_e and ν_μ neutrinos. There was however a small (3%) ν_τ component which originated from the decay of charm mesons.

The detector was located 36 metres downstream of the tungsten target and relied on a number of different detector technologies to identify ν_τ-like candidates. A schematic of the DONuT detector is presented in Figure 1.4. The key component used to distinguish ν_τ-like events from other neutrino induced processes was the emulsion target. This had the precision required to observe the signature left by the short lifetime of a $\tau^\pm$ lepton. It worked very much like pho-

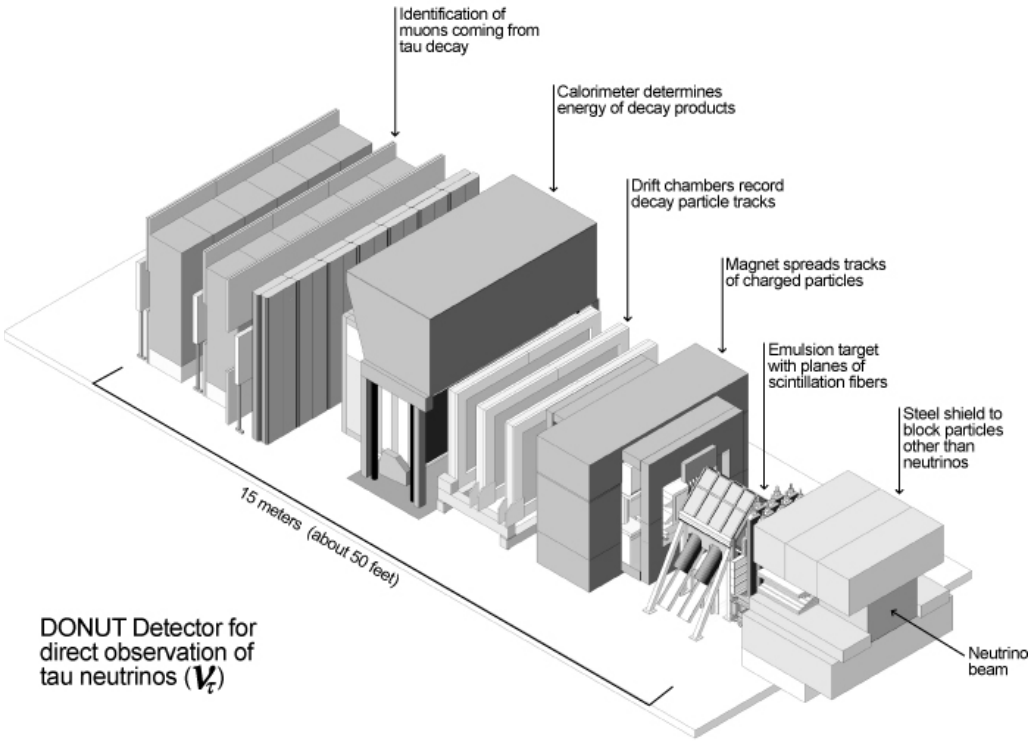

Figure 1.4: Schematic overview of the DONuT experiment identifying each sub-detector along with shielding. Source [23].

tographic film in that film is sensitive to the exposure of light whereas emulsions are sensitive to the exposure of charged particles. Note that they also required their own process of being 'developed' in order to make the images stable after exposure to the neutrino beam.

The DONuT Experiment's emulsion target comprised of four modules each with tracking scintillating planes placed downstream of the module. Each module was 7 cm thick equivalent to 2-3 radiation lengths providing it with good granularity along the neutrino beam. The scintillator planes were used to identify where in the emulsion module the vertex position lied [24].

The emulsion target was used to search for τ leptons as the only charged lepton created at an interaction vertex. This signature was identified by a kinked track as it was consistent with two vertices; the first being the interaction vertex and the second the τ decay vertex. The two vertices had to be located within 2 mm of each other [21]. Using this signal definition for ν_τ events of the 203

neutrino interactions analysed they found evidence of four tau neutrinos [20]. These candidates were consistent with the Standard Model prediction leading to the discovery of the missing neutrino.

1.3 Neutrino Oscillations

Earlier we introduced the idea that neutrino oscillations are able to account for the deficit in the 'solar neutrino problem'. We shall now review the theory associated to describing this phenomenon before summarising some of the current and future results. However, prior to this it is useful to know how together results by Super-Kamiokande and SNO were able to attribute the neutrino deficit to neutrino oscillations.

Davis first found the solar neutrino anomaly in his experiment when he tried to measure the β^+ decay of ^{8}B. Here he searched for ν_e through $\nu_e + \mathrm{Cl} \rightarrow e^- + \mathrm{Ar}$ interactions. The results placed an upper bound on the solar ν_e flux two to three times smaller than the Standard Solar Model's prediction [25]. This deficiency in the solar ν_e flux was supported by various other measurements [26–28].

The SNO Experiment's approach to measuring the solar ^{8}B flux was to focus on measuring two processes. Like Davis, they considered the ν_e flux whose signal in their heavy water based Cherenkov detector was the charged-current elastic process

$$\nu_e + d \rightarrow p + p + e^-. \tag{1.4}$$

In addition to the ν_e flux they also worked to measure the total solar flux which would allow them to probe the flux independent of neutrino flavour. This was achieved by considering the neutral-current interaction

$$\nu_\ell + e^- \rightarrow \nu_\ell + e^-. \tag{1.5}$$

The flavour independent channel yielded the first solar neutrino flux measure-

ment that was in agreement with the Standard Solar Model [12]. This in conjunction with the elastic scattering flux give strong evidence that neutrinos did indeed transform from electron-type to muon and tau-type. The measured flux ratio was found to be 0.301 ± 0.033.

What was the phenomenon behind this transformation process? This was answered by the Super-Kamiokande Collaboration which considered neutrinos produced in the upper atmosphere by cosmic ray interactions. The experiment, based 1 km underground measured the atmospheric ν_μ flux with good energy and directional reconstruction. They used these reconstruction quantities to test the following hypothesis: if neutrinos starting out as one flavour travel different distances before being detected will the event rate or probability be the same irrespective of the distance travelled? This is direct evidence for neutrino oscillations.

The Super-Kamiokande Experiment tested this hypothesis by comparing upward-going with downward-going neutrinos. Neutrinos produced in the atmosphere above Super-Kamiokande travel between 15-500 km before reaching the detector whereas neutrinos entering the detector from below have to travel through the Earth at a distance of around 500-12,000 km. This provides numerous distances or baselines that the neutrinos have to travel before being detected. From here they could then measure energy and directional information to calculate the L/E_ν ratio (which as we will see later is sensitive to neutrino oscillations). They observed the expected number of ν_es from all directions and ν_μs travelling downward but a deficit in the number of ν_μ neutrinos travelling upward. This was consistent with ν_μs transforming into ν_τs and in 1998 lead to the discovery of neutrino oscillations [11].

1.3.1 The Theory of Neutrino Transformation

Now that we have understood the evidence for neutrino oscillations, we shall move on to how this phenomenon implies that neutrinos have a non-zero mass. As we have seen in charged-current weak lepton interactions neutrinos only couple to their respective charged flavour counterpart. This implies that the propagation eigenstates must be distinct from their interaction or flavour eigenstates. For neutrinos to be massive but only interact in definite flavour eigenstates then the flavour eigenstate, ν_ℓ, must be a superposition of its propagation or mass eigenstates, ν_i. The flavour state, ν_ℓ, can therefore be written as

$$|\nu_\ell\rangle = \sum_i^N U_{\ell i}^* |\nu_i\rangle. \tag{1.6}$$

Here $U_{\ell i}$ are elements of the $N \times N$ lepton mixing matrix relating the mass to the flavour eigenstates. The number of flavours N is usually three. Standard Model weak interaction requires the mixing matrix to be unitary in order to preserve the lepton pairing – electron-type neutrinos only couple to electrons.

Before discussing the structure of this matrix further we shall outline how the states evolve as it will enable us to appreciate how mass differences dictate neutrino oscillations. To do this one must first understand how the flavour state evolves with time. This is dictated by the time evolution of the mass eigenstates which propagate as

$$|\nu_i(t)\rangle = e^{-ip_i \cdot x_i} |\nu_i(0)\rangle, \tag{1.7}$$

where p_i and x_i are the mass eigenstate's momentum and position four-vectors. Together these can be written in the lab frame as, $p_i \cdot x_i = E_i t - |\boldsymbol{p_i}| L$. Here the mass state is observed to travel a distance L over a time t with three-momentum $\boldsymbol{p}_i$. In the ultra-relativistic limit, $m_i^2 \ll E_i^2$, and knowing that neutrinos have a

small mass, the momentum can be written as

$$|\boldsymbol{p}_i| = (E_i^2 - m_i^2)^{1/2} \simeq E_i - \frac{m_i^2}{2E_i}. \tag{1.8}$$

This leads to $p_i \cdot x_i$ taking the form

$$p_i \cdot x_i \simeq E(t - L) + \frac{m_i^2 L}{2E}, \tag{1.9}$$

if we assume that, for an initial flavour eigenstate, ν_ℓ, the mass states ν_i have the same energy, E[1]. From here it is possible to write the time evolution of the flavour eigenstate as

$$|\nu_\ell(t)\rangle = e^{-iE(t-L)} \sum_i^N U_{\ell i}^* e^{\frac{-im_i^2 L}{2E}} |\nu_i(0)\rangle. \tag{1.10}$$

This can be used to determine the probability of a neutrino starting in one definite flavour eigenstate being observed some distance later in another definite flavour eigenstate. Note that nothing was said about the time here, even though a time dependent component exists. This is because the term is common to all flavour states and cancels when determining transition probabilities. For a neutrino starting in one flavour eigenstate, α, which is observed to be in another flavour eigenstate, β, at some distance L, the transition probability is

$$P(\alpha \to \beta) = \left|\langle \nu_\beta(t) | \nu_\alpha \rangle\right|^2 = \left| \sum_i^N U_{\alpha i}^* U_{\beta i} \exp\left(-i \frac{m_i^2 L}{2E}\right) \right|^2. \tag{1.11}$$

The general form of this can be written in terms of its real an imaginary parts

[1]Note that even without such an assumption between the energy of the mass eigenstates a full quantum mechanical treatment in terms of waves packets shows that the oscillation formalism is essentially unchanged.

highlighting where the mass differences, $\Delta m^2_{ij} = m^2_i - m^2_j$ occur

$$P(\alpha \to \beta) = \delta_{\alpha\beta} - 4\sum_{i>j} \mathrm{Re}\left(U^*_{\alpha i} U_{\beta i} U_{\alpha j} U^*_{\beta j}\right) \sin^2\left(\frac{\Delta m^2_{ij} L}{4E}\right) \tag{1.12}$$

$$+ 2\sum_{i>j} \mathrm{Im}\left(U^*_{\alpha i} U_{\beta i} U_{\alpha j} U^*_{\beta j}\right) \sin\left(\frac{\Delta m^2_{ij} L}{2E}\right). \tag{1.13}$$

Here we see the L/E_ν ratio used by Super-Kamiokande to prove that neutrinos transform from one flavour to another. Hence if the masses are zero then neutrinos would not exhibit any oscillatory feature.

The PMNS Matrix and $\mathcal{CP}$ Violation

The composition of a flavour state into its associated mass eigenstates is described by the PMNS matrix. PMNS are the first letters of the theorists, Pontecorvo, Maki, Nakagawa and Sakata, who developed the idea of neutrino mixing in the late sixties [29]. Their work not only outlined how neutrinos may have mass, as we have previously outlined, but also that if there exist at least three generations of neutrino then neutrinos may behave differently from anti-neutrinos. For a set of three flavour and three mass eigenstates their matrix reads

$$\begin{aligned} U &= \begin{pmatrix} U_{e1} & U_{e2} & U_{e3} \\ U_{\mu 1} & U_{\mu 2} & U_{\mu 3} \\ U_{\tau 1} & U_{\tau 2} & U_{\tau 3} \end{pmatrix}, \\ &= \underbrace{\begin{pmatrix} 1 & 0 & 0 \\ 0 & c_{23} & s_{23} \\ 0 & -s_{23} & c_{23} \end{pmatrix}}_{\text{Atmospheric}} \underbrace{\begin{pmatrix} c_{13} & 0 & s_{13} e^{-i\delta_{\mathcal{CP}}} \\ 0 & 1 & 0 \\ -s_{23} e^{i\delta_{\mathcal{CP}}} & 0 & c_{13} \end{pmatrix}}_{\text{Cross-mixing}} \underbrace{\begin{pmatrix} c_{23} & s_{23} & 0 \\ -s_{23} & c_{23} & 0 \\ 0 & 0 & 1 \end{pmatrix}}_{\text{Solar}} \underbrace{\begin{pmatrix} e^{i\alpha_1/2} & 0 & 0 \\ 0 & e^{i\alpha_2/2} & 0 \\ 0 & 0 & 1 \end{pmatrix}}_{\text{Majorana}}, \end{aligned} \tag{1.14}$$

where $c_{ij} = \cos\theta_{ij}$ and $s_{ij} = \sin\theta_{ij}$. There are a total of six free parameters that need to be experimentally measured: the three mixing angles, θ_{12}, θ_{23} and θ_{13}, and three complex phases, namely, $\delta_{\mathcal{CP}}$, which dictates the strength of Dirac $\mathcal{CP}$ violation and finally α_1 and α_2 whose size determines the amount of Majorana $\mathcal{CP}$ violation.

In Equation 1.14, the first and third matrices are those which dominate in atmospheric and solar neutrino oscillations. The final, Majorana term, is only physical if neutrinos are their own anti-particle. If this is indeed found to be true and the complex Majorana terms are non-zero it will not change oscillation results as they are diagonal in the PMNS matrix.

The second term, named the cross-term is currently the main topic of interest to the experimental community. This is due to the complex Dirac $\mathcal{CP}$ violating term which if non-zero implies that neutrinos behave differently from anti-neutrinos as $P(\alpha \to \beta) \neq P(\bar{\alpha} \to \bar{\beta})$ under $\mathcal{CP}$ transformation.

The NuFit collaboration [30] have performed a global analysis using results from various neutrino oscillation experiments. They use results from solar, reactor and accelerator based experiments to determine the best fit parameters of the mass differences and those in the PMNS matrix. Their fit results have been summarised in Table 1.1. Note that they present fit results for both normal and inverted hierarchy. The hierarchy refers to the ordering of the mass eigenstates and is only partially known experimentally. The masses of the first and second mass eigenstates, m_1 and m_2 have been measured to be $m_1 < m_2$. Therefore, the hierarchy is said to be normal ordered if $m_1 < m_2 < m_3$ and inverted if $m_3 < m_1 < m_2$.

1.3.2 Matter Effects

Up until now, we have only discussed neutrinos propagating in a vacuum but we have already seen that many of the neutrino sources used to study neutrino os-

Parameter	Ordering	
	Normal	Inverted
θ_{12} (°)	$33.62^{+0.78}_{-0.76}$	
θ_{23} (°)	$47.2^{+1.9}_{-3.9}$	$48.1^{+1.4}_{-1.9}$
θ_{13} (°)	$8.54^{+0.15}_{-0.15}$	$8.58^{+0.14}_{-0.14}$
$\delta_{\mathcal{CP}}$ (°)	234^{+43}_{-31}	278^{+26}_{-29}
Δm^2_{21} (10^{-5}eV^2)	$7.40^{+0.21}_{-0.20}$	
Δm^2_{3j} (10^{-3}eV^2)	$+2.494^{+0.033}_{-0.031}$	$+2.465^{+0.032}_{-0.031}$

Table 1.1: The January 2018 NuFIT global fit results for neutrino oscillations parameters. The j in Δm^2_{3j} represents 1 in the normal ordered case and 2 for inverted hierarchy. Source [30].

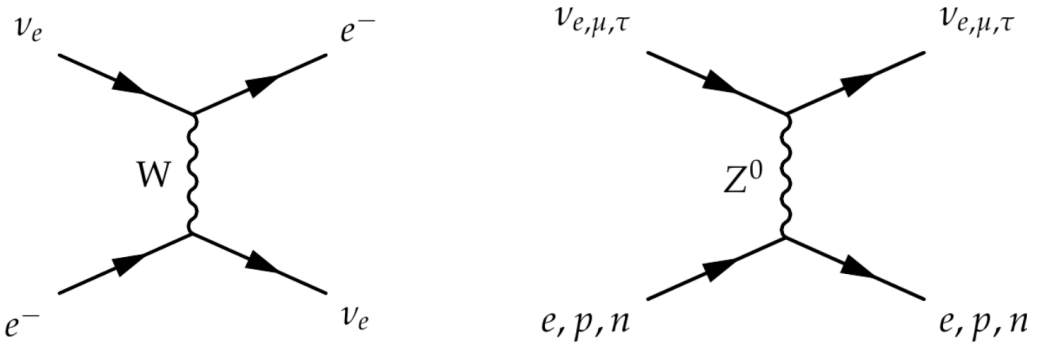

Figure 1.5: Feynman diagrams representing the Matter Effects associated to ν_e only via charged-current interactions (*left*) and those affecting all neutrinos via neutral-current interactions (*right*).

cillations in fact propagate through matter. For example, solar neutrinos which are produced in the core of the Sun, have to pass through the Sun's interior before being measured on Earth. Similarly, atmospheric measurements performed by Super-Kamiokande probe neutrinos passing through the Earth.

Neutrinos travelling within a medium actually interact with the medium and can have a significant effect on neutrino oscillation physics. Two processes that describe this phenomenon are presented in Figure 1.5. These are charged-current

electron-ν_e scattering and neutral-current neutrino scattering. Given that neutral-current processes are flavour independent they therefore interact with all types of neutrino equally. As a result, this process does not affect neutrino oscillations. The charged-current process is however flavour specific acting only on ν_e which in turn will affect the mass eigenstates according to their ν_e component. Hence as neutrinos propagate through a medium as mass eigenstates which themselves are composed of flavour eigenstates the oscillation probability will change.

Matter effects are not only different for neutrino flavours but also anti-neutrinos. Hence when trying to measure $\mathcal{CP}$ violation, if matter effects are not correctly accounted for they may lead to an incorrect determination of the $\delta_{\mathcal{CP}}$ phase. This effect comes from the fact that charged-current electron-ν_e scattering is different from that of electron-$\bar{\nu}_e$ scattering.

Can matter effects help us learn more about neutrino oscillations? In short, yes, the oscillation probability in matter is sensitive to the sign of the mass splitting Δm_{ij} unlike those that propagate in a vacuum. This is what enabled the KamLAND Experiment to determine that m_2 is greater than m_1 when measuring reactor neutrinos [31]. As we have seen, the full ordering of the masses still needs to be determined. It is hoped that future accelerator-based neutrino-oscillation experiments will be able to measure the ordering by exploiting matter effects present as neutrinos travel through the earth.

1.3.3 Future Measurements

NuFit [30] provides global constraints on the various parameters associated to neutrino oscillations by combining information from numerous experiments. However, these fits, although useful, are unable to fully account for correlations and common systematics among the experiments. For example, when accounting for detector response effects, many experiments use the same simulation to model how particle trajectories propagate inside the detector. The simulation has

an inherent uncertainty which, when combined to produce a global result, often lead to incorrectly estimated uncertainties. The long-term goal is therefore to try to extract these parameters directly from the data of the combined experiments, incorporating a common systematic approach directly in the fitting procedure. This is currently being investigated by T2K and NOνA who are working towards the first joint oscillation measurement.

Experimentally all the oscillation parameters have been measured with the exception of the mass hierarchy and $\delta_{\mathcal{CP}}$, which until recently has been excluded from being $\mathcal{CP}$ conserving to a 90% confidence level [32]. This is now the focus of current [33, 34] and future [35, 36] accelerator-based neutrino-oscillation experiments. Experiments actively pursuing $\delta_{\mathcal{CP}}$ measurements are the Japanese based, T2K Experiment, which we shall learn more about in Chapter 4, and the US's NOνA experiment at Fermilab. Although this wasn't initially the goal of either experiment, the fact that Daya Bay [37] found θ_{13} to be large has made probing $\delta_{\mathcal{CP}}$ possible. If we refer back to the cross-mixing term in Equation 1.14, we see that the $\delta_{\mathcal{CP}}$ phase is coupled to $\sin\theta_{13}$ hence θ_{13}'s large value 'amplifies' any term it's associated with.

Measurements of $\delta_{\mathcal{CP}}$ by both T2K and NOνA have however shown that accelerator-based oscillation experiments are moving into the realm of systematically limited results. The dominant uncertainties are a result of our understanding of the neutrino flux and interaction cross section. Details of the flux and its associated uncertainty are given in Chapter 4.

The cross section uncertainty lies on our limited knowledge of how neutrinos interact with matter. This is due to the complex dynamics of the nucleus affecting the kinematics and particle content of the final state measured by scattering experiments. In accelerator-based neutrino-oscillation experiments these are used to evaluate the selection efficiencies of the respective signal and backgrounds, and in the reconstruction of the neutrino's energy. This can be seen

when considering the predicted event rate of some variable, x, at a distant, L, from which the neutrinos are produced

$$N(x) = \int dE_\nu \Phi(E_\nu)\sigma(E_\nu)P(\alpha \to \beta)\varepsilon(E_\nu)S(E_\nu, x). \tag{1.15}$$

The neutrino flux produced by the source is denoted by $\Phi(E_\nu)$, the interaction cross section $\sigma(E_\nu)$ and the oscillation probability $P(\alpha \to \beta)$. The final two terms, $\varepsilon(E_\nu)$ and $S(E_\nu, x)$, account for the detector's efficiency and smearing effects. Given that oscillation parameters are encompassed in $P(\alpha \to \beta)$ it is therefore crucial to understand the flux and cross-section of neutrinos along with the detector response. This is supported by studies from DUNE, a future long-baseline neutrino experiment, which have assessed the sensitivity to the $\mathcal{CP}$ violating phase. Their work shown in Figure 1.6, presents the uncertainty in $\delta_{\mathcal{CP}}$ as a function of exposure. Comparisons of the case for no systematics to those with systematics highlights the importance of reducing uncertainties in $N(x)$, namely, those associated to the flux and cross section.

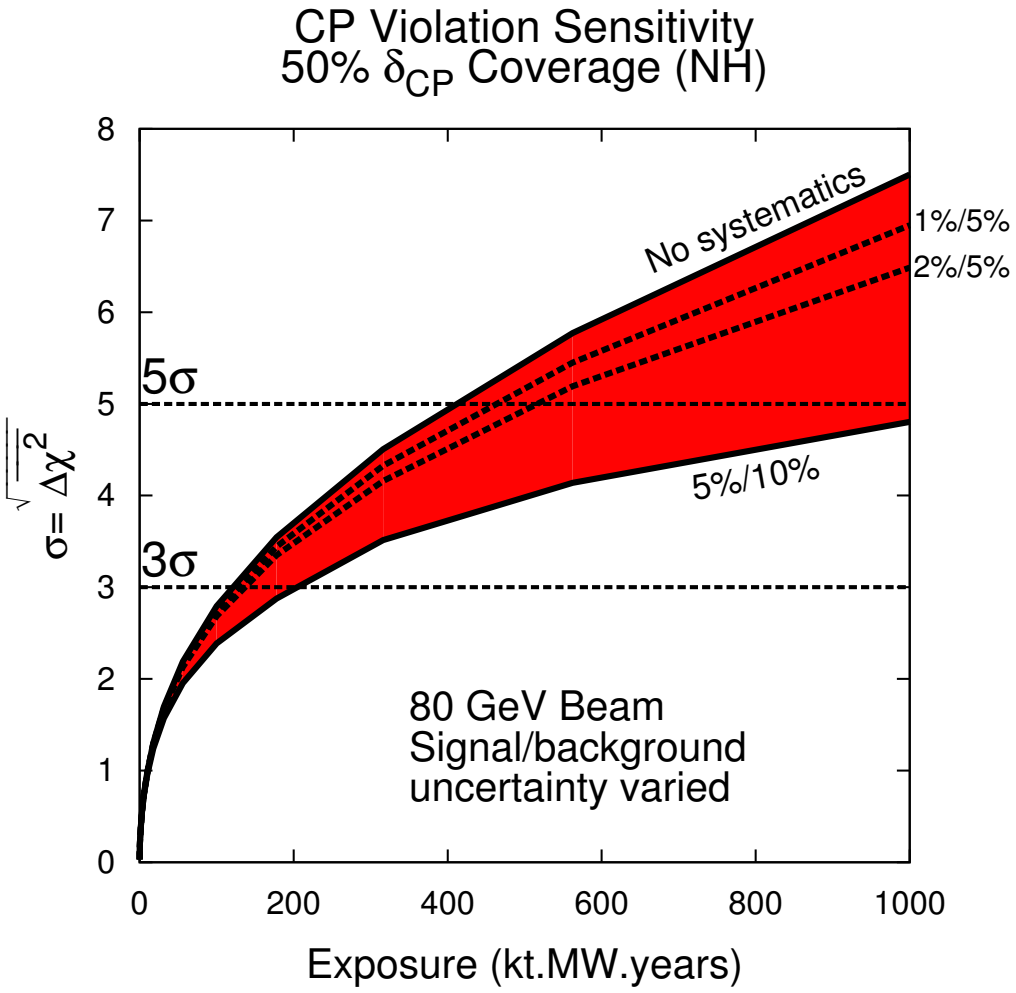

Figure 1.6: The DUNE Experiment's sensitivity for various fractional systematic uncertainties is presented as a function of exposure. Source [38].

Chapter 2

Neutrino-nucleus Interactions

In the previous chapter we discovered that our ability to probe any leptonic $\mathcal{CP}$ Violation is restricted by our current knowledge of neutrino interactions. This limited understanding is also highlighted by a number of ambiguities between experimental scattering results and their theoretical predictions. In order to overcome these issues both the experimental and theoretical communities have joined forces to improve our understanding of neutrino interactions. We shall therefore use this chapter to learn of both community's developments in this field.

In this chapter we begin with an overview of the neutrino interactions at the 'bare' neutrino-nucleon level. From here, the discussion will move onto the effects of neutrino interactions on nucleons bound within the nucleus. This will highlight the complexities in understanding neutrino scattering. We will then see how the various neutrino-nucleon interactions and nuclear effects are combined and implemented into a simulation. These simulations are used to make predictions for both neutrino interaction and oscillation experiments. This chapter concludes with additional effects that propagate through to oscillation measurements due to our limited understanding of neutrino interactions.

2.1 Neutrino-nucleon Interactions

Neutrino interactions are dictated by the V-A Weak interaction where the mediating boson may either carry charge (defined as charged-current or CC) or be neutral (defined as neutral-current or NC). Charged-current and NC processes occur over a broad neutrino energy range with different types of interaction dominating in certain regions. This can be seen in Figure 2.1 where the leading neutrino interactions are presented as a function of neutrino energy. Note that the cross section is normalised by the inverse neutrino energy and highlights the dominant interaction mode at a given energy. The processes defined in Figure 2.1 will be introduced in more detail momentarily along with sub-dominant diffractive processes. Given neutrino oscillations concern themselves with measuring differences between flavour abundances we shall only consider charged current neutrino interactions in this chapter.

General neutrino scattering theory considers the interaction cross-section whose dependence on some variable x is proportional to two terms, namely, the

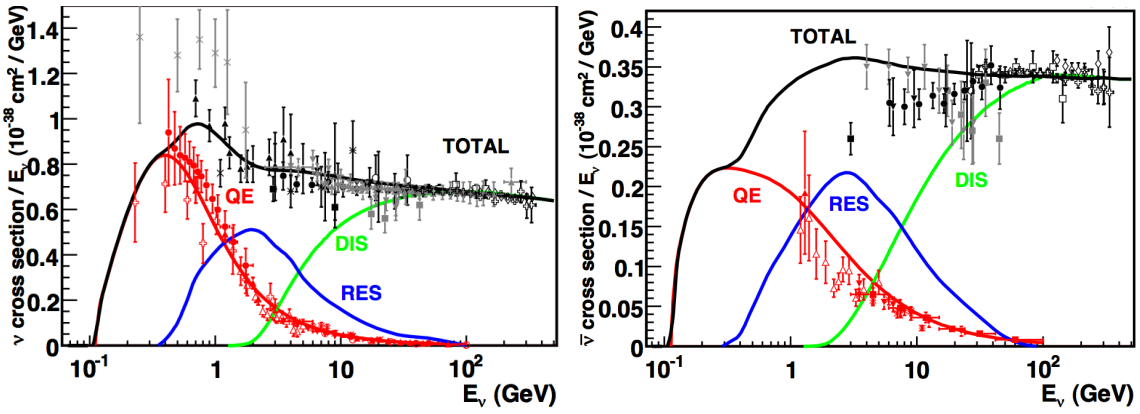

Figure 2.1: The inverse-energy normalised neutrino cross-section dependence as a function of incoming muon neutrino energy for ν_μ (*left*) and $\bar{\nu}_\mu$ (*right*). The data presented is from SKAT and various bubble chamber experiments [39]. NUANCE's [40] total cross section prediction is overlaid along with its simulation of individual interaction modes. NUANCE is a legacy neutrino interaction simulation package used between 2000-2010. Source [41].

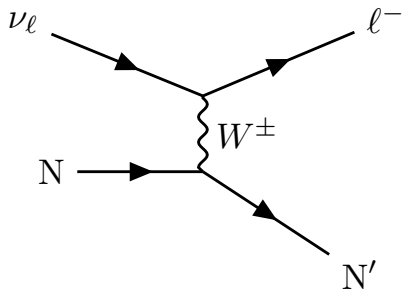

Figure 2.2: Charged-current Quasi-elastic Scattering Feynman diagram.

leptonic, $L_{\alpha\beta}$, and hadronic, $H^{\alpha\beta}$, tensors

$$\frac{d\sigma}{dx} \propto L_{\alpha\beta} H^{\alpha\beta}. \tag{2.1}$$

The lepton component is common to all interactions whereas the hadronic term defines the type of the interaction produced. In part, some of the terms in the hadronic tensor are constrained from data on electron scattering. This takes advantage of the unification of the electromagnetic and weak interaction providing information on the vector component of the electo-weak theory. As we shall see, however much of the uncertainty still lies in the hadronic term.

2.1.1 Quasi Elastic

The Charged-Current Quasi-Elastic process or CCQE dominates in the low neutrino energy region, starting from the rest mass energy of the neutrinos charged lepton counterpart to around 1.5 GeV. The Feynman diagram for this interaction is presented in Figure 2.2 and consists of an incoming neutrino exchanging a $W^\pm$-boson with a nucleon, N. The resultant final state contains a single charged lepton and a nucleon, N', with different isospin and charge to the initial nucleon. For neutrinos and anti-neutrinos the interactions are as follows

$$\nu_\ell + n \to \ell^- + p, \qquad \bar{\nu}_\ell + p \to \ell^+ + n. \tag{2.2}$$

In this energy regime the $W^{\pm}$ propagator interacts with the initial state nucleon as a whole and not individual quarks. As such the nucleon's dynamics must be modelled to include all quark contributions. However, due to the complicated nature of the strong interaction this cannot yet be solved analytically. One approach however is to calculate the cross section using form-factors that characterise the charge distribution of the nucleon. This was implemented in the Lleywellyn-Smith model. They developed a parametrisation which could rely on measurements from β-decay and electron scattering data. Their formalism reduced the number of degrees of freedom needed to be determined by neutrino scattering experiments [42]. In their model they determined the form factors from the charge distribution, $\rho(r) = \rho_0 e^{-Mr}$, leading to a form factor of the form

$$F_X(Q^2) \propto \frac{1}{\left(1 - \frac{Q^2}{M_X^2}\right)^2}. \tag{2.3}$$

Here $Q^2 \equiv -q^2$, where q^2 is the four momentum transfer from the incoming lepton to the stationary nucleon. The mass term, M_X, is distinct for the vector ($X = V$) and axial-vector ($X = A$) components of the weak interaction.

Although the vector component has been well constrained by electron scattering experiments, determining the axial term has become a topic of renewed interest. Early hydrogen and deuterium experiments found the world average for M_A to be 1.03 GeV [43], yet measurements on heavy nuclei did not agree with this value. For example, the MiniBooNE experiment, using a carbon-based target found M_A to be 1.35 ± 0.17 GeV [44].

MiniBooNE's measured axial mass was compared to various model predictions and data from other scattering experiments. These comparisons, shown in Figure 2.3, highlight the disagreement in the value of M_A. Here the reconstructed neutrino energy is presented for MiniBooNE's sensitive region (*top*) and an energy region spanning MiniBooNE, NOMAD and LSND neutrino fluxes

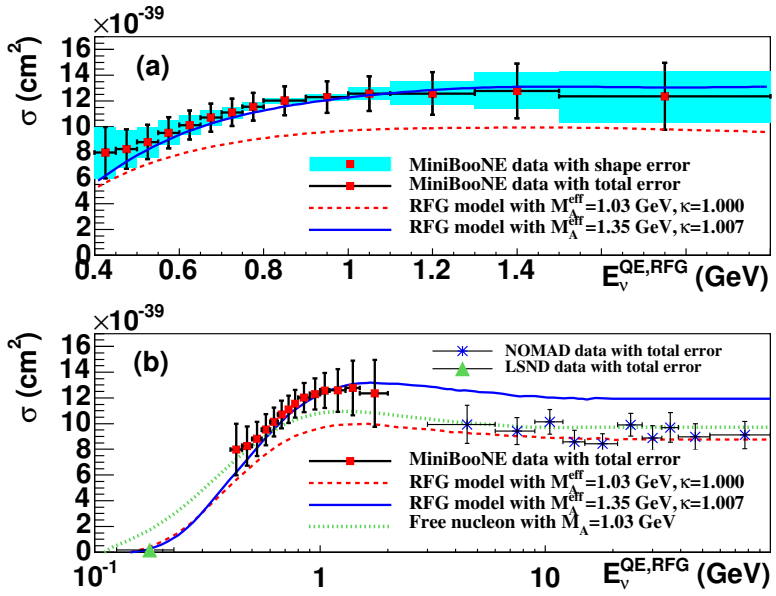

Figure 2.3: MiniBooNE CCQE measurement compared to NUANCE predictions for neutrino scatters from free nucleons and for carbon with two parameter choices for M_A. MiniBooNE's measured energy dependence (*top*) and the combined energy dependence for MiniBooNE, NOMAD and LSND (*bottom*) are presented. Source [44].

(*bottom*). From Figure 2.3 (*bottom*) there is a clear disagreement between data and prediction; no single model can fully describe CCQE interactions over a broad energy range. Data from the higher energy NOMAD experiment is well described by a free-nucleon prediction using the world average axial mass. On the other hand, the lower energy region below 2 GeV is well described by the prediction for CCQE interactions on carbon using the reported MiniBooNE M_A value. We shall see later that MiniBooNE's result indicated a presence of nuclear effects which were not incorporated into model predictions.

2.1.2 Resonance Production

Bridging the gap between quasi-elastic and deep inelastic scattering lies resonance production. This process dominates the energy region spanning $1.5 - 6.0$ GeV and produces a single pion in addition to a nucleon. The associated Feynman diagram for this interaction is presented in Figure 2.4 and can

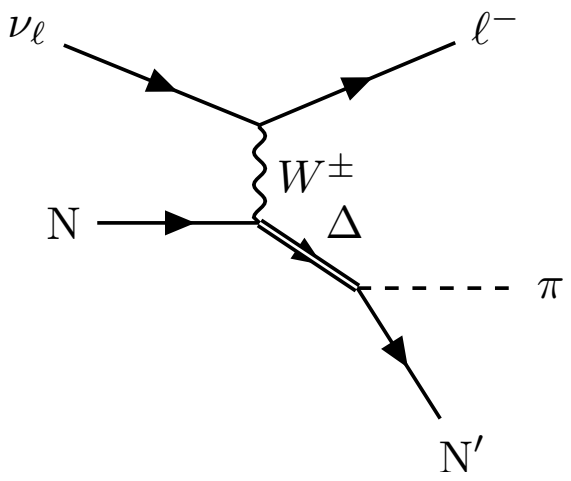

Figure 2.4: Charged-current Resonance Production Feynman diagram.

be broken down into the following interaction modes for neutrinos and anti-neutrinos

$$\nu_\ell + p \rightarrow \underbrace{p + \pi^+}_{\Delta^{++}} + \ell^-, \qquad \bar{\nu}_\ell + p \rightarrow \underbrace{p + \pi^-}_{\Delta^0} + \ell^+,$$

$$\nu_\ell + n \rightarrow \underbrace{p + \pi^0}_{\Delta^+} + \ell^-, \qquad \bar{\nu}_\ell + p \rightarrow \underbrace{n + \pi^0}_{\Delta^0} + \ell^+,$$

$$\nu_\ell + n \rightarrow \underbrace{n + \pi^+}_{\Delta^+} + \ell^-, \qquad \bar{\nu}_\ell + n \rightarrow \underbrace{n + \pi^-}_{\Delta^-} + \ell^+.$$

Here interactions produce an intermediate resonance state which subsequently decays into a baryon-pion final state. Note that only Δ resonances are presented here.

Like CCQE interactions, resonance production currently relies on a non-analytic approach when calculating the cross section. This was first developed by Rein-Sehgal where they incorporated 18 N and Δ resonances with a flat non-resonant background into their calculations [45]. The non-analytic approach is again used to describe the baryon charge distribution via form-factors and include an axial normalisation term C_5^A. Note that these form-factors are distinct from those in CCQE interactions and are often denoted M_X^{RES}.

The choice of baryon resonances was taken up to a pion-nucleon invariant

mass of 2 GeV as above this limit contributions from deep inelastic scatters begin to take effect. The region between resonance and deep inelastic scattering is complicated to calculate. Currently no single model has been developed to successfully describe the transition from form-factors to parton distribution functions used in deep inelastic scattering predictions. This leads to different interaction definitions for neutrino interaction generators.

Experimentally resonance production has been measured on a range of target nuclei however such measurements are either statistically limited or made using neutrino beam whose dynamics were not well understood [46–50]. In some cases, these measurements also include model dependences simply by their choice of cross section presented. One such case is as a flux averaged cross section like that performed in Reference [48]. It is therefore crucial for the experimental community to perform additional measurements using higher power neutrino beams and a result with reduced model dependencies. We shall also see later that resonance production is one of the dominant interactions relevant to current and future neutrino oscillation experiments. This only adds to the importance of understanding resonance production.

2.1.3 Deep Inelastic Scattering

Moving into even higher energies a process called deep inelastic scattering (DIS) begins to take effect. These scatters begin at neutrino energies of around 1.5 GeV and dominate above 10 GeV. In this energy regime, the four-momentum transfer for the $W^{\pm}$ propagator has a De Broglie wavelength small enough to resolve the individual quarks as depicted in Figure 2.5. This leads to final states containing many particles as the struck quark must hadronise as it moves away from the spectator quarks[1].

Deep inelastic processes are reliant on the modelling of two components,

[1]Spectator quarks are those that are not directly involved in the interaction but form part of the initial struck nucleon.

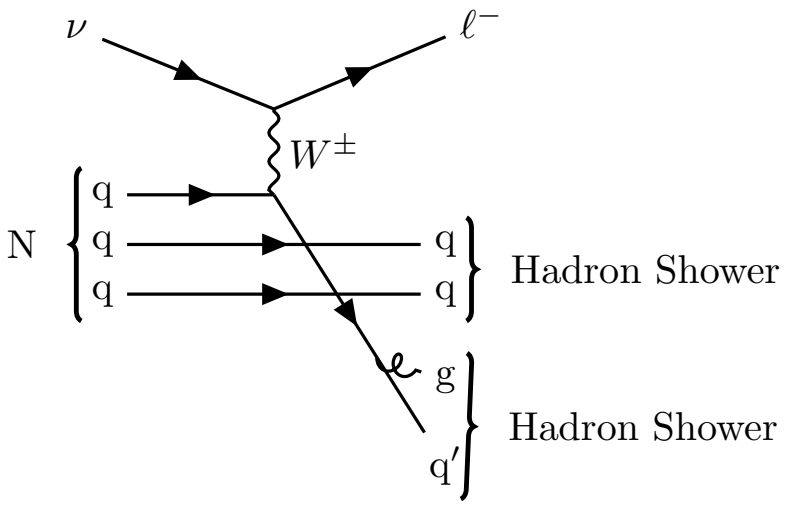

Figure 2.5: Charged-current Deep Inelastic Scattering Feynman diagram.

namely, the initial and final hadronic state. For the initial state, the probability of striking a particular quark flavour with some momentum must be determined. This is reached via the use of parton distribution functions to calculate the nucleon's structure. Parton distribution functions are well understood at high neutrino energies; however, due to the lack of data at lower energies it is unclear as to whether they can provide a good description at energies relevant to neutrino oscillation experiments. Finally, the DIS final state is determined using a fragmentation model to simulate the hadronisation process. This is typically modelled using PYTHIA – a QCD Monte Carlo algorithm [51].

2.1.4 Diffractive Scattering

The last interaction to be introduced is diffractive scattering. Here the neutrino scatters off of the nucleus as a whole given the low Q^2 process is not able to resolve individual nucleons. This produces a final state consisting of a recoiling nucleus and a single pion. As a result these are distinct from resonance production and DIS as the nuclear isotope remains unchanged pre and post interaction. There are two types of diffractive charged-current scattering, the first excites the nucleus and is known as incoherent scattering. The second type, titled coherent

scattering leaves the nuclear state unchanged. For a nucleus, A, the neutrino and anti-neutrino interactions are given by

$$\nu_\ell + A \to \ell^- + A^{(*)} + \pi^+, \qquad \bar{\nu}_\ell + A \to \ell^- + A^{(*)} + \pi^-.$$

Note that the asterisk represents the nucleus, A, being left in an excited state for the incoherent process only. Given the low Q^2 regime in which this interaction takes place a low event rate is expected for this interaction. As such, work on the theoretical framework is sparse however popular models include Rein's diffractive scattering [52] and coherent pion production by Rein-Sehgal [53, 54] or Berger-Sehgal [55].

2.2 Nuclear Effects

Having introduced the various neutrino-nucleon interactions we shall now outline effects which arise from neutrinos interacting with bound nucleons. Like in DIS nuclear effects, in general, affect both the initial and final state independently. Hence let us begin by outlining what effects arise inside the nucleus before the neutrino interacts followed by the subsequent effect of the final state system traversing through the nucleus. Although many of these processes are in principle common to all interaction types it will become clear later that most are only implemented into CCQE calculations.

2.2.1 Initial State

Up until now our focus has only been on neutrinos interacting on a static nucleon. However, if the nucleon is bound inside a nucleus the nuclear potential changes the dynamics of the interaction. The first component arising here is that of the Fermi motion produced from the potential. This causes the bound nuc-

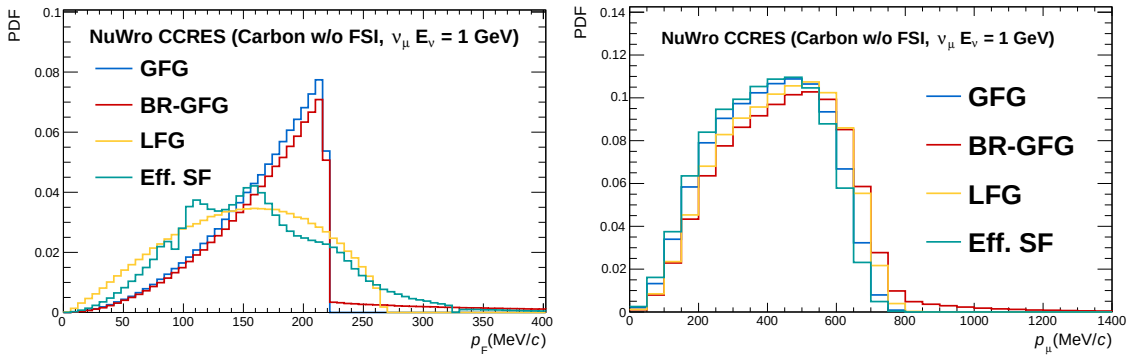

Figure 2.6: The Fermi momentum, $\boldsymbol{p}_{\mathrm{F}}$ (*left*) and muon momentum (*right*) is shown for different initial state models used in Charge Current Resonance production on Carbon. NuWro is used with no FSI and a mono-energetic 1 GeV ν_μ beam.

leons to possess some momentum. Currently four models are used to describe this phenomenon and all assume the motion to be isotropic. The Fermi motion models are summarised below and their predicted momentum distributions are given in Figure 2.6 (*left*).

- Global Relativistic Fermi Gas (GFG) – This is a simple and commonly used model which assumes non-interacting nucleons bound by a nuclear potential. The nucleons fill energy levels following Fermi-Dirac statistics up to a maximum energy equivalent to the Fermi momentum, $\boldsymbol{p}_{\mathrm{F}}$. The maximum momentum state, $p_{\mathrm{F,max}}$, results in a cliff-like feature known as a Fermi cliff which is dependent on the atomic mass, A. This is however not entirely physical as the nucleon binding energy does not depend on its position inside the nucleus.

- Bodek-Richie GFG (BR-GFG) – A modified GFG which includes a high-momentum tail in the $\boldsymbol{p}_{\mathrm{F}}$ distribution. This was introduced following the observation of this feature in electron scattering data.

- Local Fermi Gas (LFG) – This is similar to the GFG interpretation in that it assumes a set of non-interacting nucleons. The difference here is that the momentum is now dependent on the position of the nucleon within the

nucleus. It applies the local density approximation to determine the nucleon's momentum by considering the nuclear density, $\rho(r)$. Given nuclei have different atomic masses the momentum varies with A [56]. This is, in essence, a set of GFG's determined using $p_F(r) \propto \rho(r)^{1/3}$. Popular choices of the parametrisation of $\rho(r)$ are a Gaussian density and a two or three parameter Saxon-Wood potential [57].

- Spectral Function (SF)/effective SF (eSF) – Possibly the most realistic interpretation as it includes nucleon-nucleon correlations. These models like GFG and LFG are based on the shell model but include long range modifications arising from two and three nucleon interaction potentials. The models also incorporate short range correlations to describe the initial state above the Fermi cliff. Unlike the other initial state models SF may modify the final state and is therefore dependent on the final state produced. This has resulted in an effective SF being developed to describe this initial state model in interactions where SF have not been calculated [58].

Figure 2.6 (*right*) displays the predicted muon momentum, p_μ, given the various initial state models. The shape is similar in all cases making it hard to discriminate between various models using kinematics like p_μ. This indicates that other variables that are more sensitive to nuclear effects are needed to improve our understanding of neutrino-nucleus interactions.

The Pauli exclusion principle is also included in the modelling of neutrinos interacting with bound nucleons. This process, known as Pauli-blocking, ensures that the interaction only takes place if the out-going baryon momentum is greater than $\boldsymbol{p}_{\mathrm{F,max}}$. Hence when the Fermi motion of a struck nucleon, $\boldsymbol{p}_F$, and three momentum transfer $\boldsymbol{q}$ sum for an event fails $|\boldsymbol{p_F} + \boldsymbol{q}| < |\boldsymbol{p}_{\mathrm{F,max}}|$ the resultant interaction is suppressed [56].

Similar to the behaviour modelled by Spectral Functions an additional multi-nucleon effect has recently been included into cross section calculations. The

process known as 2p-2h or meson exchange currents (MEC), describes neutrinos interacting with two bound nucleons inside a nucleus. In 2p-2h interactions the final state consists of a nucleon-nucleon pair, making it distinct from CCQE scattering. This was introduced following advances in electron-scattering measurements which suggested that such multi-nucleon processes exist. It was believed that 2p-2h may help explain the MiniBooNE CCQE measurement as it would increase the predicted event rate. This phenomenon was first proposed by Nieves, Martini and collaborators when presenting an alternative approach to calculating CCQE scattering. They developed their theory to included additional contributions from 1p-1h and 2p-2h processes [59, 60]. Currently this model is limited to non-resonance final states but is believed to also be present in resonance production.

The final phenomenon known as Random Phase Approximation (RPA) describes an effect on the weak propagator. Unlike 'bare' neutrino-nucleon interactions where the $W^{\pm}$ propagator travels in vacuum, the mediator in neutrino-nucleus scatters must permeate the nuclear medium. This in-medium effect on the $W^{\pm}$ boson results in a screening effect causing in a suppression in the cross-section at low four-momentum transfer. Again this is only modelled in CCQE interactions and like 2p-2h was also developed by Nieves, Martini and collaborators. There is however strong evidence for this effect in resonance production [61].

Following the theoretical developments of 2p-2h and RPA the combined effects can be shown to resolve the MiniBooNE discrepancy. This is highlighted in Figure 2.7 which uses the same dataset as in Figure 2.3 (*top*) to compare the additional effects arising from the initial state. Interestingly the np-nh component over inflates the prediction relative to the data but RPA suppresses it. The combined effects of these processes leads to good agreement with MiniBooNE's data where a CCQE axial mass of 1.032 GeV is used [59, 62]. Note however these

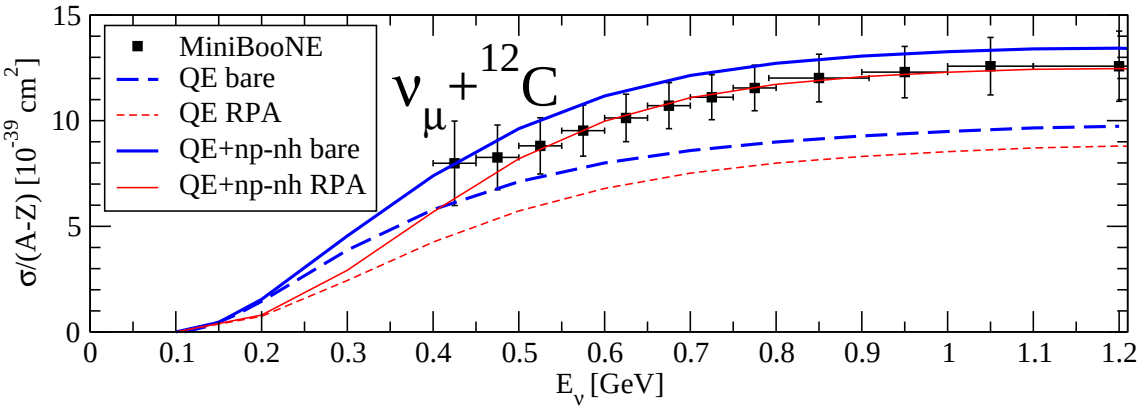

Figure 2.7: MiniBooNE's CCQE-like final state result is compared to predictions which include additional 2p2h and RPA effects. The combined prediction of QE+np-nh+RPA lead to good agreement with MiniBooNE's data. Source [62].

calculations do not include Final State Interactions which will also change the predicted event rate.

2.2.2 Final State Interactions

Following the neutrino-nucleon interaction inside the nucleus the final state travels through the nuclear medium. During this process the final state's kinematics and particle type can be altered leading to a different observed final state once the particles have escaped the nucleus. This is known as Final State Interactions or FSI and predominantly affects the hadronic transport through the nuclear medium. There are a total of six intra-nuclear processes incorporated into neutrino-nucleus simulations. Two are particle type dependent with the remainder being accessible to both pions and nucleons. Below are specific details of each process where the first four are available to all hadrons.

- Elastic Scattering – As the hadron traverses though the nucleus its kinematics are changed.
- Inelastic Scattering – Like elastic scattering except the nucleus is left in an excited state.
- Charge Exchange – A quark is exchanged between hadrons and nucleons

changing the particle type.

- Pion Production – In-medium interactions produce a pion which escapes the nucleus.
- Pion Absorption – A pion produced in a neutrino-nucleon interaction is captured by the nucleus.
- Nucleon Emission – Nucleon-nucleon collisions result in additional nucleons being emitted from the nucleus.

These processes are hard to predict due to difficulties in measuring the individual effects as multiple FSI may take place during intra-nuclear transport. It is further complicated by our inability to reliably distinguish such effects from the 'bare' neutrino-nucleon interaction. This is particularly important to the experimental community as we cannot reasonably say we are measuring a CCQE process in neutrino interactions on heavy nuclei. Let us consider a ν_μ CCQE process whose outgoing nucleon re-interacts inside the nucleus producing a π^+. Here the final state escaping the nucleus would be a single muon, proton and π^+ which is the signal definition for CC resonance production. Given this an experimentalist measuring resonance production would include CCQE events in their signal sample. Fortunately, the experimental community are now focussing on measuring final state topologies instead of interaction channels.

Although Final State Interactions generally refer to the intra-nuclear transport of hadrons the term may also affect the outgoing lepton. This is due to the nucleus' Coulomb potential changing the charged lepton's kinematics. Resonances produced inside the nucleus are also affected by the nuclear medium. This effectively narrows the resonance decay width leading to a longer lifetime. Theoretically it is implemented in a similar manner as Pauli Blocking, requiring the decayed resonance's final state nucleon to be above the Fermi momentum, $\boldsymbol{p}_{\mathrm{F,max}}$. Note these two processes are incorporated into the cross-section calculation.

2.3 Simulating Neutrino-Nucleus Interactions

If the complex dynamics of neutrino scattering is to be understood experimentally, both neutrino interactions and nuclear effects must be incorporated into event generators. These Monte Carlo simulations are used by both oscillation and scattering experiments to predict event rates like those discussed in Section 1.3.3. We shall therefore briefly outline the general approach used by GENIE [63], NEUT [64] and NuWro [65] event generators to simulate neutrino scattering.

Event generators rely on an input neutrino flux and target nucleus to produce an interaction. The process starts by randomly selecting an incoming neutrino energy for use in determining the 'bare' neutrino-nucleon interaction. This is found by calculating the relative contributions from each interaction type at the sampled neutrino energy before randomly identifying one as the candidate scatter. The chosen cross section must then be calculated given inputs like the incoming neutrino energy, $\boldsymbol{p}_{\mathrm{F}}$ and Q^2. From here the resultant cross section calculation provides a set of final state particles with kinematics dependent on the input model. Note that most event generators use precomputed cross-section look up tables to randomly sample from as this saves both time and computing power. If the interaction is on a light nucleus the simulation of an event is complete.

For heavy nuclei, the final phase of the Monte Carlo simulation is to propagate the hadronic system through the nucleus and determine whether any constituents undergo FSI. This starts at the position of the initial state nucleon(s) involved in the interaction. Each event generator has its own Cascade model which steps each hadron through the nucleus to determine if it undergoes FSI or not. The event generators differ substantially in their Cascade model. For example, GENIE's approach is to use a mean free path to determine if particles undergo FSI whereas NEUT simply assigns a probability of not undergoing FSI.

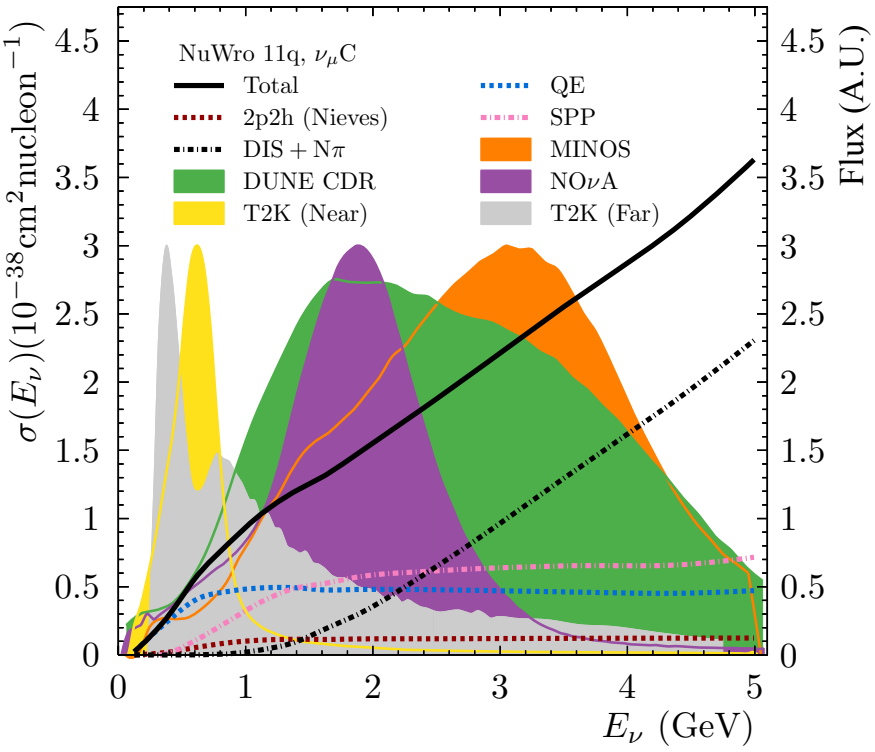

Figure 2.8: Various neutrino fluxes are presented for current and future long baseline neutrino oscillation experiments along with the neutrino cross section's energy dependence for the dominant interactions modes. The total cross section is also presented. The cross section predictions are produced using the NuWro event generator. Source [66].

From here both generators then randomly select the FSI type given the kinematics of the particle. The exact details of the cascade mechanism in each generator although interesting are beyond the scope of this thesis.

2.4 Neutrino Scattering at Oscillation Experiments

Having understood the processes involved in neutrino interactions it is now useful to consider how these affect oscillation experiments. Let us begin by reviewing which neutrino interactions dominate the various neutrino fluxes relevant to current and future long baseline neutrino experiments. This can be seen in Figure 2.8 which uses NuWro to predict the various neutrino scatters. One can

immediately see that almost all experiments are sensitive to all neutrino interaction modes. Starting from the lowest average E_ν, we see both T2K's near and far detector flux will produce predominantly QE interactions with small contributions from 2p-2h and resonance processes (SPP in Figure 2.8). As we increase in energy both the NOνA and DUNE fluxes take lead; here resonance begins to dominate over QE and a non-negligible DIS component starts to takes hold. Given our knowledge of how the event rates are predicted in Section 1.3.3, it is clear that if the $\delta_{\mathcal{CP}}$ phase is to be probed by multiple oscillation experiments all neutrino interactions must be understood.

Neutrino cross sections also enter into neutrino oscillation uncertainties through neutrino energy reconstruction. We have seen in Section 1.3 that neutrino oscillations are dependent on the neutrinos energy. Naturally, conservation of energy would tell us to simply measure the sum of the final state particle's energies. This is the approach used by NOνA, and is known as the calorimetric method

$$E_\nu = E_\ell + E_{\text{had}}, \quad \text{where} \quad E_{\text{had}} = (E_{\text{Cal}} - E_\ell). \tag{2.4}$$

Here E_ℓ represents the outgoing lepton energy, E_{had} the hadronic energy and E_{Cal} the calorimetric energy. The hadronic energy is determined by summing up all energy deposits that are not associated to the lepton track. This does not however account for Fermi motion and assumes a static nucleon in the initial state. Fortunately, Fermi motion merely cause a smearing effect in the reconstructed energy due to its isotropic nature. Although this broadening effect is dependent on the initial state model and leads to a model dependency. The added effect of FSI may also result in energy being missed by the detector. This could be due to neutral particles being emitted or a particle produced in the nucleus being absorbed by the nuclear medium.

The determination of the detector response is also dependent on nuclear effects. Experimentally we are reliant on Monte Carlo simulations to inform us

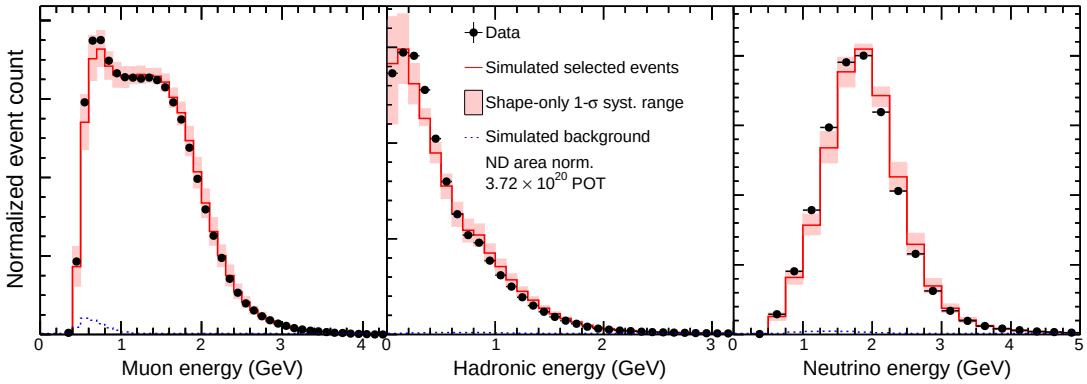

Figure 2.9: NOνA's ν_μ CC sample selected at its near detector. The reconstructed muon (*left*), hadronic (*center*) and neutrino (*right*) energy. The Monte Carlo is presented with the associated 1σ systematic uncertainty in its prediction. Source [67].

on how the reconstructed neutrino energy maps onto the true neutrino energy. The calorimetric approach therefore depends on having strong knowledge of nuclear effects. This is actually one of the dominant sources of uncertainty for NOνA and is highlighted by Figure 2.9. Presented is the calorimetric approach used for ν_μ events at NOνA's near detector. The reconstructed muon energy looks to be in good agreement with their Monte Carlo prediction but the hadron and resultant neutrino energy do not fully agree. In their publication they suggest that this is partly attributed to uncertainties in cross section and FSI models. As a result, these effects lead to some of the largest systematic uncertainties in their measurement of Δm^2_{32} [67].

An alternative method, named the kinematic approach, is often used by experiments that do not have sensitivity to the hadronic final state. The T2K experiment, given its far detector design, was designed to apply this method and resulted in the development of a flux that would predominantly induce QE interactions. Like the calorimetric approach the initial nucleon is assumed to be static leading to a similar smearing effect in the reconstructed energy. By applying this static nucleon assumption the neutrino's energy can be reconstructed using only the out-going lepton's kinematics. This enables the energy to be measured

under the QE approximation

$$E_\nu^{\mathrm{QE}} = \frac{2(m_n - E_b)E_\ell - (m_n - E_b)^2 + m_\ell^2 + m_p^2}{2(m_n - E_b - E_\ell + p_\ell \cos\theta_\ell)}, \tag{2.5}$$

where m_ℓ, m_n and m_p represent the masses of the lepton, neutron and proton respectively. The lepton's momentum and angle with respect to the incoming neutrino is given by p_ℓ and $\cos\theta_\ell$. Finally the E_b term defines the binding energy of the neutron inside the nucleus.

In addition to the smearing effect of Fermi motion the kinematic approach introduces a bias from non-QE backgrounds. This arises from non-QE events whose hadronic component are below the detection threshold passing as as QE-like events. These backgrounds would be reconstructed using the QE neutrino energy approximation (Equation 2.5) and result in incorrect energy determination. This bias can be seen in Figure 2.10 where the residual distribution for E_ν is presented. Here, using Monte Carlo, Equation 2.5 is applied to reconstruct the neutrino energy and compared to its true value. The effect of Fermi motion can be seen to smear the true QE event isotropically as expected. The backgrounds however highlight how the energy reconstruction is affected by non-QE processes. It is clear that both approaches to E_ν reconstruction are susceptible to uncertainties in neutrino scattering and demonstrates the importance of performing high precision cross section measurements.

Moving on to future experiments, like the US based DUNE experiment, it will also require precise knowledge of neutrino scattering. Currently, the DUNE experiment has a designed sensitivity of $\mathcal{O}(1-2\%)$ to the $\mathcal{CP}$ violating phase. Given the expected flux from Figure 2.8, this will lead to resonance production being one of the dominant interaction modes at DUNE . Although measurements exist for resonance production, they are on light nuclear targets like hydrogen and carbon. These measurements are either statistically limited like the early bubble chamber experiments [46–49], or do not always consider the full reson-

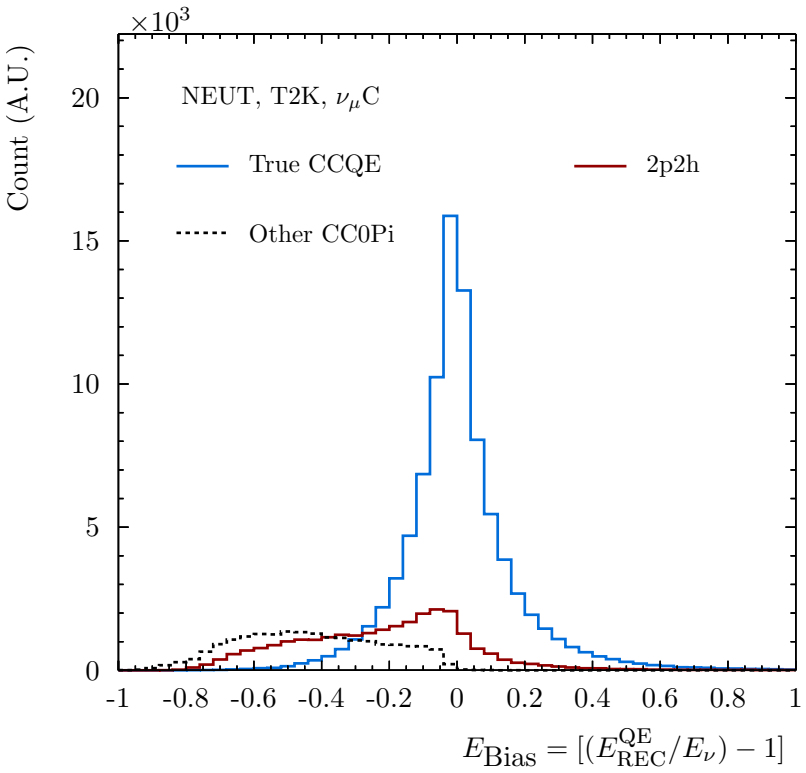

Figure 2.10: T2K's predicted bias in the reconstructed neutrino energy arising from non-QE backgrounds. Source [66].

ance final state like at MINERνA [68]. The full final state should be measured to better understand this process. Additionally, the DUNE experiment plans to use argon as its main target nuclei. Few measurements exist on argon further supporting the case for the experimental community to pursue new measurements of the resonance-like interaction mode. In conclusion we have seen how cross section uncertainties manifest themselves in oscillation measurements. We therefore require new measurements of semi-exclusive final states fulfilling the resonance topology on heavy nuclei to reduce these systematic uncertainties.

Chapter 3

Isolating Nuclear Effects

In the previous chapter it became apparent that nuclear effects conceal themselves as subtle variations in fundamental kinematics. This was highlighted in Figure 2.6 (*right*) where different initial state model predictions for muon momentum were presented. These small variations in variables that consider only part of the final state are not experimentally distinguishable given current detector technologies. An alternative approach is therefore required to probe nuclear effects.

Let us begin by considering the bare Charged-Current neutrino-proton resonance interaction. The final state would contain at least three particles: a muon, proton and pion. At the neutrino-nucleon level the sum of the final state four-momenta should equal that of the initial state. In this instance the nucleon is unbound leaving kinematic contributions coming from the neutrino only. If one now translates this interaction into a bound nucleus and performs the same measurement contributions would arise from the initial state proton. Any observation of non-conservation of four-momentum would be a direct measure of nuclear effects. Unfortunately this approach relies on the experimenters' ability to reconstruct the neutrino energy. We have already learnt that this is dependent on the nuclear model and therefore convolutes our ability to reliably understand

nuclear dynamics. Hence an approach is needed that considers semi-exclusive final states and has minimal dependence on the incoming neutrino energy.

This chapter will begin by outlining the variable used to probe nuclear effects before assessing the available interaction modes that the variable could be applied to. The ideal case will then be introduced in order to highlight the variables ability to isolate and discriminate between different nuclear effects. Expanding on from the idealised case, a topological study shall be undertaken to understand what should be expected experimentally. Comparisons will be made using the NuWro, NEUT and GENIE neutrino event generators where specific configurations are given throughout this chapter. Finally a method of directly probing Final State Interactions of pions will be presented for use in current and future experiments.

3.1 Double Transverse Momentum

The variable presented throughout this thesis, namely, Double Transverse Momentum considers a three particle final state which at the neutrino-nucleon level is produced predominantly via resonance production. This method was first introduced in Reference [69] as a means of isolating interactions on hydrogen but may also be used to probe nuclear effects. By considering a muon, proton and π^+ final state, a plane can be defined between the incoming and outgoing lepton. This is known as the leptonic plane. The hadronic system's momentum can then be projected onto the vector perpendicular to the leptonic plane as depicted in Figure 3.1. The vector perpendicular to the lepton plane, $\boldsymbol{z}_{\mathrm{TT}}$, is defined as

$$\boldsymbol{z}_{\mathrm{TT}} = \frac{\boldsymbol{d}_\nu \times \boldsymbol{p}_\mu}{\left|\boldsymbol{d}_\nu \times \boldsymbol{p}_\mu\right|}, \tag{3.1}$$

where $\boldsymbol{d}_\nu$ is the incoming neutrino's direction and $\boldsymbol{p}_\mu$ is the outgoing muon's momentum. From here the proton, $\boldsymbol{p}_{\mathrm{p}}$, and pion, $\boldsymbol{p}_{\pi^+}$, momentum can be projected

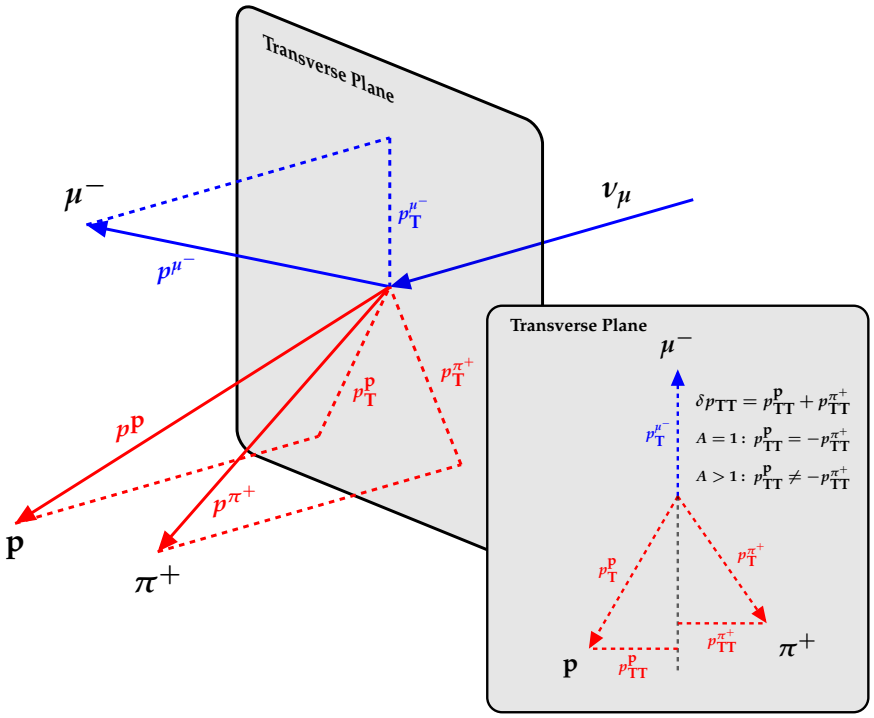

Figure 3.1: Schematic of Double Transverse Momentum in the laboratory frame (background) and the frame transverse to the incoming neutrino's direction (foreground).

onto z_{TT} leading to Double Transverse Momentum

$$\delta p_{TT} = z_{TT} \cdot \left(\boldsymbol{p}^p + \boldsymbol{p}^{\pi^+} \right) = p_{TT}^p + p_{TT}^{\pi^+}. \tag{3.2}$$

The name derives from being transverse to both the incoming and outgoing lepton, as such this probes deviations arising from the 'bare' neutrino-nucleon interaction. In the absence of nuclear effects the nucleon is static and therefore balances δp_{TT} ($p_{TT}^p = -p_{TT}^{\pi^+}$). Bound nucleons on the other hand will have contributions from both the initial and final state that can result in having hadron momentum vectors codirectional to z_{TT}. Such effects will therefore lead to non-conservation of δp_{TT} and act as a probe to nuclear effects.

Double Transverse Momentum can be extended to analyse various final states produced via Charge-Current Resonance production. These final states are outlined in Table 3.1. Unlike CCQE interactions, both neutrinos and anti-neutrinos can interact with proton's. This provides access to free nucleon interactions

Incoming	Initial Nucleon	Intermediate State	Final State		
ν_ℓ	n	Δ^+	$n\pi^+$	$p\pi^0$	ℓ^-
	p	Δ^{++}	$p\pi^+$		
$\bar{\nu}_\ell$	n	Δ^-	$n\pi^-$		ℓ^+
	p	Δ^0	$n\pi^0$	$p\pi^-$	

Table 3.1: The dominant neutrino-nucleon production modes for Charged Current three particle final states.

via neutrino scatters on hydrogen. Not only does this provide cross section measurements free from nuclear effects but also reliable reconstruction of the neutrino energy spectra [69]. Although final states containing neutrons can be measured, experimentally this would be complicated due to the low detection efficiency and kinematic reconstruction of neutrons.

3.1.1 Probing Pion FSI

One can expand upon the probing power of δp_{TT} and enable direct access to pion FSI. By redefining Double Transverse Momentum to make the proton's p_{TT} positive

$$\delta p^{q}_{\mathrm{TT}} = |p^{\mathrm{p}}_{\mathrm{TT}}| + p^{\pi^q}_{\mathrm{TT}}, \tag{3.3}$$

where q denotes the pion's charge, the signed-δp_{TT} is defined. This is sensitive the to sign and magnitude of the pion's p_{TT}. Given proton FSI are independent of the neutrino interaction it is possible to remove its contribution by considering differences between the three pion's signed-δp_{TT}. For example, π^+ and π^- FSI deviations may be evaluated by

$$\Delta p^{+-}_{\mathrm{TT}} = \delta p^{+}_{\mathrm{TT}} - \delta p^{-}_{\mathrm{TT}} = p^{\pi^+}_{\mathrm{TT}} - p^{\pi^-}_{\mathrm{TT}}. \tag{3.4}$$

Here the proton's contribution has been removed. This therefore acts as a test of whether pion FSI are type dependent. Such tests would be interesting to undertake at future experiments which have access to multiple semi-exclusive $p\pi^q$ final states. Given data of such final states is currently sparse a more in-depth evaluation of this proposal is beyond the scope of this thesis.

3.2 Resonance Production

A natural starting point is to begin by studying δp_{TT} using an idealised case. This is reached via Resonance production as it produces the required final state used to calculate δp_{TT}. We shall then systematically work towards a real world scenario making comparisons between various effects throughout.

Possibly one of the most powerful probes of Double Transverse Momentum is that it is able to isolate interactions on hydrogen. Given this, much of what is discussed in this chapter focuses on Resonance-like events containing exactly one muon with at least one proton, one $\pi^+$and no other pions. The requirement of at least one of each hadron has been chosen for comparisons with other heavier nuclei. This is because FSI can result in multiple same type hadrons exiting the nucleus. In such cases the highest momentum hadron is used to calculate δp_{TT}.

In the absence of intra-nuclear transport, Figure 3.2 presents comparisons of the δp_{TT} distribution for different nuclei. Here NuWro has been configured to produce resonance production with a mono-energetic 1 GeV ν_μ beam. Heavy nuclei (A>2) are modelled using a LFG. In Figure 3.2 hydrogen has a very distinct Dirac-delta-like function centred at zero. This is a direct result of neutrinos interacting on a static proton. The hydrogen component has been scaled down by a factor of four here to enable differences between other nuclei to be seen. One interesting feature is hydrogen's small non-zero contribution around zero. This is caused by higher resonances producing additional particles in the final state resulting in non-conservation of momentum. Studies have shown that when

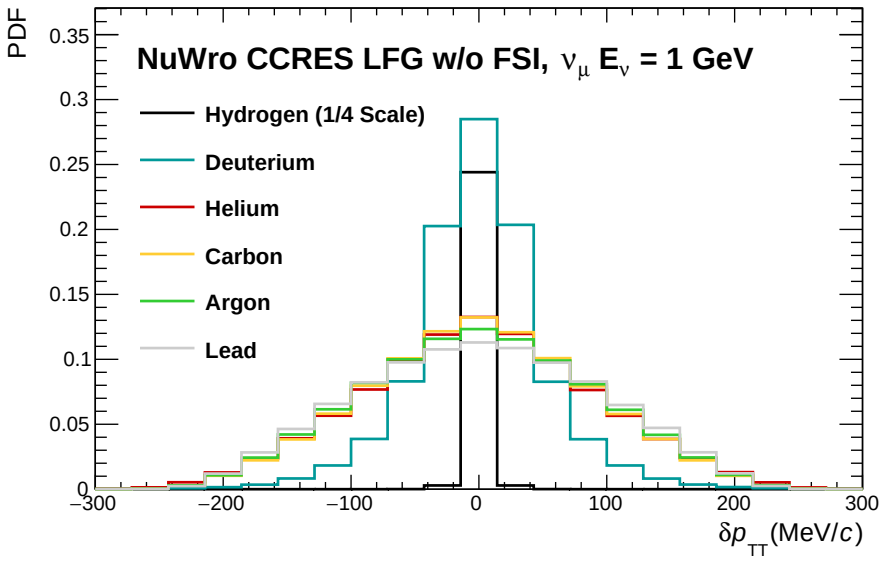

Figure 3.2: NuWro's δp_{TT} prediction for various nuclei of Charge Current Resonance production. The heavy (A>2) nuclei are modelled using a local Fermi gas where the final state undergoes no FSI. The nuclei are impinged on by a mono-energetic 1 GeV ν_μ beam.

constraints are placed on the total number of final state particles this feature disappears.

Moving on to heavier nuclei, from Figure 3.2, one can see a clear link between the atomic number, A, and the relative abundance in the central region of δp_{TT}. The local Fermi gas, whose Fermi momentum is dependent on the nuclear radius, results in a reduction in the central region and broadening in the tails as A increases. Note that the end-points of δp_{TT} are the same as the maximum Fermi motion which for carbon is approximately 220 MeV/c. A consequence of generalising the modelling of heavy nuclei leads to a very distinct transition from deuterium to helium. Deuterium's nuclear initial state is unique in that it can be solved analytically producing its Gaussian-like distribution in δp_{TT}.

From Figure 3.2 one can imagine how, in composite nuclear targets containing hydrogen, δp_{TT} could be used to isolate interactions on hydrogen. Experimentally, hydrogen's delta-like function would sit on top of the heavy nuclear back-

ground allowing the hydrogen component to be extracted on a statistical basis. This would however require good reconstruction of the final state kinematics.

Before assessing the various aspects of nuclear effects in δp_{TT}, it is important to ensure the dynamics of neutrino induced resonance production is understood. In Chapter 2 we learnt that the general approach to calculating the scattering amplitude is to use empirical form factors to model the baryon charge distribution. The choice of parametrisation is known to effect the shape in distributions like Q^2 and E_ν but what about Double Transverse Momentum? This shall now be investigated to understand how model variations change δp_{TT}'s shape, and if it is dependent on the final state produced. If δp_{TT} is sensitive to such effects, it will convolute our ability to understand nuclear effects in this variable.

The first assessment considers the axial form factor, in particular its parametrisation using both the signal definition previously defined and one in which the π^+ is exchanged with a π^0. Such comparisons are important if different final states are to be used to infer information on others. We shall learn later that this is one of the aims of the MINERνA analysis introduced in Chapter 6.

In Figure 3.3a the two final states are presented using different functional forms to the baryon charge distribution. The first case considers NuWro's default parametrisation, a dipole form factor, the second presents work by L. Alvarez-Ruso *et al.* and finally a Chiral Quark model features as our last case. Note here that the exact formalism of these form factors is beyond the scope of this thesis, however the interested reader may refer to Reference [65] for further details.

From Figure 3.3a, we clearly see that in both final states the shape is preserved and no difference is observed between all the parametrisations. Having understood the form factors independence on δp_{TT}'s shape we should briefly evaluate variations to the nominal dipole form factors free parameters, namely, M_A^{RES} and C_A^5. Different values for each of these free parameters is presented in Figures 3.3b and 3.3c. Although the choice of value for each parameter pre-

dominantly effects the normalisation, given that we present pdfs indicates that variations have no effect of the shape of δp_{TT}. We can therefore conclude that the resonance parametrisation does not change δp_{TT}'s shape.

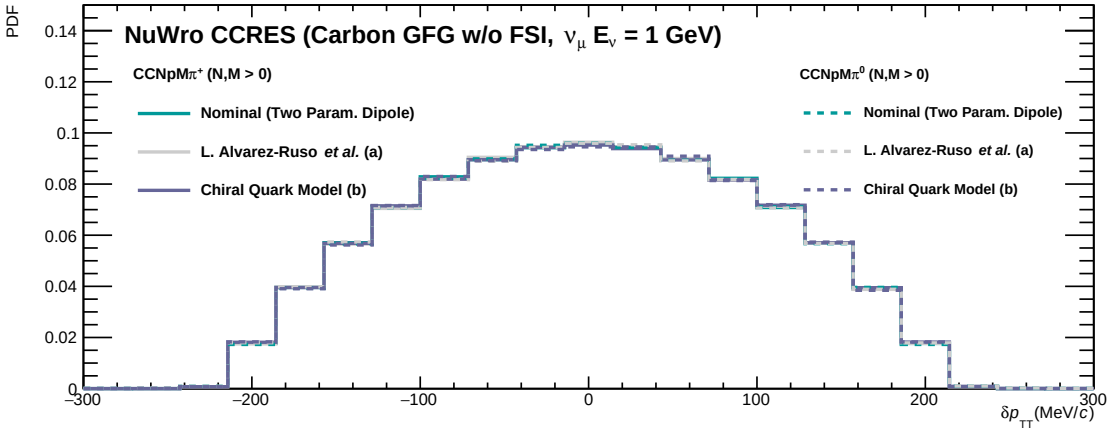

(a) Different parametrisations of the Axial Form Factor are presented.

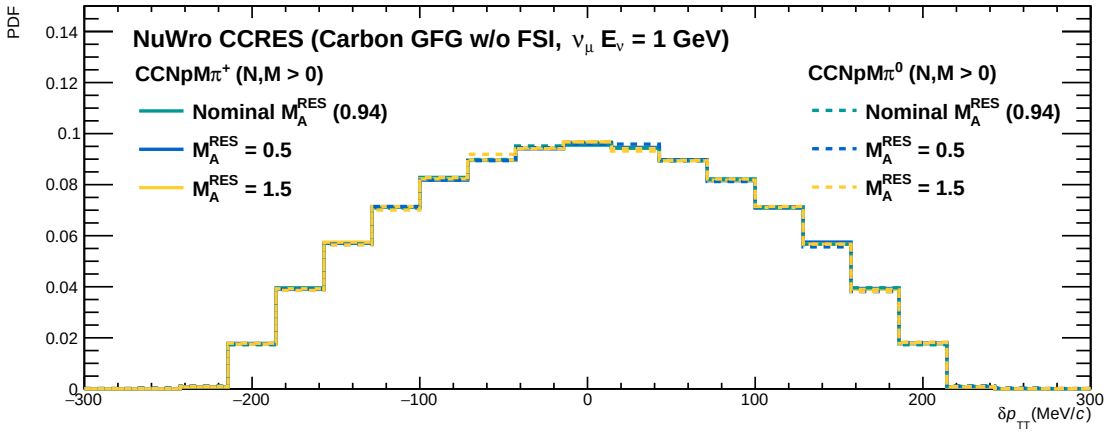

(b) The nominal two parameter Axial Form Factor is presented with different Axial mass, M_A^{RES} values.

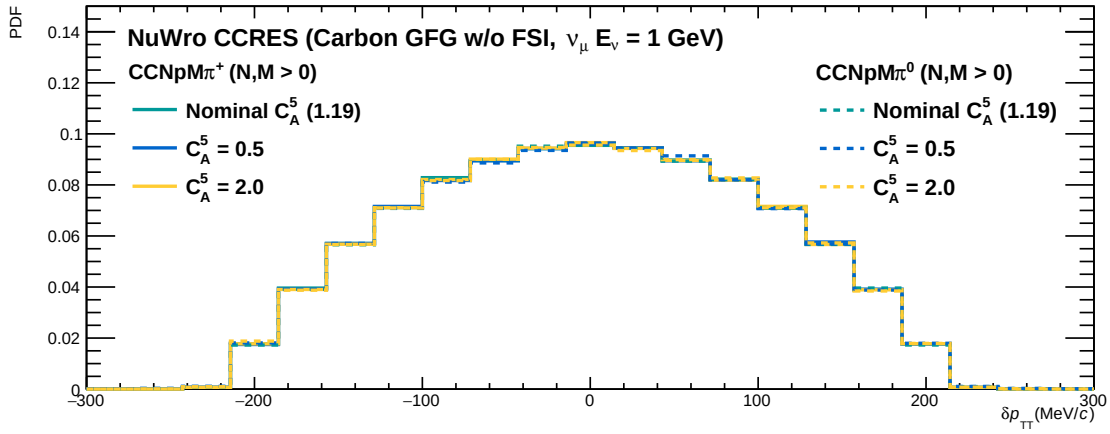

(c) The nominal two parameter Axial Form Factor is presented with different C_A^5 values.

Figure 3.3: NuWro's δp_{TT} prediction for various model variations of Charge Current Resonance production. Carbon is modelled as a Global Fermi Gas and final states undergo no FSI. The target is impinged on by a mono-energetic 1 GeV ν_μ beam.

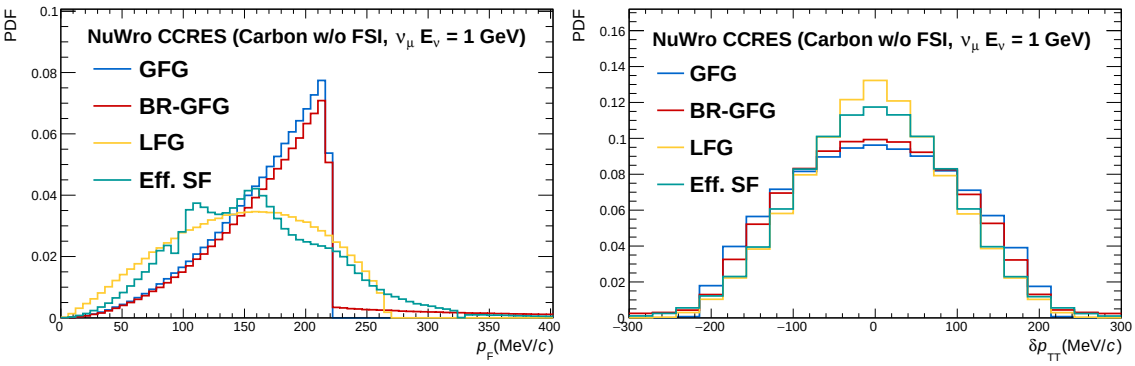

(a) $\boldsymbol{p}_{\mathrm{F}}$ distribution. (b) δp_{TT} distribution.

Figure 3.4: Different initial state models are presented for Charge Current Resonance production on Carbon. NuWro is used with no FSI and a mono-energetic 1 GeV ν_μ beam.

Given that δp_{TT} is insensitive to different resonance production parametrisations what can be learnt about nuclear effects in δp_{TT}? Starting with the nuclear initial state, Double Transverse Momentum is able to distinguish between different initial state models. This can be seen when NuWro is used to compare its four initial state models in Figure 3.4. Both the initial state Fermi momentum, $\boldsymbol{p}_{\mathrm{F}}$, and δp_{TT} distributions are presented. Note that we are now considering final states containing exactly one muon at least one proton and π^+ with no other pions. With the exception of the initial state model the configuration of NuWro is identical to that presented in Figure 3.2 for carbon.

One should notice the almost identical distribution in both δp_{TT} and $\boldsymbol{p}_{\mathrm{F}}$ for the GFG and BR-GFG models. Both have a sharp discontinuity at 220 MeV for $\boldsymbol{p}_{\mathrm{F}}$ which translates to the approximate end points in outer tails of δp_{TT}. The addition of a high momentum tail in BR-GFG model was introduced following measurements of electron scattering. They were able to fully infer $\boldsymbol{p}_{\mathrm{F}}$ given the incoming lepton's kinematics, something which is not readily accessible to neutrino experiments. The LFG and eff. SF models follow a similar shape with the latter exhibiting numerous peaks and troughs in $\boldsymbol{p}_{\mathrm{F}}$ which are believed to be caused by nuclear Resonances [70]. From Figure 3.4b it is clear that in the central

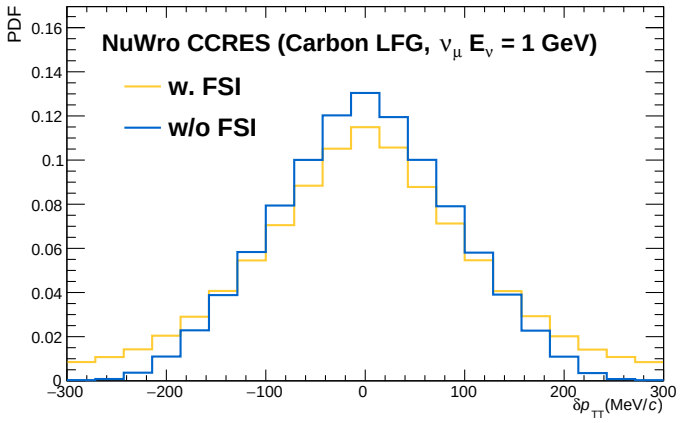

Figure 3.5: Comparisons between neutrino interactions with and without intra-nuclear transport. Here NuWro has been configured to produce Charge Current Resonance interactions on carbon (LFG) with a 1 GeV ν_μ beam.

region of δp_{TT} the models differ by up to 30%. As mentioned earlier δp_{TT} could be used to extract the hydrogen component in composite nuclear targets. This large variation would however lead to a large uncertainty in determining the event rate on hydrogen. Therefore, if such a measurement is to be realised it is crucial to constrain the shape of the nuclear background.

Having understood the predictions of different initial states and nuclei in δp_{TT}, intra-nuclear transport is examined by comparing carbon with and without Final State Interactions in Figure 3.5. There is a notable broadening feature in δp_{TT} when FSI are permitted. The δp_{TT} tails reach beyond the 220 MeV end-points caused by Fermi momentum when the final state hadrons undergo intra-nuclear transport. Similar to the effect of various initial state models, the central region is also affected by FSI resulting in up to a 10% reduction compared to no FSI. Again this emphasises the need to measure the shape of heavy nuclei in δp_{TT} for hydrogen measurements to be made.

Before moving onto a more physical scenario it is useful to gain an insight into δp_{TT}'s dependence on the incident neutrino flux. Kinematic variables which are highly dependent on the neutrino flux can lead to added unwanted sys-

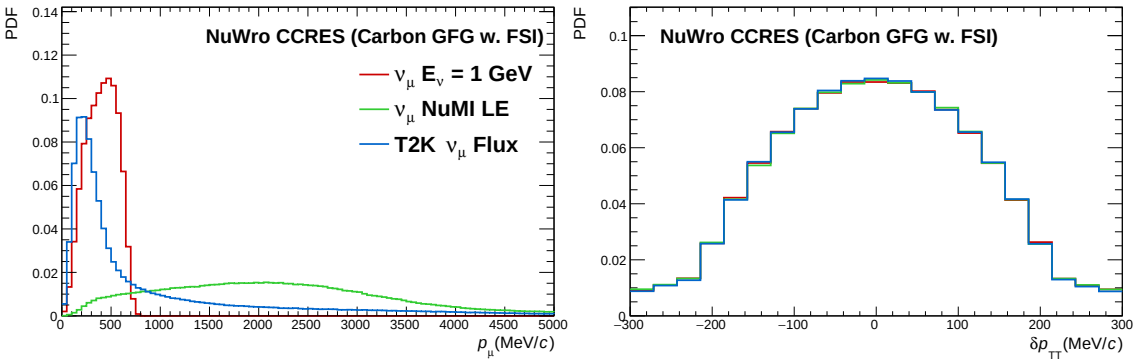

(a) Muon Momentum. (b) Double Transverse Momentum.

Figure 3.6: Various neutrino fluxes highlight the minimal dependence on δp_{TT} as opposed to muon momentum where the distribution for each flux type is very different. NuWro is configured to model carbon as a GFG and final states undergo FSI.

tematic uncertainties in the variables shape. It is therefore interesting to consider the effect of different fluxes covering a broad neutrino energy spectra on Double Transverse Momentum. This can be seen in Figure 3.6 where the a 1 GeV ν_μ flux is shown alongside the NuMi Low Energy (LE) and T2K fluxes. For comparison purposes muon momentum is also presented with δp_{TT}. This highlights how different fluxes can result in large differences in the prediction of certain kinematic variables. Clearly the muon momentum is highly dependent on the incoming flux whereas Double Transverse Momentum is almost unchanged. It is worth pointing out however that higher energy fluxes do cause a broadening in δp_{TT} , albeit small, leaving the shape fairly well preserved between the other fluxes.

3.3 Topological Study

Following on from understanding the behaviour of Resonance production in δp_{TT} focus now moves to a more physical, real world scenario. As discussed in Chapter 2 Final State Interactions can result in contributions to the final state from other neutrino-nucleon interactions. An assessment of the cumulative behaviour of all such processes in δp_{TT} is therefore needed to see how the predictions change.

At this point it is useful to compare the various Monte Carlo event generators and assess how their predictions differ. The generators are therefore configured to enable the production of all interactions before the final state previously defined is selected. By translating NuWro and GENIE's interaction modes into NEUT's definition[1] it is possible to first compare what each generator breaks its modes into. This is highlighted in Figure 3.7 where each generator has been configured to produce interactions using the NuMi LE beam and a carbon target. For each neutrino event generator two cases have been considered; one in which final states undergo no Final State Interactions (*left*) and the other where intra-nuclear transport is applied (*right*).

There are a number of notable features observed in the various distributions. The most obvious is the difference between GENIE with and without FSI (Figures 3.7e and 3.7f). This shape has been found to be a due to the elastic component of FSI. GENIE's modelling of this results in an abundance of events in the central region of δp_{TT}. This is emphasised by Figure 3.8 where the GENIE standard configuration is considered with cases where certain intra-nuclear components are removed. Here GENIE's nominal prediction is compared with three cases in which the elastic component of FSI are removed. Three scenarios are considered; the first two remove pion and proton elastic FSI individually and

[1]NEUT 's definition of interaction modes along with which group they have been classified here can be found in Appendix A.

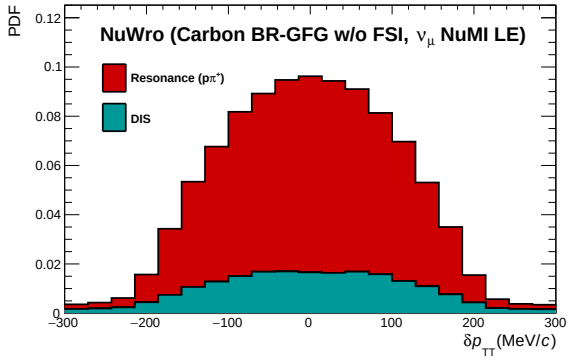

(a) NuWro without FSI.

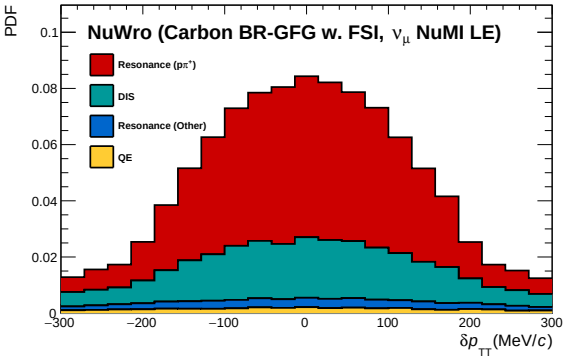

(b) NuWro with FSI.

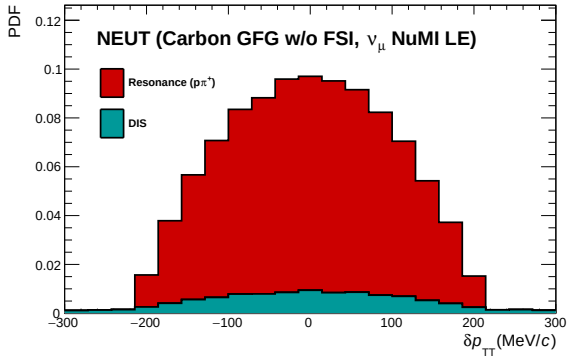

(c) NEUT without FSI.

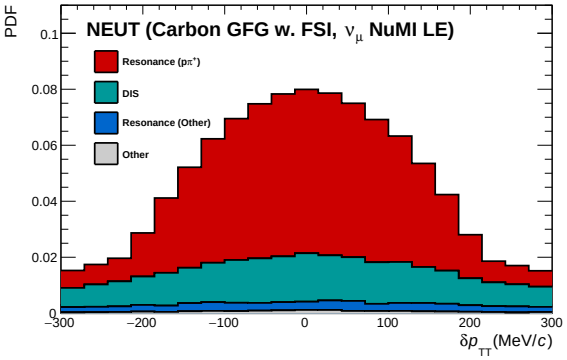

(d) NEUT with FSI.

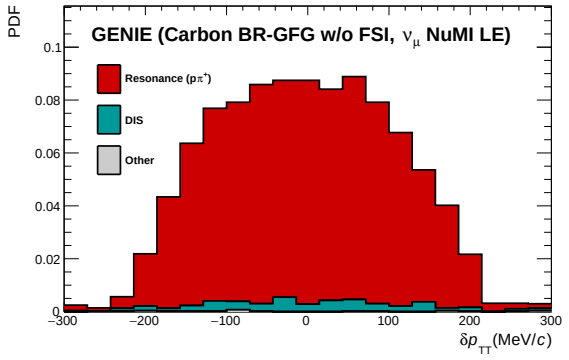

(e) GENIE without FSI.

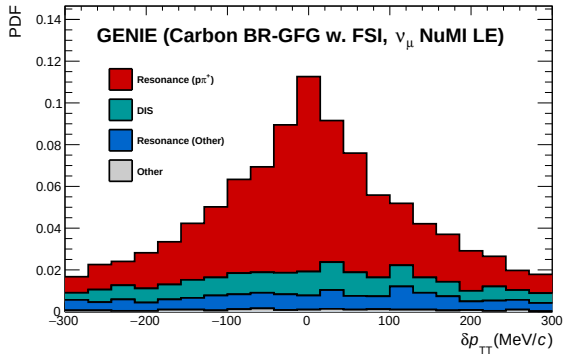

(f) GENIE with FSI.

Figure 3.7: Interaction modes are broken down into NEUT's definition of interaction modes for NuWro and GENIE. Each generator is set to produce all possible interactions on a carbon target. Here interactions induced using the LE NuMi beam and undergo no FSI (*left*) and FSI (*right*).

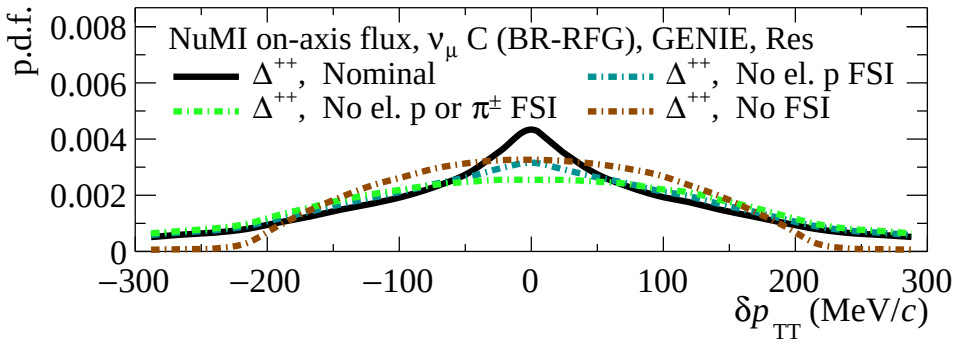

Figure 3.8: Charged Current Resonance Production on carbon (BR-GFG) is presented using GENIE where four scenarios are given. The first being GENIE's nominal prediction followed by cases in which the elastic component of FSI are removed for each particle type, namely, protons and pions. Here GENIE uses the NuMi LE beam flux when producing neutrino events. Source [71].

the last excludes both FSI. By comparing the case where GENIE has its elastic component removed ('No el. p or $\pi^{\pm}$ FSI' distribution in Figure 3.8) with the predictions made by NEUT and NuWro in Figure 3.7 (*right*) comparative agreement can be made between all of the neutrino event generators. This indicates a possible over prediction in the elastic component of FSI for GENIE in comparison to the other generators.

Let us return back to Figure 3.7. In general NEUT and NuWro's shapes look to be similar but their normalisations differ. When interactions undergo no FSI the shape of δp_{TT} is similar between all three generators with particular agreement being observed between NEUT and NuWro. All the generators include a Resonance and DIS component with GENIE including additional processes. On the other hand, when interactions undergo FSI the DIS contribution increases and other forms of scattering enter the distributions. Given that each generator is set to model all interactions, contamination from non-resonance interactions enter into the final state. This is highlighted by Figures 3.7b, d and f where Resonance (Other) undergo charge exchange and protons from QE produce pion(s) as they traverse through the nucleus.

3.3.1 Experimental Phase Space Constraints

Our final consideration lies in understanding the affect of phase space restrictions. This will enable us to assess a situation which is more in line with what can be measured experimentally. Detectors are restricted by their technology and configuration leading to limited reconstruction of low energy tracks as well as a tracks direction. These effects restrict the phase space to some region in which the experiment is sensitive. Here T2K and MINERνA's final state topologies used in Chapters 5-8 are considered. This will allow us to assess whether information is lost by kinematic constraints.

The analysis on T2K is aimed at isolating neutrino interactions on hydrogen therefore the final state of interest is a single muon and exactly one proton and one π^+. Both hydrogen and carbon are considered here as this final state is induced via neutrino-proton interactions. It is important to know how the shape of carbon is affected to ensure that kinematic constraints do not result in large changes in the δp_{TT} distribution. The MINERνA analysis focusses on understanding the shape of carbon in δp_{TT} by evaluating neutrino induced final states containing one muon and at least one proton and π^0. The details of these restrictions shall be given in Chapter 5 for the T2K analysis and Chapter 6 for MINERνA but have been summarised in Table 3.2.

The effect of applying kinematic constraints for both experiments can be seen in Figure 3.9. Here NuWro is used to compare nominal Monte Carlo with restricted phase space. A BR-GFG nuclear model is used for heavy nuclei and events may undergo FSI. Clearly such phase space constraints have minimal effect on the shape of δp_{TT}. This indicates that only the normalisation will be reduced when phase space constraints are applied.

Having noted the minimal variations observed when phase space constraints are applied, can a measurement by MINERνA on the shape of δp_{TT} for final states involving only neutral pions tell us about the background shape for T2K?

Experiment	Final State		
	μ^-	Proton	Pion
T2K	$200 \leq p_\mu(\text{MeV}/c)$	$450 \leq p_\text{p}(\text{MeV}/c)$	$200 \leq p_\pi(\text{MeV}/c)$
	$-0.6 \leq \cos\theta_\mu$	$0.4 \leq \cos\theta_\text{p}$	$0.4 \leq \cos\theta_\pi$
MINERνA	$1.5 \leq p_\mu(\text{GeV}/c) \leq 20.0$	$450 \leq p_\text{p}(\text{MeV}/c)$	$200 \leq p_\pi(\text{MeV}/c)$
	$0.94 \leq \cos\theta_\mu$	-	-

Table 3.2: Phase space constraints applied to the T2K and MINERνA analyses. Note the similarities in the hadronic momentum threshold which is a result of both experiments using similar detector technologies.

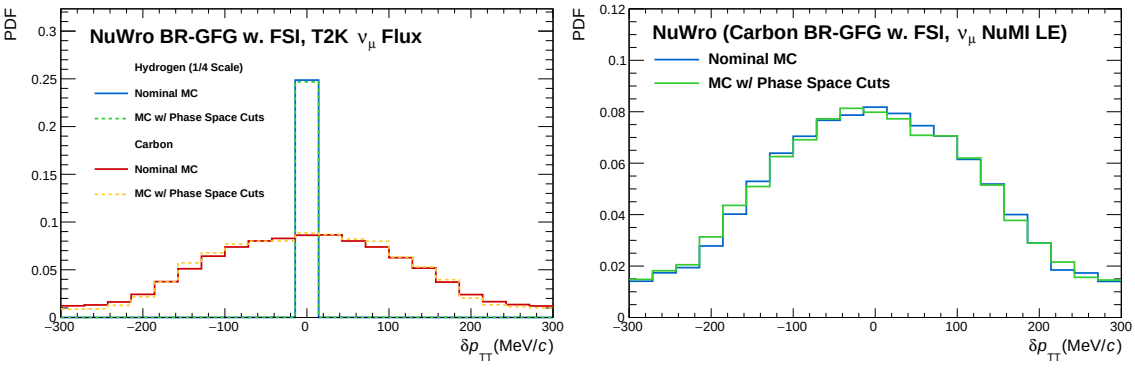

(a) T2K Experiment.

(b) MINERνA Experiment.

Figure 3.9: Effect of phase space constrains for both the T2K and MINERνA analyses. Here NuWro is configured to produce events given the respective fluxes for each experiment.

This has been assessed in Figure 3.10 where the configuration of NuWro is identical to that used in Figure 3.9. Two cases are considered here, the first case places no experimental phase space constraints (Figure 3.10a) and the second highlights the effect of such restrictions (Figure 3.10b).

It is clear that when no phase space constraints are applied the two different final states look to have similar shapes with a variation of around 5%. The MINERνA topology however looks to be slightly more broad than that of the T2K final state. We mentioned earlier that this is somewhat expected given the higher average energy neutrino flux at MINERνA, although it wasn't as prom-

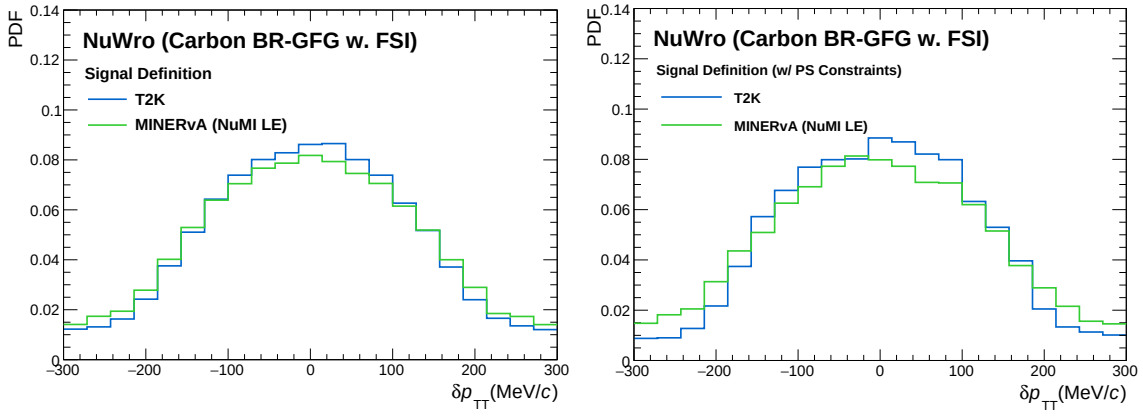

(a) No Kinematic Constraints. (b) Experimental Phase Space Restrictions.

Figure 3.10: The T2K and MINERνA Experiment's final state topologies on carbon are compared using their respective neutrino flux's. T2K's signal here is CCNpMπ^+ whereas MINERνA requires CCNpMπ^0final states. Here NuWro is models carbon as a Bodek-Richie GFG and final states undergo FSI.

inent implying such a feature is due to FSI. This feature is also present when kinematic restrictions are placed on the final state. There is also an additional change to the shape in Double Transverse Momentum.

If the MINERνA measurement is to be used to constrain the background shape in δp_{TT} it would be beneficial to follow the same approach used by Lederman and Collaborators by comparing samples with the same kinematic constraints applied [14]. To first order one would be able to place constraints on the carbon background given the similar shapes and knowing that current experimental systematic uncertainties would cover the shape differences.

3.4 Reconstruction

Following the discussion on Double Transverse Momentum's ability to probe various aspects of nuclear effects, how the neutrino direction is defined shall now be discussed. This section shall use Monte Carlo data from T2K's near detector, ND280, to firstly highlight the effect of miss-reconstructing the neutrino direction and secondly present a more accurate method of determining the neutrino's direction.

Until 2016, T2K defined the neutrino's direction as the z coordinate of ND280. This was subsequently used to reconstruct observables like $\cos\theta_\mu$ or the μ^- angle with respect to the incoming neutrino. To first order this was a good approximation of the neutrino's direction, however, as we move into the realm of high-precision measurements its definition needs re-evaluating.

An alternative method, outlined here, reconstructs the neutrinos direction using its parent decay point. The approach improves the experimental reconstruction of observables dependent on the incoming neutrino's direction. Using this technique, comparisons to the previous approach can be seen in Figure 3.11. Here the reconstructed Double Transverse Momentum and $\cos\theta_\mu$ are evaluated against their true values via residual distributions. These distributions are produced using the T2K analysis which will be outlined in Chapter 5. Fitting a Cauchy distribution to the residuals provides as an approximate quantification of the reconstruction improvements. In all cases, the alternative method out performs the previous definition of the neutrino's direction. A decrease in the spread of the reconstructed variable is observed and the bias is either less than or equal to the previous approach. There is however a bias observed in both methods of reconstruction for $\cos\theta_\mu$ and indicates that in some cases the angle is overestimated. This was found to be a result of low energy muons curving slightly due to the magnetic field before being identified by the TPCs. As such, this lead to the observed biases in both reconstruction approaches.

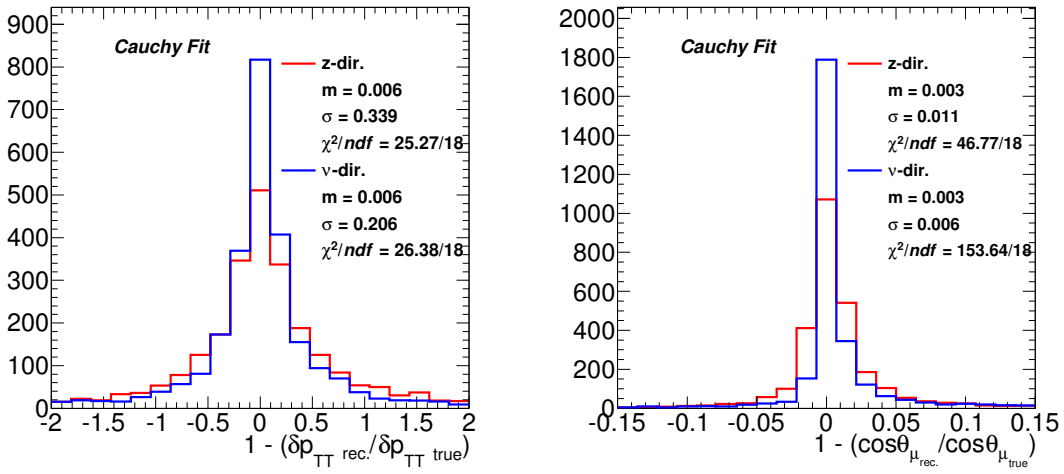

(a) Double transverse momentum.

(b) Muon $\cos\theta_\mu$.

Figure 3.11: Residual distributions highlighting the improved definition of the neutrino's direction. Here these variables are constructed using the z coordinate of ND280 (z-dir.) and the reconstructed neutrino direction (ν-dir.).

In the following, the method for reconstructing the neutrino direction shall be outlined. This technique not only improves the reconstruction of observables dependent on the neutrino direction but also enables a systematic uncertainty to be assigned due to the uncertainty in position at which the neutrino is created. Note that it is only necessary to assign this as a systematic to off-axis neutrino experiments where there is a large variation in the neutrino's parent decay point along the decay pipe[2].

Both the vertex position of the interaction and the neutrino's parent decay point are used to determine the neutrino direction. At both ND280 and MINERνA the vertex position is well defined. The parent neutrino decay point, on the other hand, is only known by the truth information in the Monte Carlo data. In reality we do not have the ability to determine the parent decay point on an event-by-event basis and therefore take the mean x, y, z decay point of the neutrino's parent. It is determined using truth information from the respective experiments.

[2]See Section 4.1 for further details on neutrino beam production.

The x, y, z distributions of the parent decay point relevant to T2K can be seen in Figure 3.12. The mean position, $\boldsymbol{d}_g$, in metres was found to be $\boldsymbol{d}_g =$

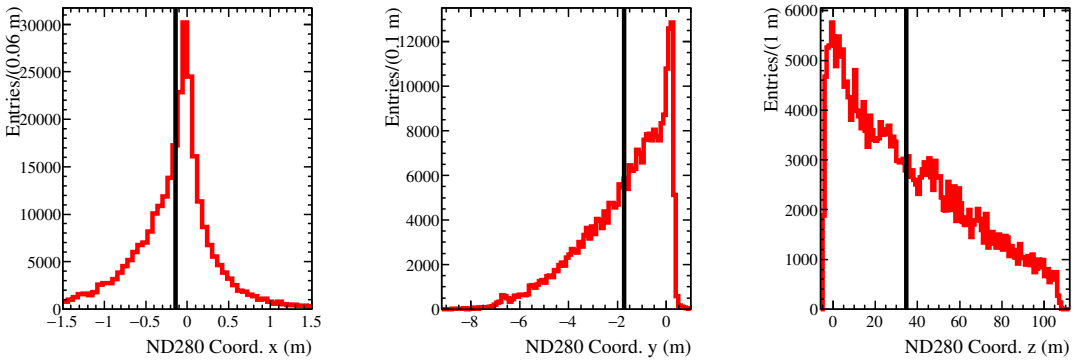

Figure 3.12: Monte Carlo modelling of the neutrino parent decay point at T2K. These were produced from the ν_μ inclusive truth information. Black lines indicate the mean positions for each distribution.

$\{-0.139, -1.729, 34.550\}$ at T2K and $\boldsymbol{d}_g = \{0.231, 45.368, -766.384\}$ at MINERνA. Here g denotes the experiment's global coordinate system which is transformed into the respective local coordinate system, l. This is achieved by taking the difference between $\boldsymbol{d}_g$ and the position of the experiment, $\boldsymbol{d}_{\text{Exp}}$ in metres

$$\boldsymbol{d}_l = \boldsymbol{d}_g - \boldsymbol{d}_{\text{Exp}}. \tag{3.5}$$

For T2K's ND280 detector this was found to be $\boldsymbol{d}_{\text{Exp}} = \{-3.222, -8.146, 280.100\}$ and at MINERνA $\boldsymbol{d}_{\text{Exp}} = \{0.249, 60.350, -1022.740\}$. From here the neutrino direction, $\boldsymbol{\nu}$, in metres is defined as the vector connecting the local parent neutrino decay point and the interaction vertex position $\boldsymbol{V}$

$$\boldsymbol{\nu} = \boldsymbol{V} - \boldsymbol{d}_l. \tag{3.6}$$

Finally the vector $\boldsymbol{\nu}$ is normalised for use in analysis resulting in the improved reconstruction of variables dependent on the neutrino direction like in Figure 3.11.

Chapter 4

The Experiments

The low interaction probability of neutrinos, in general, leads to neutrino experiments requiring large fiducial volume detectors made of dense materials. Additionally, high intensity neutrino sources are needed in order to measure the physics properties of interest with enough statistical precision. For both T2K and MINERνA the detectors are situated in intense neutrino beams produced by accelerator complexes. The T2K experiment uses its neutrino beam, situated at J-PARC in Japan, to understand neutrino oscillations, whereas the Fermilab based, MINERνA experiment in the United States aims to provide high statistics, high precision neutrino-nucleus scattering measurements.

This section discusses the key physics goals and achievements of the respective experiments along with their design and configuration. Both experiments use similar beam production methodologies and simulation techniques. As such, a general overview of both the neutrino beam production and simulation shall be given before a short overview of their individual configurations.

4.1 Neutrino Beam Production

The production of high intensity neutrino beams is a non-trivial process and reliant on the production of secondary particles. These subsequently decay into neutrinos and their charged lepton counterparts. The method adopted at J-PARC and Fermilab is to begin with H^- ions and using a linac, accelerate it to 400 MeV. The beam is stripped of its electrons as it enters a synchrotron leaving only protons that enter a final accelerator. Once the proton beam has reached its design energy it is then steered onto a static target made from graphite.

The protons interact with the target and produce a secondary beam of charged hadrons. These hadrons have a broad energy spectra and consist of predominantly pions ($\pi^{\pm}$) and kaons ($K^{\pm}$). After production, the secondary beam is focussed using magnetic horns whose polarity enables the production of a $\nu_\ell/\bar{\nu}_\ell$ rich beam. A Forward Horn Current (FHC) produces a neutrino rich beam whereas a Reverse Horn Current (RHC) results in an anti-neutrino dominated beam. The configuration of magnetic horns defines the peak energy of the neutrino beam. Finally, the neutrino beam is produced in the decay tunnel of the production facility via the following dominant decay modes

$$\begin{aligned} &\text{FHC:} && \pi^+ \to \mu^+ + \nu_\mu && \text{and} && K^+ \to \mu^+ + \nu_\mu, \\ &\text{RHC:} && \pi^- \to \mu^- + \bar{\nu}_\mu && \text{and} && K^- \to \mu^- + \bar{\nu}_\mu. \end{aligned}$$

The length of the decay tunnel is optimised to accommodate the decays of the $\pi^{\pm}$ and is dependent on the proton beam energy. Unfortunately, further wrong-sign contamination enters the neutrino beam from muon decay and sub-dominant kaon decay modes

$$\begin{aligned} &\text{FHC:} && \mu^+ \to e^+ + \nu_e + \bar{\nu}_\mu && \text{and} && K^+ \to \pi^0 + e^+ + \nu_e, \\ &\text{RHC:} && \mu^- \to e^- + \bar{\nu}_e + \nu_\mu && \text{and} && K^- \to \pi^0 + e^- + \bar{\nu}_e. \end{aligned}$$

Placed downstream of the decay tunnel lies an absorber which removes any remaining hadrons and low energy muons. The latter arise from the multi-phase neutrino production process. In this region and beyond is instrumentation to provide measurements of the beam direction and intensity. The neutrinos produced in the decay tunnel travel unimpeded towards the respective detectors.

For measurements to be performed by accelerator-based neutrino experiments the number of protons impinging on the target must be understood. The quantity defining this is known as Protons On Target or POT. This is equivalent to luminosity in collider physics experiments. POT is determined by measuring the charge of the proton beam typically via current transformers situated along the beamline [72]. The POT is used to calculate both the neutrino-interaction event rate in simulations and cross section measurements. Details of how the POT is included in neutrino-scattering measurements shall be discussed in Chapter 8.

4.2 Neutrino Flux – Predictions and Constraints

The success of accelerator-based neutrino experiments measuring cross sections and neutrino oscillations are dependent on reliable prediction of the neutrino flux. It is crucial to understand its intensity, flavour composition and spectra. Having understood how neutrino beams are produced in Section 4.1, numerous effects can impinge on the resultant neutrino flux rate. As such, any analytical calculation is infeasible. Neutrino flux predictions therefore require Monte Carlo modelling of many aspects including POT, the geometry and field strength of the magnetic horns, along with the particle propagation and interactions within and around the target. The precise simulation of such dynamics is limited by the knowledge of these factors and is one of the major sources of uncertainty in accelerator neutrino experiments.

Currently the major source of uncertainty in making flux predictions lies in

hadron production models. As protons collide with the target material QCD processes induce the production of mesons that subsequently decay to neutrinos. In order to reduce the systematic uncertainty of these processes accelerator-based neutrino experiments rely on external data from hadron scattering experiments. By placing replica targets or target material in hadron beams provides constraints on the production rates and kinematics of various hadronic final states.

4.3 Simulation

Accelerator-based neutrino interaction detectors like MINERνA and T2K's ND280 need detailed Monte Carlo simulations of their data. This is required in order to reliably estimate event selection efficiencies and background constituents. The procedure begins by using inputs from the flux prediction, detector geometry and relative masses of the detectors components. This information enables interaction vertices to be sampled from which the subsequent neutrino-nucleus scatter can be determined. Each scatter is modelled by neutrino interaction event generators like those discussed in Section 2.3. The type of interaction chosen at a particular vertex is dependent on the incoming neutrino energy and the various cross sections.

The next stage of simulation is to propagate each final state particle through the detector. This models a particle's energy deposited and scattering inside the detector. Finally, the detectors response is modelled using inputs from the propagation process where the electronics and data acquisition system is simulated. These simulations provide an 'identical' output as if it were actual data collected from the detectors other than the true underlying neutrino interaction and final state kinematics are known.

The two experiments under consideration here have had their simulation summarised in Table 4.1. Here the flux generator, neutrino interaction simulation and particle propagation are given for each experiment. Note that the sim-

Simulation Stage	Experiment	
	T2K	MINERνA
Flux Driver	FLUKA2008 [74] + GEANT3 [75]	GEANT4 [76]
Neutrino Event Generator	NEUT (6B) [64]	GENIE [63]
Particle Propagation	GEANT4 [76]	GEANT4 [76]

Table 4.1: Summary of Monte Carlo simulation packages used at each stage of the modelling process.

ulation of the electronics and data acquisition are bespoke to each experiment. Additional information of the exact configuration of neutrino event generators is given in Reference [33] for T2K and Reference [73] for MINERνA.

4.4 The T2K Experiment

4.4.1 Overview

The T2K Experiment [33] is a long-baseline neutrino oscillation experiment whose main goal is to measure the transformation of muon neutrinos to other neutrino flavours. By looking at the disappearance of ν_μ and appearance of ν_e in T2K's two running configurations, neutrino and anti-neutrino mode, it measures parameters of both the PMNS matrix and neutrino mass differences. The experiment as seen in Figure 4.1 comprises of three detectors situated along the neutrino beamline provided by J-PARC. The first two, INGRID and ND280, are positioned $\sim$280 m downstream of the production target. These detectors measure beam properties. Finally, a further 295 km downstream of the target lies the Super-Kamiokande (SK) detector, a water-based Cherenkov detector used to search for the appearance/disappearance of neutrinos. While INGRID, a sandwich configuration of iron and scintillator, is placed on-axis to the neutrino beam and measures the flux direction and intensity; ND280 and Super-

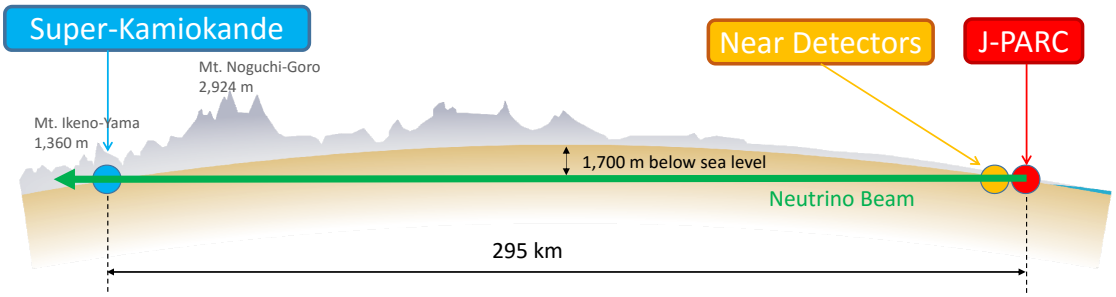

Figure 4.1: The T2K Experiment's near and far (Super-Kamiokande) detectors baseline is given in which ν_μ neutrinos transform into other flavours. Source [33].

Kamiokande are positioned 2.5° degrees off-axis. This results in each detector being exposed to a narrow neutrino flux peaked at approximately 600 MeV.

Since late 2009 T2K has been taking data and presented the first indication of ν_μ to ν_e oscillations in 2011 using a collected POT of 1.43×10^{20} [77]. As the experiment has increased its statistics it has placed the most precise measurement using the ν_μ disappearance channel of both the mass-difference, Δm^2_{23} and $\sin^2 2\theta_{23}$ [78]. Expanding on this analysis and including RHC datasets T2K's most recent oscillation result has, for the first time, excluded $\mathcal{CP}$ conservation ($\delta_{\mathcal{CP}} = 0, \pi$) to a 90% Confidence Level [79].

The T2K Experiment also performs crucial measurements of neutrino-nucleus cross sections. Such measurements aid in reducing systematics that limit our sensitivity to the oscillation parameters of interest. These scattering cross sections not only help characterise the respective signals and backgrounds observed at the far detector but has also produced a number of world leading cross section measurements [80, 81]. Finally, searches for physics beyond the standard model are also examined by T2K, most notably sterile searches [82] and tests of Lorentz and $\mathcal{CPT}$ violation [83].

The T2K analysis presented in this thesis uses only the ND280 detector, it is therefore beyond the scope of this section to discuss Super-Kamiokande and INGRID any further. For the interested reader one may refer to Reference [33] for more information on these detectors. Henceforth the discussion on T2K will

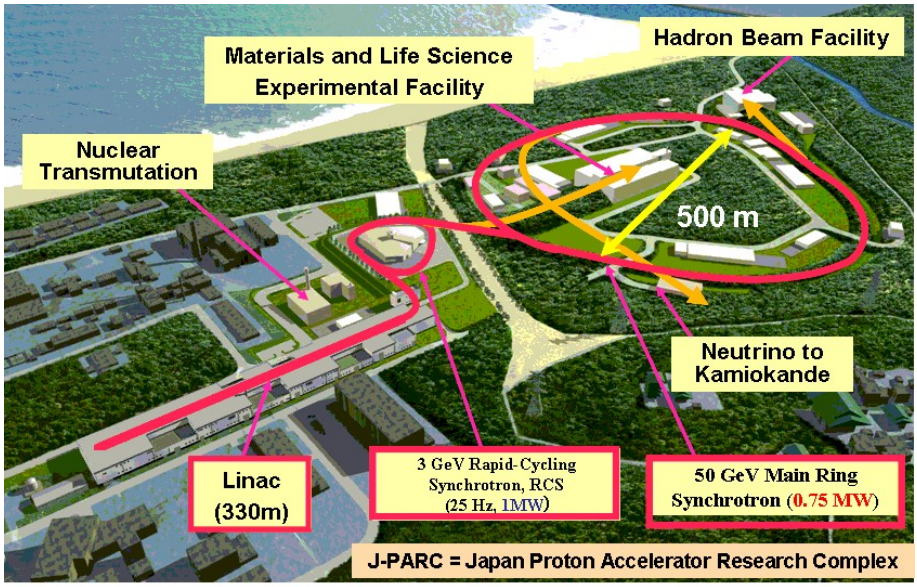

Figure 4.2: J-PARC Accelerator Facility whose Main Ring is configured to run at 30 GeV during neutrino beam production. Source [84].

focus on its beam properties and the ND280 near detector along with relevant sub-detectors used in this analysis.

4.4.2 T2K Beamline

The T2K neutrino beam is produced by the Japanese Particle Accelerator Research Complex (J-PARC) on the east coast of Japan. The accelerator facility is presented in Figure 4.2. J-PARC uses a 330 m linac to accelerate hydrogen-ions whose electrons are removed by collisions with charge stripping foils. This process of proton beam production occurs inside a 3 GeV Rapid-Cycling Synchrotron. The 3 GeV protons then enter the Main Ring (MR) for final acceleration to 30 GeV. Finally, the protons collide with the graphite target located in the most upstream magnetic horn.

Each proton beam or 'spill' is extracted within a single turn from the MR via a set of five kicker magnets. A single spill has a total duration of approximately 5 μs and contains 8 bunches. Each bunch is less than 100 ns and separated by around 560 ns. Knowledge of the beam timing structure is required for both

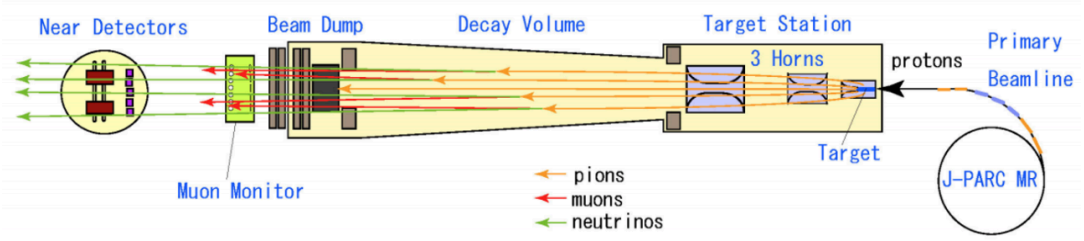

Figure 4.3: J-PARC's Neutrino Beamline Production Facility. Here the beam dump refers to the absorber. Source [85].

oscillation and cross section measurements as it enables the removal of backgrounds such as cosmic rays.

T2K's neutrino facility as depicted in Figure 4.3 uses a three horn set-up to focus and tune the secondary beam. This results in a neutrino beam energy peaked at around 2 GeV. The secondary beam has a 110 m decay region in which to produce neutrinos. Any remaining muons above 5 GeV passing through the absorber are measured by MUMON providing real time information on the beam direction and intensity.

4.4.2.1 The Off-axis Technique

Both Super-Kamiokande and ND280 are positioned 2.5° off-axis to the neutrino beam centre. Although this reduces the intensity it provides numerous benefits for oscillation physics. This method takes advantage of the kinematics of pion decay by considering the dominant mode, $\pi^{\pm} \rightarrow \mu^{\pm} \overset{(-)}{\nu}_{\mu}$. Given the negligible mass of the neutrino its energy dependence, E_{ν}, on the pion's kinematics can be written as

$$E_{\nu} = \frac{m_{\pi}^2 - m_{\mu}^2}{2\left(E_{\pi} - |\boldsymbol{p}_{\pi}| \cos\theta\right)}. \tag{4.1}$$

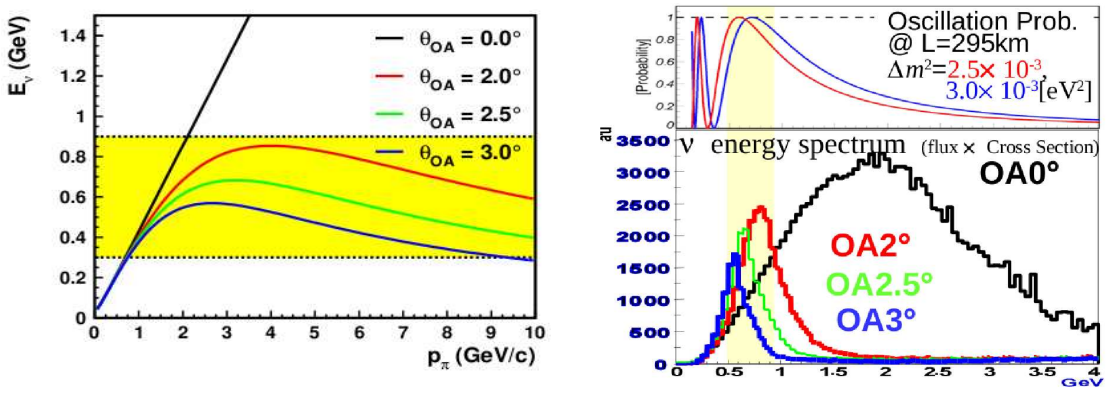

(a) E_ν dependence as a function of pion momentum highlights the off-axis effect of narrowing the neutrino energy.

(b) Neutrino flux spectrum (bottom) and the oscillation probability (top) for muon appearance.

Figure 4.4: Three different off-axis angles are compared to an on-axis neutrino beam. Source [86].

From Equation 4.1 one can see that the neutrino energy is dependent on the ratio of the mass difference between the pion, m_π, and muon, m_μ, to the pion's kinematics, E_π, and $\boldsymbol{p}_\pi$. Hence for some opening angle of the neutrino with respect to the pion's direction, θ, it is possible to produce a narrow neutrino energy spectra peaked at a particular energy. The effect of varying the off-axis angle can be see in Figure 4.4a where the neutrino energy is presented as a function of pion momentum. It is clear that even a small off-axis angle dramatically reduces the maximum E_ν.

This technique provides numerous benefits that outweigh the loss of intensity. As discussed in Section 1.3, neutrino oscillations are dependent on the ratio between the distance travelled by and the energy of the neutrino. Given this, the off-axis angle can be optimised to produce a narrow neutrino beam which is tuned to maximise or minimise the oscillation probability at the far detector. This effect is highlighted in Figure 4.4b which compares the neutrino flux with the oscillation probability. By comparing the on-axis beam in Figure 4.4b to the various off-axis configurations it becomes apparent that this technique reduces the un-oscillated neutrino beam contamination. This is especially good at reducing backgrounds from NC events producing π^0. Finally, this approach

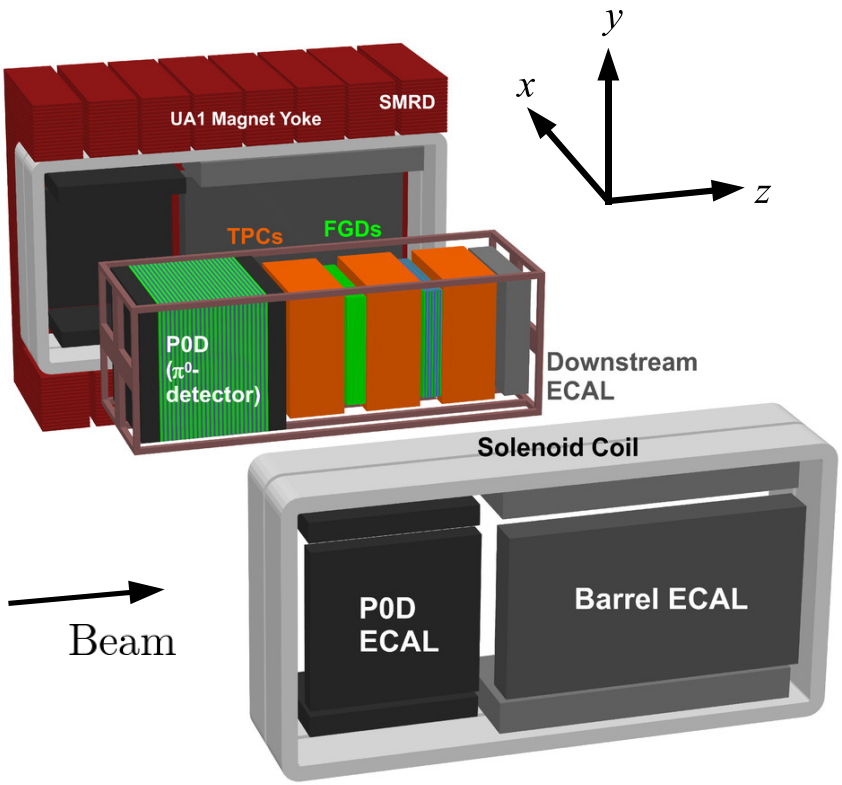

Figure 4.5: The ND280 off-axis near detector. The UA1 magnet which houses the SMRD surrounds the various sub-detectors. Source [33].

also aids in reducing the intrinsic ν_e background produced at J-PARC that reach Super-Kamiokande which for the ν_e appearance measurement is crucial due to the expected low event rate.

4.4.3 The ND280 Off-Axis Near Detector

T2K's dedicated cross-section scattering experiment, ND280, as depicted in Figure 4.5, is a composite detector comprising of several specialised sub-detectors immersed in a 0.2 T magnetic field. The horizontal magnetic field provided by the former UA1 experiment's magnet is aligned transverse to the neutrino beam direction. It contains all the sub-detectors other than the side range muon detector (SMRD). The SMRD interlaces the UA1 magnet and comprises of scintillator pads. The main task of the SMRD is to identify high-angle muons exiting the central detectors and veto background tracks entering the central region.

The central region contains an array of tracking detectors; beginning at the most upstream point sits the Pi-Zero Detector, PØD, whose purpose is to identify neutral pions. This is realised by identifying the photons produced in π^0 decay and takes advantage of materials whose conversion length is small. The PØD is formed of a sandwich configuration of plastic scintillator and a combination of either lead, brass or fillable water bags. The fillable water bags provide a means of performing scattering measurements on water, the same target used at Super-Kamiokande. These measurements on water reduce model dependency when predicting event rates at the far detector.

Downstream of the PØD are a set of alternating Time Projection Chambers (TPCs) and Fine Grained Detectors (FGDs). A total of three TPCs deliver high resolution tracking to enable precise measurements of the curvature of charged tracks. This not only facilitates charge separation but also momentum reconstruction. The two FGDs are similar in design and construction, each acting as active targets in which neutrino interactions have a higher probability of taking place. Both FGDs collect light via plastic scintillator but FGD2, like the PØD, can be partially filled with water.

Finally the active tracker region which encompasses the PØD, TPCs and FGDs is surrounded by an electromagnetic calorimeter (ECAL). The ECAL comprises of layers of iron interleaved with scintillator and takes advantage of the density of lead as it increased the probability of electromagnetic showers. This property of lead aids in containing such electromagnetic topologies within the calorimeter. The ECAL has two roles in analysis at ND280, the first being able to provide complimentary information on an event enabling the analyser to improve the selection of particular topologies. Secondly, it can act as an alternative form of particle identification in regions of phase space where the TPCs fail to distinguish particle type.

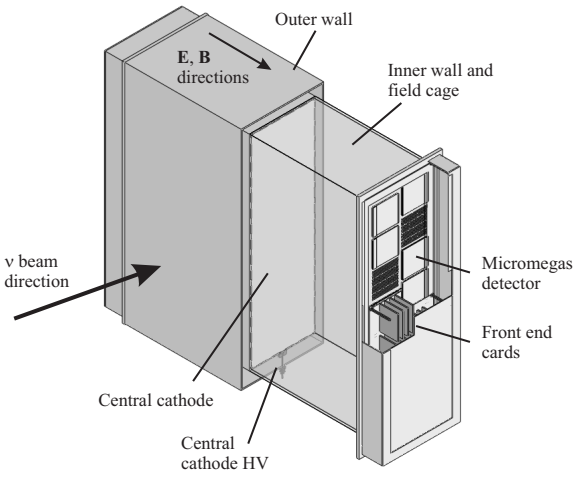

Figure 4.6: Schematic of the Time Projection Chambers used in the ND280 near detector. Source [87].

4.4.3.1 Time Projection Chambers (TPCs)

The three gaseous argon TPCs are identical in design and are able to reconstruct events in three dimensions. This makes them capable of easily identifying the multiplicity and orientations of charged particles. A TPC module consists of an outer box held at ground potential and an inner box containing the argon based drift gas. There is a carbon dioxide gas layer in between the inner and outer boxes which acts as an electrical insulator.

Situated in the centre of the inner box and perpendicular to the neutrino beam is the cathode as seen in Figure 4.6. This configuration provides two electric fields parallel and anti-parallel to the magnetic field resulting in two readout planes each facing the central cathode. The inert nature of argon enables charged particles entering the TPC to produce ionisation electrons. These 'drift' electrons travel up to 90 cm away from the cathode towards the two readout planes where they are detected by an array of avalanche sensors called MicroMEGAS [87].

A MicroMEGAS comprises of 1728 charge-collection elements each measuring 68.6 mm^2 which are arranged in 48 rows and 36 columns. Each row is offset so that passive regions are not aligned. This results in a point spatial resol-

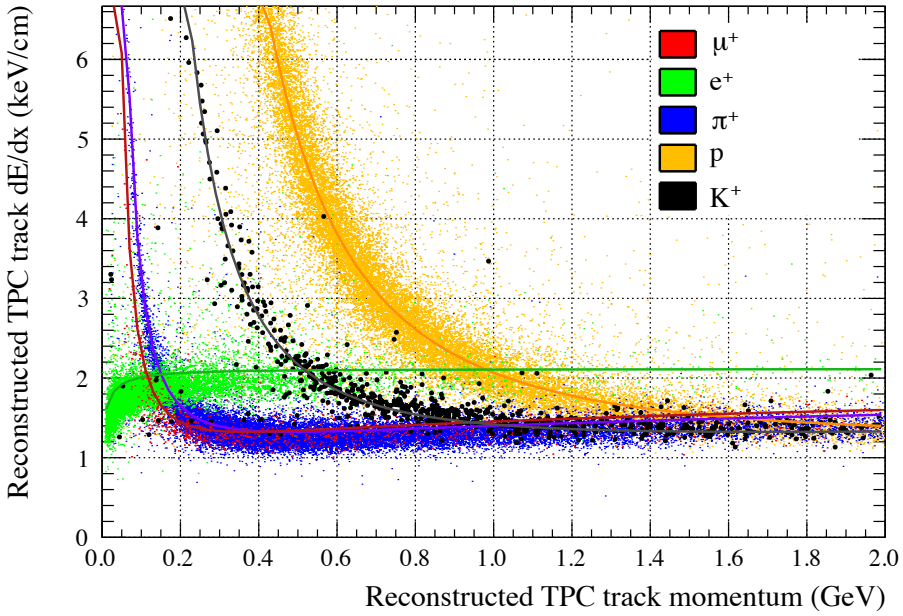

Figure 4.7: The TPCs reconstructed energy loss as a function of momentum used for particle identification at ND280. Source [88].

ution of approximately 0.7 mm in the zy-plane where relative timing between hits determines the x-position. Over the two readout planes there are twelve MicroMEGAS forming an active readout area of approximately 3 m^2 per TPC.

Each TPC with its excellent tracking resolution and being situated in a magnetic field provides for the identification of particle type. This is achieved by measuring the tracks momentum by curvature and the energy loss per unit distance, dE/dx. Note that the curvature of a charged track is induced by the magnetic field. The TPC's ability to distinguish between particle type can be seen in Figure 4.7, where the dE/dx profile of different particle hypotheses are presented as a function of momentum.

4.4.3.2 Fine Grained Detectors (FGDs)

In addition to acting as a target mass for neutrino interactions, the FGDs also serve to track charged particles close to the interaction vertex. Each FGD is finely granulated enabling the identification of short-ranged tracks like protons from nuclear emission that fail to enter the TPCs. The key task of each FGD is to

identify the interaction vertex, measure individual charged tracks and determine their direction.

The two 1.1 ton FGDs have an active target material made of polystyrene scintillator bars. Each bar is 1864.3 mm long and has a width of 9.6 $\times$ 9.6 mm. These are assembled into planes made up of 192 bars that are then orientated in pairs perpendicular to one another. The two perpendicular planes produce a single 'XY module' that face the incoming neutrino beam. This configuration provides good granularity for 3D tracking.

FGD1 is a fully active tracker, constructed of 15 XY modules. The second FGD, FGD2, can be configured to hold water and consequently contains less active scintillator modules. FGD2 therefore houses 7 XY modules which are interlaced with six 25.0 mm water layers.

The scintillator bars are extruded to hold a wavelength shifting (WLS) fibre down its centre and coated in a reflective titanium oxide layer. This is to maximise the light yield and direct the light towards the WLS fibre. A single end of the WLS fibre is instrumented with a Multi-Pixel Photon Counter (MPPC) with the other masked with aluminium film that acts as a mirror.

A single MPPC has an area of 1.3 $\times$ 1.3 mm^2 that contains a total of 667 pixels. Each pixel is an avalanche photo-diode whose readout is a binary hit or no hit. The individual pixels are therefore independent of the number of photons incident on the pixel. Hence the signal produced by an MPPC is a linear sum of the number of pixels fired. This same MPPC detection technique is also used in the ECAL , P∅D and SMRD.

Like the TPCs the FGDs are capable of particle identification and momentum reconstruction. However due to the detectors resolution and size, determining a tracks dE/dx profile and momentum by curvature is not possible. For each track the FGDs therefore consider their start position and then, as seen in Figure 4.8, sum the energy deposited given the distance travelled between the previous

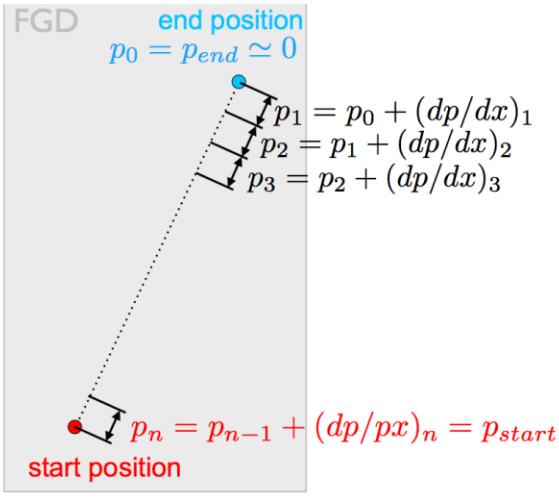

Figure 4.8: Contained FGD tracks momentum is reconstructed by summing the momentum loss along the track. Source [89].

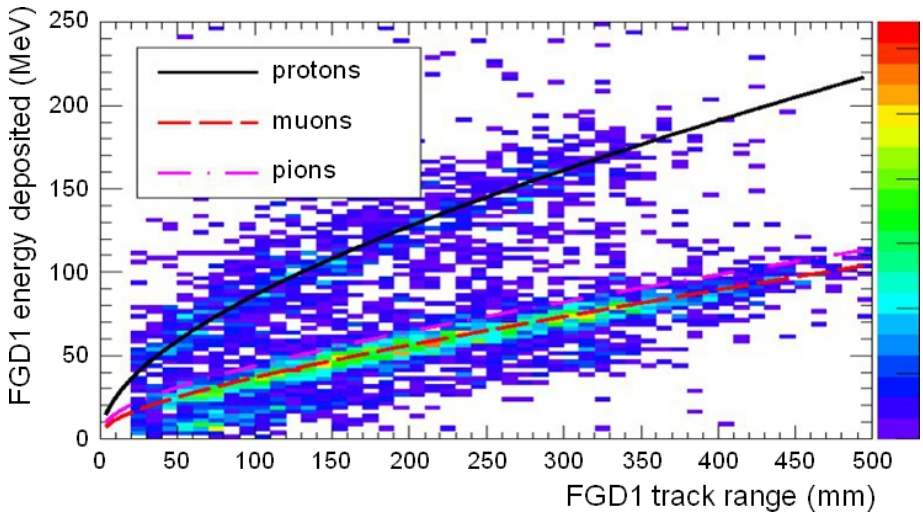

Figure 4.9: Particle identification in an FGD is performed by comparing the tracks range and total energy deposited by the track. Test beam data is presented with an overlay of the proton, pion and muon Monte Carlo expectations. Source [90].

and current measurement point. The summation is continued until the end of the track is reached. This method provides particle identification by comparing the tracks total energy deposited with its distance travelled. The discriminating power of this particle identification method can be seen in Figure 4.9.

4.4.4 Performance

The FGDs provide good particle identification of tracks contained in its fiducial volume. This is highlighted by Figure 4.9 where test beam data is compared to three particle hypotheses. Each FGD is proficient in distinguishing between protons and charged pions, however differentiation between muons and pions is limited. The same is observed for the TPCs but they are also able to identify kaons and electrons. In general, discrimination between muons and pions is complicated due to their similar masses. This results in the particles having a similar energy loss resulting in the observed behaviour in both sub-detectors.

The TPCs ability to identify between muons and electrons is down to both its good energy resolution, and the energy loss of muons in argon being roughly half that for electrons. The TPC's energy resolution is $7.8 \pm 0.2\%$ for minimum ionising particles leading to a 0.2% probability of identifying muons as electrons [87]. The TPCs provide a momentum resolution of about $0.1 p_{\perp}/(\mathrm{GeV}/c)$ and can be seen in Figure 4.10. This is the momentum resolution of a track transverse to the magnetic field. The observed resolution is thanks to the 70 cm sampling length, MicroMEGAS good space point resolution of about 0.7 mm and the TPCs operating in a 0.2 T magnetic field.

4.5 The MINERνA Experiment

4.5.1 Overview

The MINERνA Experiment is a dedicated neutrino-nucleus scattering experiment whose main goal is to provide measurements on various nuclei of exclusive and semi-exclusive final states. Unlike the ND280 detector at T2K, MINERνA is situated on axis exposing it to the broad neutrino energy spectra. This enables measurements of scatters induced at low energies, like CCQE, to high-energy deep inelastic processes. Such information is critical as neutrino oscillation ex-

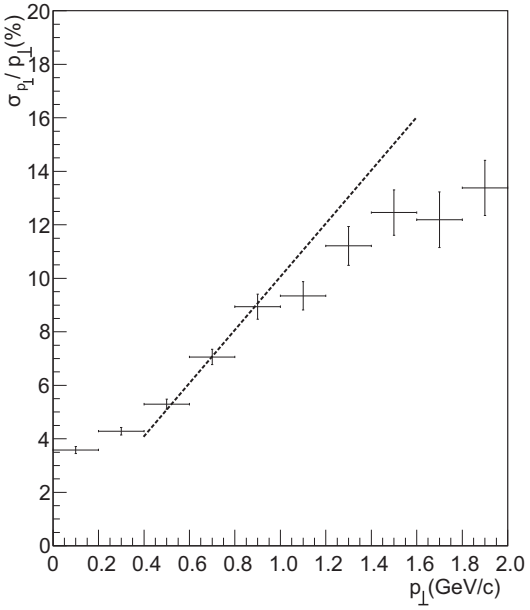

Figure 4.10: Momentum resolution for a single TPC is presented as a function of momentum perpendicular to the magnetic field. The data points are Monte Carlo simulations of muons and the dashed line represents the momentum resolution goal. Source [87].

periments enter an era of precision that is limited by cross-section model systematics. Being able to provide results over a broad energy range aids in reducing systematics for a wide array of current [33, 34] and future [35, 36] oscillation experiments.

Since taking data in 2010, MINERνA has collected a combined total of 4.27×10^{20} POT from the LE neutrino beam in FHC and RHC mode. These datasets have led to a number of notable publications; those closely related to oscillation systematics are measurements of nuclear effects such as $2p2h$ and RPA in neutrino and anti-neutrino interactions [91, 92]. Additionally, using neutrino-electron scattering, MINERνA was able to provide additional flux constraints of the NuMi LE flux. This information has been used by other experiments situated in the NuMi beam [93]. Finally, MINERνA has also provided evidence of rare neutrino-induced Kaon scattering processes at the three sigma level [94].

The MINERνA experiment as seen in Figure 4.11 where the beam is enter-

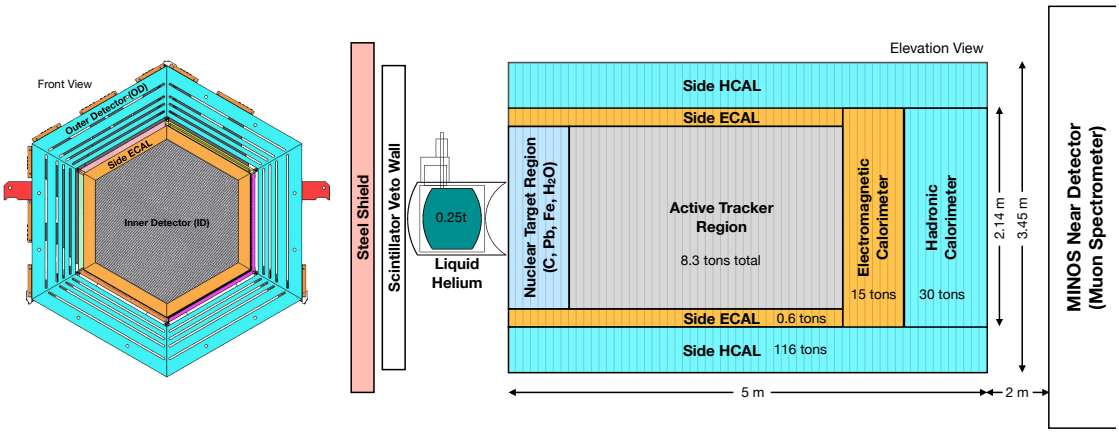

Figure 4.11: The MINERνA detector's front view (*left*) and side view (*right*) where the neutrino beam enters from left to right. Source [73].

ing from left to right, is situated approximately 100 m below ground and 960 m downstream of the NuMi target. The detector consists of an array of active and passive targets. Starting from the most upstream part of the experiment to the neutrino beam lies a steel shield followed by a veto wall. Situated in between the veto wall and the main body of the MINERνA detector is an uninstrumented cryostat containing helium. The veto wall is used to reject events entering MINERνA upstream of the cryostat in analysis studying neutrino interactions on helium.

Continuing downstream of the passive helium target is the main MINERνA detector. This is comprised of an inner detector (ID) surrounded by calorimetry. The inner detector contains a set of passive nuclear targets which including carbon, lead, iron and H_2O, interleaved with plastic scintillator. The scintillator provides particle tracking and identification of the vertex position. A fully active tracker made of plastic scintillator forms the rest of the ID and acts as a hydrocarbon target. This enables precise determination of the direction and energy of charged tracks. Surrounding ID reside two calorimeters, one ECAL which is enclosed by a hadronic calorimeter (HCAL). This configuration can be seen in Figure 4.11 (left).

Finally, the magnetised MINOS detector sits downstream of MINERνA to

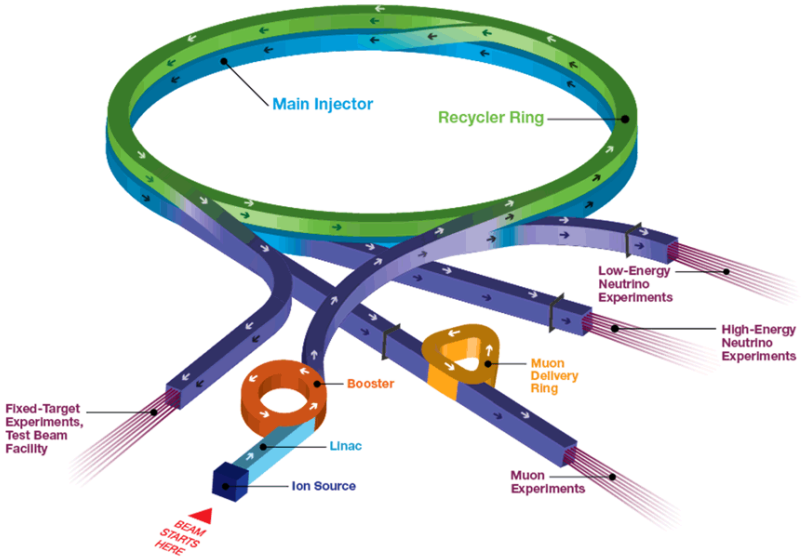

Figure 4.12: Fermilab Accelerator Complex. Source [96].

perform charge identification and momentum reconstruction of muon-like tracks. A full overview of the MINOS detector's technology and readout can be found in Reference [95]. The analysis presented in the thesis using data from the MINERνA experiment only considers events in the active tracker where muon-like tracks enter MINOS. For this reason all components upstream of the active tracker shall not be discussed further. The interested reader may however refer to Reference [73] for more details.

4.5.2 NuMi Beamline

MINERνA is situated in the Neutrino at the Main Injector (NuMi) beam whose accelerator complex can be seen in Figure 4.12. The set-up is similar to J-PARC however the facility works at much higher energies. The first stage of acceleration is performed by the Booster which produces a 8 GeV proton beam. The Main Ring (MR) subsequently builds the proton energy up to 120 GeV before it collides with the target. Fermilab has designed the spill to have less bunches than at T2K. NuMi's beam structure is formed from 5 or 6 bunches lasting a period of 8-10 μs.

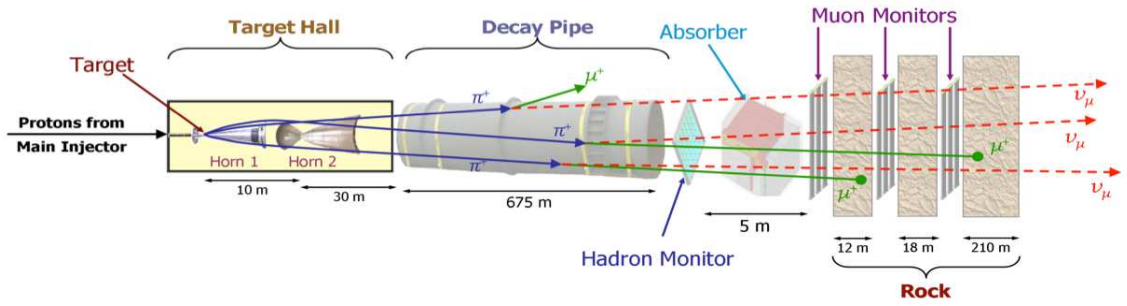

Figure 4.13: The NuMi beamline production facility. Source [97].

The configuration of the NuMi beam presented in Figure 4.13 has two magnetic horns and a 675 m decay tunnel. The much larger decay tunnel than T2K is a result of the much higher proton beam energy. In addition to muon monitors downstream of the absorber, like at J-PARC, the NuMi facility also has a hadron monitor 80 cm upstream of the absorber. Given only around 20% of the primary protons interact with the target the hadron monitor provides information on the primary beam angle and position along with the horn positions. The NuMi beam is configurable to three energy peaks, a low (LE), medium (ME) and high (HE) energy. These different configurations are made by varying the distance between the two horns. The various flux predictions can be seen in Figure 4.14 where the LE peaks at around 3.5 GeV, the ME at $\sim$6 GeV and the HE is centred at $\sim$10 GeV.

4.5.3 Construction

The MINERνA detector is made of 114 regular hexagon modules each constructed using up to two scintillator planes. These break down into three categories; tracking, ECAL and HCAL. For ease of fabrication and erection a single module contains the ID and calorimetry as shown in Figure 4.11 (left). The tracking modules are configured in two ways using three orientations of scintillator plane. As presented in Figure 4.15, MINERνA defines the X plane as vertical scintillator strips and the other two planes, U and V, are orientated $\pm 60^{\circ}$ to the X plane. The

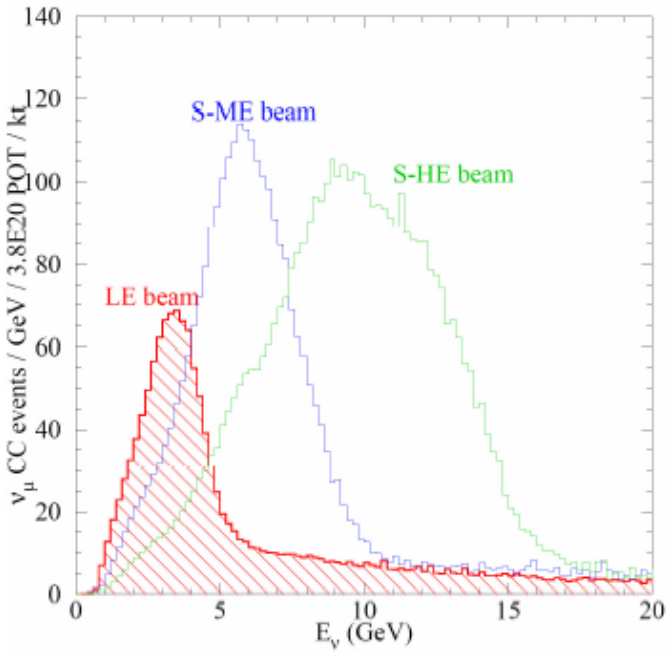

Figure 4.14: On-axis flux prediction for the MINOS detector. Source [98].

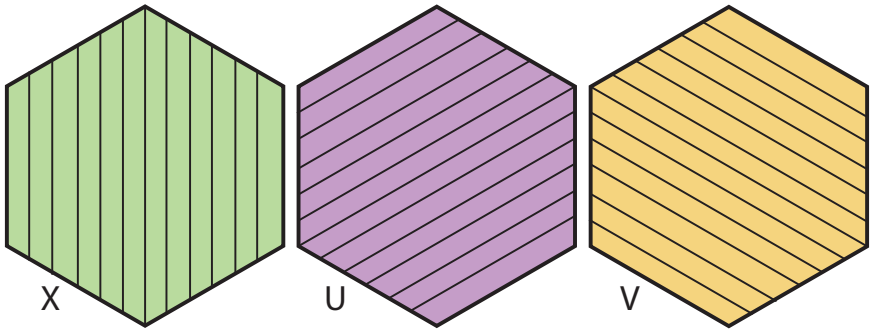

Figure 4.15: The orientations of the X, Y and V scintillator layers providing concise 3D track reconstruction. Source [99].

detector is formed from UX and VX modules which alternate between the respective modules. This configuration enables precise 3D reconstruction of tracks in MINERνA.

MINERνA's coordinate system is defined such that the z-axis is horizontal and pointing downstream from the nuclear targets towards the MINOS detector. The x and y coordinates whose origin when facing a tracker module, like in Figure 4.11 (left), is centred in the middle and defines the x-axis as horizontal and y-axis as vertical. In this coordinate system the neutrino beam is centred in the

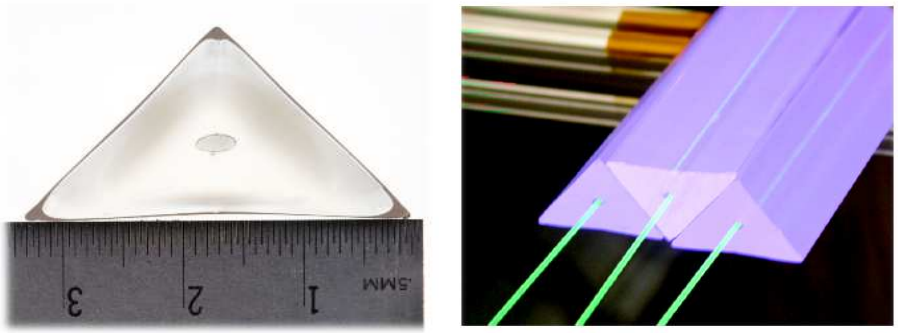

Figure 4.16: The triangular scintillator bars used at MINERνA. Source [73].

$y - z$ plane pointing downward 3.34°.

4.5.3.1 Scintillator Planes

The scintillator planes are similar in construction to T2K's FGDs. They are also made using bars of extruded polystyrene scintillator containing a central WLS fibre. A total of 127 bars in each plane are coated with a reflective titanium oxide layer. The key difference between the bars used at MINERνA and in T2K's FGD is the geometry; MINERνA applies the principle of charge sharing between bars leading to bars having a triangular cross section as depicted in Figure 4.16. This will ensure that particles traversing through a single plane deposit energy in at least two bars. Charge sharing provides two benefits; the first being better discrimination between signal and noise and second an improved position determination.

Each bar has a width of 33 mm and hight of 17 mm, depending on where the bar is situated in the detector its length is either 1220 or 2450 mm. The light collected by the WLS fibres are readout by multi-anode photomultiplier tubes (PMT). Each PMT at MINERνA contains 64 pixels in a 20 $\times$ 20 mm^2 area and measures light from up to 64 scintillator bars. Therefore unlike the MPPCs used on T2K, here each pixel measures the energy deposited in a single bar. Although a single PMT can read many individual bars this is at the cost of irreducible cross talk between pixels. In order to overcome this problem the mapping of

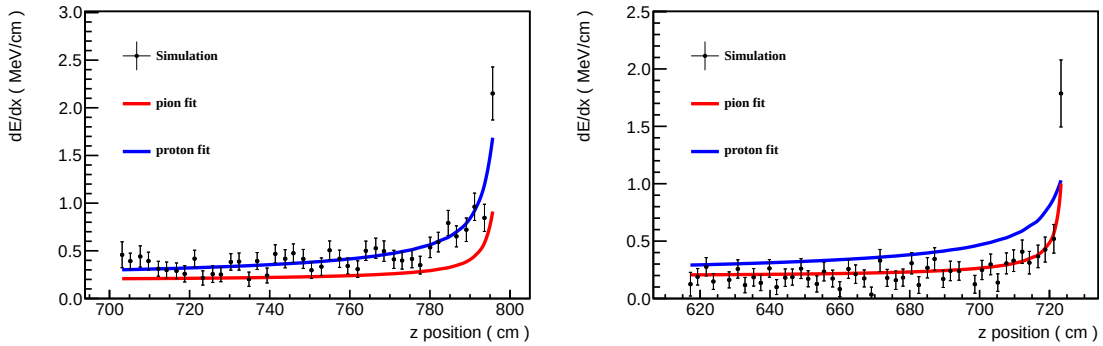

Figure 4.17: Comparisons of the dE/dx profiles for simulated protons (left) and pions (right) presented against their true expectation. Source [73].

bars in the detector to an individual pixel was chosen such that no adjacent bars are read out by adjacent pixels.

4.5.3.2 Active Tracker

In the core of MINERνA lies the active tracker which is made of 62 tracker modules. This acts as a precise 8.3 ton tracking target volume making it capable of resolving multi-particle final states containing low energy particles. The large volume and high granularity allows for contained tracks in the active tracker to have their particle type determined through dE/dx measurements. By considering the energy deposited as a function of the distance travelled by a track, particle type can be identified. This can be seen in Figure 4.17 where simulations of protons and pions in MINERνA are compared to their expected profile.

4.5.3.3 Calorimetry

MINERνA contains side calorimeters surrounding the nuclear targets and active tracker regions along with dedicated calorimeter modules situated at the most downstream point of the detector. The side ECAL is formed by attaching 2 mm thick lead sheets to the outermost 150 mm of the tracking modules. The side HCAL improves containment of events by using 349 mm thick steel, a material with a short radiation length, segmented with scintillator bars.

The downstream ECAL comprises of 10 ECAL modules. A single module is identical to a tracker module but has a 2 mm thick lead plate attached to the upstream side of the scintillator planes. This provides excellent directional information of electrons and photons along with good energy resolution.

Finally, the downstream HCAL acts as a hadronic particle 'absorber' and enables containment and energy reconstruction of charged hadrons. This is achieved by replacing one of the scintillator planes in a standard tracker module with 254 mm of steel. In order to preserve directionality in the reconstruction of hadronic showers a total of 20 HCAL modules are configured in a single, repeating X, U and V pattern.

4.5.4 The MINOS Near Detector

Situated 2.1 metres downstream of the last HCAL module in MINERνA is the MINOS near detector. The MINOS detector acts as a muon spectrometer measuring both the charge and momentum of very forward going tracks exiting MINERνA. A full description of the detector can be found in Reference [95]. The MINOS near detector, as shown in Figure 4.18, is composed of planes of 10 mm plastic scintillator sandwiched between 282 magnetised iron sheets measuring a width of 254 mm. This tracking calorimeter has a 1.3 T toroidal magnetic field running through the entire length of the detector enabling both the charge identification and momentum determination by curvature. The long length of MINOS also opens the to door to momentum measurements by range analogous to those made in T2K's FGDs.

4.5.5 Performance

The MINERνA detector, thanks to its well understood detector alignment and calibration procedures enable a per plane $x - y$ position resolution of 3.1 mm. This knowledge also provides a hadronic calorimetric energy resolution of $\sigma / E =$

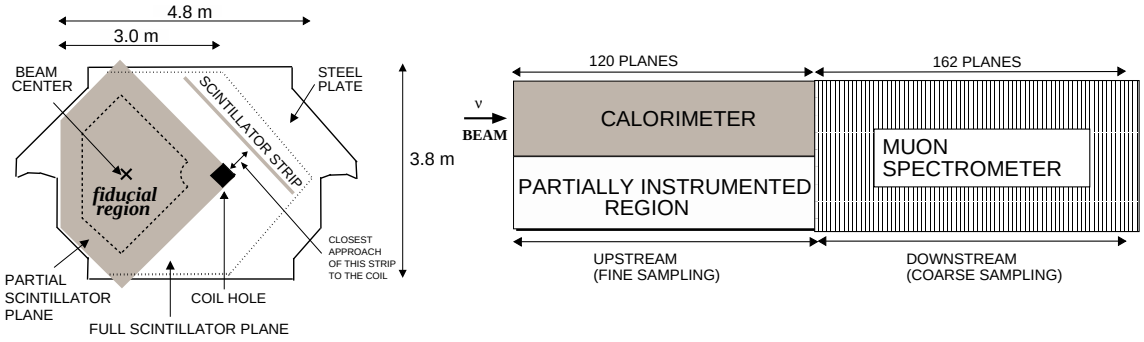

Figure 4.18: MINOS Near Detector. Source [73].

$0.134 \oplus 0.290/\sqrt{E}$ for the active tracking region of MINERνA. This energy resolution is a convolution of effects from FSI to attenuation along scintillator strips and is improved for low recoil energies below 1 GeV. In such cases where single tracks are identified, like in CCQE interactions, their ionization (dE/dx) profile can be used leading to an energy resolution of around 5% for hadrons. Using the dE/dx profile for particle identification shows good separation between protons and pions. This can be seen in Figure 4.17 for simulated 1 GeV momentum protons. The χ^2 for the proton hypothesis is 34 for 41 degrees of freedom ($d.o.f.$) where the $d.o.f.$ is the number of planes traversed by the track. In the case for the same simulated protons being compared to the pion hypothesis the χ^2 is 177 for the same $d.o.f.$ and highlights MINERνA's particle identification capability. Finally, using the MINOS detector, the momentum uncertainty for muons measured using their range in MINOS is known to a 2% precision.

Chapter 5

T2K Analysis

This chapter outlines the current status of the T2K analysis which aims to isolate neutrino interactions on hydrogen contained within a composite nuclear target. Such a measurement would be the first resonance-like neutrino-nucleon cross section since the early 80s [46–49]. Although such measurements do exist, knowledge of the neutrino flux was not well understood leading to a large associated uncertainty.

Performing measurements on hydrogen has numerous benefits; not only may it provide an updated cross-section result with reduced systematics arising from the neutrino flux but also aid in understanding nuclear effects. This can be achieved by providing a direct measurement of the 'bare' neutrino-nucleon interaction which can then be compared to heavier nuclei. It is therefore beneficial to perform new measurements of neutrino-hydrogen interactions, not only providing an updated cross section measurement but also as a proof of principle that hydrogen can be isolated in multi-nuclei targets containing hydrogen. As mentioned in Chapter 3, being able to isolate interactions on hydrogen can lead to improved reconstruction on the neutrino energy spectra and therefore reduce the systematic uncertainties in neutrino oscillation measurements [69].

5.1 Signal Definition

Having seen how hydrogen can be differentiated from other nuclei in Chapter 3 there is only one interaction mode available in neutrino interactions that achieves this. At the nucleon level the resonance production reaction for hydrogen is given by

$$\nu_\mu p \rightarrow \Delta^{++}\mu^- \rightarrow p\pi^+\mu^-. \tag{5.1}$$

We see that in the absense of FSI from Table 3.1 the signal definition is therefore defined as neutrino-hydrogen induced events containing exactly three tracks; one muon, one proton and a single π^+ (H-CC1p1π^+).

Although this final state is predominantly produced via resonance production it can also be created via deep inelastic scatters (DIS). Note however that the DIS contribution is expected to be small given T2K's neutrino flux. Irrespective of this expectation the signal definition in this analysis will consider only final state topologies and not the 'bare' neutrino-nucleon interaction. This will minimise model dependence and remove any Monte Carlo generator specific signal definitions.

Having defined the signal topology, constraints are also placed on the target region within ND280. There are three active tracking targets each containing a large amount of hydrogen, namely, the PØD and two FGDs. In principle the PØD could be used as a target, however it is limited by its ability in reconstructing charged pions. The PØD is constructed using dense materials like steel and brass that increase the secondary interaction probability of charged pions. Such secondary interactions lead to limited kinematic reconstruction making the PØD an inadequate target for this analysis given good momentum reconstruction is required for all final states. The PØD is therefore ignored in this analysis leaving FGD1 and FGD2 as targets.

The fiducial volume for each FGD is defined in Table 5.1. In addition to

Fine Grained Detector	Coordinate (mm)					
	x		y		z	
	Start	End	Start	End	Start	End
1	-932.17	932.17	-877.17	877.17	115.63	436.93
2					1473.63	1807.38

Table 5.1: FGD1 and FGD2 vertex position fiducial volume cuts applied to both the signal definition and selection in ND280 coordinates.

Phase Space Constraints		
$250 \leq p_{\mu}$ (MeV/c)	$250 \leq p_{\pi^+}$ (MeV/c)	$450 \leq p_{\mathrm{p}}$ (MeV/c)

Table 5.2: Kinematic restrictions applied to the signal definition used at T2K leading to a Fiducial Cross Section.

these detector related signal constraints, ND280's acceptance is included in the signal definition. These account for the minimum momentum T2K's near detector can reliably reconstruct and are summarised in Table 5.2. This 'reduced' phase-space refinement in the signal definition helps to reduce the model dependence and is often referred to as a Fiducial Cross Section. The lower limits are determined by considering the minimum number of XY layers required by the FGD's reconstruction. This is approximately 2.5 XY planes and is equivalent to a range of around 5 cm travelled by a particle. From here each particle types low momentum threshold are identified using momentum by range tables [22].

It is worthwhile pointing out that although the signal definition is H-CC1p1π^+ the selection will search for events passing the CC1p1π^+ criteria. This is because δp_{TT} will be used to determine the relative hydrogen contribution. Given this, it is useful to gauge the approximate hydrogen contributions from each FGD as it may provide more insight into any ambiguities in the selection. This can be achieved by considering the target nucleon as a proton and the nuclear compos-

ition of each FGD.

For FGD1 the dominant target is CH and it is therefore expected that 14% of the CC1p1π^+ topology will be on hydrogen seeing as one in seven protons are hydrogen. For FGD2 the relative hydrogen contribution needs to account for the the six water and seven scintillator planes. By taking the hydrogen composition of CH and H_2O and the total number of protons in each molecule the probability of interacting on hydrogen is 17%. Both expectations assume no other target nuclei and negates any effects of FSI but to first order act as a good guide as to the expected rates on hydrogen for each target.

5.2 Truth Study

Before considering the selection of CC1p1π^+ final states in ND280, a truth study was undertaken to understand the expected topologies that may be observed. The approach here was to use the Monte Carlo's true kinematics and topologies to understand the interactions behaviour. This began by considering the H-CC1p1π^+ final state without any phase-space constraints applied. Performing such a study not only acted as a guide to develop the selection but as a means of assessing the ability of the selection framework at T2K.

The first phase of the truth study identified all possible topologies that the final state may produce. Then the detectors with which each particle traversed is determined and assessed as to whether it passed the active region of each sub-detector. The following truth study can consider FGD1 only, the arguments apply to FGD2 as well by translational symmetry. This is due to the TPC/FGD sandwich configuration being the same for each FGD resulting in only one set of topologies to be determined.

The true topologies are given in Figure 5.1 and present four cases where the blue lines represent the true particle trajectories. Defining contained FGD tracks as those which occupy the active region of an FGD and TPC tracks as those

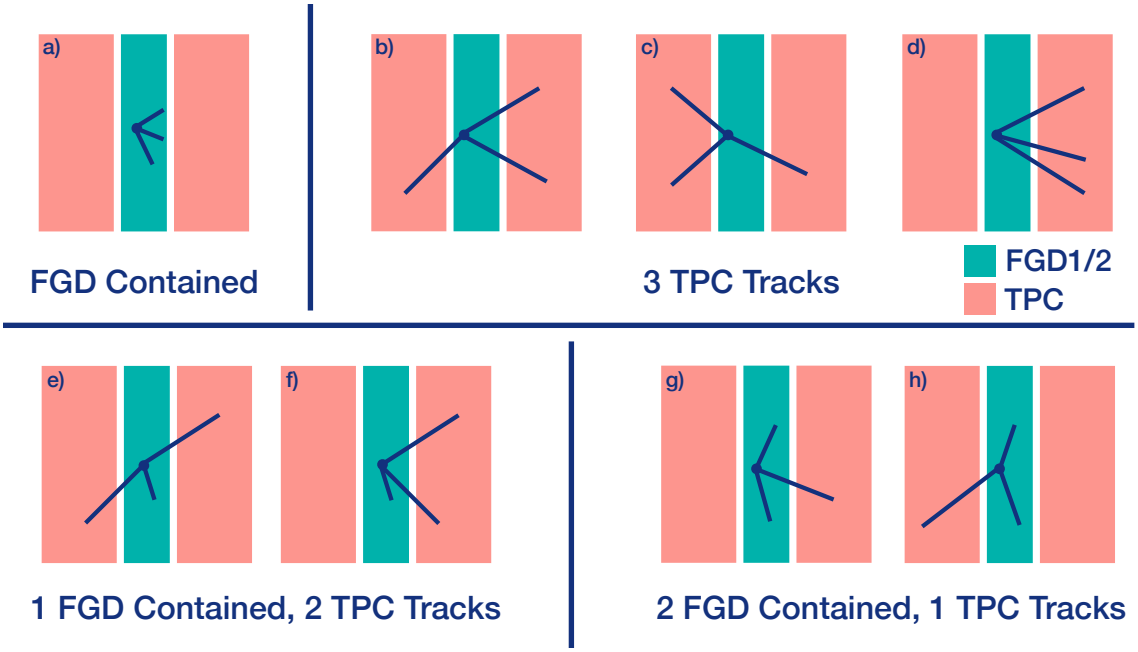

Figure 5.1: The true final state topologies considered in ND280's FGDs. The particle type is interchangeable for each topology considered.

that possess both an FGD and TPC component the cases are; fully contained FGD tracks, a single contained FGD track, two FGD tracks and three TPC tracks. For all topologies considered the particle type is interchangeable between each track.

Given the topologies defined in Figure 5.1 H-CC1p1π^+ events are selected from T2K's NEUT Monte Carlo dataset equivalent to 7×10^{21} POT. This POT is ten times T2K's FHC dataset. Before considering the relative abundances for each topology the naming convention from Figure 5.1 is refined to reflect that all possible orientations of TPC tracks are considered for each particle type.

While the definition of an FGD contained track remains unchanged, tracks with TPC components are now categorised as either Out-Going (OG) Forward (F), or OG Backward (B) tracks. Forward going tracks are those that enter the downstream TPC of the respective FGD whereas backward are those tracks that enter the upstream TPC. Hence for topology e) in Figure 5.1, for a forward going muon, an FGD contained π^+ and a backwards going proton the respective topology reads: Cont. π^+, OG p (B) and μ^- (F). In instances where an event fails all

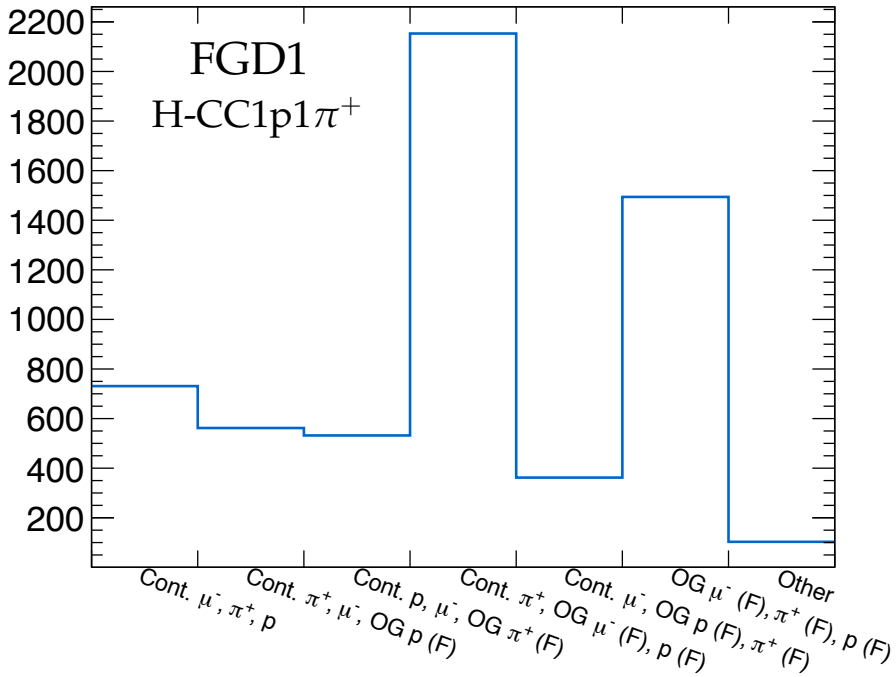

Figure 5.2: The true final state topologies identified in FGD1. Events entering Other are those that do not immediately enter a TPC such as topologies that have tracks starting from the FGD and enter the ECAL.

the topologies such as a track originating from the FGD and entering the barrel ECAL are defined as 'other'.

The results of the truth study for FGD1 is presented in Figure 5.2 where only non-zero entries are provided. It is interesting to note that given all the possible combinations of three tracks in ND280 only forward going tracks are observed. This feature is somewhat expected given that the final state particles are likely to be boosted in the same direction as the incoming neutrino. Further effects may also cause this such as the low to medium Q^2 region in which resonance production dominates generally leads to the outgoing muon in the forward direction with respect to the incoming neutrino.

Clearly two topologies dominate the final state of interest. In both cases they contain a forward going muon and proton where the topologies are distinguished by the position of the π^+. The first categorises the π^+ as contained in the FGD and the second defines it as forward going and entering the TPC. Given these topologies contain over 50% of the signal, the selection should focus

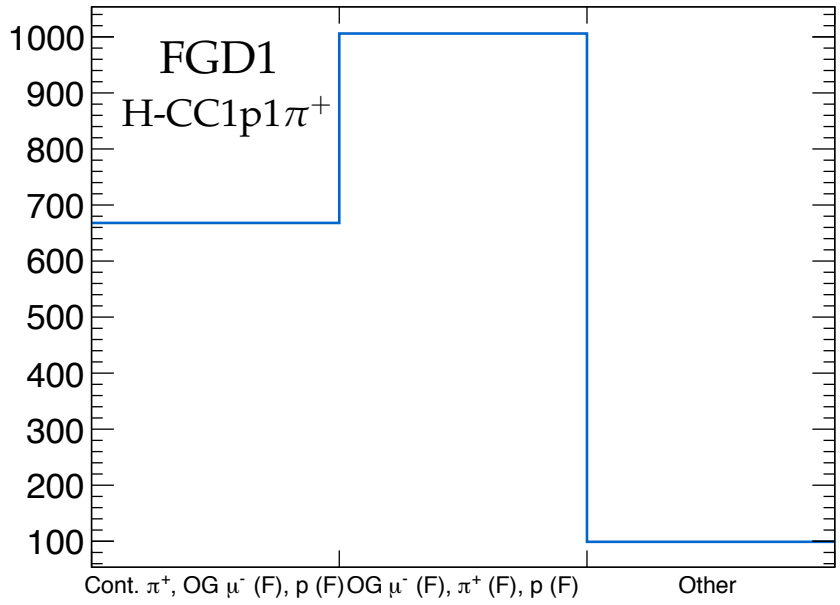

Figure 5.3: The true final state topologies identified in FGD1. Note the y-axis is zero suppressed.

on identifying such events within ND280.

The assessment of final state topologies in Figure 5.2 does not account for experimental limitations such as the energy threshold of the detectors. By including the kinematics restrictions defined in Table 5.2, we can provide a more realistic insight into what topologies may be observed in ND280. Kinematic thresholds are placed on the final state particles based on the FGDs low energy limit of $\sim$110 MeV. This restriction translates to a lower momentum threshold of 250 MeV/c for muons and π^+s and 450 MeV/c for protons. The subsequent topologies passing the kinematic constraints are presented in Figure 5.3. Note that this plot's y-axis has a suppressed zero. These phase-space restrictions leaves only the dominant two topologies from Figure 5.2.

The low predicted event rate is expected given T2K's incoming neutrino flux and detector design. For the production of a final state containing a muon, proton and π^+ a minimum incident neutrino energy of 490 MeV/c is required. The additional phase-space constraints further increases this to 820 MeV. Comparing this threshold to T2K's neutrino flux in Figure 4.4a indicates that the final state

is induced from neutrinos in the high energy tail. This therefore reduces the probability of producing the desired final state leading to a lower event rate.

If we consider the remaining two topologies after phase-space restrictions are applied, they loose approximately half their events when compared to the unrestricted case. Obviously our study ignores the detector's ability to identify track multiplicity and implies an idealised case. In reality the detectors ability in identifying final states needs to be included. Regardless of this, our results presented here still act as a good measure of the success of selecting signal events.

One of the key outcomes of this study is that the expected number of signal events will be small. In the dominant topology containing three forward-going tracks, the Monte Carlo contains approximately one thousand events after kinematic constraints are applied. If the Monte Carlo dataset is scaled to actual data POT, the signal statistics reduces to a tenth of this size. The development of the selection should therefore focus on maximising statistics by applying cuts that retain as many signal-like events as possible.

Following our assessment of available signal topologies two have been identified that may be reconstructed at T2K. Going forward we shall assess the selection capabilities of three forward-going tracks and events that have two forward-going tracks and a contained FGD track. The former shall be referred to as the 3TPC Tracks sample and the latter the FGD Contained sample.

5.3 Event Selection

In order to isolate interactions on hydrogen, candidate CC1p1π^+ events must be identified in ND280. Two topologies are investigated following their determination from the truth study in Section 5.2. The selection is evaluated using Monte Carlo equivalent to 10 times data POT. This Monte Carlo production models

neutrino interactions in both the magnet and tracker region of ND280[1] and may include multiple neutrino interactions in each spill.

In this section we evaluate the selection of final states where events contain three forward going tracks whose charge composition is formed of one negative and two positive tracks. We also assess the performance of selecting the second topology containing two forward going tracks entering the TPC, one positive and one negative, along with a contained FGD track.

The analysis flow used to select events for these two topologies are defined in Figure 5.4 where both the FGD contained π^+ and three TPC track samples are presented. Both selections begin with four identical steps before branching off into separate sample specific cuts. Note that this selection analyses interactions in FGD1 and FGD2 independently i.e. they are considered as separate targets. Hence we shall now discuss each phase of the analysis flow using Monte Carlo results produced for events originating from FGD1.

Event Quality

This is a standard analysis cut applied to all T2K ND280 analysis. Its purpose is to perform two checks on the data. The first ensures the spills GPS timing, horn current and beam direction are within expectation. The second assesses the global ND280 data quality which validates that the relevant sub-detectors were acquiring 'good' data during the data taking period. For Monte Carlo this cut is always passed.

Contains Tracks

The TPC reconstruction framework works by considering the three TPCs as a single detector containing dead regions in which the FGDs lie. The individual TPC tracks are used in conjunction with the FGD information to bring the re-

[1]This used T2K Production 6B Monte Carlo and the March 2017 software freeze.

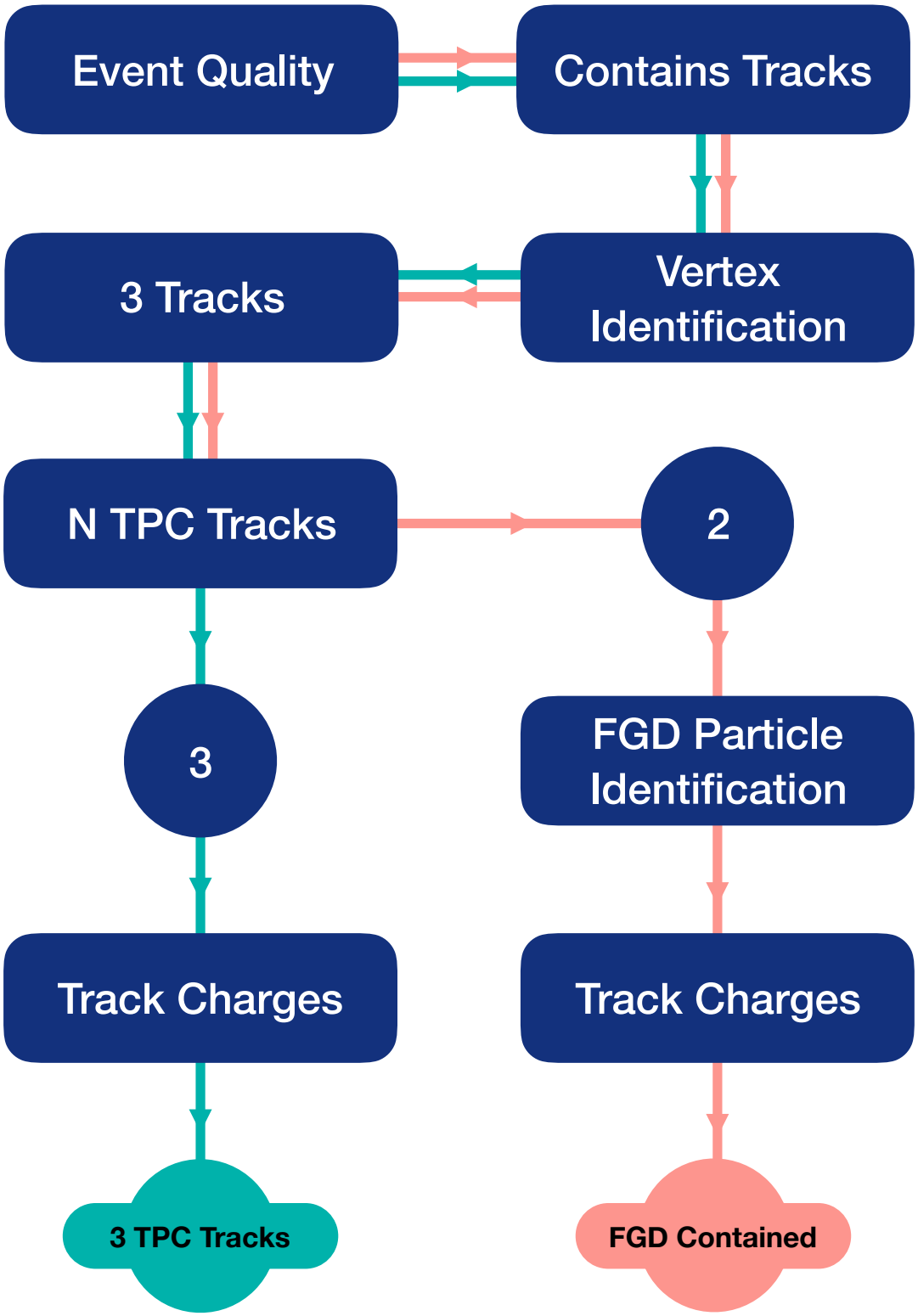

Figure 5.4: The analysis flow for the selection of two signal samples; one requiring three TPC tracks and the other a contained FGD track along with two TPC tracks.

spective components together. This creates a set of global tracks which are then grouped depending on what sub-detector components they have and where the track originated from. A tracks origin is determined by considering the start position of each track. The groups used in this analysis are defined as

- FGDN-TPC Tracks – Charged TPC tracks originating from an FGD where N is either 1 or 2 to represent FGD1 or FGD2,
- FGDN Tracks – Tracks contained in a single FGD where N represents FGD1 or FGD2,
- TPC Only Tracks – Tracks consisting of TPC information only,
- TPC Tracks – All global TPC tracks. This contains FGDN-TPC tracks and TPC only tracks,
- All Tracks – Contains all tracks in ND280. This includes FGDN, FGDN-TPC tracks and TPC-only tracks,

where each group containing TPC information is further divided into positive and negative as determined by charge identification through track curvature. Once the tracks have been categorised, the 'All Tracks' group for a particular FGD target is selected. From here the event is checked to ensure that it contains at least one global TPC track. Prior to applying this cut, the total number of TPC tracks is presented in Figure 5.5 where both the signal topology (CC1p1π^+) and background are presented. The signal component is invisible here as there are only a few thousand signal events. This cut alone removes around 90% of the Monte Carlo events where no tracks are identified by ND280's TPCs.

Vertex Identification

A candidate interaction vertex is identified by first searching for a negative FGDN-TPC track. In cases where multiple negative tracks exist the highest mo-

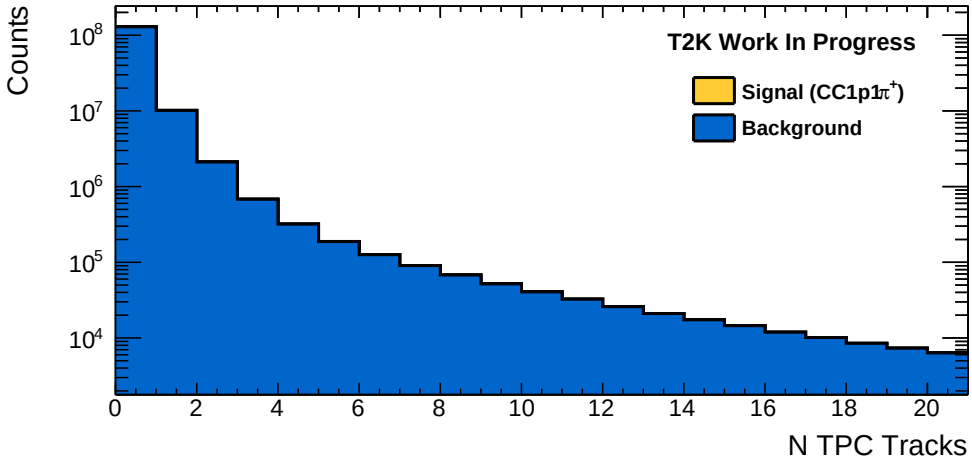

Figure 5.5: The total number of TPC tracks having identified the 'All Tracks' group for FGD1. Here the signal component is invisible as there are only a few thousand signal events.

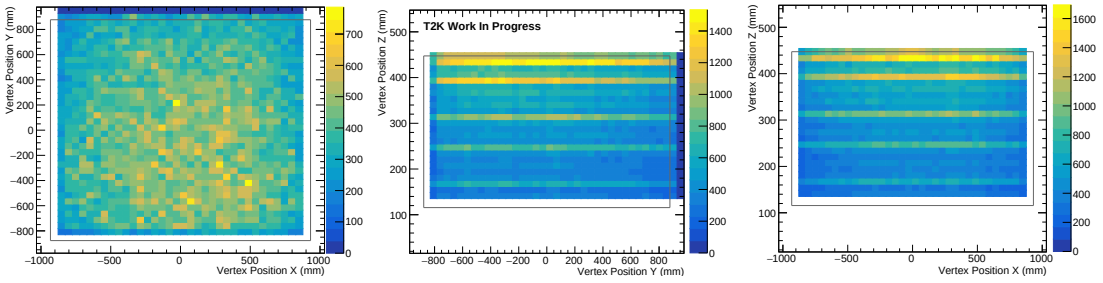

Figure 5.6: The XY (*left*), YZ (*centre*) and ZX (*right*) vertex positions identified prior to the fiducial volume restrictions are applied for FGD1. The gray boxes in each distribution define the fiducial volume.

mentum track is chosen. The selected track has its FGD component checked to ensure that its start position is contained within the respective FGD fiducial volume defined in Table 5.1. Events whose vertex is confined within the fiducial volume pass on to the next stage of the selection.

By requiring the vertex to be within the fiducial volume has a minimal effect on the total number of events passing the cut. This can be seen explicitly in Figure 5.6 where the XY, YZ and ZX vertex positions are presented. Events lying outside the gray boxes in each distribution are rejected by this cut.

There are a number of interesting features observed in each distribution

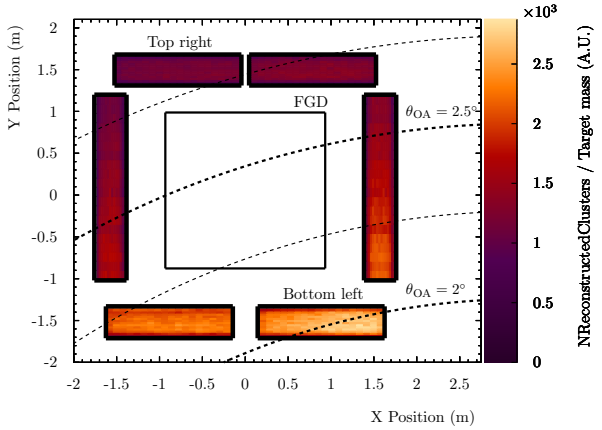

Figure 5.7: XY view of ND280 where various off-axis angles are overlaid. Taken from [66] where the analyser considered events occurring on lead within the ECAL. There is a clear decrease in the number of interactions as the off-axis angle increases.

of Figure 5.6. Firstly, the off-axis nature of the T2K beam should present itself as decreasing event rate from bottom-right to top-left of the XY interaction vertex (Figure 5.6 *left*). This is highlighted by Figure 5.7 taken from Reference [66] which presents the intensity at various off-axis angles. The analysis in Reference [66] searches for interactions in the ECAL. This feature is present in the XY distribution (Figure 5.6 *left*) although it is much less prevalent than in Figure 5.7.

Moving on to looking at looking at ND280 from the side, like in Figure 5.6 (*centre*) or from above as shown in Figure 5.6 (*right*), there is a clear increase in vertex identification as interactions take place further downstream of the incoming neutrino beam. Here the beam enters from the bottom of each plot. Interactions occurring in the upstream region of the FGD must contain higher energy tracks in order for them to be reconstructed by the TPC leading to the observed gradient. The yellow bars in Figure 5.6 YZ (*centre*) and ZX (*right*) are a result of our choice of binning and granularity of the detector.

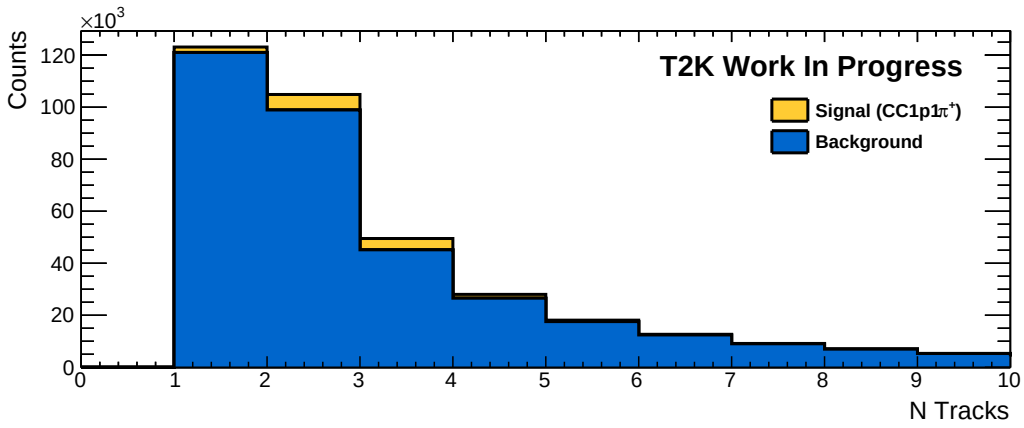

Figure 5.8: Total number of global tracks identified in ND280.

Three Tracks and N TPC Tracks

The total number of tracks in the 'All Tracks' group is counted and required to equal three. If the event contains TPC-only tracks the event is rejected. This means that we require all the tracks to be either FGDN-TPC or FGDN type tracks. At this point the selection splits to identify the two topologies of interest. The first sample requires three TPC tracks and no other reconstructed tracks for the event to pass this cut. The second sample passes events which have a single FGD contained track and two tracks that extend into the TPC.

Let us consider how the CC1p1π^+ signal is broken down into the number of tracks identified. In Figure 5.8, the total number of tracks is split into signal and background. Although small, the signal is most prevalent in cases where two or three tracks exist. Events in which two tracks are identified contain approximately twice the signal events than those where three tracks are reconstructed. This may be due to the pion decaying within the FGD, leaving only a time-delayed energy deposit which may not be reconstructed as a track due to a lack of directionality. The effect of this cut will therefore be large given one, two and four track events will be rejected. We saw from the truth study that about 5% of the events are classified as 'other' and may contain events that enter the ECAL. These events could result in secondary interactions producing additional tracks

and form part of the four track component.

FGD Particle Identification

For the two TPC tracks sample, the contained FGD track has its particle type determined. In order to ensure good particle identification the FGD track is analysed to ensure that it is fully contained in the sub-detectors fiducial volume[2]. This ensures that the track length can be reliably determined for use in dE/dx comparisons.

The measured dE/dx for the track is compared to the proton and pion dE/dx hypothesis. This uses information from Figure 4.9 to determine which particle hypothesis best suits the track. For each hypothesis the pull

$$p = \frac{x_{\text{meas}} - x_{\text{hyp}}}{\sigma_{\text{meas}}}, \tag{5.2}$$

is calculated and used to asses how well the reconstructed track matches the particle hypothesis. Here the measured dE/dx, x_{meas} with uncertainty σ_{meas} is compared to the respective hypotheses, x_{hyp}. The hypothesis closest to zero indicates what particle type best suits the track. We therefore chose the hypothesis whose pull modulus is closest to zero. No maximum pull threshold is applied to the pion-like track. The muon hypothesis is ignored as muons and pions have similar dE/dx profiles. This hypothesis was neglected as it may result in signal events being rejected due to the pulls being similar. Both of these considerations were chosen to maximise statistics given the expected low event rate. Hence only events whose track is pion-like passes on to the final cut.

The proton and pion hypothesis pulls for FGD contained tracks is presented in Figure 5.9. Immediately we see that the contained track is predominantly a charged pion forming over 50% of the distribution. There is a non-negligible electron component which is believed to be a result of π^0 decay products pro-

[2]The fiducial volume for each FGD is defined in Table 5.1

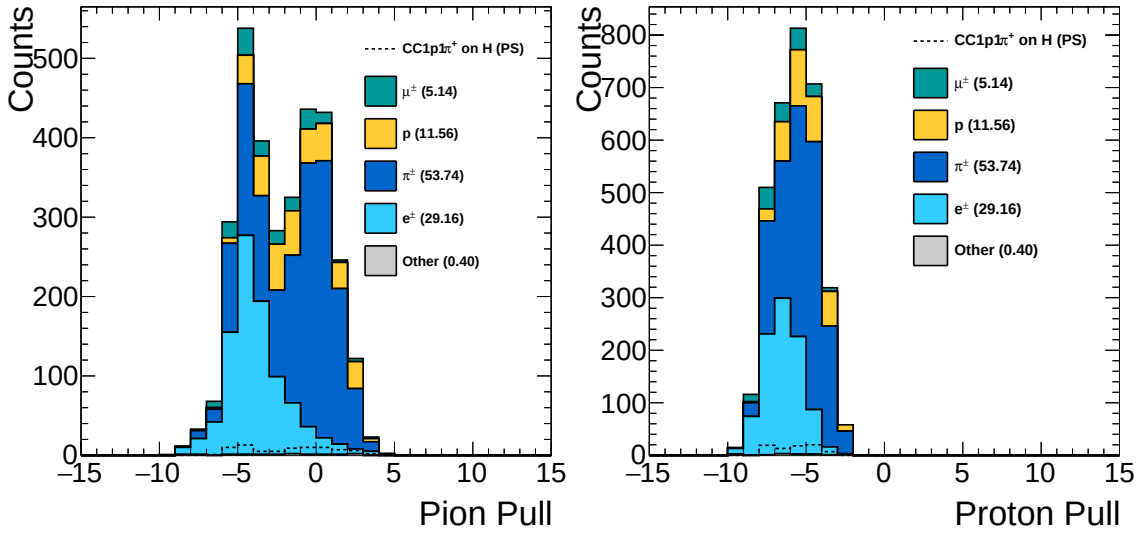

(a) Pion Hypothesis. (b) Proton Hypothesis.

Figure 5.9: Pulls for proton and pion hypothesis of FGD contained tracks for the FGD1 target prior to particle identification being performed.

ducing electrons and positrons. The pull from Figure 5.9a for the track being a pion is seen to be centred at zero unlike that for the proton case in Figure 5.9b. This highlights how pions may be discriminated from protons. There is however an overlap in between the two hypothesis at around -5 which may result in this approach for particle identification removing signal pions.

Track Charges

Finally the two samples have their TPC track charges evaluated. The FGD contained, two TPC track sample requires a single positive and negative track as the topology restricts the muon and proton to entering the TPC. Here the positive track is set as the proton candidate and the negative track as the muon candidate where the remaining FGD track as the pion candidate.

For the three TPC track sample, a single negative TPC track is required and set as the muon candidate. The remaining two TPC tracks must be positive where the candidates are set via particle identification. Only the highest momentum positive track is evaluated in the particle identification. Here the mo-

3TPC Tracks	
Track Charges	Percentage
3 +ve	0
2 +ve, 1 -ve	72
1 +ve, 2 -ve	26
3 -ve	2

FGD Contained	
Track Charges	Percentage
2 +ve	0
1 +ve, 1 -ve	94
2 -ve	6

Table 5.3: Breakdown of the charge composition identified by the TPCs for both samples where events originate from FGD1. Note that positive tracks are represented by $+$ve and negative $-$ve.

mentum and dE/dx profile is measured and subsequently used to compare it with the proton and pion hypothesis.

In the three track sample particle identification is used to improve momentum reconstruction. If we refer back to TPC reconstruction, a tracks FGD component is combined with the TPC information to create a global track. The global tracks final momentum relies on knowledge of the tracks particle type to determine the FGD momentum by range. This is achieved by comparing the proton and pion hypothesis using a Log Likelihood test of the highest momentum positive track. The hypothesis with the largest Likelihood sets the tracks particle type and the remaining hypothesis defines the second tracks particle type. For example, if the highest momentum track is determined to be more proton-like it is set as the proton candidate and the remaining track to the pion candidate.

Let us consider breaking the two interesting topologies into the TPC tracks charge composition. This is highlighted in Table 5.3 where all possible charge configurations are considered. Here $\pm$ve represents positively and negatively charged tracks respectively. Both samples contain a majority of events with the correct charge composition. The 3TPC tracks sample will see around a 25% reduction following this cut and less than 10% decrease in FGD contained events. The TPC charge composition presents an interesting feature in that both samples

fail to contain any significant positive only component. This is expected given that this work analyses FHC events where the neutrino beam is almost entirely ν_μ (1-3% non-ν_μ contamination [72]).

5.4 Selection Performance

Having outlined the selection developed for the two samples of interest, it is now useful to understand how effective each selection is at identifying the respective topologies. The two metrics used to do this are as follows

$$\text{Purity} = \frac{\text{N(Signal)}}{\text{N(Total Events)}}, \tag{5.3}$$

$$\text{Efficiency } (\varepsilon) = \frac{\text{N(Signal)}}{\text{N(Total Signal)}}, \tag{5.4}$$

where N(Signal) represents the number of signal events forming the sample, N(Total Events) the number of events in the sample and N(Total Signal) is the true number of signal events prior to any selection requirements. Given our Monte Carlo predictions, the purity gives us an insight into what proportion of the sample contains the events of interest, namely, the signal. The efficiency on the other hand measures the selections ability to retain signal events. Clearly maximising both metrics is important when developing the selection however seeing as δp_{TT} enables good signal to background discrimination our driving force here is therefore the efficiency.

We shall begin by evaluating the three TPC tracks sample before reviewing the selection ability of a single FGD contained track with two forward going TPC tracks. Before each sample is evaluated individually, one should note that two 'signals' are assessed using the metrics recently defined. The first is the CC1p1π^+ topology where phase space constraints are included and the second places an additional requirement that the target material must be hydrogen. The

Cut	FGD1		FGD2	
	Events	Signal (on H)	Events	Signal (on H)
No Cuts	1.43×10^8	7343 (3467)	1.43×10^8	8267 (4274)
Event Quality	1.43×10^8	7343 (3467)	1.43×10^8	8267 (4274)
Contains Tracks	1.41×10^7	6432 (2717)	1.41×10^8	7532 (3408)
Vertex Identification	497165	6432 (2717)	529196	7532 (3408)
Three Tracks	384676	5700 (2522)	381674	6490 (3106)
3 TPC Tracks	6773	830 (374)	10841	1173 (566)
Tracks Charges	4863	696 (316)	6792	802 (373)

Table 5.4: Summary of the 3TPC Track samples selection performance using T2K's NEUT Monte Carlo equivalent to 7.0×10^{21} POT for both FGD1 and FGD2 targets. Each step's statistics is broken into events passing the cut and what proportion of those events are signal. Here the signal is the topology, CC1p1π^+, and those that are on hydrogen (H) where phase space constraints are included.

latter is the standard H-CC1p1π^+ signal introduced earlier. These will provide as a cross check for the expected ratio between events on hydrogen and those that are not. FGD1 is expected to have a ratio of approximately 14% whereas FGD2 should hold a larger hydrogen yield of around 17%.

5.4.1 3TPC Tracks Sample

Beginning with the 3TPC Track selection a step-by-step breakdown of the event statistics passing each cut is summarised in Table 5.4. Both FGD1 and FGD2 targets are presented with the respective number of signal events passing each analysis step. The final cut, namely, Tracks Charges, represents the total number of events passing all cuts.

As expected FGD2 contains more signal events on hydrogen than FGD1 and is a direct result of each target's nuclear composition. Interestingly, the number of events on hydrogen is approximately half that of the signal topology. At first

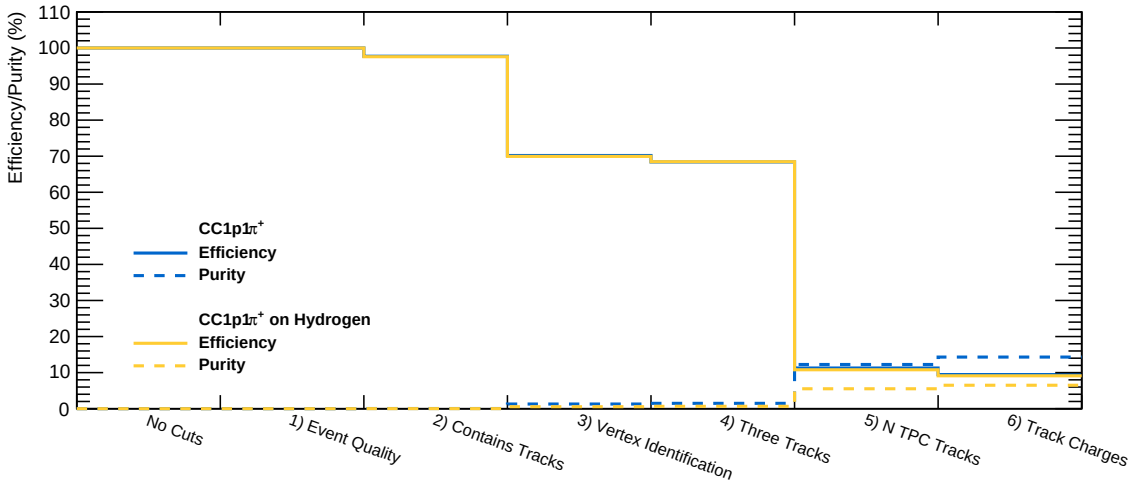

Figure 5.10: Running Efficiency and Purity for the 3TPC sample where FGD1 is the target. Note that the sold blue line is underneath the yellow.

glance this may seem incorrect given that we expect 14% of all FGD1 events to be on hydrogen. This higher than expected hydrogen contribution may however be attributed to FSI in heavy nuclei. Although at the 'bare' neutrino-nucleon level the interaction may indeed have started as the CC1p1π^+ signal, however the effect of FSI may emit more particles from the nucleus, and change the kinematics removing it from the signal definition.

Moving on to assessing the differences between the outcome of the selection developed here and that of the truth study. For FGD1[3] we see that the selection captures around 30% of the available three forward-going track events. This seems to be a result of the combined effect of the reconstruction algorithm and final state of interest. We saw in Figure 5.8 that a large amount of the CC1p1π^+ events lie above and below the three tracks requirement. This is backed up when the efficiency and purity are considered as a function of cuts like those shown in Figures 5.10 and 5.11 for each FGD target.

The effect of requiring three tracks dramatically reduces the efficiency but at the benefit of increasing the purity. Using this selection on actual data, equivalent to $1/10^{\text{th}}$ of the Monte Carlo statistics, one would expect to see around

[3]True number of three forward-going track events for FGD1 can be found in Figure 5.3.

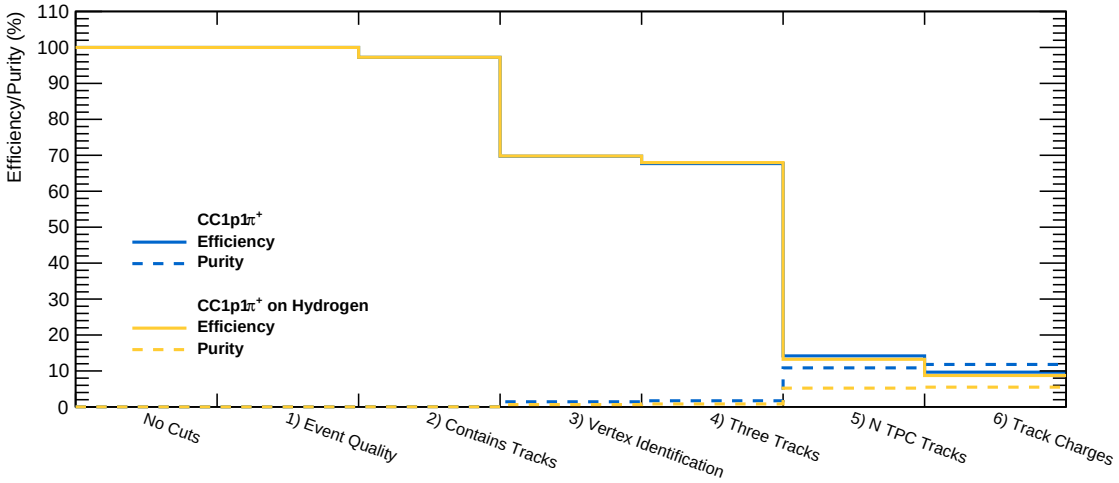

Figure 5.11: Running Efficiency and Purity for the 3TPC sample where FGD2 is the target.

70 signal events when using both FGDs. Clearly such a low yield would lead to a large statistical uncertainty making any measurement statistically limited. It is however possible using Monte Carlo to build δp_{TT} distributions for each FGD target from the respective samples.

5.4.2 FGD Contained Sample

Following the outcome of selecting 3TPC track events, the FGD Contained sample is now discussed. Like in the 3TPC track case the event yield following each cut is presented in Table 5.5. The first four cuts are identical to those in Table 5.4 however when two TPC tracks are required the events passing the cut is less than that in the three TPC tracks case. Given the result of the truth study in Section 5.2 this difference is expected but may also be due to difficulties in FGD contained track reconstruction.

The additional cut applied to the FGD Contained selection has a dramatic effect on event rate in both FGDs. This cut effectively leaves this sample unusable in this analysis as the hydrogen yield can only be determined using δp_{TT} on a statistical basis. This sample therefore has no use in the analysis.

Cut	FGD1		FGD2	
	Events	Signal (on H)	Events	Signal (on H)
No Cuts	1.43×10^8	7343 (3467)	1.43×10^8	8267 (4274)
Event Quality	1.43×10^8	7343 (3467)	1.43×10^8	8267 (4274)
Contains Tracks	1.41×10^8	6432 (2717)	1.41×10^8	7532 (3408)
Vertex Identification	497165	6432 (2717)	529196	7532 (3408)
Three Tracks	384676	5700 (2522)	381674	6490 (3106)
2 TPC + FGD Cont.	5091	351 (168)	2551	224 (106)
FGD Particle Id	3272	189 (81)	1784	144 (63)
Tracks Charges	373	47 (24)	100	12 (3)

Table 5.5: Summary of both FGD1 and FGD2 targets selection performance for the FGD Contained sample using T2K's NEUT Monte Carlo equivalent to 7.0×10^{21} POT. Each step's statistics is broken into events passing the cut and what proportion of those events are signal. Here the signal is the topology, CC1p1π^+, and those that are on hydrogen (H) where phase space constraints are included. Note that Cont. stands for contained tracks.

5.4.3 Summary

The two selections developed here indicate that we are able to identify signal events, however only those fulfilling the three forward-going tracks topology are statistically viable. The selection of this topology is however statistically limited and had to compromise on purity to avoid the efficiency being too low. This work analysed Monte Carlo equivalent to approximately ten times data POT. If this selection was applied to T2K data from run periods one to seven the resultant signal from both FGDs would yield around 70 events. This would make any signal extraction using δp_{TT} unfeasible due to the low purity and limited statistics.

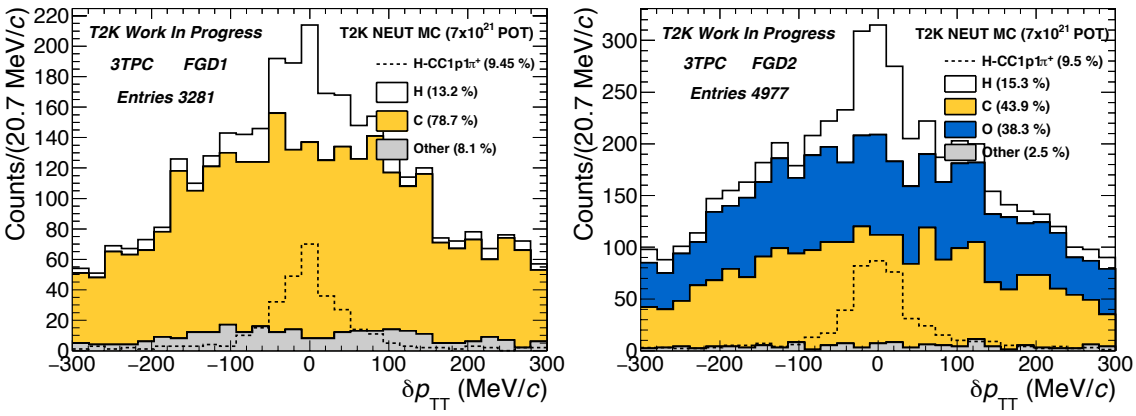

(a) FGD1 Target. (b) FGD2 Target.

Figure 5.12: Double Transverse Momentum distributions for the 3TPC Tracks samples at T2K. The interactions are broken down into target nuclei where the H-CC1p1π^+ signal is overlaid highlighting where the signal component lies in δp_{TT}.

5.5 Transverse Variables

The selections developed here provides two usable samples for the reconstruction of δp_{TT}, namely the 3TPC Track samples for each FGD target. Using these two samples it is interesting to assess whether the hydrogen component is visible in either target. By applying the approaches defined in Chapter 3 to reconstruct the neutrino's direction, each FGD's δp_{TT} distribution is presented in Figure 5.12. In both cases the δp_{TT} distribution is broken down into target nuclei and the H-CC1p1π^+ signal is overlaid to highlight where it lies. Note that the H-CC1p1π^+ signal is a subset of the hydrogen component in each FGD.

From Figure 5.12, it is clear that neutrino interactions on hydrogen producing the final state of interest can be seen in δp_{TT}. This indicates that detectors like ND280 have sufficient resolution for the δp_{TT} variable to be useful when measuring nuclear effects. There is a noticeable difference between the two samples, firstly, the water in FGD2 (Figure 5.12b), increases the number of background events entering the distribution. The water target also increases the signal component and is therefore much more prominent in FGD2 than in FGD1 (Figure 5.12a).

Focussing on the H-CC1p1π^+ distributions one should comment on the broadening in δp_{TT} between the two samples. This feature is due to the reconstruction capabilities of the detector as a perfect detector would lead to hydrogen having a delta-function in δp_{TT}. Hence this difference between each FGD implies that FGD2 suffers from a larger mis-reconstruction of each tracks momentum.

One possible explanation of the broadening is down to FGD2 containing water. When a global track is reconstructed in ND280, a TPC track is assessed to see if it matches a track within the FGD. If a track is found to match then the momentum of the whole track needs to be determined. During this process the momentum of each detector is summed to produce the tracks total momentum. Given the FGD reconstructs the momentum by range, the track's length in the FGD may be mis-reconstructed due to the passive water regions. This would lead to a larger smearing effect resulting in the larger broadening observed in FGD2.

From Figure 5.12, it can be seen that T2K has the reconstruction capability needed to identify neutrino interactions on hydrogen. However, if the signal component is to be reliably determined the background shape needs to be constrained. Unfortunately, this is not possible using T2K alone as the heavy nuclear background cannot be isolated and constrained independently from hydrogen. Although work relying on knowledge gained from the CC0πNp (N > 0) analysis [100] was investigated and assessed to see whether the shape could be constrained, it was found to be infeasible due to the different initial state model used in CCQE-like interactions. NEUT uses a RFG for resonance production and a Spectral function for CCQE processes making such comparisons impractical. Therefore if hydrogen is to be measured at T2K external sources are needed to help reduce uncertainties in the event yield. This possibility is investigated in Chapters 6-8 using a similar final state topology.

Chapter 6

MINERνA Analysis: Signal and Selection

We have seen from Chapter 3 that in the central region of δp_{TT} carbon has large disparities in the prediction of its shape. If the hydrogen measurement outlined in Chapter 5 is to be realised at T2K the δp_{TT} shape of the carbon background needs to be understood. From the previous chapter we also learnt that the experimental configuration of T2K without a pure carbon target will result in a large systematic uncertainty due to our limited knowledge of the nuclear dynamics. The shape of carbon in δp_{TT} therefore needs to be constrained, not only to aid in measuring interactions on hydrogen but to also improve our knowledge of nuclear effects.

The MINERνA Experiment is an ideal detector at measuring the carbon shape in Double Transverse Momentum for numerous reasons. Being situated in the NuMi beam provides a higher energy neutrino flux enabling the production of three-particle final states well above the production threshold. This improves our ability to reconstruct such final states. Like T2K it also contains an active tracker region made of plastic scintillator ($^8C^8H$) removing the need to rely on any complicated extrapolation method to translate information to/from a heav-

ier or lighter nuclei.

The following analysis is an extension of the recent measurement presented by MINERνA on π^0 production [68]. Although the final state is distinct from that needed for measurements on hydrogen, we are taking advantage of our understanding of the similar shape predictions in δp_{TT} between the two final states. Such an approach would be infeasible and impractical at T2K as converted photons in ND280 are difficult to reliably reconstruct. Photons that do convert have poorly reconstructed kinematics leading to reduced sensitivity in measuring carbon's nuclear dynamics.

We will analyse the Low Energy NuMi dataset consisting of a total collected POT of 3.33×10^{20}. The selection of signal-like events are the same for both the analysis presented in Reference [68] and in the following chapters. Note however that the signal definitions differ. The original signal definition and updated signal are given in Section 6.1 where comparisons are made throughout this chapter.

This chapter shall begin by outlining the signal definition under study in this analysis. Using the same approach as in Reference [68] the selection of the final state of interest shall then be introduced. The chapter culminates in defining the methodology used to constrain the dominant backgrounds passing the selection.

6.1 Signal Definition

In order to constrain the background shape of δp_{TT} in a composite nuclear target containing hydrogen, a final state needs to be identified that passes the following criteria:

- A muon neutrino-induced charged-current interaction,
- Must contain at least one pion,
- The interaction cannot occur via neutrino interactions on hydrogen,

- A three particle final state for use in the construction of Double Transverse Momentum,
- The final state must provide information on carbon's δp_{TT} shape.

Given these criteria it is clear that at the 'bare' neutrino-nucleon level, interactions are required to occur on neutrons. This leaves only one readily detectable final state from Table 3.1 to form our signal definition

$$\nu_\mu + n \rightarrow \mu^- + \pi^0 + p. \tag{6.1}$$

Although a final state containing a μ^-, neutron and π^+ could also be used, due to the low detection probability of neutrons, such a signal would be statistically limited.

The signal definition is further refined to account for the experimental set up. Our measurement therefore looks for events on hydrocarbon within the active tracker region of MINERνA whose fiducial volume is given in Table 6.2. Additional constraints are applied to the signal definition to account for MINERνA's detector acceptance. This places limits on the phase-space of various kinematics in order to reduce model dependence. The kinematic constraints applied are described in Table 6.1. The 'reduced' phase-space will lead to a fiducial cross section measurement.

In summary our signal events are defined as originating from hydrocarbon and contain a single μ^- and at least one proton and π^0 with any number of neutrons outside of the nucleus. No other hadrons can be observed in the final state and kinematic restrictions are placed on the out-going particles. The signal definition would therefore include events whose 'bare' neutrino-nucleon interaction have undergone final state interactions as discussed in Chapter 2. Such a signal definition shall be referred to as CCNpMπ^0 throughout the remaining chapters where N,M > 0 is implied throughout.

Phase Space Constraints	
Original [68]	New
$60.0 \leq m_{\gamma\gamma}\ (\mathrm{MeV}/c^2) \leq 200.0$	
$\theta_\mu \leq 25.0^\circ$	
$1.5 \leq E_\nu\ (\mathrm{GeV}) \leq 20.0$	$1.5 \leq E_\mu\ (\mathrm{GeV}) \leq 20.0$
$W \leq 1.8$ GeV	$450 \leq p_\mathrm{p}\ (\mathrm{MeV}/c)$

Table 6.1: Phase space constraints applied to the signal definition for use in the measurement of a fiducial cross section. Original refers to those used in the 2017 paper [68] and new are the constraints applied in this analysis.

The signal definition outlined in Reference [68] looks for a similar final state to what is being studied here; the key difference being the number of π^0s. In Reference [68] the analysis requires exacly one π^0 whereas this work asks for at least one π^0. By requiring at least one π^0 reduces model dependence as the π^0 multiplicity is poorly understood. This is due to our current, limited knowledge of Final State Interactions. Note that Reference [68] does not require a proton in its signal.

Additionally, neutrino generator specific signal definitions are removed from our analysis. If we recall the invariant mass of the hadronic system, W, is generator specific as it is effected by FSI and the treatment of the transition region between Resonance production and DIS. Given this, the constraint on W is removed in our definition and it relaxes the requirement of isolating resonance events. The resultant measurement will therefore be of a purely topological final state.

Finally, defining a neutrino energy (E_ν) range complicates the problem as it can only be reconstructed using the visible energy and particles identified in the detector. This becomes a highly degenerate problem as many different combinations of final state kinematics can lead to a single neutrino energy. As a result, the acceptance for the various associated phase-spaces need to be well

understood. It is also complicated by the missing energy from neutral particles in the detector and relies on model dependence to account for this. We therefore ignore any E_ν considerations in our signal definition.

6.2 Event Selection

The selection presented here is identical to that outlined in the 2017 π^0 analysis [68]. From Reference [68] we use the 'delta-rich' selection where a proton is required. This sub-sample forms the basis of the selection of the CCNpMπ^0 signal definition. Given this, the following is an overview of the selection used to identify candidate events along with the relevant sidebands used to constrain the dominant backgrounds.

The selection of CCNpMπ^0 candidates in MINERνA comprises of six analysis steps which have been optimised in order to maximise both efficiency and purity. The schematic in Figure 6.1 provides a clear outline of the analysis flow used. Beginning from the first requirements, an explanation of each step follows.

6.2.1 Time Slicing

The configuration of the NuMi beam provides a large interaction window within which neutrinos produced at the target can interact inside MINERνA. The experiment starts recording data 1 to 2 μs before a single spill of up to 10 μs is expected, acquiring data over a total duration of 16 μs. A total duration of 16 μs is known as a gate. During this period, multiple interactions can occur and therefore require separation in time for individual interactions to be identified.

Multiple interactions are separated via a time slicing algorithm which analyses all hits in a gate and groups them according to their time. A single time slice is identified as starting when a hit above 10 photo-electrons (PE) is observed and ends once the last hit is below 10 PE. This can be seen in Figure 6.2 where

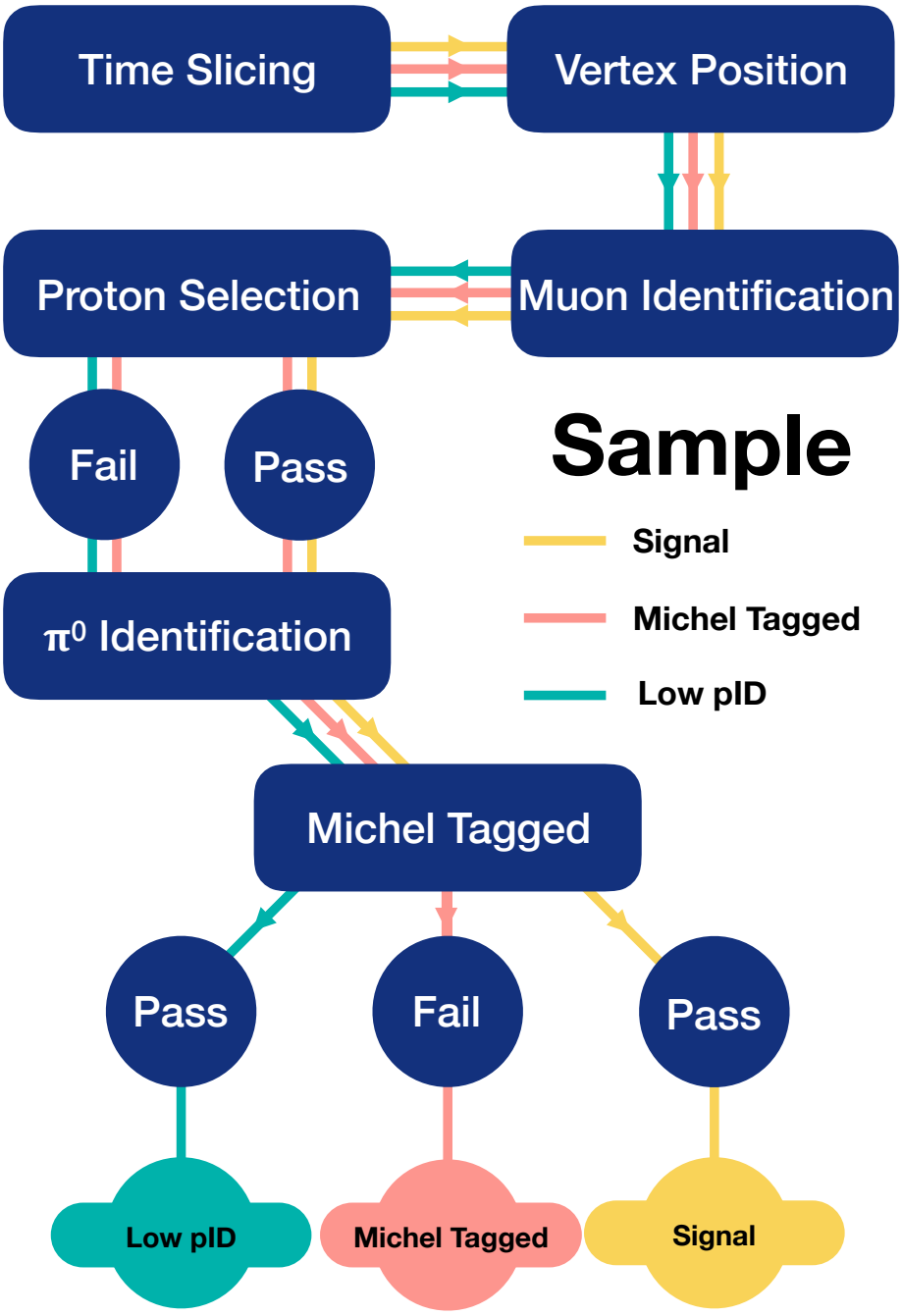

Figure 6.1: Analysis flow for the selection of the signal sample along with additional samples used to constrain the dominant backgrounds. Further details of Michel Tagging can be found in Section 6.2.6. Note that the Michel Tagged Sample doesn't require protons but in cases where a proton like track has been identified it must pass the proton pID.

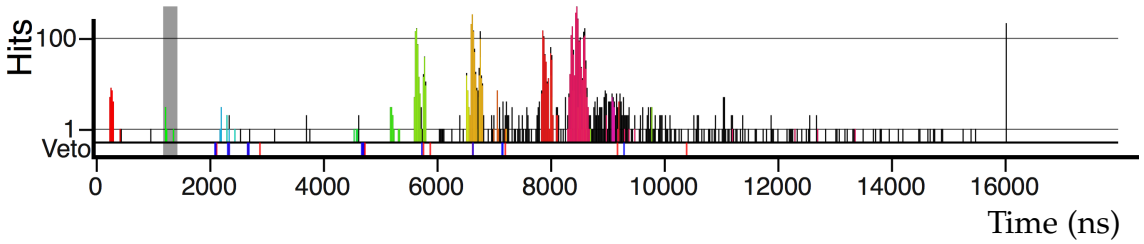

Figure 6.2: Different colours represent the numerous time slices identified during a single gate of 16 μs. Each time slice has an individual colour. For example, at around 6 μs an interaction has been identified and the time slicing algorithm highlights this in green.

a single gate of MINERνA is presented during which it receives a NuMi beam spill. The different colours specify various time slices identified by the algorithm.

6.2.2 Vertex Position

By default the vertex position is defined as the start position of the muon-like track. The muon-like track is identified by the standard reconstruction algorithm from which this selection is based on. This vertex position is further refined by requiring it to lie within the reconstruction volume.

Once a vertex candidate is identified it is assessed to see if short tracks surround the vertex. If additional short tracks are found the vertex is re-evaluated to account for the additional information provided by the extra tracks. Finally a fiducial volume cut is performed to ensure that the interaction vertex is well within the active tracker region. This fiducial volume cut increases the probability of interacting on a hydrocarbon target. Both the reconstruction and fiducial volumes are provided in Table 6.2.

6.2.3 Muon Selection

Negatively charged muons are identified by requiring the track to have a matching track in the MINOS detector. This requirement allows the charge and mo-

Volume	Apothem (mm)	Z Region (mm)	
		Upstream	Downstream
Reconstruction	1000.00	5810.00	8600.00
Fiducial	850.00	5991.37	8363.92

Table 6.2: Detector volumes used to identify candidate vertices. The apothem is defined as the distance between the centre of a hexagon (or MINERνA's central axis) to the midpoint of its side.

mentum of the track to be determined, but confines our events to have only very-forward going muons. This is why the signal definition has a low muon angle cut applied.

6.2.4 Proton Identification (pID)

Following the recognition of short tracks within the reconstruction volume each track's dE/dx profile is compared with those of a proton or charged pion hypothesis. If any of the tracks fail to be compatible with either hypothesis, the event is rejected. If the four-momentum of the track cannot be determined it is also removed from the selection.

Proton-like tracks are identified by considering their dE/dx profile based on MC simulations. The test statistic used to select proton candidates is a Log Likelihood Ratio (LLR) and can be seen in Figure 6.3. Only tracks whose LLR score is greater than -5.0 are classified as proton-like tracks and pass onto the next stage of the selection.

6.2.5 Neutral Pion Selection

Prior to reconstructing π^0-like objects in MINERνA, a set of global checks are performed on energy not associated to any reconstructed tracks. Each event must fulfil the following criteria for it to pass the pre-checks.

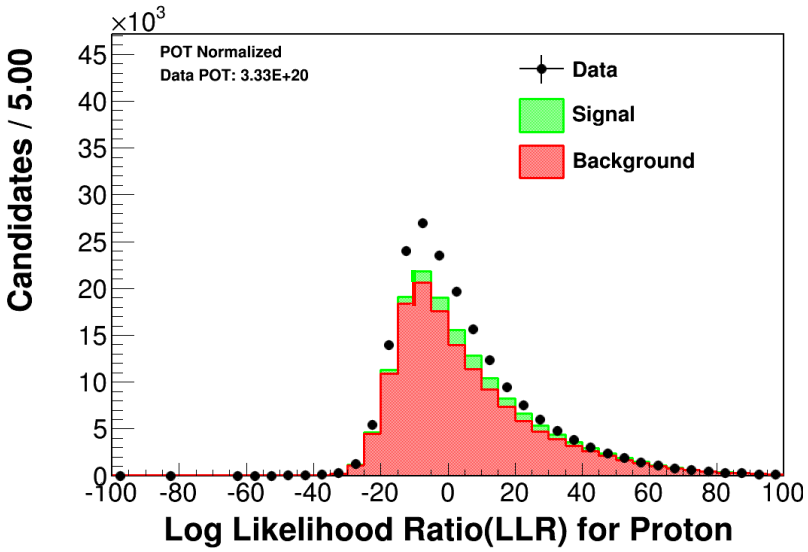

Figure 6.3: The Log Likelihood Ratio for proton and pion dE/dx hypotheses define the proton score. Events whose score is above -5 pass the proton hypothesis. Adapted from Reference [101].

- Unused energy must exceed 50 MeV in the Tracker and/or Calorimeters in order to pass the pre-checks.
- If energy above 20 MeV is observed in the nuclear targets region the event is rejected.
- Events are rejected if deposits of energy above 2500 MeV are observed anywhere in MINERνA.

These constraints remove events which are either unlikely to be signal-like or fail to be used in the π^0 reconstruction algorithm. The algorithm used to identify π^0s searches for the dominant decay channel, $\pi^0 \rightarrow \gamma\gamma$, whose branching ratio is 98.82% [22]. By requiring exactly two EM showers within MINERνA, checks are made on their directionality ensuring that they are consistent with originating from the interaction vertex. This is achieved by fitting a straight line from the vertex position to the energy deposits forming each EM shower. The line determined from the fit is used in unison with the EM shower energy to reconstruct the photon's momentum. The topology of the photon pair forming the π^0 candidate is then examined to require the following features

- The leading, high energy photon, γ_1, must start at least 14 cm away from the vertex.
- The sum of the two EM showers ($E_1 + E_2$) and the cosine of the opening angle ($\cos\theta_{\gamma\gamma}$) are required to be more than 400 MeV and less than 0.95.
- The two-photon invariant mass must be within 60 and 200 MeV/c^2.

Applying these requirements ensures that mis-reconstructed events along with background dominated regions of phase-space are removed from the selection.

6.2.6 Michel Tagging

Events containing charged pions are removed by checking for the absence of Michel electrons – a well defined time structure of a π^+ decay. This is achieved by searching for energy deposits shortly after the main interaction takes place and considers various positions in the event. It first looks around the primary vertex before checking track end-points. Finally by searching at the start and end point of the EM showers verify that no Michel-like properties exist in the event.

6.2.7 Kinematic Checks

As defined in Section 6.1, the signal definition has phase space restrictions to account for the detector acceptance. These were determined by knowing the physical limits of the detector for each particle type and assessing the effect of placing constraints on the true kinematics. For example, the two photons produced from the π^0 decay have checks placed on both the energy and opening angle. These restrictions were placed on the true kinematics but showed negligible change in the predicted event rate. It was therefore decided that such a kinematic constraint was not necessary in our signal definition.

Cut	Total Events	Signal	Efficiency (%)	Purity (%)
No Cuts	2294530	283614	100.00	12.36
Vertex Position	2294530	197734	69.72	8.62
Muon ID	2285850	197597	69.67	8.64
Proton ID	1246790	146669	51.71	11.76
π^0 ID	173416	50481	17.80	29.11
Michel Tag	106518	40684	14.34	38.19
$0 \leq E_\mu$ (GeV) ≤ 20	100617	40326	14.22	40.08
$60 \leq m_{\gamma\gamma}$ (MeV/c^2) ≤ 200	53628	27103	9.56	50.54
Have Proton	31212	16038	5.65	51.38

Table 6.3: Summary of the selection performance of the Signal sample searching for CCNpMπ^0 final states where $M, N > 0$. The total number of events passing each cut along with the signal contribution (CCNpMπ^0) is given. The change in efficiency and purity is also presented. These figures were produced using Monte Carlo equivalent to 2.22×10^{21} POT.

6.2.8 Selection Performance

Using the purity and efficiency metrics defined in Section 5.4 each cut is assessed in order to understand the effectiveness of selecting CCNpMπ^0 events. This is summarised in Table 6.3. Note the order of the cuts here. The proton kinematic cut is included in the Proton ID and the requirement of having a final state proton is checked last. This is a facet of extending on the analysis in Reference [68].

From Table 6.3 there are three cuts which have a dramatic effect on our ability to select CCNpMπ^0 final states. They are the π^0 ID, Michel tag and invariant mass cut. We see that MINERνA looks to reliably identify one in three π^0 events. This low efficiency is caused by MINERνA's inability to separate photon showers. Although this cut induces a large reduction in the efficiency, the purity is increased substantially.

Michel tagging is particularly effective at removing charge pion backgrounds

resulting in a 31% improvement in the purity. The final cut which has a substantial effect on the purity is the invariant mass constraint. This yields a further 25% improvement in purity but at the loss of a third in the efficiency.

By comparing the two different signal definitions, the 2017 paper [68] has a smaller efficiency than this analysis (5%). We also observe a marginally better purity when using our signal definition. The 2017 paper [68] using the same selection leads to a 50.7% purity whereas our signal definition results in a 51.38% purity [101]. These are expected given the old signal definition, requiring exactly one π^0 is a sub-sample of the signal used here.

Although the selection is capable of identifying signal events with a purity of 51.38%, approximately half of the events passing the selection criteria are background. It is useful to consider how the background component breaks down both in terms of topologies and interaction modes. Let us begin by splitting the background topologies into four categories

- π^0 with charged mesons – Events which contain at least one π^0 and any number of charged mesons. If a signal event fails to fulfil the kinematic constraints outlined in Table 6.1 they fall into this category.
- Charged mesons – Final states which include only charged mesons.
- Zero mesons – Topology containing zero mesons where the final state predominantly consists of nucleons.
- Other – Events failing to fulfil any of the above criteria. Also included are signal events which are out of acceptance.

Given these background definitions, what is our background composed from? Table 6.4 and Figure 6.4 indicate that the dominant background topology is 'Charged mesons'. This is closely followed by 'π^0 with charged mesons' and 'Zero meson' whose contribution are very similar. Although the purity in the

Sample	Entries	Topology (%)				
		Signal	π^0 w/ $q^\pm$	$q^\pm$ mesons	Zero mesons	Other
Signal	57884	36.10	17.56	25.30	17.77	3.27
Michel	19982	4.47	40.61	51.17	1.66	2.09
pID Fail	31667	11.70	24.24	56.24	6.39	1.44

Table 6.4: Breakdown of the true topologies passing the selection along with the expected number of events for each sample. Here we consider entries whose invariant mass lie within $0 \leq m_{\gamma\gamma}$ (MeV/c^2) ≤ 500 and the signal topology has no invariant mass cut applied. Note $q^\pm$ denotes charged mesons and that a Monte Carlo dataset equivalent to 2.22×10^{21} POT was used.

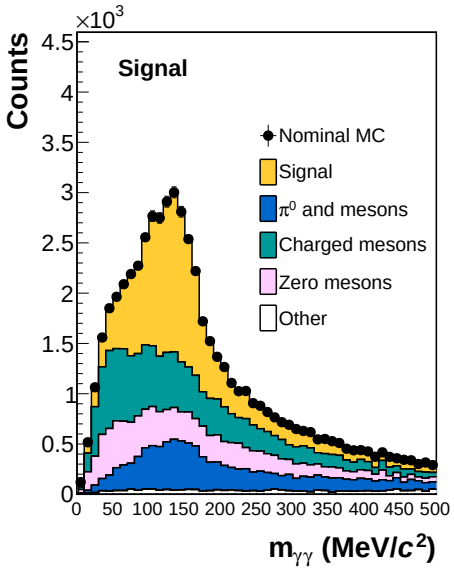

Figure 6.4: The invariant mass distribution for the signal sample using Monte Carlo POT equivalent to 2.22×10^{21}. The data points presented here is the same as the Monte Carlo prediction.

signal invariant mass range is 51.38% Table 6.4 shows a smaller purity as it includes events spanning $0 \leq m_{\gamma\gamma}(\text{MeV}/c^2) \leq 500$. These substantial background contributions need to be constrained given our limited knowledge of cross section models.

6.2.9 Additional Samples and Sidebands

It is clear from Table 6.4 that there are three backgrounds which dominate the signal region. These are π^0 with charged mesons, charged mesons and zero mesons. If they are left unconstrained and their relative contributions to the signal region are reliant on Monte Carlo predictions alone, the final cross section result will be highly model dependent and may result in larger uncertainties. It is therefore necessary to define additional samples that provide information on the relative background contributions. Individually, each sample should be statistically rich in a particular background type. This is achieved by selecting events which fail certain cuts already introduced.

In Figure 6.1, the analysis flow for the selection of the respective sideband samples is also outlined. There are a number of minor differences applied to either maximise statistics or improve the background purity for a given sample. Firstly, the Michel sample requires a Michel-like signature in the event however unlike the signal sample does not require events to have a proton track. If an event does contain a proton it must be proton-like and pass the LLR score. This results in a sample rich in charged mesons as seen in Table 6.4 where both topologies containing charged mesons dominate.

The second sample, pID, provides information on the charged meson contribution and contains events which fail the proton LLR score. Note that this and the Michel sample do not require any kinematic constraints on the hadronic final state. Finally, using the high ($200 \leq m_{\gamma\gamma}(\mathrm{MeV}/c^2) \leq 500$) and low ($0 \leq m_{\gamma\gamma}(\mathrm{MeV}/c^2) \leq 60$) invariant mass regions in the signal sample gains an insight into the zero mesons background.

In summary, there are a total of three samples that will be used to gain an insight into the relative contributions from the dominant backgrounds. These are the Signal, Michel and pID samples each passing their own selection criteria summarised in Figure 6.1. The signal sample must however be used with care

when trying to understand the backgrounds. This is because we want to use the additional samples and sidebands to extrapolate what has been learnt about the background in the signal region. Therefore, only part(s) of the Signal sample can be used that contain a small signal component.

6.3 Monte Carlo Tuning

Until now we have only discussed the results of Monte Carlo predictions, which at the time of production may not fully describe the data today. This could be due new physics models like 2p2h that had not been fully integrated into the neutrino event generator or more recent measurements of the neutrino flux providing a better insight into its behaviour. The Monte Carlo prediction therefore needs to be updated in order to incorporate changes given a more 'up-to-date' knowledge of the experimental set up and physics models.

Although one could reproduce the simulation to include such changes it is generally unfeasible due to the timely and costly process of Monte Carlo production. The approach popularly used to include additional effects is to reweight the Monte Carlo following some constraint provided by either external measurements or the outcome of internal cross section results.

Reweighting is integrated into the analysis on an event-by-event basis. Each event has a weight that is determined using a set of multiplicative weights each incorporating a different response to the nominal Monte Carlo. A full discussion of how the various weights were determined is beyond the scope of this thesis but for completeness shall be summarised here.

- Flux Tuning – This accounts for numerous effects that change the flux distribution. These include horn geometry corrections, beam focussing and external constraints from hadron production experiments [102].

- Delta Non-isotropy – GENIE's implementation of the Rein-Seghal model

assumes the delta decays isotropically in the delta's rest frame. This changes the angular distribution of the decay products of Δ^{++} resonances to account for the non-isotropic nature of the decay [103, 104].

- Resonance Production Normalisation – Improvements to GENIE's nominal normalisation for resonance and non-resonance single pion production is implemented following re-analysis of bubble chamber data. See Reference [105] for more details.

- Delta low-Q^2 Suppression – Following re-analysis of charged-current interactions at MINOS from Reference [61] a Q^2 suppression is applied to resonance production. The suppression is believed to be a nuclear effect like RPA which reduces the cross section at low Q^2.

- 2p2h MINERνA Constraint – Following the recent MINERνA result in Reference [91] 2p2h event weights are calculated using the tune developed by Rodrigues *et al.* within the MINERνA collaboration.

- Tracking Efficiency Correction – A correction is made dependent on each data run and accounts for the track matching efficiency between MINERνA and MINOS.

In certain circumstances where it is not possible to reweight the Monte Carlo, a new production is required. This was the case for 2p2h interactions as it was not included in the nominal event generator at the time of original production. A second Monte Carlo dataset was produced using a 2p2h model developed by Nieves *et al.* that includes RPA correlations. The 2p2h production is included as a second Monte Carlo dataset which is passed through the same analysis framework as the nominal prediction.

The additional Monte Carlo events, although 2p2h interactions, are tagged using the same definitions as those used for the signal and background already discussed. This enables us to correctly identify the final state emitted from the

nucleus and not at the bare neutrino-nucleon level. The 2p2h dataset has a different POT than the nominal Monte Carlo which is also incorporated into the analysis ensuring correct POT scaling is achieved. Going forward Monte Carlo shall refer to the combined nominal and 2p2h Monte Carlo datasets which have been 'tuned' following the changes to Monte Carlo defined above unless stated otherwise.

6.4 Background Constraints

Having determined sideband samples that may provide constraints on the dominant backgrounds, it is now necessary to outline the fit procedure used to perform such a task. It is first necessary to identify a kinematic distribution available to all samples that could be used by the fit. The two-photon invariant mass distribution was chosen as it fulfils the requirement of being reproducible by all samples. Ideally one would use δp_{TT} to perform the background constraints leading to a one-to-one mapping of the backgrounds onto the variable of interest. Unfortunately, the Michel sample does not require a proton-like track and is also statistically limited making δp_{TT} infeasible to be used as the variable to perform the fit.

The $m_{\gamma\gamma}$ invariant mass distribution to be used to constrain the various backgrounds can be seen in Figure 6.5 for each sample. Here the distributions use a constant bin width of 10 MeV leading to each sample containing 50 bins. The data points in Figure 6.5 have been set to be 'Nominal MC', i.e. identical to the Monte Carlo prediction. As mentioned in Section 6.2.9 only part of the Signal sample is used in the fit, namely, the low and high $m_{\gamma\gamma}$ regions. One can see that the two sidebands in the Signal sample are dominated by background and can therefore be used in the fit.

The dominant backgrounds are constrained by performing a χ^2 fit to data where for each background a scaling parameter, c_j, is to be determined. This

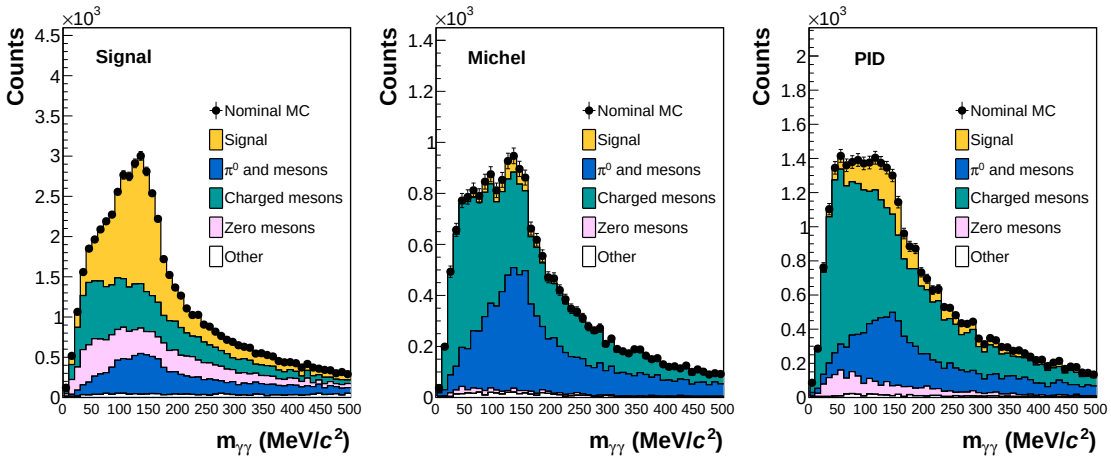

Figure 6.5: The invariant mass distributions for the Signal (*left*), Michel (*right*) and pID (*right*) samples. Note that the Signal sample only considers the region outside $60 \leq m_{\gamma\gamma}\ (\mathrm{MeV}/c^2) \leq 200$.

parameter simply scales the respective background Monte Carlo prediction given the data. Defining the χ^2 to minimise as

$$\chi^2 = \sum_{s=1}^{N} \chi^2_s, \tag{6.2}$$

where s spans the Signal, Michel and pID sideband samples (hence $N = 3$) whose individual Pearson χ^2 can be described by

$$\chi^2_s = \sum_{i=1}^{M} \frac{\left(N_i^D - N_i^{MC}\right)^2}{N_i^{MC}}, \text{ where } N_i^{MC} = R_{\mathrm{POT}} \sum_{j=1}^{5} c_j N_{j,i}. \tag{6.3}$$

The superscript D denotes Data and MC represents the Monte Carlo prediction to be constrained. For each bin i in the respective samples the Monte Carlo prediction consists of a POT scaling term, R_{POT}, accounting for the difference in collected POT to the Monte Carlo sample size.

Each model component, j, has an associated scaling parameter c_j which are common to all samples leading to a total of five scaling parameters. This implies that each component has its own scaling term which is indeed the case, however when the fit is performed the terms relating to the Signal and Other are fixed.

Therefore the fit reduces to determining three free parameters, one for each of the dominant backgrounds, namely, π^0 with charged mesons, Charged mesons and Zero mesons. Using the definition for the number of degrees of freedom (*ndf*) as

$$ndf = N_{\text{Data}} - N_{\text{Par}} - 1, \tag{6.4}$$

where in our case N_{Data} is the total number of bins used to determine the number of free parameters, N_{Par}, in the fit. This leads to the total *ndf* equal to 135 as each sample contains 50 bins with the exception of the signal sample which ignores the region spanning $60 \leq m_{\gamma\gamma}\ (\text{MeV}/c^2) \leq 200$ reducing it to 36 bins.

A number of studies were undertaken to assess the performance of the fit allowing us to understand if any bias is observed and the coverage of the result is consistent with expectation. This began with a closure test, fitting the Monte Carlo to itself where, as expected, the fit converged with a χ^2 of zero and found unity scaling terms. The second two tests rely on repeating the fit procedure many times where for each fit parameter, j, the ensemble of fit results is assessed by considering its pull, p_j

$$p_j = \frac{\left(x_j^{\text{fit}} - x_j^{\text{exp}}\right)}{\sigma_{\text{j,fit}}}. \tag{6.5}$$

Here x_j defines the parameter value, 'exp' refers to the expectation value for the 'fit' result whose uncertainty is given by $\sigma_{\text{j,fit}}$.

Reliable fit results are expected to populate each parameters pull distribution so to have a mean of zero and a RMS of one. Given that both tests are essentially Monte Carlo to Monte Carlo minimisation procedures the expected χ^2/ndf should be unity if the fitting technique is functioning correctly. For each pull study, the Monte Carlo is scaled to simulate the MC/data POT difference where MC is approximately seven times (15% of Monte Carlo POT) collected POT. Note that the MC is acting as data in the following studies and is defined as 'fake data'.

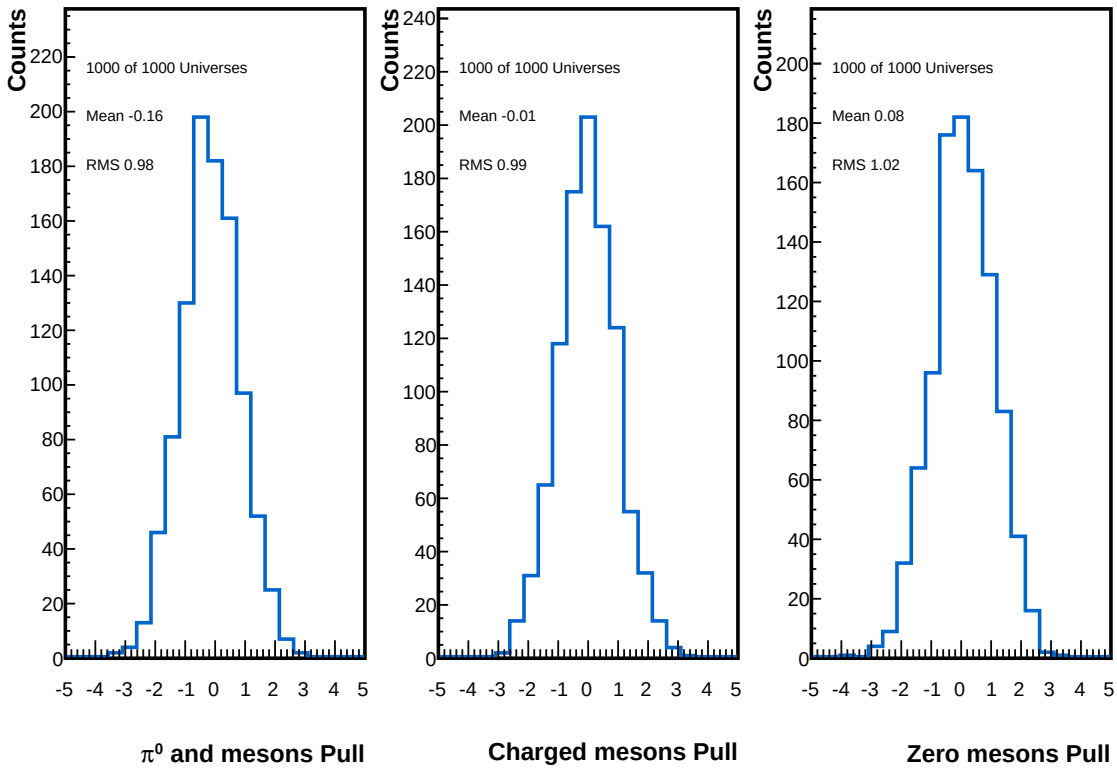

Figure 6.6: Pull distributions determined for each free parameter in the statistical fluctuation study using 2.22×10^{21} POT Monte Carlo statistics. Here both the Fake Data and Monte Carlo are scale to 15% of their original size in order to simulate fitting with actual data statistics. The background results for π^0 and mesons (*left*), Charged mesons (*centre*), Zero mesons (*right*) are presented.

6.4.1 Statistical Fluctuations

The first test considers 1000 Poisson fluctuations of the fake data and compares the fitted x_j to unity as the relative background rates should be the same for both fake data and Monte Carlo. For every Poisson toy, each data sample is varied following Poisson statistics before performing the fit. The scaling parameters determined by the fit are then used to produce the pull results.

The outcome of the statistical fluctuations is presented in Figure 6.6 and resulted in the mean $\chi^2/ndf \sim 1$. Here the pull results for the ensemble of 1000 statistical variations is given for the scaling parameters relating to the three backgrounds. In each case the RMS is within 2% of expectation indicating that the statistical fluctuations are being varied correctly. There is a minimum bias ob-

served for the charged mesons c_j whereas the π^0 and mesons and Zero mesons parameters have a non-negligible bias. The former π^0 and mesons term looks to be under estimated and looks to result in the Zero mesons c_j absorbing this reduction by being increased in the fit.

6.4.2 Systematics Effects

The second study performed reviews systematic effects associated to detector modelling, flux prediction along with uncertainties in the interaction model and nuclear dynamics predicted by the Monte Carlo generator. Full details of the systematics will be outlined in Section 7.2 and will be defined as 'universes' for the duration of this discussion.

A systematic universe comprises of the nominal Monte Carlo where a single systematic variation is applied to the prediction. This results in an alternative Monte Carlo which has been modified following the systematic effect. In total there are 1190 universes considered in this study.

Given that the Pearson χ^2 asks 'how well does a given model with some associated uncertainty fit to data' the fake data therefore remains unchanged; hence in each universe, variations are made to Monte Carlo prediction before the fit is performed.

In contrast to the statistical study, the systematic study uses the integral of events in the signal region when calculating the pull. The expectations for the various backgrounds therefore remains unchanged however in each systematic universe it will have a different prediction for the relative signal and background components. Given this, the fit result is constructed by taking the integral in the signal region for said background, j, and multiplying it by its scaling factor, c_j. Similarly, the uncertainty uses the same integral but scales it by the error on the

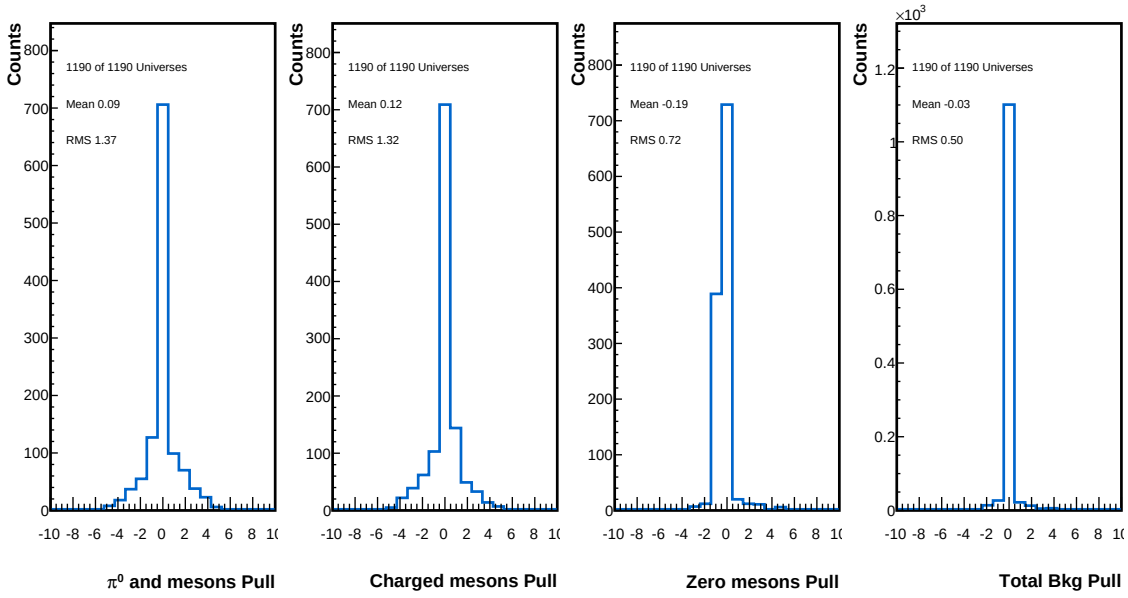

Figure 6.7: Pull distributions determined for each free parameter in the systematic variations study using 2.22×10^{21} POT Monte Carlo statistics scaled to data equivalent POT (approx. 15% MC POT). The background results for π^0 and mesons (*left*), Charged mesons (*centre left*), Zero mesons (*centre right*) and Total background (*right*) are presented.

scaling parameter. These are given explicitly by

$$x_j^{\text{fit}} = c_j \sum_{k=1}^{N_{\text{bins}}} N_{j,k}, \qquad \sigma_j = \sigma_{c_j} \sum_{k=1}^{N_{\text{bins}}} N_{j,k}. \tag{6.6}$$

The results of the systematic bias study is presented in Figure 6.7 and includes an additional pull distribution which assesses the total background bias. In comparison to the statistical study one can immediately see that the RMS does not follow Gaussian statistics but the χ^2/ndf is found to be situated around unity. Given this study considers systematics variations the interpretation here differs as the variations may not, as an ensemble of toys, be Gaussian distributed resulting in the observed RMS. This indicates that the RMS has no physical meaning in this study and therefore the key guide is the mean of each distribution.

It can be seen from Figure 6.7 that 59% of the universes correctly determine the respective background component resulting in the observed Dirac-delta like

peak centred at zero. The mean of each pull are also seen to be close to zero indicating minimal bias is introduced when systematic variations are considered. This is supported by the total background pull which is determined by summing the x_j^{fit} background terms and adding the uncertainties, σ_j, in quadrature. We see that the total bias from fits to all systematics universes is approximately 3% which is acceptable given the systematic uncertainties of $\mathcal{O}(5\%)$ will encompass this bias (see Section 7.2 for discussion on systematics).

6.4.3 Data Constraint

Having understood the fit procedure using Monte Carlo studies, it is now time to perform the background constraint on data. Prior to performing the fit the 'tuned' Monte Carlo is scaled by $R_{\text{POT}} = 0.15$ in order to account for POT differences between data and Monte Carlo. Using a total of 3.33×10^{20} POT collected during the Low Energy data taking period the input data and Monte Carlo can be seen in Figure 6.8. Each sample is considered and below each distribution the ratio between data and Monte Carlo is presented. Note that in the ratio the black data points are data/data and the red crosses represent data/Monte Carlo.

Using the inputs presented in Figure 6.8 the background constraint is performed, resulting in the post-fit distributions in Figure 6.9. The χ^2/ndf between the data and Monte Carlo having performed the fit was found to be 1.46 which is a reduction of around 10% when compared to the pre-fit value of 1.57. This indicates that the Monte Carlo/data agreement has improved when the background components are scaled using the values in Table 6.5. These fit results were determined in the minimisation procedure.

As expected the difference between the pre and post fit invariant mass distributions is small given the marginal improvement in the χ^2/ndf. There is however a noticeable improvement when the data/Monte Carlo ratios are compared for each sample. In particular, the signal region bound between $60 \leq$

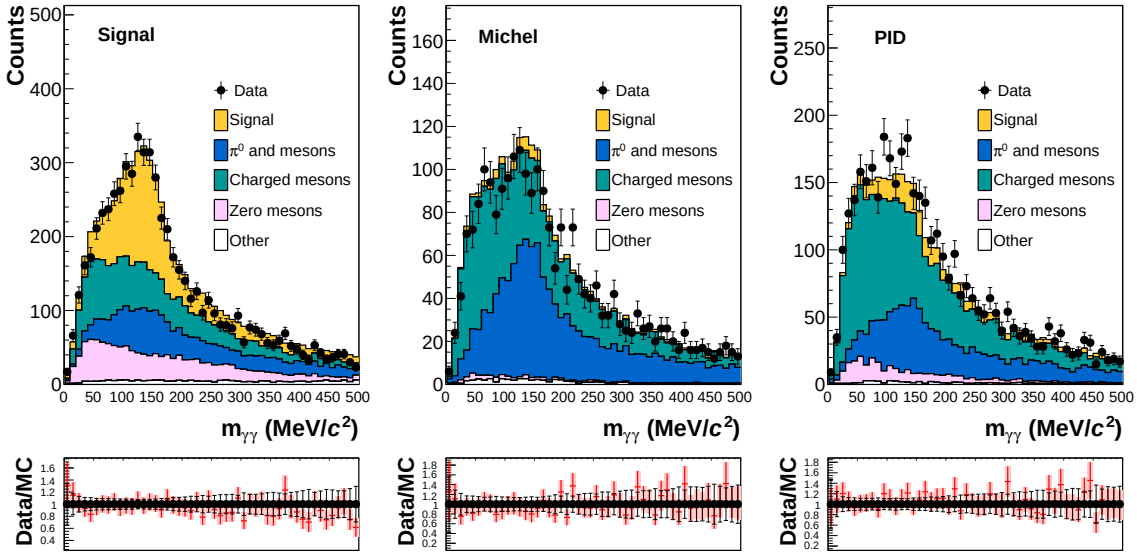

Figure 6.8: The input invariant mass distributions used to constrain the three dominant background components. The Signal sample is shown on the left, in the centre the Michel sample is given and the pID sample on the right. The collected data POT is 3.33×10^{20}.

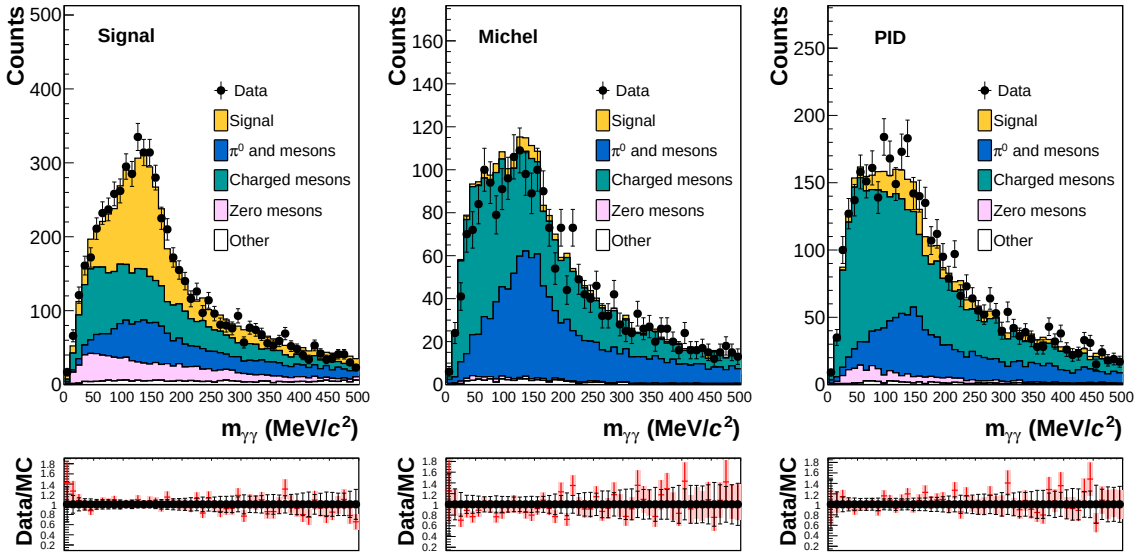

Figure 6.9: The scaled Monte Carlo invariant mass distributions following the background fit for the Signal (*left*), Michel (*centre*) and pID (*right*) samples. The collected data POT is 3.33×10^{20}.

Scaling Parameter	Fit Result	Error ($\pm$)
π^0's and mesons	0.924	0.056
Charged Mesons	1.122	0.046
Zero Mesons	0.670	0.094

Table 6.5: Fit results determined for the Monte Carlo scaling parameters when fitting to data totalling 3.33×10^{20} POT.

$m_{\gamma\gamma}$ (MeV/c^2) $\leq$ 200 in the Signal sample indicates good agreement between data and Monte Carlo.

Given this work is an extension to the analysis in Reference [68], it is possible to compare our results given the difference in the signal definition and further requirement of a proton in the signal sample. In both analyses all the backgrounds scale in the same way; the charged meson component increases whereas the π^0 with mesons and zero mesons contribution decreases. They do not however fully agree with one another's fitted values.

The zero meson contribution in Reference [68] was determined to be 0.47 ± 0.05 and more than three sigma less than that found here. A similar difference was observed for the π^0 with mesons where they measured it to be 0.83 ± 0.05. Such a difference in the resultant scaling terms is somewhat expected given the differences in signal definition. This is perhaps due to the relaxation on the requirement of exactly one π^0 to at least one π^0. Firstly, this can now lead to final states which would have been a background in Reference [68] becoming signal in the analysis presented here. There is also the added issue of introducing model dependence when requiring exact one π^0 as hadron multiplicities are not well understood in Final State Interactions.

Until now, we have only considered the two-photon invariant mass distribution. It is therefore interesting to assess the change to the δp_{TT} distribution, before and after the background constraints have been applied. This can be

seen in Figure 6.10 and as expected the variation between the pre and post fit is small. The distributions in Figure 6.10 include the reconstruction improvements and choice of analysis binning determined in the next chapter.

The backgrounds are stacked in order of size in Figure 6.10 starting with the least dominant at the bottom, to the dominant background at the top. One can see that the fit leads to the Zero mesons component becoming the smallest background. Like in the invariant mass distributions the ratio between data and Monte Carlo provide the most notable change. The overall reduction in backgrounds move the Monte Carlo closer to the data in the central region between $\pm$200 MeV/c but leads to a lesser agreement in the tails.

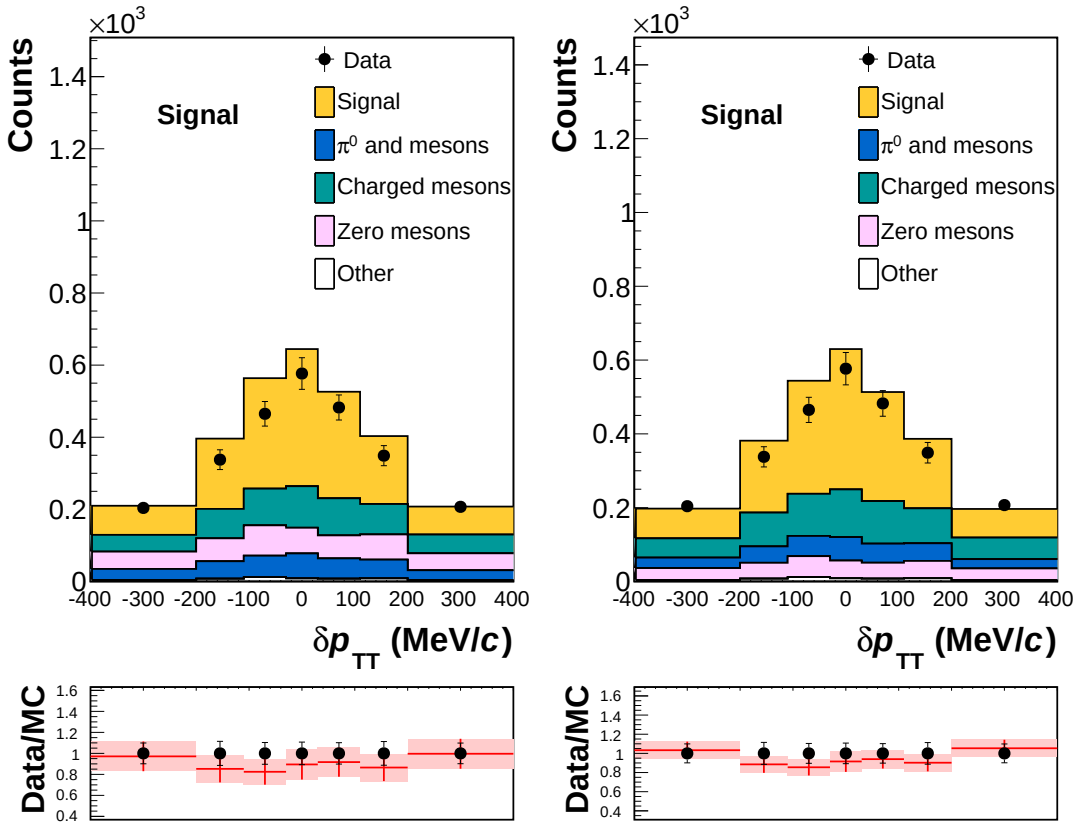

Figure 6.10: The pre (*left*) and post (*right*) fit δp_{TT} distribution are broken down in to signal and background topologies using a collected data POT of 3.33×10^{20}. Note here that the reconstruction improvements have been performed in the construction of δp_{TT}. A full discussion of the reconstruction improvements shall be discussed in Chapter 7.

Chapter 7

MINERνA Analysis: Recon. and Systematics

Following the selection of CCNpMπ^0 final states and the background constraints determined in the previous chapter the reconstruction and systematics used in the MINERνA analysis are discussed. Composite variables like δp_{TT} require good momentum reconstruction as mis-reconstruction could lead to mimicking the physics of interest. We shall begin by introducing the default reconstruction of δp_{TT} before discussing our approach to improving the kinematic reconstruction of final states. This chapter shall close with a review of the relevant systematics included in this measurement.

7.1 Reconstruction

Using the default momentum reconstruction in MINERνA, the reconstructed Double Transverse Momentum is presented in Figure 7.1a and compared with that of its underlying true distribution. This uses the procedure outlined in Section 3.4 to reconstruct the neutrino's direction. It is clear that the standard reconstruction used at MINERνA results in a large spreading effect and is highlighted

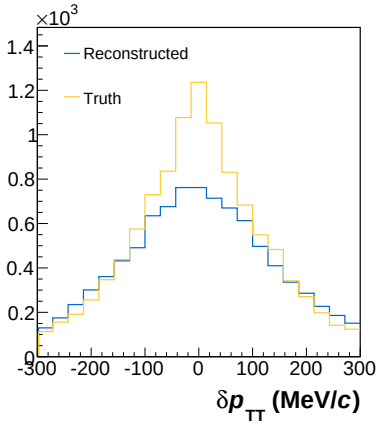

(a) Reconstructed δp_{TT} distribution with true δp_{TT} overlay.

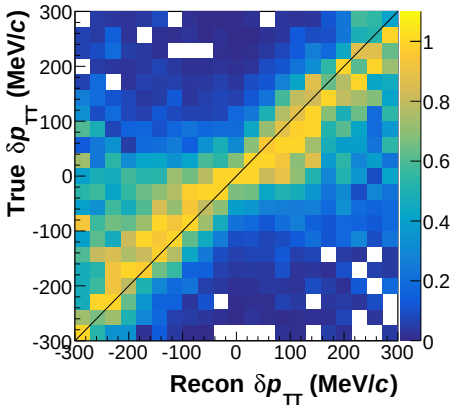

(b) Smearing matrix of δp_{TT} indicating a large spreading effect in the tails of δp_{TT}.

Figure 7.1: Double Transverse Momentum distribution using the default reconstruction algorithms in MINERνA.

by Figure 7.1b. Here the smearing effects of the reconstruction can be seen.

There are a number of notable features observed in the smearing matrix of δp_{TT}; possibly the most significant being the increasing broadening in the tails of the Double Transverse Momentum distribution. It is also brought to our attention the presence of an S-shape in Figure 7.1b which implies that the magnitude of δp_{TT} is being overestimated resulting in a large spread in δp_{TT}. Finally, a less obvious feature is the resolution available using the default reconstruction and suggests that an increased bin size would reduce bin-to-bin migration.

The current reconstruction needs to be improved as it could lead to detector effects mimicking physics phenomena and, we also want to be less model dependent in our migration from the reconstructed to the true distribution. Therefore our aim is to improve the reconstruction of our final state particles used to reproduce δp_{TT} in order to construct a more diagonal smearing matrix.

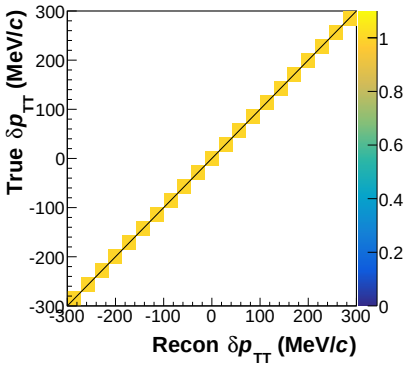

Figure 7.2: True δp_{TT} vs. True δp_{TT}.

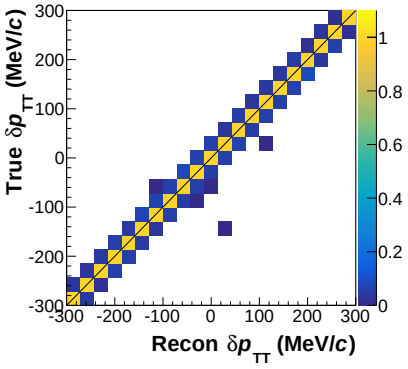

Figure 7.3: Reconstructed neutrino direction results in minimum smearing in δp_{TT}.

7.1.1 Truth Swapping

Identifying the underlying kinematics that lead to the greatest effects in the mis-reconstruction of δp_{TT} began by performing a truth-reconstruction swapping study in Monte Carlo events. Such a study began by constructing δp_{TT} using only the true kinematics of the system such as the true neutrino direction and momentum of the μ^-, p and π^0.

Following the procedure in Figure 7.1b where the true distribution is compared to the reconstructed distribution, we begin with all the reconstructed quantities replaced by Monte Carlo truth and hence the distribution is diagonal like in Figure 7.2. Then by replacing one of the final state kinematic quantities with its reconstructed counterpart, it is possible to assess the smearing effect of the reconstructed variable.

It is possible to delve further into where the mis-reconstruction lies by breaking the momentum into its constituent parts, namely, the magnitude and direction. By swapping the true variables it is possible to deduce which variable has the largest effect i.e. which can subsequently be studied to determine where reconstruction improvements need to be investigated further. Starting from the reference point of the diagonal smearing matrix of the true-δp_{TT} vs. true-δp_{TT} (Figure 7.2), comparisons of the swapped reconstructed particle kinematics can be

seen in Figure 7.3 for the reconstructed neutrino direction, Figure 7.4 for muon kinematic variables, Figure 7.5 for the proton and Figure 7.6 for the π^0.

Clearly the hadronic system is least well reconstructed. We can see from Figure 7.5 that the reconstructed direction of the proton causes the greatest smearing effect whereas the opposite is observed in Figure 7.6 for the π^0; the smearing is dominated by the calorimetric mis-reconstruction. Having attributed the proton's momentum mis-reconstruction to the estimation of its direction, any improvements in measuring this quantity are not possible. This is because the direction is limited by the detector's resolution and so require a detector redesign for improvements to be seen. In fact, this is true for all tracks and showers and we are therefore limited to developing improvements via a more refined approach.

7.1.2 Proton Quality Cuts

Our limited ability to improve MINERνA's direction and dE/dx determination requires a more sophisticated approach to improving the proton's momentum. By taking advantage of our knowledge of the underlying physical principles of particles traversing through matter, it is possible to identify and remove protons which inelastically scatter within the detector. In inelastic scatters such as $pA \rightarrow nA'$, the tracked proton's range is incorrectly determined and results in protons having a smaller measured dE/dx.

The approach here is to remove events where protons inelastically scatter inside MINERνA. This should result in an improved reconstruction of the proton's momentum. Let us begin by recalling how MINERνA is constructed. The detector is predominantly built using X, U and V planes made of scintillator bars. As a charge particle travels through the detector it deposits energy in each plane's scintillator bars. These act as measurement nodes of a tracks trajectory and can be seen schematically for the proton in Figure 7.7. Here we depict a proton moving through numerous X, U and V planes as it deposits energy into

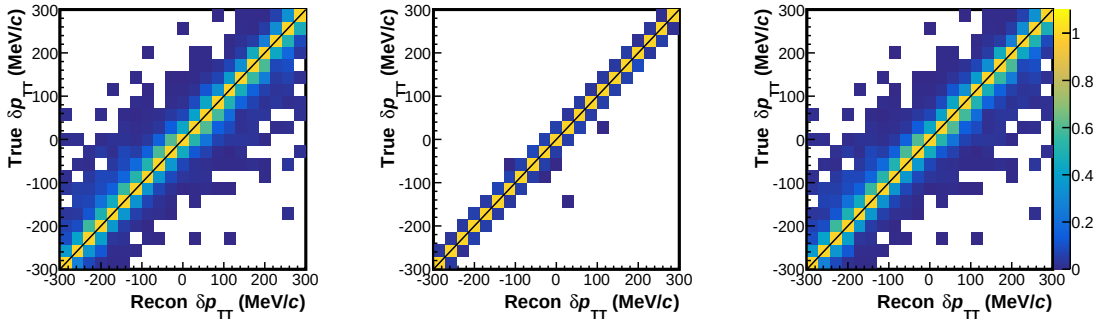

Figure 7.4: Effect of replacing the muon's true kinematic variables with their reconstructed counterpart. The three-momentum (*left*) is further broken down into reconstructed Energy (*centre*) and direction (*right*).

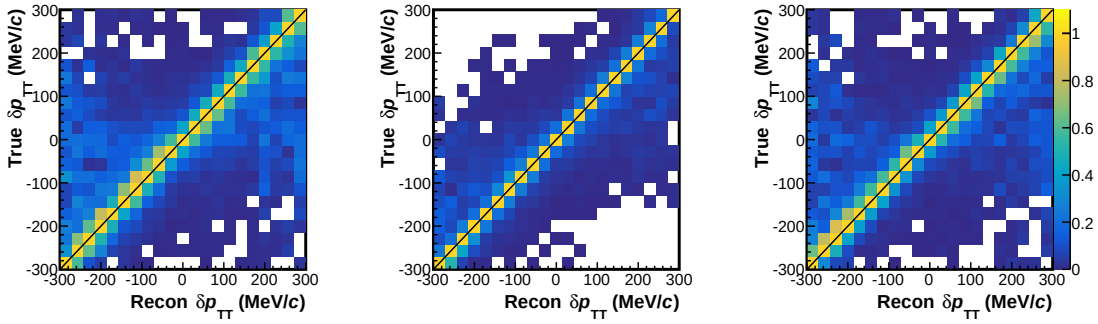

Figure 7.5: Effect of replacing the proton's true kinematic variables with their reconstructed counterpart. The three-momentum (*left*) is further broken down into reconstructed Energy (*centre*) and direction (*right*).

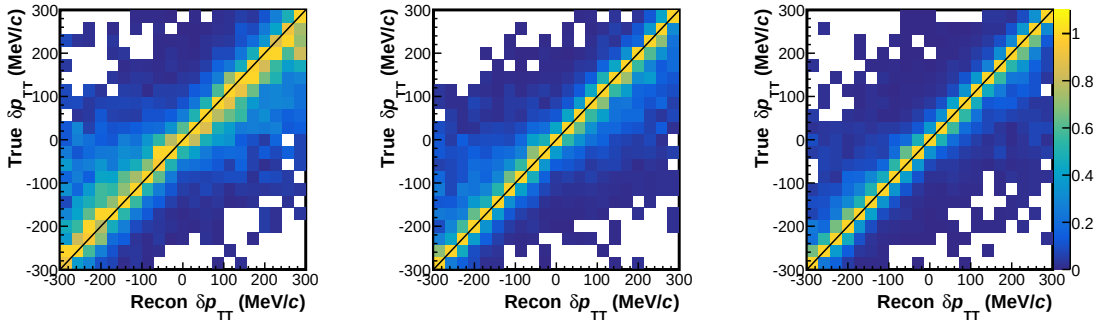

Figure 7.6: Effect of replacing the π^0's true kinematic variables with their reconstructed counterpart. The three-momentum (*left*) is further broken down into reconstructed Energy (*centre*) and direction (*right*).

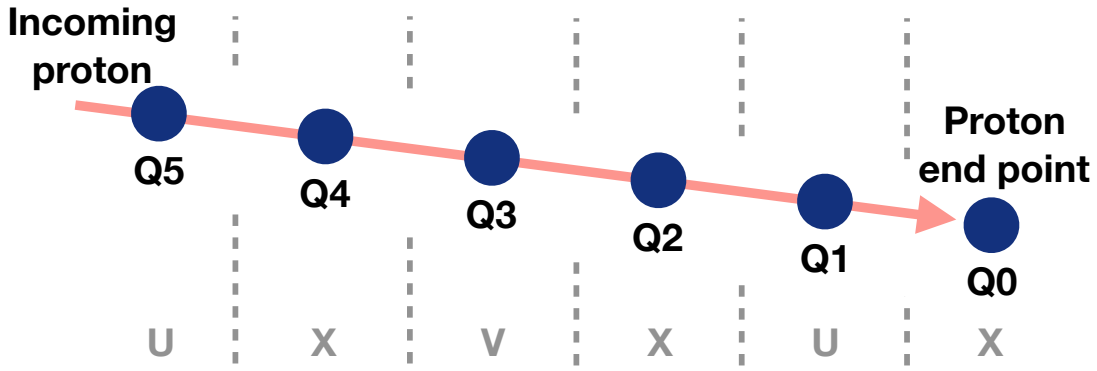

Figure 7.7: Schematic of last 6 measurement nodes for a proton track. U, V and X denote the plane in which the measurement node lies.

measurement nodes.

Removing inelastically scattered events is achieved by first requiring that each proton track has deposited energy in at least six measurement nodes. For the inelastically scattered events the energy deposited in a node will be less than those from elastically scattered events and the amount of energy should be independent of the proton's momentum. Hence one can determine a threshold at each measurement node by considering the ratio of true to reconstructed momentum vs. energy deposited. One observes that above some energy threshold the ratio is flat indicating that the proton has elastically scattered. This can be seen in Figure 7.8, where the proton's reconstructed to true momentum ratio is presented as a function of node energy. The node presented here is furthest most measurement point from the end-point or Q5 in Figure 7.7.

Starting from the Q5 node, the ratio and deposited energy is assessed to determine the minimum amount of energy required to pass the cut. This process is applied to each measurement node where in the case of the last two nodes, Q1 and Q0 are summed before determining the threshold. All nodes must pass their respective thresholds for the event to be used in the analysis. The relevant node energy distributions along with their cumulative distribution are presented in Figures 7.8-7.13 from which the thresholds in Table 7.1 are determined.

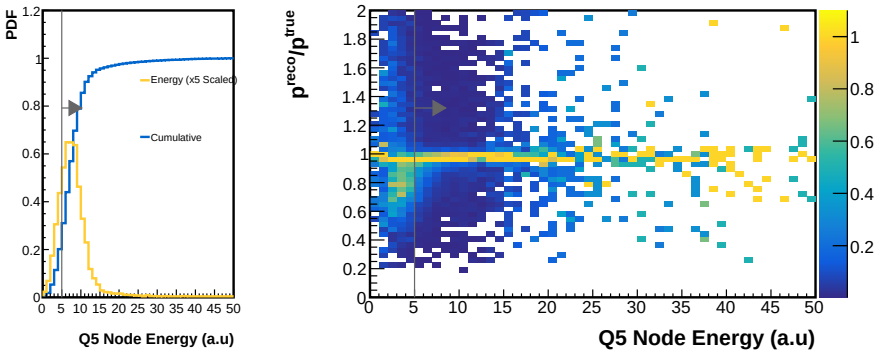

Figure 7.8: Q5 Node Energy.

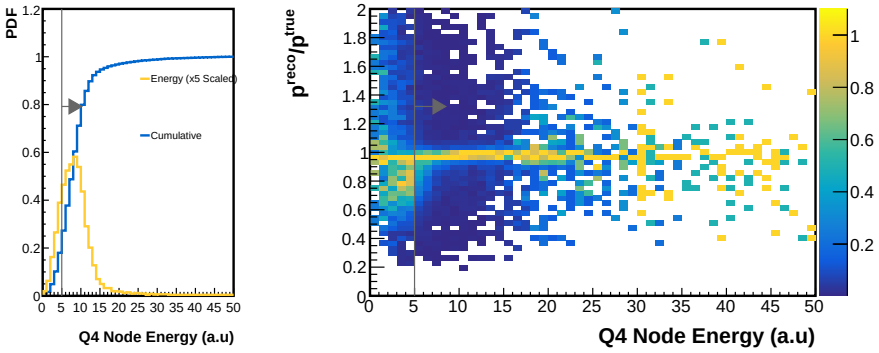

Figure 7.9: Q4 Node Energy.

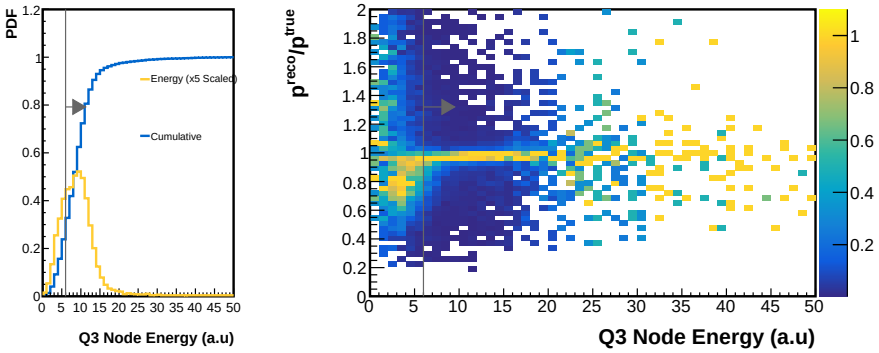

Figure 7.10: Q3 Node Energy.

The effect of this cut based quality improvement can be seen in Figure 7.14 and Figure 7.15. Figure 7.14 compares the protons momentum residuals pre and post quality cuts where the residual is defined as $R = 1 - x^{\text{recon}}/x^{\text{true}}$. The spread in the momentum residual is decreased by over 40.0%. It is also

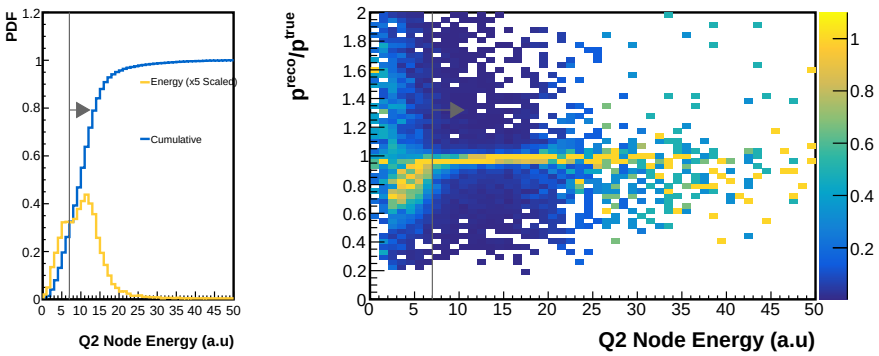

Figure 7.11: Q2 Node Energy.

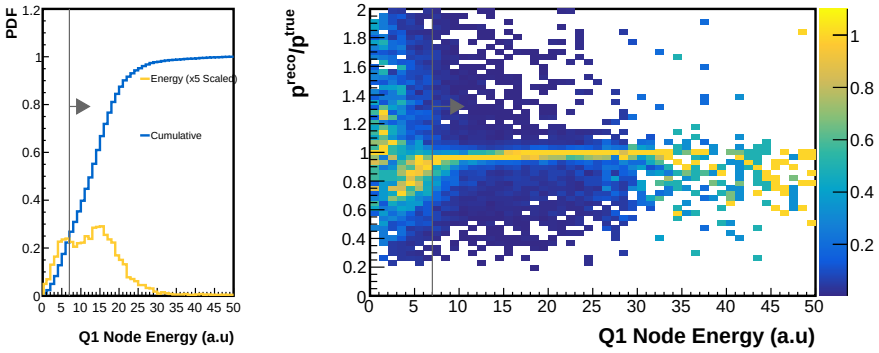

Figure 7.12: Q1 Node Energy.

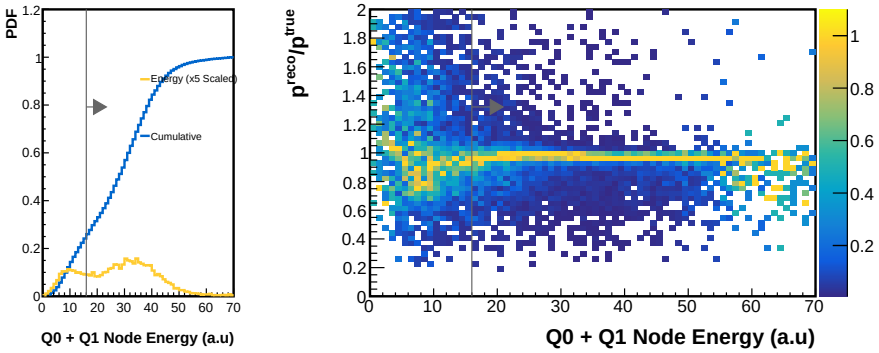

Figure 7.13: Q0 + Q1 Node Energy.

clear from Figure 7.15 that many of the high momentum protons are discarded from the selection as expected by such a cut based approach. This method is an effective means of improving the proton momentum reconstruction however at the cost of a 50% reduction in statistics.

Measurement Node	Threshold	Events	Efficiency (%)
Q5	5.0	8900	75.7
Q4	5.0	7970	67.8
Q3	6.0	7046	59.9
Q2	7.0	6388	54.3
Q1	7.0	6085	51.8
Q1 + Q0	16.0	5880	50.0

Table 7.1: Energy thresholds applied to each measurement node used to remove inelastically scattered protons. The number of events passing each cut along with the running efficiency are presented.

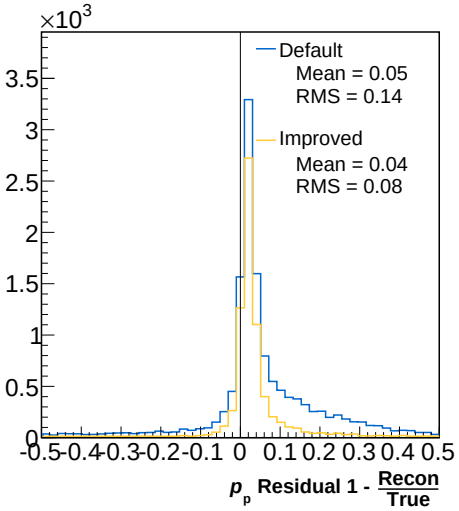

Figure 7.14: Residual distributions for the proton's momentum pre and and post reconstruction improvements.

7.1.3 π^0 Optimisation

The π^0's momentum is constructed using information from the two photons identified in MINERνA using the relation $\boldsymbol{p}_{\pi^0} = \boldsymbol{p}_{\gamma_1} + \boldsymbol{p}_{\gamma_2}$. Given this relationship, the investigation began by considering the residuals of the reconstructed photon momenta along with the π^0 momentum. In Figure 7.16 it is clear that the reconstruction is limited by MINERνA's calorimetric reconstruction especially

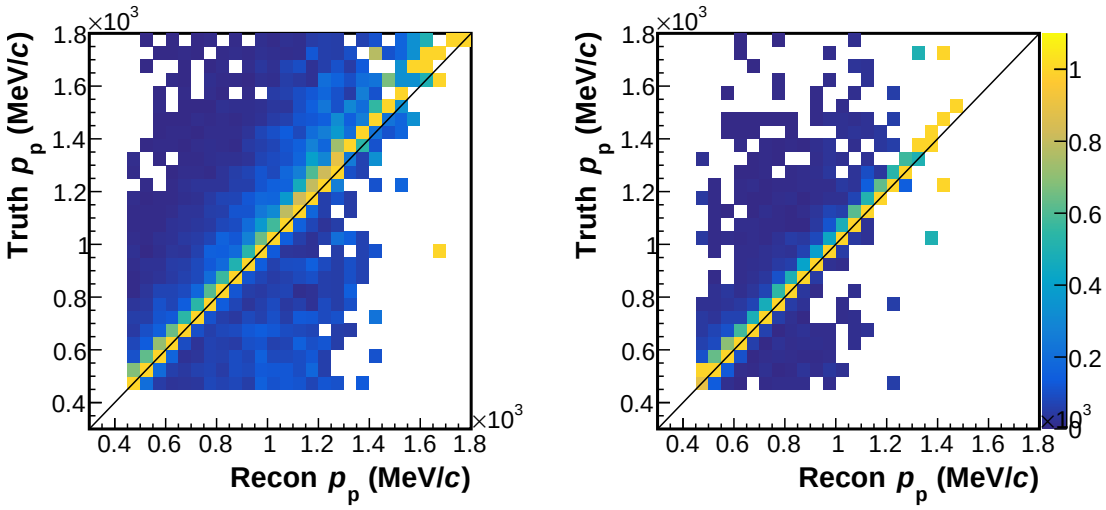

Figure 7.15: Smearing distributions pre (*left*) and post (*right*) momentum reconstruction improvements for the proton.

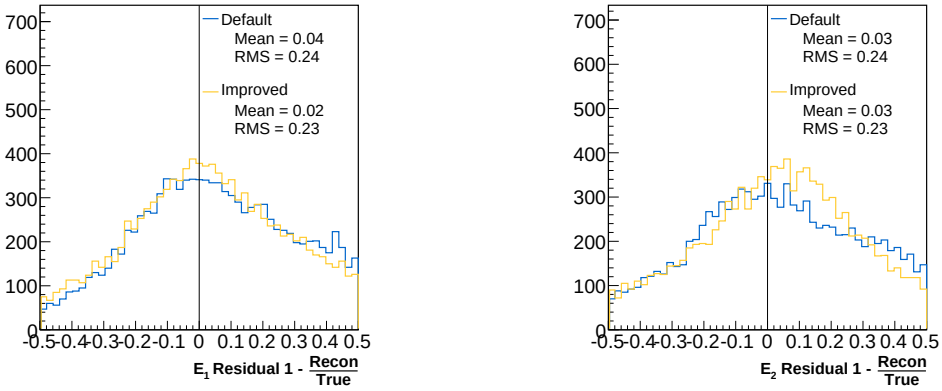

(a) High energy photon (γ_1). (b) Low energy photon (γ_2).

Figure 7.16: Residual distributions of the two reconstructed photons before and after reconstruction improvements.

for the low energy photon, γ_2. Although their energy is poorly reconstructed, the direction of the photons are much more well defined. This is highlighted by the ability to determine the opening angle, θ_{12}, between the two photons as shown in Figure 7.16 and Figure 7.17. The residual in Figure 7.17 with a mean of 0.02 and rms of 0.16 confirms MINERνA's angular reconstruction out performs its calorimetric reconstruction (Figure 7.16). This observation concluded in focusing efforts to obtain a kinematic relation which would improve the photon's

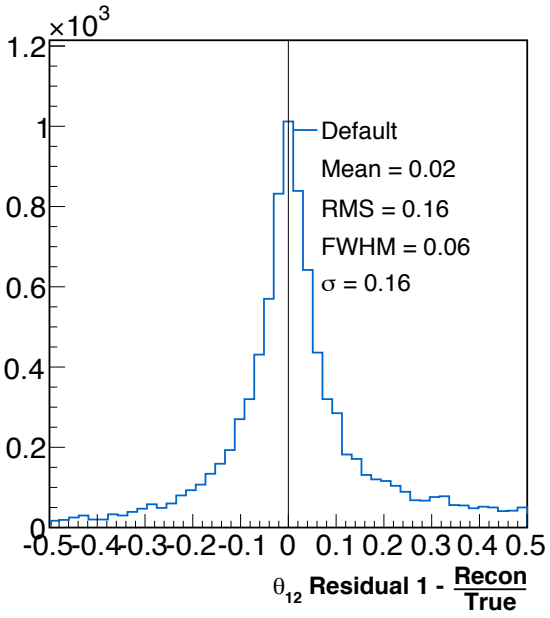

Figure 7.17: The π^0's photon opening angle residual.

reconstructed energies using angular information. This should subsequently lead to improvements to the π^0 momentum resolution.

Naturally a suitable kinematic relationship was determined by conservation of 4-momenta for the dominant π^0 decay, $\pi^0 \rightarrow \gamma\gamma$. This lead to the use of the π^0 invariant mass which uses the opening angle, θ_{12}, and both the photon's energies E_1, E_2

$$m^2_{\gamma\gamma} = 2E_1E_2(1 - \cos\theta_{12}). \tag{7.1}$$

The high (γ_1) and low (γ_2) photon's reconstructed energy are used as inputs into an event-by-event χ^2 fit. The fit is provided with four inputs, two of which are treated as data, namely, the known π^0 mass and measured opening angle. The other two parameters, the measured energies E_i' are used as initial E_i values as well as in the penalty terms. The fit considers a χ^2 of the form

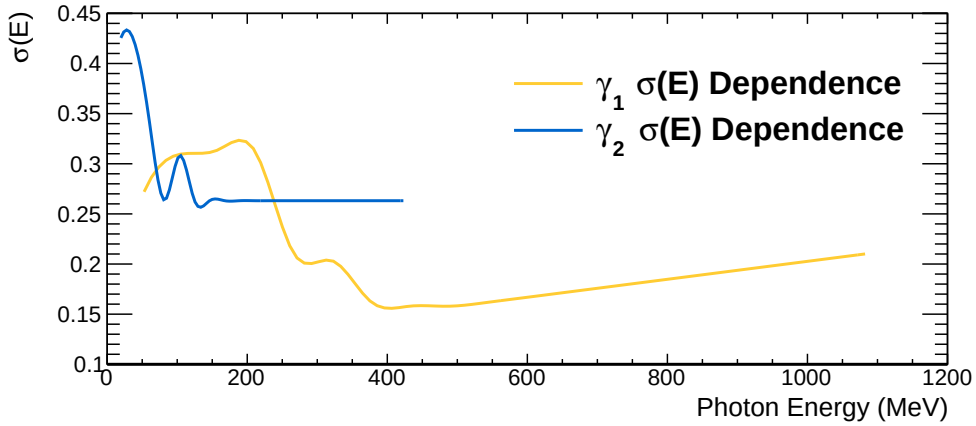

Figure 7.18: The high (γ_1), and low (γ_2) photons energy dependent uncertainties (% of energy).

$$\chi^2 = \frac{\left(m^2_{\pi^0} - 2E_1E_2(1-\cos\theta_{12})\right)^2}{\sigma^2_{m^2}} + \sum_{i=1}^{2} \frac{\left(E_i - E_i'\right)^2}{\sigma^2_{E_i}}. \tag{7.2}$$

In Equation 7.2, the first term compares the two photon energies and opening angle against the known π^0 mass (134.98 MeV/c^2 [22]) to determine optimal photon energies given the angular constraint. The uncertainty in the first term, $\sigma^2_{m^2}$, is used as an optimisation parameter and was varied in order to maximise the number of successfully converged events. This resulted in a fit efficiency of 99.7%. The last term acts as a penalty term and is included to ensure that the fitted energies are within the uncertainty, σ_{E_i}, of their measured value, E_i'. The energy uncertainty is dependent on the measured energy as in general calorimetric detectors are better able to reconstruct higher energies. The photon's energy uncertainty dependence determined via Monte Carlo studies can be found in Figure 7.18.

The zero suppressed energy dependence on the uncertainty in Figure 7.18 is produced using Monte Carlo to calculate the modulus of the residuals for each photon. We begin by finding a binning in photon energy that contains

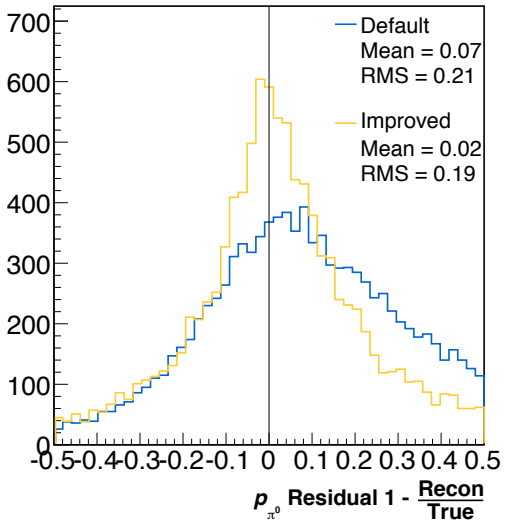

Figure 7.19: The pion momentum's residual for the default and improved reconstruction.

approximately the same number of events in each bin. This is then used to fill the residual as a function of energy from which splines were calculated to produce a smooth percentage error dependence.

We see from Figure 7.18 that the error dependence is similar to expectation in that the uncertainty generally decreases as a function of energy. There are however some spurious features; the low energy photon has a peak at around 100 MeV and above 400 MeV the high energy photon fractional uncertainty increases. The first is due to the calculation of the spline not being able to determine a smooth distribution from one bin to the next. The feature present in the high energy photon, although not verified is believed to be due to saturation in the electronic readout resulting in missing energy.

The fit based approach results in a notable improvement to the pion's reconstructed momentum. Firstly by comparing the residuals of the photons energies in Figure 7.16 and subsequently the pion's fitted momentum in Figure 7.19 we can see improvements in the respective means pre and post fit. Interestingly, the higher energy photon, γ_1, has a slightly increased RMS however the region centred around zero contains more events. This indicates that more of our events are better reconstructed. It is also clear from the pion momentum's smearing

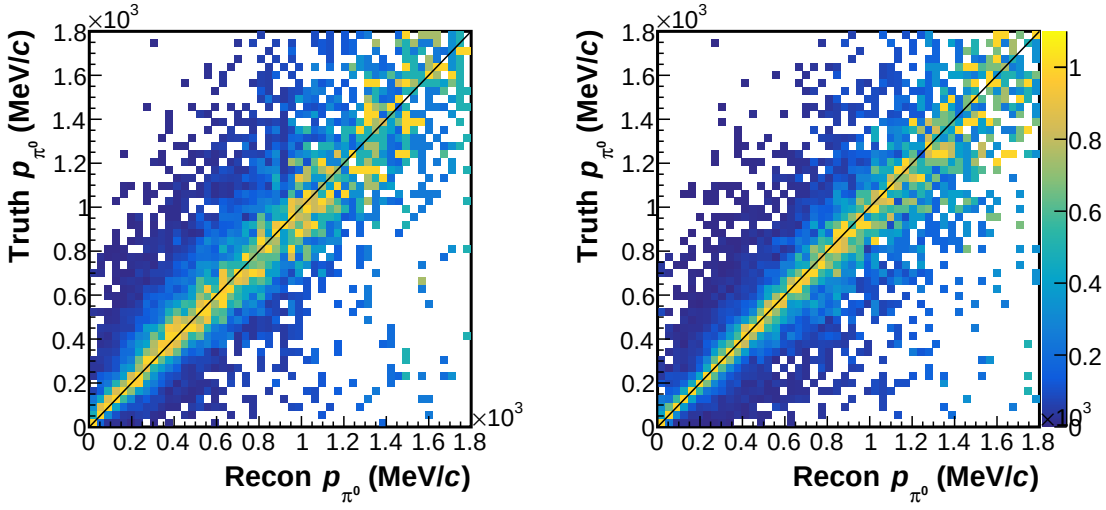

Figure 7.20: The pion true vs. reconstructed momentum is presented using the default (*left*) and improved (*right*) π^0 reconstruction.

matrix in Figure 7.20 that the smearing effect is reduced throughout much of the phase-space.

One should note that in Section 6.1, our signal definition applies an invariant mass constraint ($60 \leq m_{\gamma\gamma}$ (MeV/c^2) ≤ 200). Clearly, such an optimisation technique which relies on minimising the E_i's to the π^0 mass will result in both signal and background events entering this region. It should be made clear that this procedure does not change the reconstructed π^0 mass but only its momentum when used in calculating composite kinematics like δp_{TT}.

7.1.4 Kinematic Corrections

The last reconstruction improvement is to correct for any bias in the final state particles kinematics. If left unchanged this could lead to further mis-reconstruction in Double Transverse Momentum. The first correction accounts for biases in the photon's electromagnetic energy (EM) scale. It was found that both the data and Monte Carlo's calorimetric reconstruction either over or under estimated the known π^0 invariant mass. As such both datasets needed to be scaled to correct the measured invariant mass peak making it in line with expecta-

tion (135.0 MeV/c^2). This was achieved by fitting a double Gaussian to the $m_{\gamma\gamma}$ distribution spanning $0 < m_{\gamma\gamma}(\text{MeV}/c^2) < 280$ for both data and Monte Carlo. The first Gaussian was used to determine the peak and the second parametrised the broader $m_{\gamma\gamma}$ shape. The Monte Carlo $m_{\gamma\gamma}$ peak was found to be 130.3 ± 1.6 MeV/c^2 and the data peak measured 137.8 ± 2.6 MeV/c^2. This lead to an increase in the Monte Carlo EM scale of 2% and decrease in the data's EM scale of 3%. Given this bias is a facet of the detector's EM reconstruction any variable dependent on the two photons kinematics had the respective correction scales applied to them.

A second set of corrections are applied following the reconstruction improvements. Our approach was to first consider how δp_{TT} can be constructed to assess if different final state kinematics may be used. If we recall the equation for calculating δp_{TT}, it can be rewritten as

$$\delta p_{\text{TT}} = \hat{z}^{\text{T}}_{\text{TT}} \cdot (\boldsymbol{p}^{p}_{\text{T}} + \boldsymbol{p}^{\pi^0}_{\text{T}}), \quad \text{where} \quad \hat{z}^{\text{T}}_{\text{TT}} = \frac{\boldsymbol{d}_\nu \times \boldsymbol{p}^{\mu}_{\text{T}}}{|\boldsymbol{d}_\nu \times \boldsymbol{p}^{\mu}_{\text{T}}|}. \tag{7.3}$$

Here each final state's momentum are exchanged with their momentum transverse to the incoming neutrino's direction, $\boldsymbol{p}^{f}_{\text{T}}$. The superscript f represents a muon, proton and π^0 respectively. Given this there are now two momenta for each final state particle that can be used to construct δp_{TT}.

The next phase was to assess which form of δp_{TT} should be used given how well each momenta are calculated for each final state particle. As we saw in Figures 7.14 and 7.19 for the proton and π^0 momentum, both cases presented a small bias. Although not presented here it was also true for the muon's momentum. A similar case was seen for the proton and muon's transverse momentum, however, the π^0 showed no bias in its $\boldsymbol{p}^{\pi^0}_{\text{T}}$. This led to Equation 7.3 being the formalism to calculate δp_{TT}.

Having found an alternative form for δp_{TT}, the muon and proton's transverse momentum need to be corrected in order to reduce miss-reconstruction effects

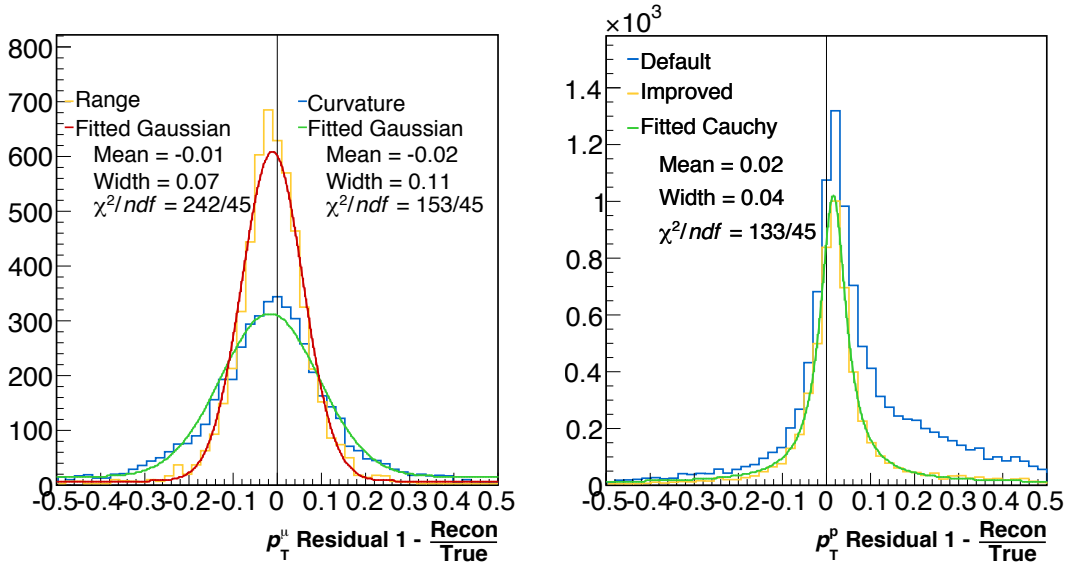

Figure 7.21: The pion true vs. reconstructed momentum is presented using the default (*left*) and improve (*right*) π^0 reconstruction.

further. This was achieved by finding an analytical form for the respective final states $|\boldsymbol{p}_{\mathrm{T}}^{f}|$ residuals. It was found that a Gaussian best described the muon's transverse momentum residual whereas the proton's was shown to be Cauchy distributed. This can be seen in Figure 7.21. From here the biases could be determined by the fitting the respective distributions to each particles residual. Note here that there are two residuals for the muon's $\boldsymbol{p}_{\mathrm{T}}^{\mu}$, this is because its momentum is determined either by curvature or range in MINOS. The mean determined for each residual defined the correction needed for the transverse momentum scale.

7.1.5 Summary

The combined effect of all reconstruction improvements can be seen in Figure 7.22 for Double Transverse Momentum. Here both the default and improved smearing matrices are presented so that comparisons can be made. The improved δp_{TT} is noticeably more diagonal than its predecessor but at the cost of a 50% reduction in statistics. Although we halve the number of event, the im-

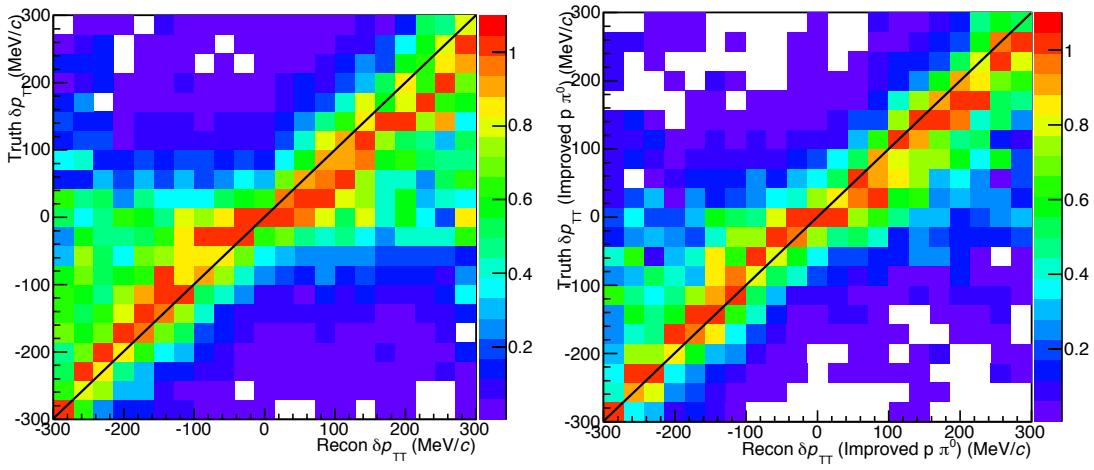

Figure 7.22: The default (*left*) and combined improvements of proton and pion reconstruction (*right*) smearing matrix is presented for Double Transverse Momentum.

Number of Bins	Bin Edges							
7	-400.	-200.	-110.	-30.	30.	110.	200.	400.

Table 7.2: Analysis binning chosen following the reconstruction improvements.

proved reconstruction capabilities will aid in reducing uncertainties when the cross section is calculated later. This will be discussed further in Chapter 8.

There is an interesting feature in the central region of δp_{TT}, namely, a broadening effect centred around zero in reconstructed δp_{TT}. This is seen in both distributions and implies that MINERνA is not capable of well reconstructing low Double Transverse Momentum. We also observed a non-negligible off-diagonal component in negative δp_{TT} which indicates an over estimation of negative Double Transverse Momentum. In order to combat some of the smearing effects still present in the improved reconstruction a better binning of δp_{TT} was determined. This considered both the broadening effects and statistics in each bin finding the binning in Table 7.2. Going forward this will be the analysis binning for Double Transverse Momentum.

7.2 Systematics

Systematics are implemented at MINERνA by defining an 'alternative universe' where a single systematic variation is applied leaving all other parameters at their nominal value. The analysis steps are then undertaken in each universe producing a result given the different parameter values whose difference from nominal defines the systematic uncertainty. In addition to the flux uncertainty, the other systematics are classified into three groups, namely, the detector, neutrino interactions and Final State Interactions. The systematics implemented in this analysis have been carried over from the 2017 paper in Reference [101]. An overview of each systematic shall now be discussed.

7.2.1 Detector

The detector's response to detecting each particle type is considered along with their energy estimation. We also include the effect of secondary particle responses as well as our ability to determine the detector mass.

Muon Uncertainties

- Momentum – The MINOS collaboration estimated the uncertainty to be $\pm 2\%$ [95].
- Angle – MINERνA determines the angular uncertainty by fitting the muon-like track twice. The first fit uses information from the vertex position to the muon-like track's mid-point to determine the outgoing angle. The second fit estimates the angle using the mid-point to the track's end point. The difference between the two fit results defines the uncertainty to be 2 mrad [106].
- Tracking Efficiency – MINERνA requires both MINOS and MINERνA to have matched tracks for a muon track to be reconstructed. The uncertainty

in failed matching between the two detectors is determined by studying the ratio of events containing a reconstructed track in MINERνA to those with events reconstructed by MINOS. Depending on the run period and momentum range, an efficiency is determined along with its uncertainty and is outlined in [107].

Proton Uncertainties

- Tracking Efficiency – Using test beam data, the efficiency and its uncertainty was determined for two event topologies, namely, QE-like and Charge pion production. Given the CCNpMπ^0 final state is topologically similar to QE-like events it was therefore used as the efficiency and uncertainty for this analysis. Note that the efficiency is dependent on the number of planes traversed by the proton [108].

- Energy – The proton's energy is dependent on the dE/dx profile of the track and has four associated uncertainties

  - Bethe-Bloch – The associated uncertainty in the average energy loss was determined by comparing the muon energy loss in MINERνA to muon energy range tables. Depending on the type of material the uncertainty ranges from 1-3% [109–111].

  - Detector Mass Model – Our understanding of the material dimensions used to build MINERνA affects the particles energy loss as it will change the amount of energy deposited as the particle traverses the detector. It was found that the uncertainties for the key materials used in MINERνA were less than 1.5% [110].

  - Muon Equivalent Unit (MEU) – By taking advantage to the well understood energy loss of muons in plastic scintillator, an absolute energy scale can be determined. This is used to convert the number of photo-

electrons in a single plane into an energy and has an uncertainty of 2.4% [73, 112].

– Birks' Quenching Factor – The light yield of a charged particle traversing a scintillator is defined by Birks' law [113] and estimates the light yield per path length as a function of energy loss. The GEANT4 simulation used by MINERνA uses a different quenching factor to that measured by test beam data. The difference in these two factors acts as the uncertainty.

Electromagnetic Energy Scale Uncertainties

Following the correction applied to the photon's EM scales for both data and Monte Carlo in Section 7.1.4 an associated uncertainty from the each fit is included. This is only included in variables built from the two photons, such as the π^0 momentum. The uncertainty from the fit results for data and Monte Carlo are added in quadrature resulting in an Electromagnetic energy uncertainty of 2.3% [101].

Michel Tagging Uncertainty

The efficiency in identifying Michel electrons in MINERνA is determined by studying stopped rock muons inside the detector. Defining two cases: One in which the Michel tagging algorithm correctly identifies Michel events and those where a false positive is observed. The efficiency of the former is $70.0 \pm 1.1\%$ whereas the latter has an efficiency of $1.0 \pm 0.5\%$ [114].

Pion Charge Exchange Uncertainty

As charged pions traverse the detector they can undergo charge exchange creating a π^0 and hence mimic the signal definition. External measurements of charge exchange are used to apply an uncertainty in simulated events which undergo

charge exchange. This is defined to be 50% [115].

Neutron Uncertainty

Although neutrons are invisible in MINERνA, in instances where they inelastically scatter they can be observed as a disassociated energy blob from the vertex. Such instances can pass the π^0 reconstruction algorithm and therefore need to understood. This was estimated to be 6% [116].

Detector Mass Uncertainty

Neutrino interaction rates are dependent on the target mass. The active tracker has a mass uncertainty in the number of nucleons of 1.4% [110].

Summary

Having outlined the detector uncertainties, they are broken down into fractional errors in Figure 7.23 for both the invariant mass and δp_{TT} distributions. Both distributions are made using the Signal sample defined in Section 6.2. Note that this shall be the case when each systematic group is summarised.

From Figure 7.23 (*left*), the most notable uncertainty in the invariant mass distribution is the EM scale. This uncertainty varies the energies of each photon's reconstructed energy leading to a lateral change in $m_{\gamma\gamma}$. The fine binning used here leads to sharp discontinuities between bins which vary by around 2-6%. In δp_{TT} this feature is not seen and is now the sub-dominant uncertainty. We see that in general the detector uncertainties are approximately flat resulting in an overall detector uncertainty of 5% for $m_{\gamma\gamma}$ and 3.5% for δp_{TT}.

7.2.2 Neutrino Interactions

Monte Carlo neutrino event generators have large uncertainties in their cross-section prediction due to current constraints on the input parameter values meas-

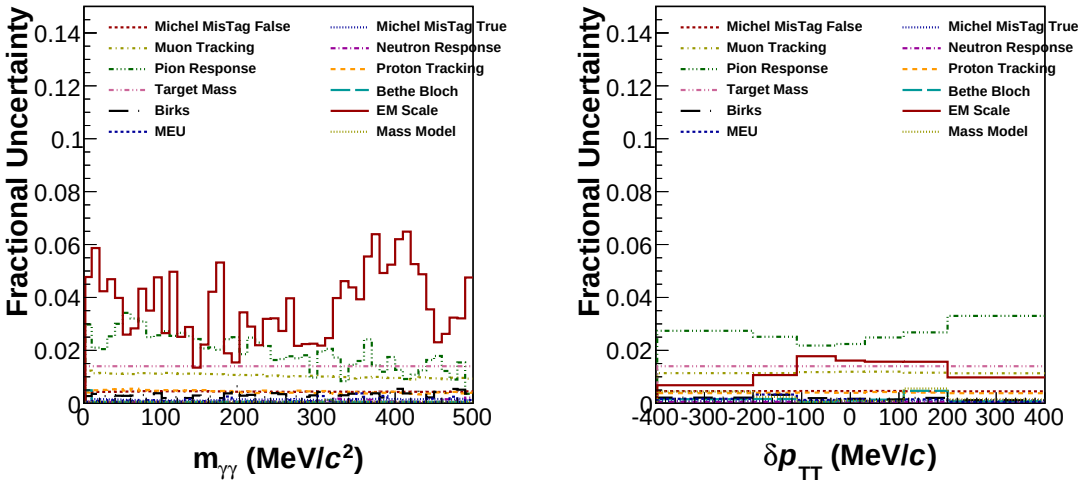

Figure 7.23: Breakdown of detector errors for the reconstructed photon's invariant mass (left) and δp_{TT} (right).

ured by other experiments. These can affect the estimation of the background components and the total signal. It is therefore necessary to include these variations as a systematic uncertainty in this analysis.

MINERνA's default event generator, GENIE, provides one sigma variations for the various model parameters as seen in Table 7.3. These model variations are applied on an event-by-event basis and are dependent on the interaction type. From here each dial is included as a systematic via the alternative universe approach.

The fractional uncertainty of the cross section model errors are presented in Figure 7.24. Here the the invariant mass and δp_{TT} uncertainties are given. The dominant uncertainties are those associated to non-resonance multi-pion production and the resonance axial mass. As we saw in Chapter 3, the axial mass only affects the normalisation in δp_{TT} leading to a flat fractional uncertainty. The combined effect of these model uncertainties lead to a total uncertainty in $m_{\gamma\gamma}$ of around 7% and δp_{TT} of 7.5%.

Interaction		Uncertainty
Model	Parameter	
NC Elastic	M_A	$\pm$25%
	η	$\pm$30%
CCQE	M_A	$+$25%
		$-$15%
	Low Q^2 Pauli blocking	$\pm$30%
Resonance Production	M_A	$\pm$20%
	M_V	$\pm$10%
	Δ Anisotropy	$\pm$50%
NC Resonance Production	Normalisation	$\pm$20%
1π Non-Res. Prod.	$\nu p/\bar{\nu}n$	$\pm$50%
	$\nu n/\bar{\nu}p$	$\pm$50%
2π Non-Res. Prod.	$\nu p/\bar{\nu}n$	$\pm$50%
	$\nu n/\bar{\nu}p$	$\pm$50%
Bodek-Yang	A_{HT}	$\pm$25%
	B_{HT}	$\pm$25%
	C_{V1u}	$\pm$30%
	C_{V2u}	$\pm$40%

Table 7.3: One sigma systematic uncertainties associated to GENIE's interaction model parameters applied in this analysis.

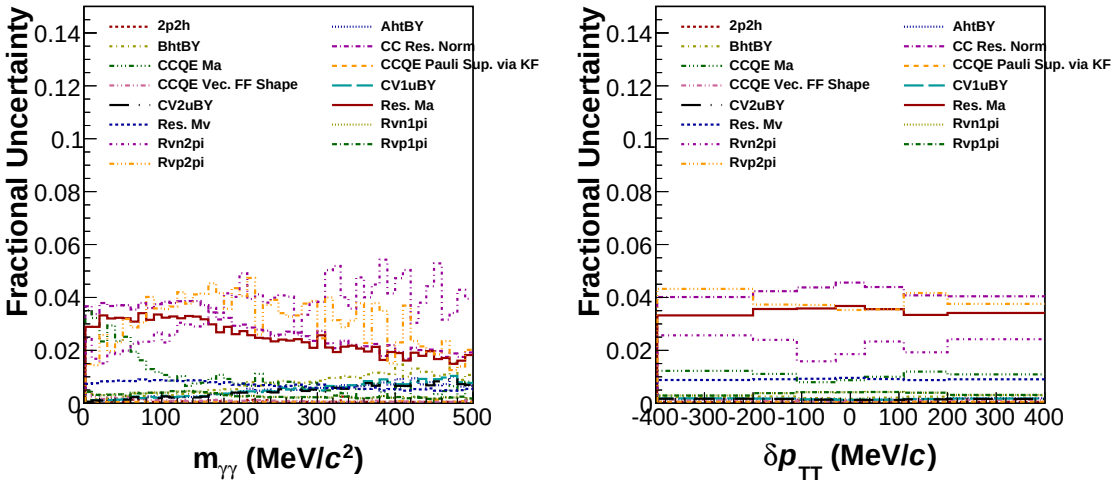

Figure 7.24: Breakdown of neutrino-interaction uncertainties for the reconstructed photon's invariant mass (left) and δp_{TT} (right).

7.2.3 Final State Interactions

Intranuclear dynamics of Final State Interactions are not well understood and therefore have large uncertainties associated to their modelling. Again, these parameters in GENIE have one sigma variations which, in the same manner as interaction uncertainties, are included as a systematic uncertainty. The associated model parameter uncertainties are presented in Table 7.4.

Following the inclusion of uncertainties in the FSI modelling their fractional change can be seen for $m_{\gamma\gamma}$ (*left*) and δp_{TT} (*right*) in Figure 7.25. Interestingly, above the π^0 invariant mass (135 MeV/c^2) both the pion absorption and inelastic scattering uncertainty looks to increase. This feature is likely due to the FSI cross-section dependence on π^0 energy although its exact origin is unknown.

Moving on to the δp_{TT} distribution, the most notable feature is nucleon elastic scatters which results in up to a 6% uncertainty in the central δp_{TT} bin. This is however expected given our studies in Chapter 3 on FSI effects in δp_{TT}. This property in GENIE was observed to be much more prominent than in other neutrino event generators.

Final State Interaction	Uncertainty	
	Pion	Nucleon
Absorption	±30%	±20%
Elastic Scattering	±10%	±30%
Mean Free Path	±20%	
Charge Exchange	±50%	
Inelastic Scattering	±40%	
Pion Production	±20%	
AGKY Hadronisation	±20%	

Table 7.4: One sigma systematic uncertainties associated to GENIE's Final State Interactions model parameters applied to this analysis.

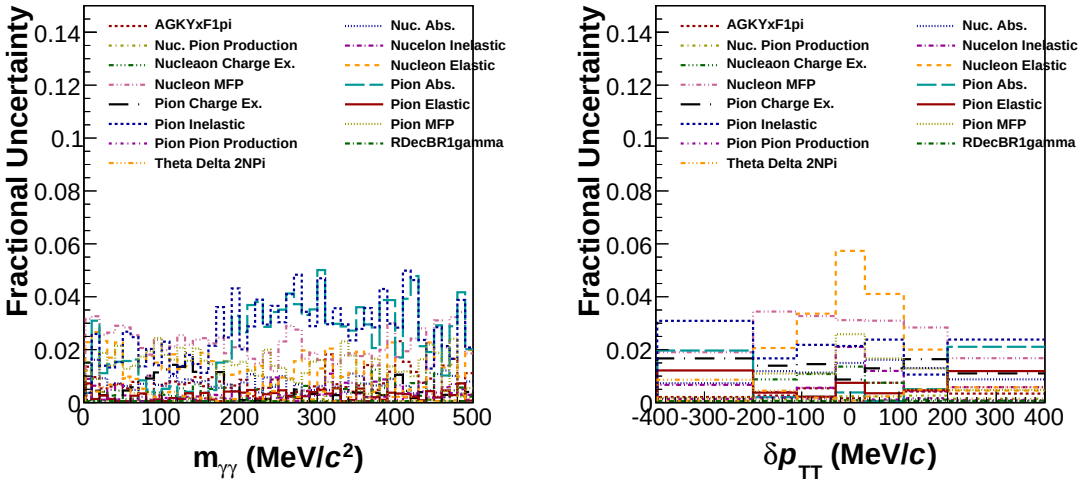

Figure 7.25: Breakdown of Final State Interactions uncertainties for the reconstructed photon's invariant mass (*left*) and δp_{TT} (*right*).

7.2.4 Summary

Now that each systematic group has been assessed individually their combined effects are now discussed. Let us begin by presenting a summary of the fractional uncertainty for $m_{\gamma\gamma}$ and δp_{TT} like that shown in Figure 7.26. Note here that the statistical uncertainty is that of the Monte Carlo. We see that in both variables

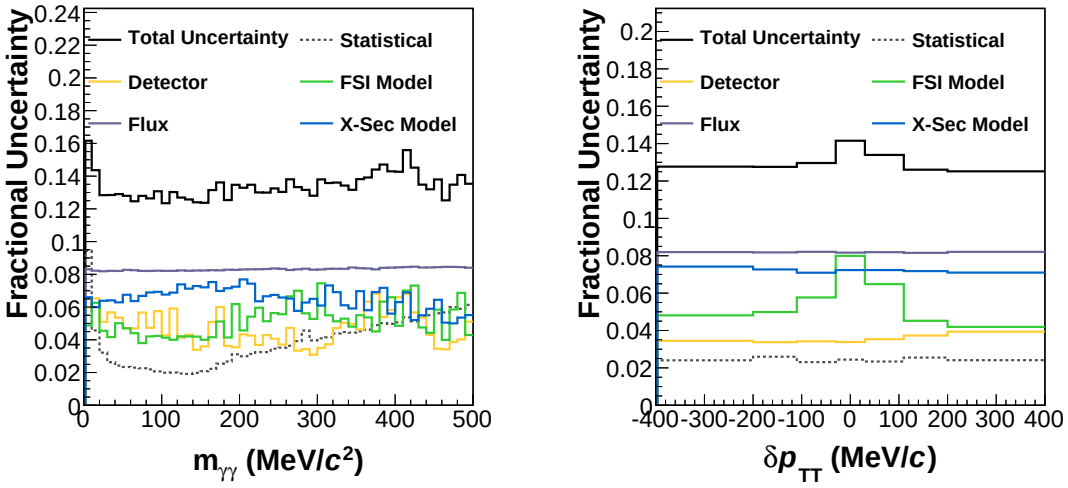

Figure 7.26: Summary of the four systematic groups along with the Monte Carlo statistical uncertainty of the reconstructed invariant mass (left) and δp_{TT} (right).

the uncertainty is dominated by our understanding of the neutrino flux which results in a flat uncertainty of approximately 8%.

In both $m_{\gamma\gamma}$ and δp_{TT} the overall uncertainty is flat implying that in general our systematics are not dependent on the kinematics presented here. There is however a dependence observed in the central region of Double Transverse Momentum. We mentioned that this was associated to nucleon FSI effects and given that δp_{TT} is sensitive to nuclear effects a dependence is expected. Although our systematics uncertainties lead to a combined uncertainty of approximately 11% in reality we will be statistics limited. The statistical uncertainty presented here is around 6.5 times smaller than our data as such we expect it to be between 15-20%.

Chapter 8

MINERνA Analysis: Cross Section Extraction

The aim of the MINERνA analysis is to provide a flux integrated differential cross section of δp_{TT}. This is with the view to gain an insight into the shape of carbon for use in the extraction of hydrogen in the T2K analysis. The formalism for such a bin-by-bin differential cross section reads

$$\frac{\mathrm{d}\sigma}{\mathrm{d}\left(\delta p_{\mathrm{TT}}\right)_i} = \frac{1}{\mathrm{T}\Phi}\frac{N_i^{\mathrm{Selected}}}{\Delta\left(\delta p_{\mathrm{TT}}\right)_i \varepsilon_i}. \tag{8.1}$$

Each bin, i, contains N_i^{Selected} selected CCNpMπ^0 events within a bin width $\Delta\left(\delta p_{\mathrm{TT}}\right)_i$. The reconstruction and selection efficiency of selecting the signal definition outlined in Section 6.1 is given by ε_i and corrects for the detector's ability to reconstruct events. The efficiency relies on information provided by the Monte Carlo prediction for both signal events passing the selection and those in the full Monte Carlo sample. Finally two scaling terms, Φ and T account for the total flux, Φ, presented to the detector during the data taking period and T the total number of nucleons within the fiducial volume.

Using the background constraints found in Chapter 6 and applying the re-

construction improvements from Chapter 7 we will outline our methodology to extracting a differential cross section dependence on δp_{TT}. This chapter shall begin by introducing how signal events are extracted in true kinematics before we review the propagation of systematics through the cross-section extraction process. From here the variation of systematics will be evaluated at each stage of the extraction process after which the final result is presented.

8.1 Determining the number of Selected Events

The signal sample does not contain purely signal events and on that account the background component needs to be removed from the data when determining N_i^{Selected}. Such a background subtraction method relies on using the constrained Monte Carlo outlined in Section 6.4. The number of selected events reads

$$N_i^{\mathrm{Selected}} = \sum_j U_{ij}(N_j^{\mathrm{data}} - N_j^{\mathrm{bkg}}) \tag{8.2}$$

and encompasses an unfolding term, U_{ij}, which maps the reconstructed data distribution to the underlying true kinematics of interest. The U_{ij} term effectively accounts for detector resolution and reconstruction effects. The principle behind unfolding is in essence matrix inversion. Therefore given some reconstructed number of signal events, N_i^{reco}, we want to know its true counterpart, N_i^{true} via the relation

$$N_i^{\mathrm{true}} = \sum_{\text{Reco Bins},j} U_{ij} N_j^{\mathrm{reco}} \qquad \text{or} \qquad N_j^{\mathrm{reco}} = \sum_{\text{True Bins},i} S_{ji} N_i^{\mathrm{true}}, \tag{8.3}$$

where $U_{ij} \equiv S_{ji}^{-1}$. This implies that an unsmearing matrix, U_{ij}, needs to be determined in a manner that can correctly account for the detector's response and statistical fluctuations. In an ideal world, one would desire a one-to-one mapping from the reconstructed to true quantities leading to a diagonal smear-

ing matrix. However, reality is not like that and we are limited to the detectors resolution resulting in non-zero off diagonal matrix elements.

The approach used in this analysis is to apply iterative D'Agostini Bayesian Unfolding to determine the underlying true distribution [117]. Its formalism is based on Bayes theorem and can be used to define the unsmearing matrix as the conditional probability for the number of true events, T_i, in true bin i given the number of reconstructed events, R_j, in reconstructed bin j

$$U_{ij} \equiv P(T_i|R_j) = \frac{P(R_j|T_i)P(T_i)}{P(R_j)}. \tag{8.4}$$

Here the reconstruction prior is $P(R_j) = \sum_k P(R_j|T_k)P(T_k)$. This enables us to determine the true signal distribution, $P(T_i)$, given the reconstructed data, N_j^{reco}, and the smearing matrix $P(R_j|T_i)$. It relies on two Monte Carlo inputs, namely, a smearing matrix and an initial true signal distribution prior, $P(T_i)$. Immediately, one may be concerned that the unfolded result will be effected by the choice of prior as dependencies on the Monte Carlo's ability to reproduce both the data and cross section model are introduced. This is however overcome via the iterative approach which enforces a data driven methodology to estimate the true number of events in each true bin.

Let us begin by rewriting the first term in Equation 8.3 in its iterative form with the U_{ij} term in full

$$N_i^{\text{true }(m+1)} = \sum_{\text{Reco Bins},j} \frac{P(R_j|T_i')P^m(T_i)}{\sum_k P(R_j|T_k')P^m(T_k)} N_j^{\text{reco}}. \tag{8.5}$$

Here $P^m(T_i)$ now defines the prior and is dependent on the number of iterations, m. There is a subtle difference between the U_{ij} in Equation 8.4 and that shown here in that the truth component of the smearing matrix, T_j', may now be distinct from that in the true signal prior. This is because the smearing matrix remains unchanged throughout the iterative process.

The iterative procedure begins by calculating $N_i^{\text{true }(m+1)}$ using the initial Monte Carlo prior such that $P^0(T_i) \equiv P(T_i')$. This can then be used to update the true signal prior given the data using

$$P^m(T_i) = \frac{N_i^{\text{true }(m+1)}}{\sum_k N_k^{\text{true }(m+1)}}. \tag{8.6}$$

From here subsequent iterations can be calculated using a prior which becomes increasingly dependent on the data. This iterative process continues until the analysers optimal number of iterations has been reached.

Care needs to be taken when finding the optimal number of iterations for a each analysis. For example, if the underlying Monte Carlo truth prior is believed to be a poor description of the data then one may want to use a large number of iterations or weak regularisation strength. This however becomes a more degenerate problem as the number of reconstructed bin combinations to produce a single true bin increases. As a result this can lead to large bin-to-bin anti-correlations and added uncertainty in the unfolded result. It is therefore crucial to understand the unfolding procedure given ones knowledge of different model predictions and the detector's response.

8.2 Optimal Number of Iterations in Bayesian Unfolding

Our approach to determining the regularisation strength is based on Monte Carlo studies where, like in the background constraints section, Monte Carlo is used as fake data. The framework developed to do this relies on performing 1000 toy experiments. In each toy experiment we begin by Poisson fluctuating the reconstructed signal before passing it to the unfolding framework. We unfold over a range of iterations, calculating a three metrics between the true Monte

Carlo distribution and the unfolded result. These metrics are used to assess the effect of unfolding after each iteration.

The first metric is the χ^2 calculated between the true input Monte Carlo distribution and the unfolded result. This can be used to assess the change in χ^2 as a function of iterations and allows us to find where the unfolded distribution has found agreement with the true result. For this statistical study, we are looking for an iteration that results in a $\chi^2/ndf \sim 1$. Once this has been satisfied the second metric is then used as the driving force behind finding the optimal regularisation strength. Note that the *ndf*s here is the number of bins which totals seven indicating that the unfolding has converged once a mean χ^2 of seven has been observed.

The second metric is a bin-by-bin pull which is used to learn of how biases change from iteration to iteration. The expectation is that in each bin the pull should have a mean of zero and width of one once a unbiased regularisation strength has been found. Here we are looking for an iteration that results in the unfolded distribution having the smallest bias. The bin-by-bin pull is calculated using the unfolded histogram, unfolding covariance matrix and true Monte Carlo distribution. In each bin the difference between the unfolded number of events and true number is determined before being divided by the associated diagonal element of the covariance matrix related to the bin of interest.

Finally, the correlation matrix for each iteration is found using the unfolded covariance matrix. Given each iteration has its own correlation matrix a mean correlation matrix is calculated over all the toys. This provides us with an assessment in to how anti-correlated the result is for a certain iteration.

We saw that D'Agostini unfolding requires three inputs for the mechanism to work. These were the smearing matrix mapping true to reconstructed quantities, the true Monte Carlo prediction for use as our initial prior and lastly the dataset to be unfolded. This analysis uses the binning defining in Table 7.2 for both true

and reconstructed quantities. The resultant binning leads to the following Monte Carlo input distributions in Figure 8.1 for use in the unfolding studies. Here the reconstructed δp_{TT} is calculated using the improved hadronic momentum reconstruction resulting in a more diagonal smearing matrix.

Before we go about determining the optimal number of iterations a brief validation study is performed. This is to ensure that both the mechanisms behind this study and the unfolding framework are working correctly. The approach here is to unfold the Monte Carlo to itself and check that the first two metrics are to their respective expectations. Here the number of iterations assessed spans from one to thirty-five or from a heavily regularised to an un-regularised result. As the Monte Carlo is unfolded to itself the unfolding procedure should not change the true distribution implying that the χ^2/ndf should be situated around unity for all iterations. We also expect the bin-by-bin pull to be unbiased in all iterations. The results of our validation study support this and can be seen in Figure 8.2. Here the χ^2 dependence on the iterations is given along with the bin-by-bin pull for the first and last iteration. All are within expectation however there is a odd feature in the χ^2 distribution. In Figure 8.2 (*left*), although the distribution looks to be χ^2 distributed there are a number of stripes that break away from the general population. These are certain fluctuated toys that are unstable when they are unfolded leading to lesser agreement with the true distribution. Fortunately these cases are rare and for the 1000 toys less then 1% are effected.

Now that our unfolding framework has been validated we shall undertake two tests to determine the optimal number of iterations. Both work using realistic data POT statistics, which at the time, was set to 10% of the Monte Carlo dataset. This down scaling is applied to both Monte Carlo and fake data. The first study simply tests the capabilities of unfolding given the expected LE dataset. Like the validation study, the results were the same as those presented in Fig-

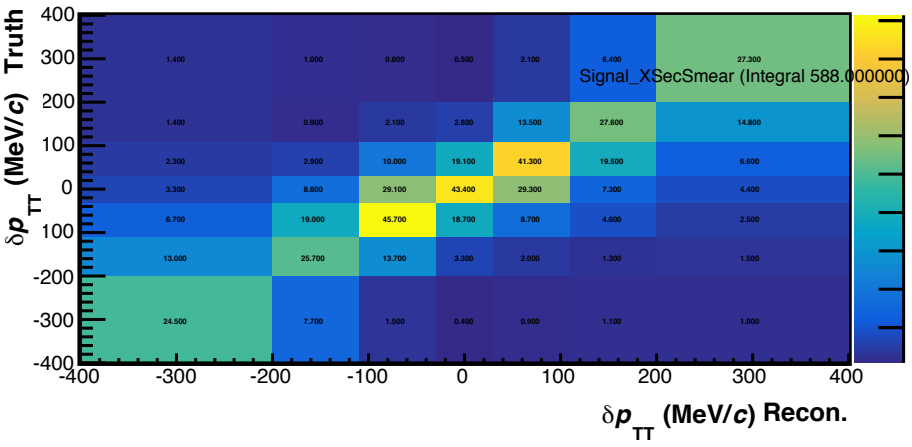

(a) Smearing Matrix.

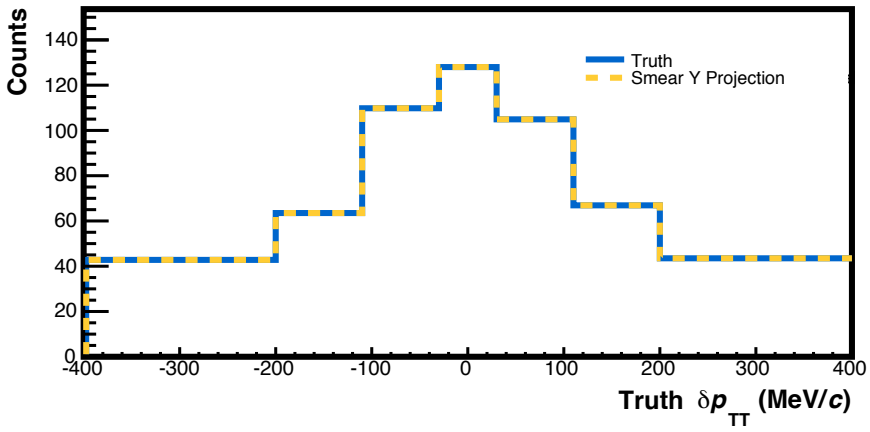

(b) Monte Carlo Truth Prior.

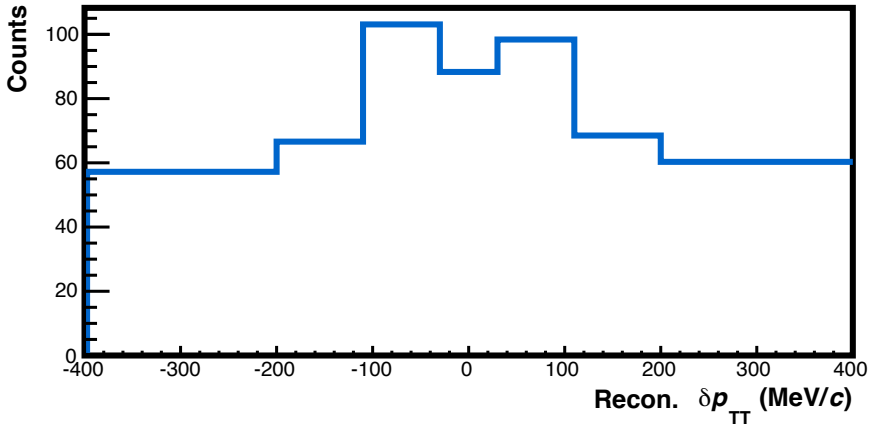

(c) Monte Carlo Fake Data.

Figure 8.1: The smearing matrix (*top*), initial true prior (*centre*) and the Monte Carlo reconstructed fake data (*bottom*). Note here that all distributions have been scaled to 10% of their original size.

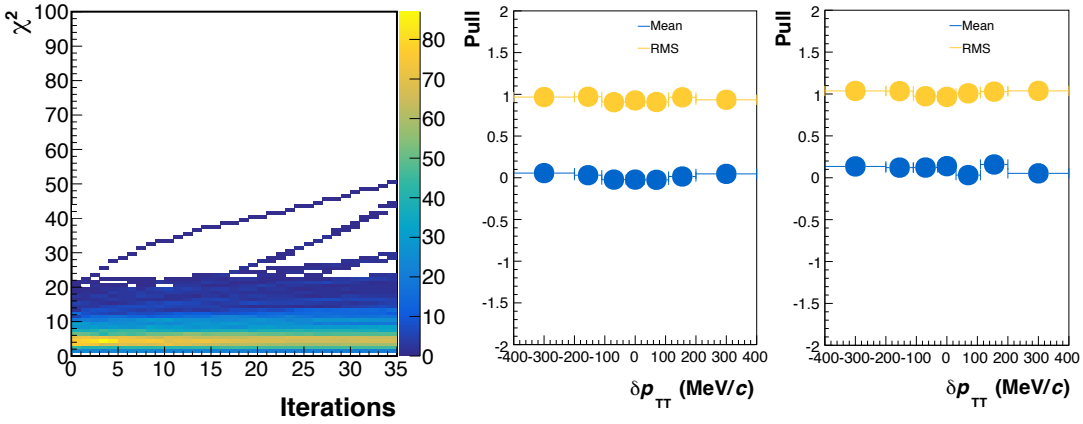

Figure 8.2: The result of validation study for Monte Carlo to Monte Carlo unfolding. The χ^2 as a function of iterations is given (*left*). The bin-by-bin pull for one (*centre*) and thirty-five iterations (*right*) is also presented.

ure 8.2. We saw that the two metrics were in line with expectation.

We noted in our discussion of d'Agostini unfolding that as our regularisation strength decreases the problem becomes more degenerate leading to larger uncertainties and bin-to-bin anti-correlations. This effect is highlighted when considering the ensemble of unfolded results along with the correlation matrix for a low and high number of iterations. The effect is seen in Figure 8.3 when comparing two and thirty iterations. The distribution on the left compares the known true distribution with the unfolded result for each fluctuated toy. We see that a un-regularised result (thirty iterations) leads to a much larger spread in the unfolded result when compared to one that is highly regularised (two iterations). There are also increasing bin-to-bin anti-correlations which become more diagonal as the number of iterations increases. Both suggest a larger degeneracy when unfolding is performed with a weak regularisation strength.

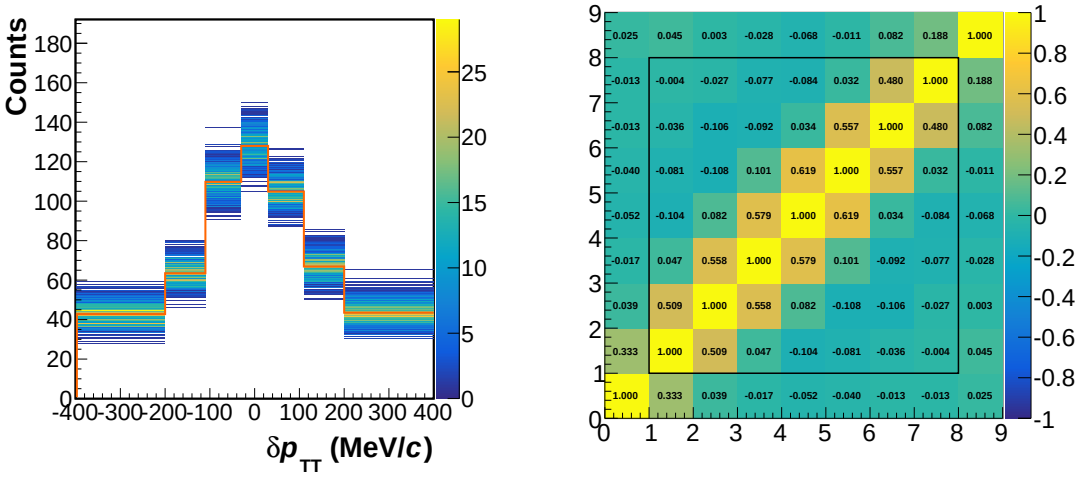

(a) Two Iterations.

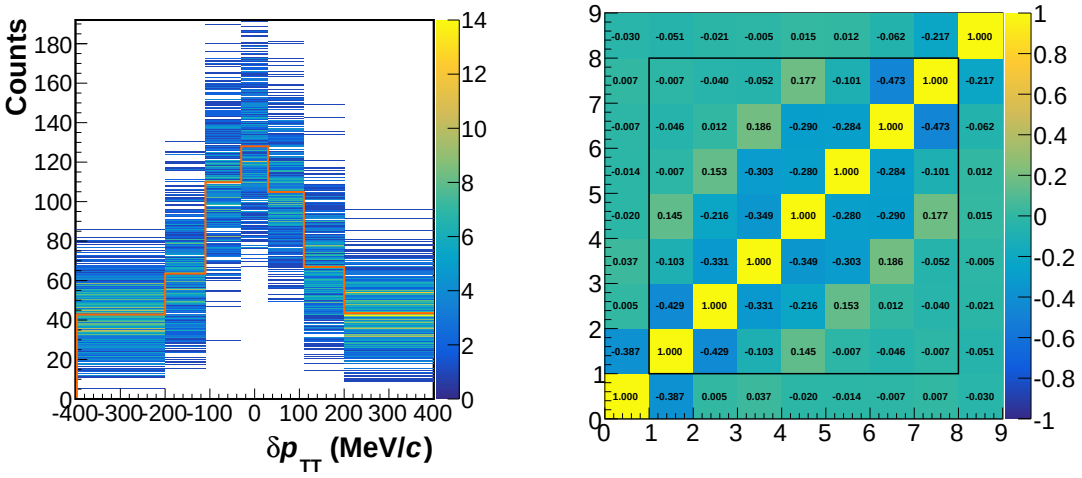

(b) Thirty Iterations.

Figure 8.3: The ensemble of unfolded results for two and thirty iterations is presented using realistic data POT, which at the time was set to 10% of the original Monte Carlo. The unfolded distributions are compared to the known true distribution (*left*) and the mean correlation matrix (*right*). Note that the entries outside the box in the correlation matrix represent the correlations for the under and overflow bins. The numbering here defines the analysis bin number. Hence between 1 and 2 lies the bin ranging from -400 to -200 MeV.

We know from earlier chapters that nuclear dynamics are not well understood and leads to numerous different predictions in δp_{TT}. It is therefore important to ensure that the unfolding framework is capable of reliably extracting alternative true distributions. Our approach to achieve this was through the development of a set of warping studies. Here the underlying true distribution was first varied to change its shape and then smeared simulating detector effects providing both different true and reconstructed distributions to the nominal Monte Carlo.

A total of four warping studies were considered; two central warps where we simulated the effect of an excess and deficit from the nominal true prediction. This was to ensure that if, in nature, the nucleus behaves more like a LFG than a GFG we can reproduce the true kinematics. The second set looked at the effect of a left and right asymmetric excesses to the true distribution.

The warping of the nominal Monte Carlo was implemented using the same binning as the true distribution. We began by producing a unit normalised Gaussian whose width and mean dictated the warping position and shape in the true quantity. A second histogram was then filled with unit weights after which it then had the Gaussian added or subtracted. During this process the Gaussian was scaled to change the warping strength. Even though the scaling is variable it was fixed to 0.5 in each study. By adding or subtracting the Gaussian defined where there was an excess or dip in the true quantity. These warping weights are shown in Figure 8.4 whose choice of Gaussian parametrisation for each warp is shown in Table 8.1.

The true and reconstructed quantities were built using the warped weight histogram and nominal Monte Carlo smearing matrix. This process transformed a warped weight histogram into a its two dimensional equivalent i.e. one which has the same binning as the smearing matrix but each true bin weight is projected into its related reconstructed bins. From here the two dimensional weight histogram and smearing matrix were multiplied together to produce a mapping

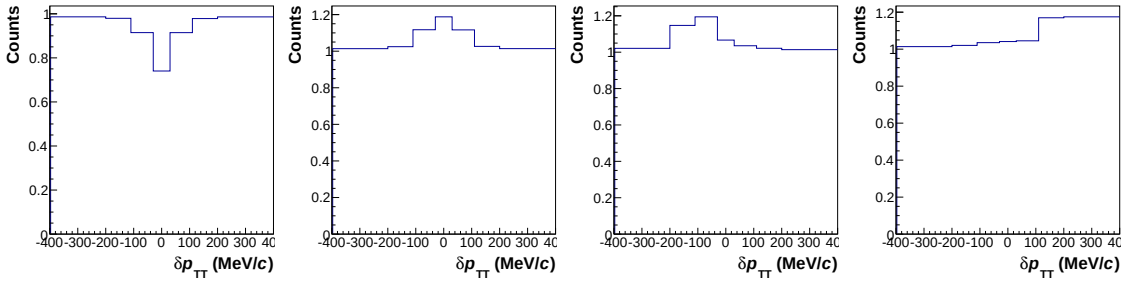

Figure 8.4: The warp weights for central dip (*left*) and excess (*centre left*) followed by left (*centre right*) and right (*right*) asymmetric variations. The Gaussian parametrisation for each warp is presented in Table 8.1.

Parameter	Central		Asymmetric	
(MeV/c)	Excess	Deficit	Left	Right
Mean	0	0	-100	+200
Width	50	30	50	50

Table 8.1: Input parameters for each Gaussian used to warp the underlying true distribution.

of warped true to reconstructed quantities. The result was an alternative one dimensional true and its related reconstructed distribution. Note the that under and over flow bins were also included in the warping of the true and reconstructed distribution.

We shall now assess the unfolding for each warp study presenting the respective true and reconstructed warped distributions used in the unsmearing process. In each study we begin by producing χ^2 as a function of iterations which once the χ^2/ndf has reached expectation the bin-by-bin pull is analysed for any bias. In both cases the warped true distribution is used to calculate these two metrics. The optimal regularisation strength is determined when there is negligible change in the bin-by-bin pull as the number of iterations increases. We will therefore present the bin-by-bin pull and associated correlation matrix for the first $\chi^2/ndf \sim 1$ and once the bias has stabilised.

Starting with the central excess whose true and reconstructed quantities are

shown in Figure 8.5. The unfolding procedure for this warp looks to flatten off at around five iterations as seen in Figure 8.6 (*left*). However, from Figure 8.6 (*centre*) this regularisation strength looks in incur a bias in the central region of δp_{TT} implying more iterations are required. A further eight iterations are applied before the bias looks to reduce to an acceptable level. This is highlighted by Figure 8.7 (*left*) where the bin-by-bin pull is now close to zero and flat between bins. There is an interesting feature when comparing the correlations matrices for five (Figure 8.6 *right*) and thirteenth (Figure 8.7 *right*) iterations. The latter, being the optimal number of iterations, looks to have increased anti-correlations in the next-to-next bins. This is apparent from the two blue off diagonal stripes, however the anti-correlations are no larger than -0.423.

Moving onto the central deficit study where the input true and reconstructed distributions in Figure 8.8 are used. The results of which are presented in Figures 8.9 and 8.10. A similar feature is observed as before for the χ^2 and bin-by-bin pull. Here we see that although the χ^2 */ndf* looks to plateau after around ten iterations, further iterations are needed to minimise the bias. In fact thirty-three iterations are required before the bias looks to stabilise. From Figure 8.10 we see the bin-by-bin pull for thirty-three iterations. There is still a noticeable bias in some bins which is likely due to the degeneracy leading to bin-to-bin anti-correlations. This is supported by the anti-correlations observed in adjacent bins from Figure 8.10 (*right*).

The asymmetric studies tell a similar story, both χ^2s flattening off at around five iterations but require further deregulation to minimise the bias. The inputs for each study are presented in Figures 8.11 and 8.14 with their χ^2 iteration dependence in Figures 8.12 and 8.15. The latter two Figures also include the first bin-by-bin pull highlighting the presence of a bias when the χ^2 first plateaus. Similar to the central deficit study, both asymmetric tests require many more iterations before the bias is stabilised. This is shown in the left asymmetric warp

in Figure 8.13 and the right asymmetric warp in Figure 8.16 where both instances have a regularisation strength of sixteen. The common number of iterations implies that the unfolding procedure is capable of unfolding with minimal bias irrespective of the asymmetry.

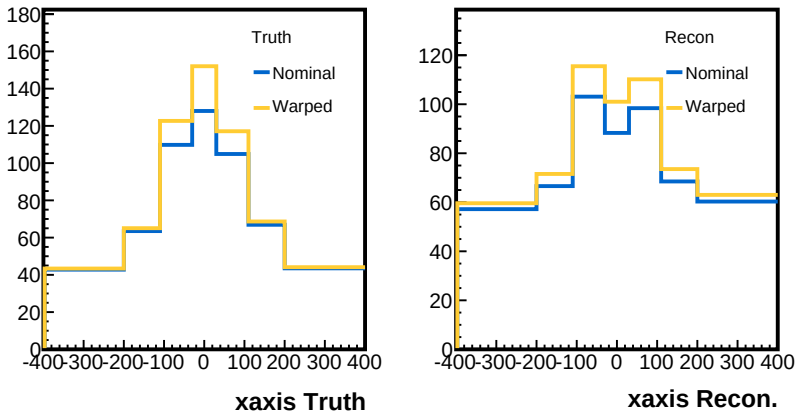

Figure 8.5: The central excess warped true (*left*) and reconstructed (*right*) δp_{TT} distributions are compared to their nominal counterparts.

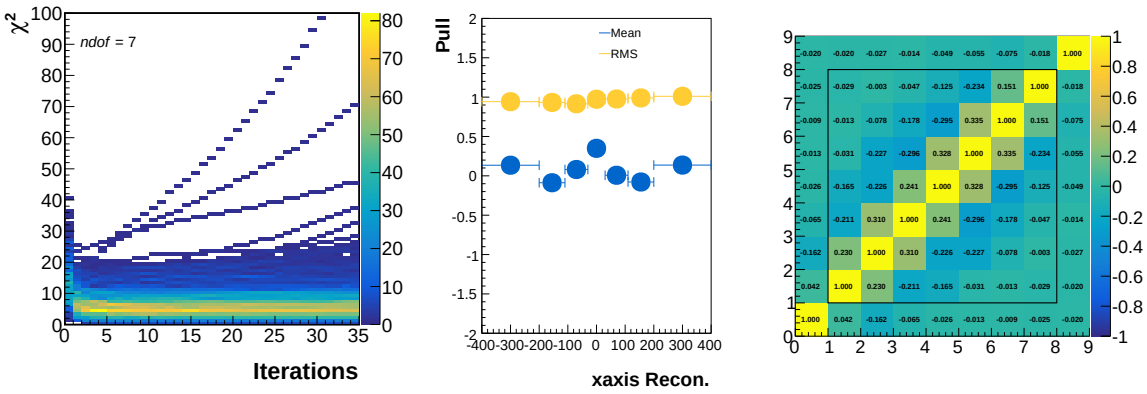

Figure 8.6: The results of the central excess study. The χ^2 as a function of iterations (*left*) and the fifth iteration's bin-by-bin pull (*centre*) and mean correlation matrix (*right*) are presented.

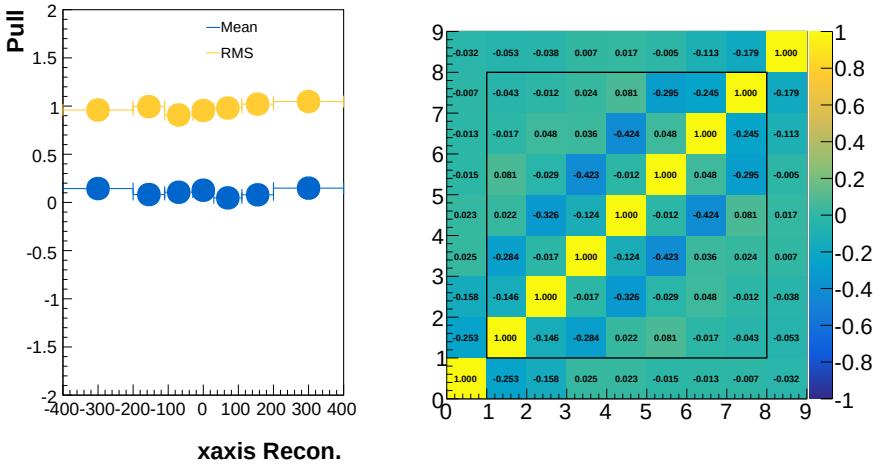

Figure 8.7: The optimal regularisation strength for the central excess study. The bin-by-bin pull (*left*) and associated correlation matrix (*right*) is presented for the first minimal bias regularisation strength, namely, the 13$^{\mathrm{th}}$ iteration.

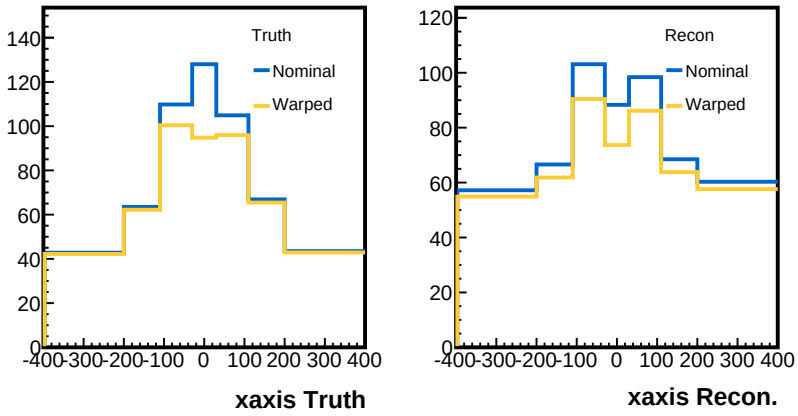

Figure 8.8: The central deficit warped true (*left*) and reconstructed (*right*) δp_{TT} distributions are compared to their nominal counterparts.

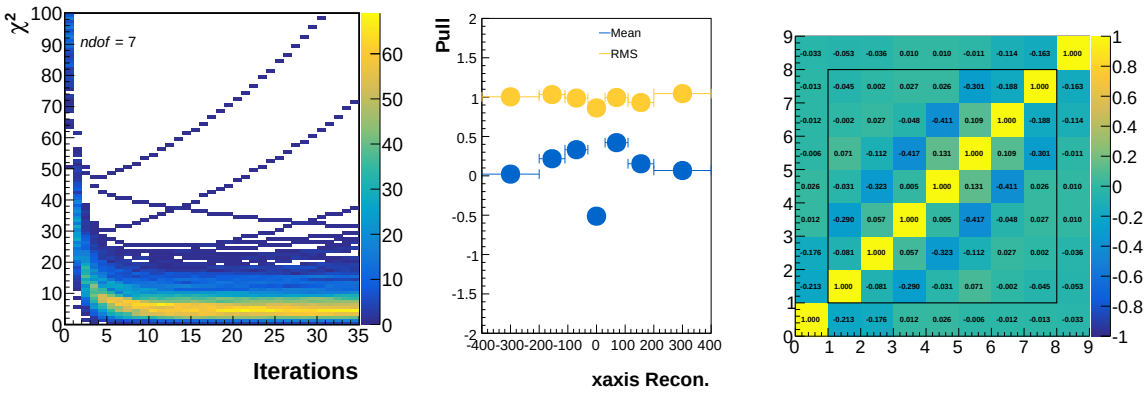

Figure 8.9: The results of the central deficit study. The χ^2 as a function of iterations (*left*) and the tenth iteration's bin-by-bin pull (*centre*) and mean correlation matrix (*right*) are presented.

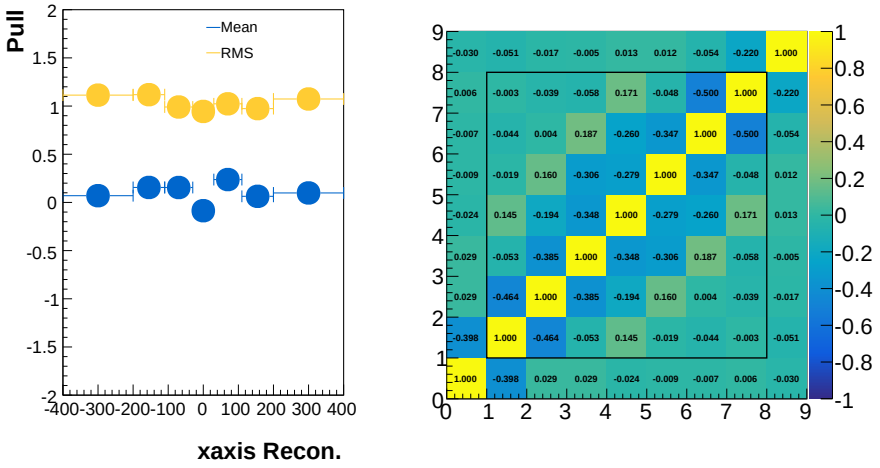

Figure 8.10: The optimal regularisation strength for the central deficit study. The bin-by-bin pull (*left*) and associated correlation matrix (*right*) is presented for the first minimal bias regularisation strength, namely, the 33$^{\mathrm{rd}}$ iteration.

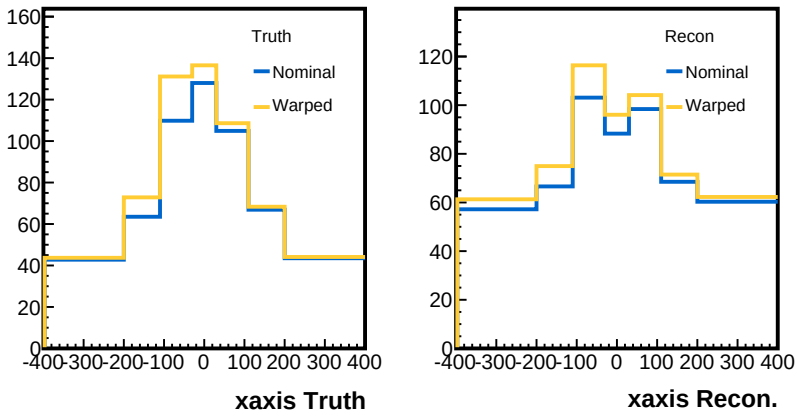

Figure 8.11: The left warped asymmetric true (*left*) and reconstructed (*right*) δp_{TT} distributions are compared to their nominal counterparts.

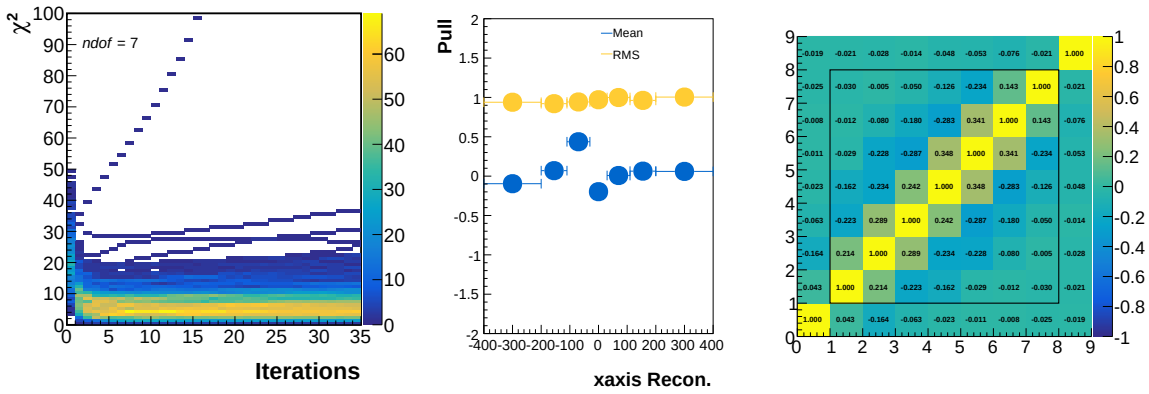

Figure 8.12: The results of the left asymmetric study. The χ^2 as a function of iterations (*left*) and the fifth iteration's bin-by-bin pull (*centre*) and mean correlation matrix (*right*) are presented.

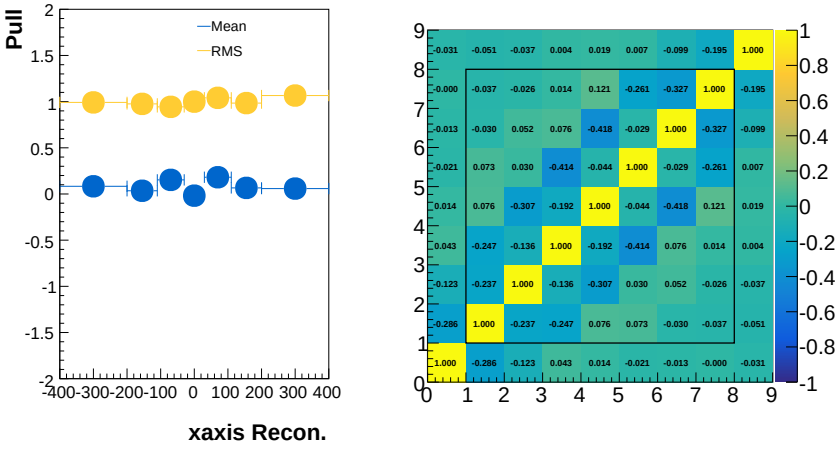

Figure 8.13: The optimal regularisation strength for the left asymmetric excess study. The bin-by-bin pull (*left*) and associated correlation matrix (*right*) is presented for the first minimal bias regularisation strength, namely, the 16$^{\mathrm{th}}$ iteration.

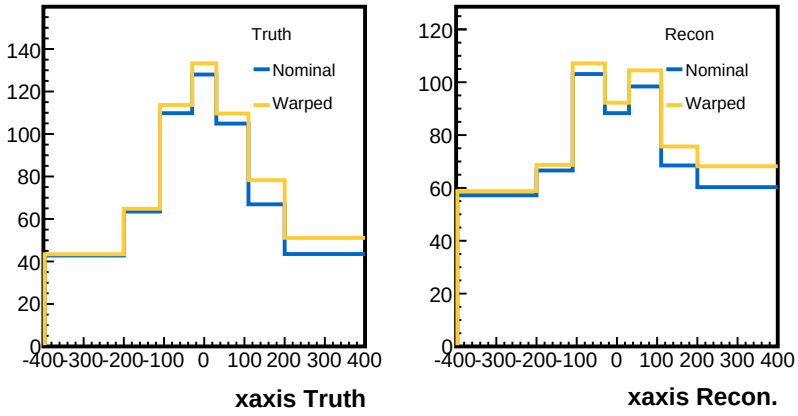

Figure 8.14: The right warped asymmetric true (*left*) and reconstructed (*right*) δp_{TT} distributions are compared to their nominal counterparts.

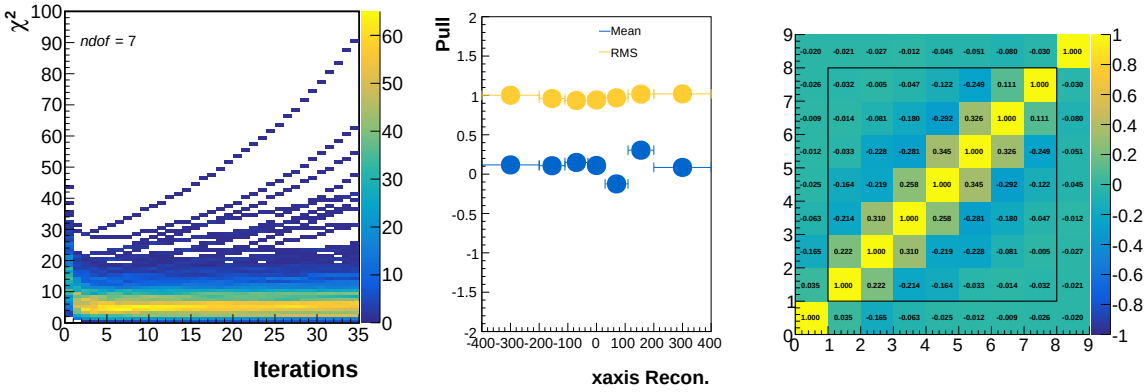

Figure 8.15: The results of the right asymmetric excess study. The χ^2 as a function of iterations (*left*) and the fifth iteration's bin-by-bin pull (*centre*) and mean correlation matrix (*right*) are presented.

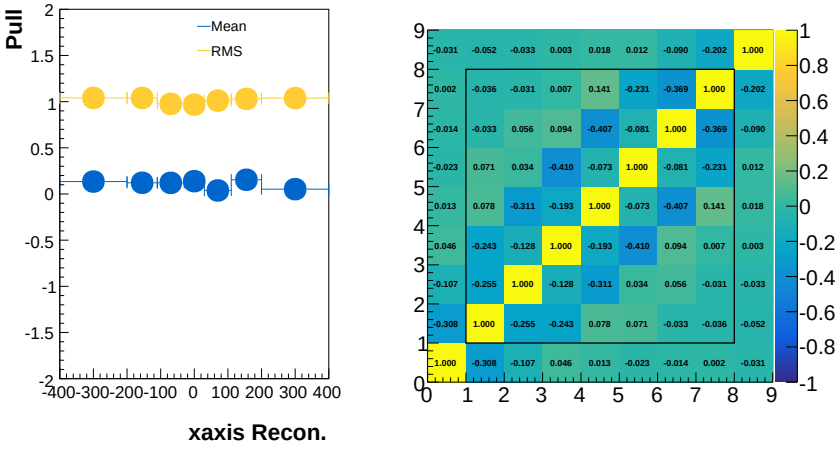

Figure 8.16: The optimal regularisation strength for the right asymmetric excess study. The bin-by-bin pull (*left*) and associated correlation matrix (*right*) is presented for the first minimal bias regularisation strength, namely, the 16$^{\mathrm{th}}$ iteration.

	Number of Iterations			
Study	Central		Asymmetric	
	Excess	Deficit	Left	Right
χ^2 Plateaus	5	10	5	5
Stable Bias	13	33	16	16

Table 8.2: Number of iterations required for each warping study's χ^2 to plateau and for the bin-by-bin bias to stabilise.

Having evaluated how the unfolding framework behaves given different underlying true distributions an optimal regularisation strength needs to be chosen. The number of iterations for each warping study is summarised in Table 8.2 where we present the regularisation strength for when the χ^2 plateaus and when the bin-by-bin pull stabilises. By sixteen iterations all but one study has either stabilised or the $\chi^2/ndf \sim 1$. The exception to this trend is the central deficit warp which requires further sixteen iterations before stability in the bin-by-bin pull is observed.

Clearly there is no common iteration in which all the studies are stable, so how should the regularisation strength be chosen? A starting point may be to be conservative and unfold to thirty-three iterations. This would however lead to non-negligible anti-correlations making the final cross section result harder to interpret. Another possibility may be to consider what GENIE's default nuclear model is and assess how well the unfolding performs when transitioning to alternative models. If we recall the δp_{TT} distribution for the various initial states, like in Figure 8.17, we see that GENIE's default model, a GFG, would need to be increased in the central region if nature is similar to an LFG. This would therefore imply that one could use thirteen iterations and reliably reach all alternative nuclear models. However, we do not know if nature is asymmetric in δp_{TT} and therefore a more conservative choice would be sixteen. Given this

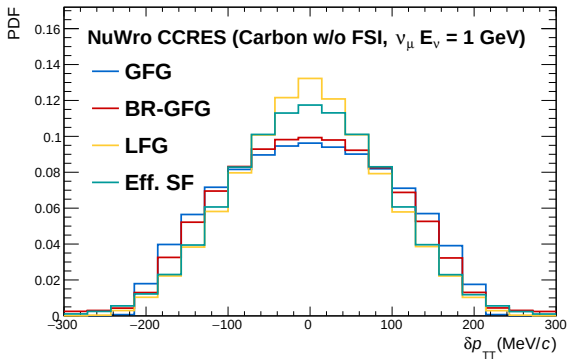

Figure 8.17: The various predictions for different initial states in δp_{TT} is presented for Charge Current Resonance production on Carbon. NuWro is configured with no FSI and a mono-energetic 1 GeV ν_μ beam. Note that this is a reproduction of Figure 3.4b.

our regularisation strength for use on data will be sixteen.

Prior to moving onto calculating the cross section, one final test of the unfolding framework needs to be performed. Unlike the previous studies this uses data and the aim is to check that unfolding on data is stable. We mentioned earlier that the there were certain statistical fluctuations that lead to stripes in the χ^2's dependence on the regularisation strength. For us to reliably unfold the data we want to ensure that, as the regularisation strength is relaxed, the χ^2 at some point plateaus. By comparing the unfolded data to the Monte Carlo's true distribution we can calculate the χ^2 as a function iterations. As the number of iterations increases the unfolded result becomes more dependent on the data. We should expect the χ^2 to stabilise from iteration to iteration implying that the unfolding procedure is working.

In preparation of testing d'Agostini unfolding for use on data, we constrain the background and subsequently subtract it from the data. The background subtracted data is then unfolded after which the data's χ^2 dependence as a function of iterations is calculated. This can be seen in Figure 8.18 when unfolding the data up to fifty iterations. The χ^2 slowly increases from 17.5 to 25 as the regularisation strength decreases indicating that the unfolding procedure is stable when unfolding the data.

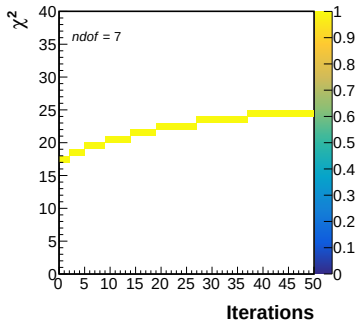

Figure 8.18: Using 3.33×10^{20} POT the χ^2 is calculated between the data and Monte Carlo true δp_{TT} distribution as a function of iterations.

8.3 Cross Section Extraction with Systematics

Systematic effects are propagated through to the cross section result by calculating the differential cross section in each 'alternative' universe. Given this is encapsulated by the Monte Carlo, the terms in Equation 8.1 that are affected by systematic effects are therefore N_i^{Selected} and ε_i. More precisely given the data does not change, then the background and unfolding matrix components in Equation 8.2 are sensitive to such systematic variations.

The smearing matrix, Monte Carlo background and efficiency are dependent on both model and detector variations. Note however that the efficiencies numerator and denominator are treated differently. The numerator is only affected by normalisation and the denominator, as one would expect, is only affected by model changes. Flux uncertainties are incorporated by including their variation as an 'alternative' universe in the reconstructed Monte Carlo, smearing matrix and efficiency.

We shall now analyse how systematics change as they propagate through each stage of the cross section extraction process. At each step both the data and Monte Carlo prediction are presented along with the fractional error. Note that the data with Monte Carlo overlay are bin width normalised so that the shape of δp_{TT} is preserved. The error bars on the data are systematic plus statistical uncertainties whereas the Monte Carlo error is statistical only.

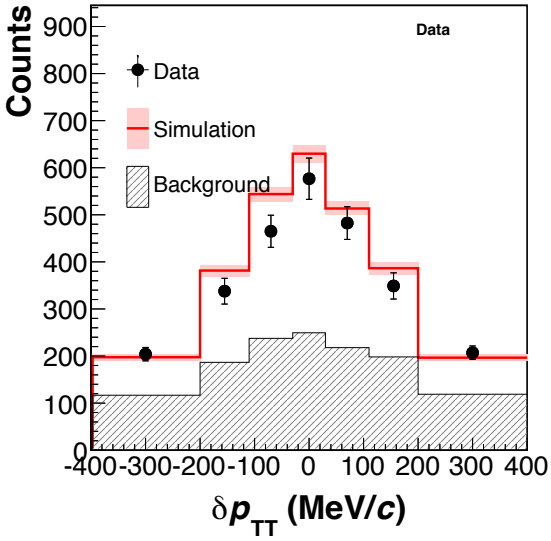

Figure 8.19: The reconstructed data and Monte Carlo prediction for signal and background using a dataset of 3.33×10^{20} POT.

The process begins with the reconstructed data and associated Monte Carlo prediction for both signal and background in Figure 8.19. Using the background constraints determined in Section 6.4 the background is rescaled given the results of the fit before being subtracted from the data and Monte Carlo. The resultant background subtracted δp_{TT} distributions can be seen in Figure 8.20. It is clear that, at the reconstructed level, there is a deficit in the data compared to the Monte Carlo prediction in the region encompassing ± 200 MeV/c. Given our knowledge of various nuclear effects in δp_{TT} this deficit is somewhat expected.

The fractional uncertainty in the background subtracted data indicates that we are statistically limited. We also see that the fractional systematic uncertainties are largest in the tails of δp_{TT} . This a result of the large background component in these outer bins which when background constraints are applied leads to greater uncertainty.

Having subtracted the backgrounds the δp_{TT} distribution is unfolded producing the true underlying distribution in Figure 8.21. The consistent shapes between the fractional uncertainties implies that the unfolding procedure does

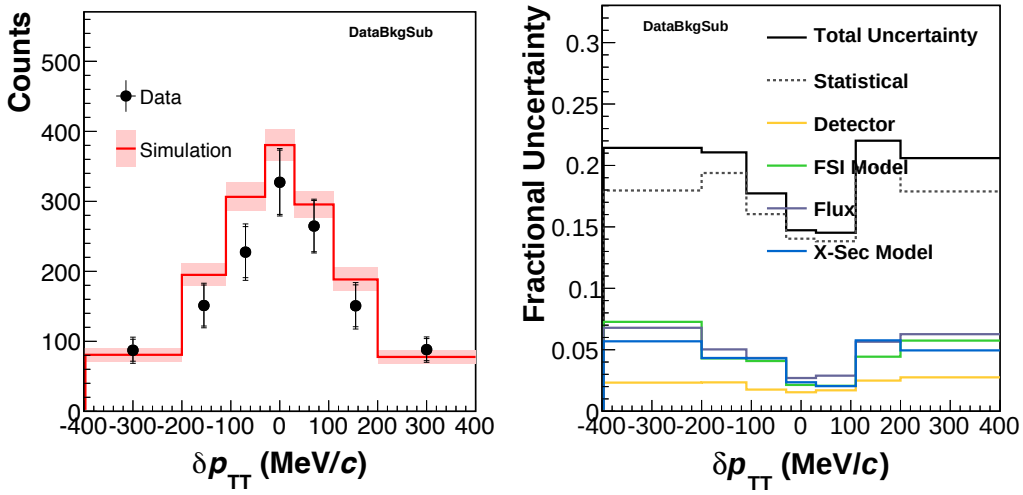

Figure 8.20: The background subtracted data and Monte Carlo overlay (*left*) and the systematic fractional uncertainty (*right*) are presented.

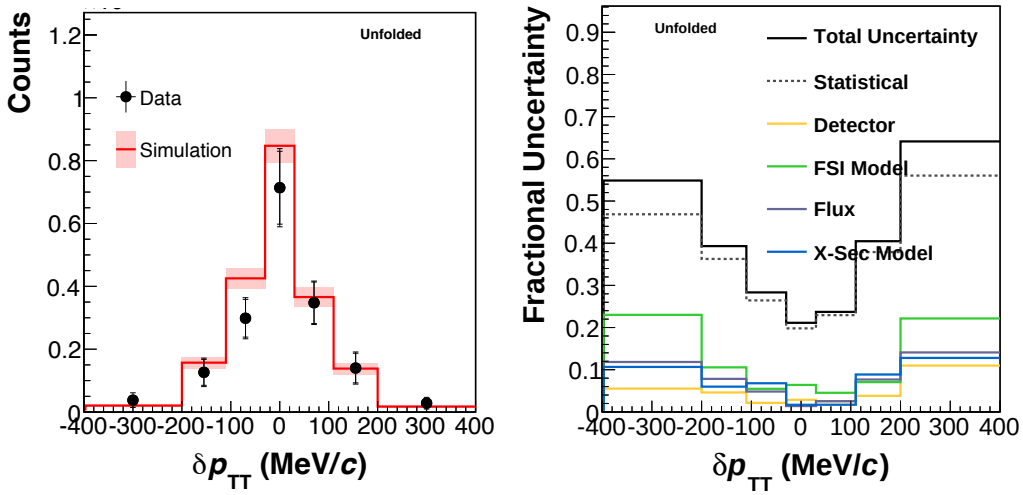

Figure 8.21: The unfolded data and Monte Carlo distributions (*left*) and the systematic fractional uncertainty (*right*) are presented.

not introduce large variations when unfolding in a given systematic universe. It is interesting to note that the dominant systematic uncertainty is the FSI model in the outer regions of δp_{TT}. This is no surprise given the broadening effect of FSI in δp_{TT}, which given is not well understood results in large variations in the spread of δp_{TT}.

The final phase is to apply the efficiency correction and normalisations which account for the number of target nucleons and flux integral. By integrating the low energy NuMi flux from 0 to 50 GeV the scaling terms used in this analysis

are

$$\Phi = \text{POT} \times 2.88154 \times 10^{-8} \qquad \text{T} = 3.17488 \times 10^{30}. \tag{8.7}$$

Note here that POT refers to the data POT (3.33×10^{20}). The efficiency correction is presented in Figure 8.22 and includes the efficiencies fractional uncertainty. We see that the efficiency is consistent with the total efficiency of 5.65% for selecting CCNpMπ^0 events in Chapter 6. Throughout the δp_{TT} region of interest we see a small variation (total spread of 1.5%) from bin to bin. Given the efficiency is fairly flat implies that the correction has little model dependence in δp_{TT}. Although MINERνA has a low efficiency of selecting CCNpMπ^0 events, the uncertainty on selecting such final states is small. This leads to a total fractional uncertainty of approximately 6% in all δp_{TT} bins.

One remaining cross check that could be done is a closure test. This would ensure that our unfolding and efficiency correction produce the correct result. Such an approach could be to extract the cross section for Monte Carlo using the framework used here and then compare it to the true Monte Carlo cross section. By using the true event generator prediction it is possible to produce a true differential cross section for δp_{TT} which if our extraction method is correct will be identical to the true Monte Carlo prediction. Although from the unfolding closure study and given our δp_{TT} efficiency is consistent with expectation this is unlikely to yield any unexpected deviation from the true Monte Carlo cross section.

8.4 The Result

The world's first flux integrated differential cross-section dependence on δp_{TT} has been measured for CCNpMπ^0 final states. This result is presented in Figure 8.23 along with the fractional uncertainty. In general the Monte Carlo looks to over predict the signal component in the central region of δp_{TT}. However, given the

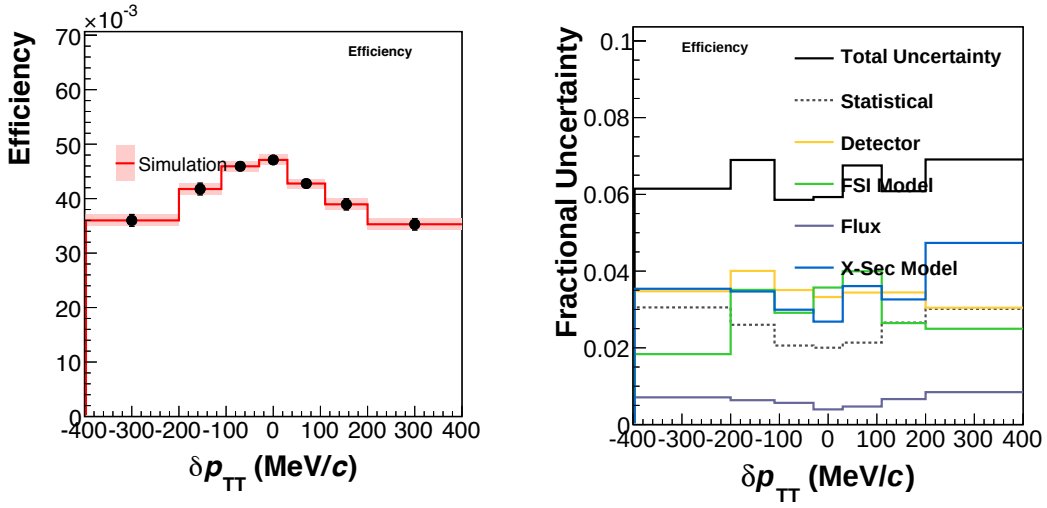

Figure 8.22: The efficiency correction used to account for the detector's reconstruction efficiency is presented along with the associated fractional systematic uncertainties. Note the data points are actually Monte Carlo and are not bin width normalised. The statistical uncertainty presented here is that of the Monte Carlo.

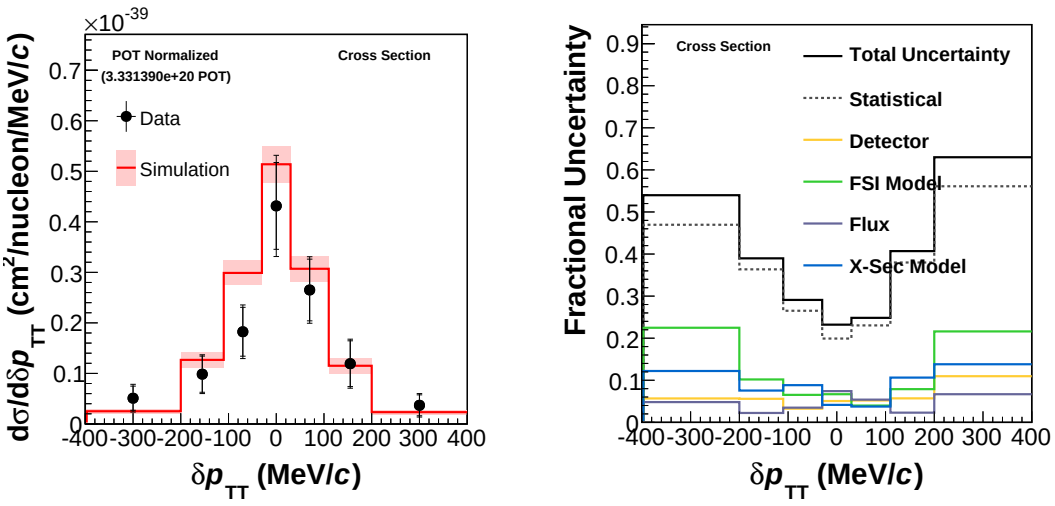

Figure 8.23: The flux integrated differential cross section using 3.33×10^{20} POT is presented (*left*) and the fraction uncertainty on the result (*right*).

large statistical uncertainty we are unable to state any disagreement between the data and Monte Carlo.

We mentioned earlier that this over prediction is somewhat expected. The central region is sensitive to the elastic component of FSI, which in GENIE predicts a larger strength than in other event generators. This mis-modelling is also supported by recent results by the T2K [100] and MINERνA [118] Collab-

orations. Both analysis probe nuclear effects in charge-current ν_μ induced final states containing proton(s) and zero pions. They, like what is seen here, observed a deficit in the data compared to Monte Carlo which is attributed to elastic Final State Interactions. Their work also suggests that the initial state model is better described by an LFG or Spectral Function. This appears to contradict the result presented here as GENIE uses an GFG.

It would be interesting to further analyse this result by comparing various predictions made by event generators. This may provide information on which initial state model and whether a reduction in the strength of elastic FSI better describes the data. The outcome of a data-model comparison study would enable future analysers who use δp_{TT} to isolate interactions on hydrogen to apply any constraints found on carbon's shape in δp_{TT}.

Chapter 9

Conclusion

Since their discovery, neutrinos have presented some of the most puzzling problems in physics; from the continuous energy spectrum in β-decay to neutrino flavour transformation. Our quest now lies in studying the flavour transformation in more detail as this may answer two questions; can $\mathcal{CP}$ violation in neutrino oscillations describe why matter dominates our universe and what is the ordering of the neutrino masses? Current and future accelerator-based neutrino oscillation experiments hoping to answer these questions, which as they move into the high precision era, are shown to be limited by our knowledge of nuclear effects. We saw this in Chapter 2 where we highlighted numerous issues arising from our knowledge of few-GeV neutrino-nucleus interactions. This has renewed interest by both the experimental and theoretical communities to better understand neutrino interactions with specific focus on nuclear effects.

9.1 Main Achievements

This thesis has outlined a means of probing nuclear effects in neutrino induced pion production. By analysing final states containing a muon, proton and pion we showed how Double Transverse Momentum may be used to understand both

initial and final state nuclear effects. The phenomenological studies indicated that δp_{TT} has minimal dependence on the incoming neutrino flux and that various form factor parametrisations leave its shape unchanged. This enables us to reliably discriminate between the various nuclear effects. We also presented a possible approach that may be used by future high statistics neutrino scattering experiments to access pion specific Final State Interactions. This method may shed light on whether pion FSI is type dependent.

One of the key abilities of δp_{TT} is that it may be used to isolate neutrino interactions on hydrogen in composite nuclear targets. This was studied at T2K's near detector, ND280, to assess the feasibility of performing such a measurement. We highlighted that using current detector technologies it is, in principle, possible to perform such a measurement albeit statistically limited at T2K. We did however learn that this would be reliant on improving our understanding of the heavy nuclear background.

Our approach to constrain the dominant background at T2K was to measure the δp_{TT} shape of carbon using MINERνA. By defining the final state as a single muon with at least one proton and π^0 we were able to measure the shape of carbon in δp_{TT}. Although the final states are different, phenomenological studies had shown similarities between the two final states. As such, our result may provide as a reliable external constraint for experiments like T2K which look to isolate interactions on hydrogen.

The differential cross section measurement by MINERνA was made possible through various reconstruction improvements. We developed a cut based approach to remove events where protons inelastically scattered inside MINERνA. This led to better dE/dx determination as predominantly elastically scattered protons remained resulting in a two fold improvement in the proton's momentum resolution. The π^0 momentum reconstruction was also investigated resulting in the development of a π^0 momentum optimisation technique. Our

approach saw a 10% reduction in the residual spread and a third increase in the number of correctly reconstructed π^0 momenta. Both improvements were needed for reliable extraction of the total number of true signal events.

The MINERνA result, using the Low Energy NuMi dataset, showed a small discrepancy between data and Monte Carlo. Our measurement seems to imply that the Monte Carlo over predicts the event rate in the central region of Double Transverse Momentum. This has not yet been confirmed but it is believed to be associated to the elastic FSI component in GENIE. Measurements by T2K and MINERνA have supported a reduction in the elastic FSI component and appears to be supported by the result presented here.

9.2 Going Forward

It would be interesting to assess how various model predictions compare to the extracted differential cross section at MINERνA. This may provide further insight into which model configuration best describes the data and validate our belief in the requirement of a reduction in GENIE's elastic component of FSI. In addition to GENIE, the other neutrino event generators predictions should be compared with the measurement presented here. This will help the theoretical community to refine and improve their Monte Carlo simulation of neutrino interactions.

Once the model comparisons are complete the result presented in this thesis may be used by future analysers trying to isolate interactions on hydrogen using δp_{TT}. Our work may provide a constraint on the shape of carbon's background in δp_{TT} leading to reliable extraction of the hydrogen event yield. The information learnt from the model comparisons could also be used to aid oscillation experiments in reducing their systematic uncertainties related to cross section models. This knowledge is crucial for future accelerator-based neutrino oscillation experiments like DUNE that have a designed sensitivity of $\mathcal{O}(1-2\%)$ to the

$\delta_{\mathcal{CP}}$ phase.

The MINERνA result was produced using the Low Energy NuMi dataset but it has many other datasets that could be analysed using δp_{TT}. One may want to first expand on the analysis developed here and measure the same final state using the High Energy NuMi data. Given we learnt that the differential cross section was statistically limited, the High Energy NuMi dataset could provide a result with a better statistical precision.

The MINERνA experiment has data from anti-neutrinos in both Low and High Energy NuMi configurations which could be used in conjunction with Double Transverse Momentum to probe nuclear effects. Note however, if nuclear effects are to be analysed in anti-neutrinos impinging on the active tracker, measurements may be statistically limited. This is because anti-neutrinos predominantly produce final states containing neutrons and are therefore difficult to reconstruct. There is however a channel where the final state contains a proton. Unfortunately the target nucleon for this final state is a proton and so, if such a final state was to be analysed in the active tracker, it would result in interactions on hydrogen. This would make any probe of nuclear effects alone infeasible. Fortunately, MINERνA has a number of passive nuclear targets including carbon which could be used to study nuclear effects in anti-neutrino induced final states.

The μ^+, proton and π^- final state could be used to measure the anti-neutrinos cross section energy dependence free from nuclear effects. Obviously this would be dependent on external constraints being found for the carbon background. It would be interesting to expand on the phenomenological studies in Chapter 3 and compare the μ^+, proton and π^- final state with that of the MINERνA measurement presented here. Given we found relative agreement between the shape of δp_{TT} for two distinct final states, it may also be the case for μ^+, proton and π^- and μ^-, proton and π^0 final states. If this is the case then our measurement

could also help improve our knowledge of anti-neutrino cross sections.

Finally, it would be interesting to see how future detectors may be able to isolate neutrino interactions on hydrogen. The proposed upgrade to T2K's near detector is to build a highly granulated detector surrounded by high angle TPCs [119]. This is with the aim of increasing ND280's acceptance and improve the reconstruction of low energy particles. The proposed Super-FGD [120], which is designed with 1 cm^3 scintillator cubes may be able to substantially improve the low energy sensitivity and increase the selection efficiency of final states containing a single muon, proton and π^+. This could be used to extract the hydrogen component using Double Transverse Momentum and the cross section result presented in this thesis as a constraint to the carbon background.

Appendix A

NEUT Interaction Mode Definitions

Following the convention defined in NEUT version 5.3.6 the interaction modes have been categorised in Table A.1 for Charge-current neutrinos, Table A.3 for Charge-current anti-neutrinosand Neutral-current interactions in Table A.2. In Table A.4 the interactions have been categorised into the N groups used to categorise modes in Chapter 3.

Interaction	State	
	Initial	Final
Quasi-Elastic	$\nu_\ell + n$	$\ell^- + p$
	$\nu_\ell + n + X$	$\ell^- + p + X$ ($X = n$ or p)
Resonance Production	$\nu_\ell + p$	$\ell^- + p + \pi^+$
	$\nu_\ell + n$	$\ell^- + p + \pi^0$
	$\nu_\ell + n$	$\ell^- + n + \pi^+$
	$\nu_\ell + n$	$\ell^- + n + \gamma$
Single Kaon Production	$\nu_\ell + n$	$\ell^- + n + K^+$
	$\nu_\ell + n$	$\ell^- + p + K^0$
	$\nu_\ell + n$	$\ell^- + p + K^+$
	$\nu_\ell + n$	$\ell^- + \Lambda + K^+$
Single η from Δ Resonance	$\nu_\ell + n$	$\ell^- + p + \eta^0$
Multi-π ($1.3 < W$ (GeV/c^2) < 2.0)	$\nu_\ell + n$ or p	$\ell^- + n$ or $p + N\pi$
Deep Inelastic ($2.0 > W$ GeV/c^2)	$\nu_\ell + n$ or p	$\ell^- + n$ or $p + N$ mesons

Table A.1: NEUT Charged Current neutrino interactions modes.

Interaction	State	
	Initial	Final
Quasi-Elastic	$\bar{\nu}_\ell + p$	$\ell^+ + n$
	$\bar{\nu}_\ell + p + X$	$\ell^+ + n + X$ ($X = n$ or p)
Resonance Production	$\bar{\nu}_\ell + n$	$\ell^+ + n + \pi^-$
	$\bar{\nu}_\ell + p$	$\ell^+ + n + \pi^0$
	$\bar{\nu}_\ell + p$	$\ell^+ + p + \pi^-$
	$\bar{\nu}_\ell + p$	$\ell^+ + n + \gamma$
Single Kaon Production	$\bar{\nu}_\ell + n$	$\ell^+ + n + K^+$
	$\bar{\nu}_\ell + n$	$\ell^+ + p + K^0$
	$\bar{\nu}_\ell + n$	$\ell^+ + p + K^+$
	$\bar{\nu}_\ell + p$	$\ell^+ + \Lambda + K^0$
Single η from Δ Resonance	$\bar{\nu}_\ell + p$	$\ell^+ + n + \eta^0$
Multi-π ($1.4 < W$ (GeV/c^2) < 2.0)	$\bar{\nu}_\ell + n$ or p	$\ell^+ + n$ or $p + N\pi$
Deep Inelastic ($2.0 > W$ GeV/c^2)	$\bar{\nu}_\ell + n$ or p	$\ell^+ + n$ or $p + N$ mesons

Table A.2: NEUT Charged Current anti-neutrino interaction modes.

Interaction	State	
	Initial	Final
Quasi-Elastic	$\nu_\ell + n$ or p	$\nu_\ell + n$ or p
Resonance Production	$\nu_\ell + n$	$\nu_\ell + n + \pi^0$
	$\nu_\ell + p$	$\nu_\ell + p + \pi^0$
	$\nu_\ell + n$	$\nu_\ell + p + \pi^-$
	$\nu_\ell + p$	$\nu_\ell + n + \pi^+$
	$\nu_\ell + n$ or p	$\nu_\ell + n$ or $p + \gamma$
Single η from Δ Resonance	$\nu_\ell + n$ or p	$\nu_\ell + n$ or $p + \eta^0$
Single K from Δ Resonance	$\nu_\ell + n$	$\nu_\ell + \Lambda + K^0$
	$\nu_\ell + p$	$\nu_\ell + \Lambda + K^+$
Multi-π $(1.3 < W$ (GeV/c^2) $< 2.0)$	$\nu_\ell + n$ or p	$\nu_\ell + n$ or $p + N\pi$
Deep Inelastic $(2.0 > W$ GeV/$c^2)$	$\nu_\ell + n$ or p	$\nu_\ell + n$ or $p + N$ mesons

Table A.3: NEUT Neutral Current neutrino interactions modes.

Interaction	NEUT Interaction Mode
Quasi-Elastic	Quasi-Elastic
ν_ℓ Resonance Production	$\nu_\ell + p \to \ell^- + p + \pi^+$
$\bar{\nu}_\ell$ Resonance Production	$\bar{\nu}_\ell + p \to \ell^+ + p + \pi^-$
Resonance (Other)	Resonance Production (excluding above)
Deep Inelastic Scattering	Deep Inelastic Scattering
Other	Single Kaon Production
	Single η from Δ Resonance
	Multi-π $(1.4 < W$ (GeV/c^2) $< 2.0)$

Table A.4: Interaction modes defined for generator comparisons using NEUT's definitions of interaction modes.

References

[1] Henri Becquerel, "On the rays emitted by phosphorescence", Compt. Rend. Hebd. Seances Acad. Sci. vol. 122 (8) pp. 420–421 (1896)

[2] J. Chadwick, "The intensity distribution in the magnetic spectrum of beta particles from radium (B + C)", Verh. Phys. Gesell. vol. 16 pp. 383–391 (1914)

[3] David Halliday, Introductory Nuclear Physics, Wiley

[4] Kai Zuber, Neutrino Physics, CRC Press

[5] W Pauli, Letter of the 4th December 1930, Pauli Archive at CERN

[6] E. Fermi, "Versuch einer Theorie der β-Strahlen. I", Zeitschrift für Physik vol. 88 (3) pp. 161–177 (1934), doi:10.1007/BF01351864, URL `https://doi.org/10.1007/BF01351864`

[7] F. Reines and C. L. Cowan, "Detection of the Free Neutrino", Phys. Rev. vol. 92 pp. 830–831 (1953), doi:10.1103/PhysRev.92.830, URL `https://link.aps.org/doi/10.1103/PhysRev.92.830`

[8] C. L. Cowan et al., "Detection of the free neutrino: A Confirmation", Science vol. 124 pp. 103–104 (1956), doi:10.1126/science.124.3212.103

[9] Raymond Davis, "Attempt to Detect the Antineutrinos from a Nuclear Reactor by the $Cl^{37}(\overline{\nu}, e^{-})A^{37}$ Reaction", Phys. Rev. vol. 97 pp. 766–769

(1955), doi:10.1103/PhysRev.97.766, URL https://link.aps.org/doi/10.1103/PhysRev.97.766

[10] Raymond Davis, "Solar Neutrinos. II. Experimental", Phys. Rev. Lett. vol. 12 pp. 303–305 (1964), doi:10.1103/PhysRevLett.12.303, URL https://link.aps.org/doi/10.1103/PhysRevLett.12.303

[11] Y. Fukuda et al. (Super-Kamiokande Collaboration), "Evidence for Oscillation of Atmospheric Neutrinos", Phys. Rev. Lett. vol. 81 pp. 1562–1567 (1998), doi:10.1103/PhysRevLett.81.1562, URL https://link.aps.org/doi/10.1103/PhysRevLett.81.1562

[12] Q. R. Ahmad et al. (SNO Collaboration), "Direct Evidence for Neutrino Flavor Transformation from Neutral-Current Interactions in the Sudbury Neutrino Observatory", Phys. Rev. Lett. vol. 89 p. 011301 (2002), doi:10.1103/PhysRevLett.89.011301, URL https://link.aps.org/doi/10.1103/PhysRevLett.89.011301

[13] S. Frankel et al., "New Limit on the $e + \gamma$ Decay Mode of the Muon", Phys. Rev. Lett. vol. 8 pp. 123–125 (1962), doi:10.1103/PhysRevLett.8.123, URL https://link.aps.org/doi/10.1103/PhysRevLett.8.123

[14] G. Danby et al., "Observation of High-Energy Neutrino Reactions and the Existence of Two Kinds of Neutrinos", Phys. Rev. Lett. vol. 9 pp. 36–44 (1962), doi:10.1103/PhysRevLett.9.36, URL https://link.aps.org/doi/10.1103/PhysRevLett.9.36

[15] Steven Weinberg, "Charge Symmetry of Weak Interactions", Phys. Rev. vol. 112 pp. 1375–1379 (1958), doi:10.1103/PhysRev.112.1375, URL https://link.aps.org/doi/10.1103/PhysRev.112.1375

[16] M. L. Perl et al., "Evidence for Anomalous Lepton Production in $e^+ - e^-$ Annihilation", Phys. Rev. Lett. vol. 35 pp. 1489–1492 (1975),

doi:10.1103/PhysRevLett.35.1489, URL https://link.aps.org/doi/10.1103/PhysRevLett.35.1489

[17] "Precision electroweak measurements on the Z resonance", Physics Reports vol. 427 (5) pp. 257 – 454 (2006), doi:https://doi.org/10.1016/j.physrep.2005.12.006, URL http://www.sciencedirect.com/science/article/pii/S0370157305005119

[18] M.M. Block et al., "Neutrino interactions in the CERN heavy liquid bubble chamber", Physics Letters vol. 12 (3) pp. 281 – 285 (1964), doi:https://doi.org/10.1016/0031-9163(64)91104-7, URL http://www.sciencedirect.com/science/article/pii/0031916364911047

[19] J.K. Bienlein et al., "Spark chamber study of high-energy neutrino interactions", Physics Letters vol. 13 (1) pp. 80 – 86 (1964), doi:https://doi.org/10.1016/0031-9163(64)90316-6, URL http://www.sciencedirect.com/science/article/pii/0031916364903166

[20] K. Kodama et al. (DONUT), "Observation of tau neutrino interactions", Phys. Lett. vol. B504 pp. 218–224 (2001), doi:10.1016/S0370-2693(01)00307-0, hep-ex/0012035

[21] K. Kodama et al. (DONuT), "Final tau-neutrino results from the DONuT experiment", Phys. Rev. vol. D78 p. 052002 (2008), doi:10.1103/PhysRevD.78.052002, 0711.0728

[22] C. Patrignani et al. (Particle Data Group), "Review of Particle Physics", Chin. Phys. vol. C40 (10) p. 100001 (2016), doi:10.1088/1674-1137/40/10/100001

[23] Fermilab Office of Communication, "Schematic of the DONuT Detector", (2016), URL http://news.fnal.gov/wp-content/uploads/2016/07/detector.jpg

[24] K Kodama et al., "Detection and analysis of tau–neutrino interactions in DONUT emulsion target", Nuclear Instruments and Methods in Physics Research Section A: Accelerators, Spectrometers, Detectors and Associated Equipment vol. 493 (1) pp. 45 – 66 (2002), doi:https://doi.org/10.1016/S0168-9002(02)01555-3, URL http://www.sciencedirect.com/science/article/pii/S0168900202015553

[25] Raymond Davis, Don S. Harmer, and Kenneth C. Hoffman, "Search for Neutrinos from the Sun", Phys. Rev. Lett. vol. 20 pp. 1205–1209 (1968), doi:10.1103/PhysRevLett.20.1205, URL https://link.aps.org/doi/10.1103/PhysRevLett.20.1205

[26] K. S. Hirata et al., "Observation of ^{8}B solar neutrinos in the Kamiokande-II detector", Phys. Rev. Lett. vol. 63 pp. 16–19 (1989), doi:10.1103/PhysRevLett.63.16, URL https://link.aps.org/doi/10.1103/PhysRevLett.63.16

[27] M. Cribier et al., "Results of the whole GALLEX experiment", Nuclear Physics B - Proceedings Supplements vol. 70 (1) pp. 284 – 291 (1999), doi:https://doi.org/10.1016/S0920-5632(98)00438-1, proceedings of the Fifth International Workshop on topics in Astroparticle and Underground Physics, URL http://www.sciencedirect.com/science/article/pii/S0920563298004381

[28] J. N. Abdurashitov et al., "Solar neutrino flux measurements by the Soviet-American gallium experiment (SAGE) for half the 22-year solar cycle", Journal of Experimental and Theoretical Physics vol. 95 (2) pp. 181–193 (2002), doi:10.1134/1.1506424, URL https://doi.org/10.1134/1.1506424

[29] V. Gribov and B. Pontecorvo, "Neutrino astronomy and lepton charge", Physics Letters B vol. 28 (7) pp. 493 – 496 (1969),

doi:https://doi.org/10.1016/0370-2693(69)90525-5, URL http://www.sciencedirect.com/science/article/pii/0370269369905255

[30] Ivan Esteban et al., "Updated fit to three neutrino mixing: exploring the accelerator-reactor complementarity", Journal of High Energy Physics vol. 2017 (1) p. 87 (2017), doi:10.1007/JHEP01(2017)087, URL https://doi.org/10.1007/JHEP01(2017)087

[31] K. Eguchi et al. (KamLAND Collaboration), "First Results from KamLAND: Evidence for Reactor Antineutrino Disappearance", Phys. Rev. Lett. vol. 90 p. 021802 (2003), doi:10.1103/PhysRevLett.90.021802, URL https://link.aps.org/doi/10.1103/PhysRevLett.90.021802

[32] K. Abe et al. (T2K), "Measurement of neutrino and antineutrino oscillations by the T2K experiment including a new additional sample of ν_e interactions at the far detector", Phys. Rev. vol. D96 (9) p. 092006 (2017), doi:10.1103/PhysRevD.96.092006, 10.1103/PhysRevD.98.019902, [Erratum: Phys. Rev.D98,no.1,019902(2018)], 1707.01048

[33] K. Abe et al. (T2K), "The T2K Experiment", Nucl. Instrum. Meth. vol. A659 pp. 106–135 (2011), doi:10.1016/j.nima.2011.06.067, 1106.1238

[34] R.B. Patterson, "The NOvA experiment: status and outlook", Nuclear Physics B - Proceedings Supplements vol. 235 pp. 151 – 157 (2013), doi:http://dx.doi.org/10.1016/j.nuclphysbps.2013.04.005, URL http://www.sciencedirect.com/science/article/pii/S0920563213001266

[35] K. Abe et al. (Hyper-Kamiokande Working Group), "A Long Baseline Neutrino Oscillation Experiment Using J-PARC Neutrino Beam and Hyper-Kamiokande", (2014), 1412.4673, URL https://inspirehep.net/record/1334360/files/arXiv:1412.4673.pdf

[36] R. Acciarri et al. (DUNE), "Long-Baseline Neutrino Facility (LBNF) and Deep Underground Neutrino Experiment (DUNE)", (2015), 1512.06148

[37] F. P. An et al. (Daya Bay), "Observation of electron-antineutrino disappearance at Daya Bay", Phys. Rev. Lett. vol. 108 p. 171803 (2012), doi:10.1103/PhysRevLett.108.171803, 1203.1669

[38] C. Adams et al. (LBNE), "The Long-Baseline Neutrino Experiment: Exploring Fundamental Symmetries of the Universe", (2013), 1307.7335, URL https://www.arXiv:hep-ex/13077335

[39] J. A. Formaggio and G. P. Zeller, "From eV to EeV: Neutrino Cross Sections Across Energy Scales", Rev. Mod. Phys. vol. 84 pp. 1307–1341 (2012), doi:10.1103/RevModPhys.84.1307, 1305.7513

[40] D. Casper, "The Nuance neutrino physics simulation, and the future", Nucl. Phys. Proc. Suppl. vol. 112 pp. 161–170 (2002), doi:10.1016/S0920-5632(02)01756-5, [,161(2002)], hep-ph/0208030

[41] Fundamental Physics at the Intensity Frontier (2012), doi:10.2172/1042577, 1205.2671, URL https://inspirehep.net/record/1114323/files/arXiv:1205.2671.pdf

[42] C.H. Llewellyn Smith, "Neutrino reactions at accelerator energies", Physics Reports vol. 3 (5) pp. 261 – 379 (1972), doi:https://doi.org/10.1016/0370-1573(72)90010-5, URL http://www.sciencedirect.com/science/article/pii/0370157372900105

[43] Véronique Bernard, Latifa Elouadrhiri, and Ulf-G Meißner, "Axial structure of the nucleon", Journal of Physics G: Nuclear and Particle Physics vol. 28 (1) p. R1 (2002), URL http://stacks.iop.org/0954-3899/28/i=1/a=201

[44] A. A. Aguilar-Arevalo et al. (MiniBooNE), "First Measurement of the Muon Neutrino Charged Current Quasielastic Double Differential Cross Section", Phys. Rev. vol. D81 p. 092005 (2010), doi:10.1103/PhysRevD.81.092005, 1002.2680

[45] Dieter Rein and Lalit M Sehgal, "Neutrino-excitation of baryon resonances and single pion production", Annals of Physics vol. 133 (1) pp. 79 – 153 (1981), doi:https://doi.org/10.1016/0003-4916(81)90242-6, URL http://www.sciencedirect.com/science/article/pii/0003491681902426

[46] J. Campbell et al., "Study of the Reaction $\nu p \to \mu^- \pi^+ p$", Phys. Rev. Lett. vol. 30 pp. 335–339 (1973), doi:10.1103/PhysRevLett.30.335, URL https://link.aps.org/doi/10.1103/PhysRevLett.30.335

[47] J. Bell et al., "Cross-Section Measurements for the Reactions $\nu p \to \mu^- \pi^+ p$ and $\nu p \to \mu^- K^+ p$ at High Energies", Phys. Rev. Lett. vol. 41 pp. 1008–1011 (1978), doi:10.1103/PhysRevLett.41.1008, URL https://link.aps.org/doi/10.1103/PhysRevLett.41.1008

[48] G. M. Radecky et al., "Study of single-pion production by weak charged currents in low-energy νd interactions", Phys. Rev. D vol. 25 pp. 1161–1173 (1982), doi:10.1103/PhysRevD.25.1161, URL https://link.aps.org/doi/10.1103/PhysRevD.25.1161

[49] S. J. Barish et al., "Study of the Isospin Properties of Single-Pion Production by Neutrinos", Phys. Rev. Lett. vol. 36 pp. 179–183 (1976), doi:10.1103/PhysRevLett.36.179, URL https://link.aps.org/doi/10.1103/PhysRevLett.36.179

[50] A. A. Aguilar-Arevalo et al. (MiniBooNE), "Measurement of Neutrino-Induced Charged-Current Charged Pion Production Cross Sections on

Mineral Oil at $E_\nu \sim 1$ GeV", Phys. Rev. vol. D83 p. 052007 (2011), doi:10.1103/PhysRevD.83.052007, 1011.3572

[51] Torbjörn Sjöstrand, Stephen Mrenna, and Peter Skands, "PYTHIA 6.4 physics and manual", Journal of High Energy Physics vol. 2006 (05) p. 026 (2006), URL http://stacks.iop.org/1126-6708/2006/i=05/a=026

[52] Dieter Rein, "Diffractive pion production in neutrino reactions", Nuclear Physics B vol. 278 (1) pp. 61 – 77 (1986), doi:https://doi.org/10.1016/0550-3213(86)90106-9, URL http://www.sciencedirect.com/science/article/pii/0550321386901069

[53] Dieter Rein and Lalit M. Sehgal, "Coherent π^0 production in neutrino reactions", Nuclear Physics B vol. 223 (1) pp. 29 – 44 (1983), doi:https://doi.org/10.1016/0550-3213(83)90090-1, URL http://www.sciencedirect.com/science/article/pii/0550321383900901

[54] D. Rein and L.M. Sehgal, "PCAC and the deficit of forward muons in π^+ production by neutrinos", Physics Letters B vol. 657 (4) pp. 207 – 209 (2007), doi:https://doi.org/10.1016/j.physletb.2007.10.025, URL http://www.sciencedirect.com/science/article/pii/S0370269307012580

[55] Ch. Berger and L. M. Sehgal, "PCAC and coherent pion production by low energy neutrinos", Phys. Rev. vol. D79 p. 053003 (2009), doi:10.1103/PhysRevD.79.053003, 0812.2653

[56] S. K. Singh and E. Oset, "Inclusive quasielastic neutrino reactions in ^{12}C and ^{16}O at intermediate energies", Phys. Rev. C vol. 48 pp. 1246–1258 (1993), doi:10.1103/PhysRevC.48.1246, URL https://link.aps.org/doi/10.1103/PhysRevC.48.1246

[57] Roger D. Woods and David S. Saxon, "Diffuse Surface Optical Model for Nucleon-Nuclei Scattering", Phys. Rev. vol. 95 pp. 577–578 (1954),

doi:10.1103/PhysRev.95.577, URL https://link.aps.org/doi/10.1103/PhysRev.95.577

[58] Yoshinari Hayato, "Private Communication",

[59] M. Martini, M. Ericson, G. Chanfray, and J. Marteau, "Unified approach for nucleon knock-out and coherent and incoherent pion production in neutrino interactions with nuclei", Phys. Rev. C vol. 80 p. 065501 (2009), doi:10.1103/PhysRevC.80.065501, URL https://link.aps.org/doi/10.1103/PhysRevC.80.065501

[60] J. Nieves, I. Ruiz Simo, and M. J. Vicente Vacas, "Inclusive charged-current neutrino-nucleus reactions", Phys. Rev. C vol. 83 p. 045501 (2011), doi:10.1103/PhysRevC.83.045501, URL https://link.aps.org/doi/10.1103/PhysRevC.83.045501

[61] P. Adamson et al. (MINOS), "Study of quasielastic scattering using charged-current $\nu_m u$-iron interactions in the MINOS near detector", Phys. Rev. vol. D91 (1) p. 012005 (2015), doi:10.1103/PhysRevD.91.012005, 1410.8613

[62] M. Martini, M. Ericson, G. Chanfray, and J. Marteau, "Neutrino and antineutrino quasielastic interactions with nuclei", Phys. Rev. C vol. 81 p. 045502 (2010), doi:10.1103/PhysRevC.81.045502, URL https://link.aps.org/doi/10.1103/PhysRevC.81.045502

[63] C. Andreopoulos et al., "The GENIE Neutrino Monte Carlo Generator", Nucl. Instrum. Meth. vol. A614 pp. 87–104 (2010), doi:10.1016/j.nima.2009.12.009, 0905.2517

[64] Yoshinari Hayato, "A neutrino interaction simulation program library NEUT", Acta Phys. Polon. vol. B40 pp. 2477–2489 (2009)

[65] Tomasz Golan, Cezary Juszczak, and Jan T. Sobczyk, "Effects of final-state interactions in neutrino-nucleus interactions", Phys. Rev. C vol. 86 p. 015505 (2012), doi:10.1103/PhysRevC.86.015505, URL https://link.aps.org/doi/10.1103/PhysRevC.86.015505

[66] Luke Pickering, Measurement of lead-target neutrino interactions using the whole T2K nead detector, Ph.D. thesis, Imperial College London (2017)

[67] P. Adamson et al. (NOvA Collaboration), "Measurement of the Neutrino Mixing Angle θ_{23} in NOvA", Phys. Rev. Lett. vol. 118 p. 151802 (2017), doi:10.1103/PhysRevLett.118.151802, URL https://link.aps.org/doi/10.1103/PhysRevLett.118.151802

[68] O. Altinok et al. (MINERvA), "Measurement of ν_μ charged-current single π^0 production on hydrocarbon in the few-GeV region using MINERvA", Phys. Rev. vol. D96 (7) p. 072003 (2017), doi:10.1103/PhysRevD.96.072003, 1708.03723

[69] X.-G. Lu et al., "Reconstruction of energy spectra of neutrino beams independent of nuclear effects", Phys. Rev. D vol. 92 p. 051302 (2015), doi:10.1103/PhysRevD.92.051302, URL http://link.aps.org/doi/10.1103/PhysRevD.92.051302

[70] Kevin Mcfarland and Jan Sobczyk, "Private Communication",

[71] Luke Pickering and Xianguo Lu, "Theoretical predictions of transverse kinematic imbalance in neutrino-nucleus interactions", in "Proceedings, Prospects in Neutrino Physics (NuPhys2015): London, UK, December 16-18, 2015", (2016), 1606.04403, URL https://inspirehep.net/record/1469255/files/arXiv:1606.04403.pdf

[72] K. Abe et al. (T2K Collaboration), "T2K neutrino flux prediction", Phys. Rev. D vol. 87 p. 012001 (2013), doi:10.1103/PhysRevD.87.012001, URL https://link.aps.org/doi/10.1103/PhysRevD.87.012001

[73] L. Aliaga et al. (MINERvA), "Design, Calibration, and Performance of the MINERvA Detector", Nucl. Instrum. Meth. vol. A743 pp. 130–159 (2014), doi:10.1016/j.nima.2013.12.053, 1305.5199

[74] G. Battistoni et al., "The FLUKA code: description and benchmarking", AIP Conference Proceedings vol. 896 (1) pp. 31–49 (2007), doi:10.1063/1.2720455, https://aip.scitation.org/doi/pdf/10.1063/1.2720455, URL https://aip.scitation.org/doi/abs/10.1063/1.2720455

[75] R. Brun et al., "GEANT3", (1987)

[76] S. Agostinelli et al. (GEANT4), "GEANT4: A Simulation toolkit", Nucl. Instrum. Meth. vol. A506 pp. 250–303 (2003), doi:10.1016/S0168-9002(03)01368-8

[77] K. Abe et al. (T2K Collaboration), "Indication of Electron Neutrino Appearance from an Accelerator-Produced Off-Axis Muon Neutrino Beam", Phys. Rev. Lett. vol. 107 p. 041801 (2011), doi:10.1103/PhysRevLett.107.041801, URL https://link.aps.org/doi/10.1103/PhysRevLett.107.041801

[78] K. Abe et al. (T2K Collaboration), "Precise Measurement of the Neutrino Mixing Parameter θ_{23} from Muon Neutrino Disappearance in an Off-Axis Beam", Phys. Rev. Lett. vol. 112 p. 181801 (2014), doi:10.1103/PhysRevLett.112.181801, URL https://link.aps.org/doi/10.1103/PhysRevLett.112.181801

[79] K. Abe et al. (T2K Collaboration), "Combined Analysis of Neutrino and Antineutrino Oscillations at T2K", Phys. Rev. Lett. vol. 118 p. 151801

(2017), doi:10.1103/PhysRevLett.118.151801, URL https://link.aps.org/doi/10.1103/PhysRevLett.118.151801

[80] K. Abe et al. (T2K Collaboration), "First measurement of the ν_μ charged-current cross section on a water target without pions in the final state", Phys. Rev. D vol. 97 p. 012001 (2018), doi:10.1103/PhysRevD.97.012001, URL https://link.aps.org/doi/10.1103/PhysRevD.97.012001

[81] K. Abe et al. (The T2K Collaboration), "Measurement of Coherent π^+ Production in Low Energy Neutrino-Carbon Scattering", Phys. Rev. Lett. vol. 117 p. 192501 (2016), doi:10.1103/PhysRevLett.117.192501, URL https://link.aps.org/doi/10.1103/PhysRevLett.117.192501

[82] K. Abe et al. (T2K Collaboration), "Search for short baseline ν_e disappearance with the T2K near detector", Phys. Rev. D vol. 91 p. 051102 (2015), doi:10.1103/PhysRevD.91.051102, URL https://link.aps.org/doi/10.1103/PhysRevD.91.051102

[83] K. Abe et al. (T2K Collaboration), "Search for Lorentz and *CPT* violation using sidereal time dependence of neutrino flavor transitions over a short baseline", Phys. Rev. D vol. 95 p. 111101 (2017), doi:10.1103/PhysRevD.95.111101, URL https://link.aps.org/doi/10.1103/PhysRevD.95.111101

[84] Accelerator Division, "J-Parc Accelerator Complex", http://www.teilchen.at/news/334/ (2018)

[85] J-Parc, "J-Parc Neutrino Facility", https://j-parc.jp/Neutrino/en/nu-facility.html (2018)

[86] Christophe Bronner, Contribution to the characterization of the T2K neutrino beam using the INGRID near detector, Ph.D. thesis, l'Ecole Polytechnique (2011)

[87] N. Abgrall et al., "Time projection chambers for the T2K near detectors", Nuclear Instruments and Methods in Physics Research Section A: Accelerators, Spectrometers, Detectors and Associated Equipment vol. 637 (1) pp. 25 – 46 (2011), doi:https://doi.org/10.1016/j.nima.2011.02.036, URL http://www.sciencedirect.com/science/article/pii/S0168900211003421

[88] Martti Nirkko, "Measurement of the K^+ production cross section from charged current ν_μ interactions in hydrocarbon at the T2K near detector", Tech. rep., T2K Collaboration (2016)

[89] Stephen Dolan, Probing Nuclear Effects in Neutrino-Nucleus Scattering at the T2K Off-Axis Near Detector Using Transverse Kinematic Imbalances, Ph.D. thesis, University of Oxford (2017)

[90] P. A. Amaudruz et al. (T2K ND280 FGD), "The T2K Fine-Grained Detectors", Nucl. Instrum. Meth. vol. A696 pp. 1–31 (2012), doi:10.1016/j.nima.2012.08.020, 1204.3666

[91] P. A. Rodrigues et al. (MINERvA), "Identification of nuclear effects in neutrino-carbon interactions at low three-momentum transfer", Phys. Rev. Lett. vol. 116 p. 071802 (2016), doi:10.1103/PhysRevLett.116.071802, 1511.05944

[92] R. Gran et al. (MINERvA), "Anti-neutrino charged-current reactions on scintillator with low momentum transfer", (2018), 1803.09377

[93] J. Park et al. (MINERvA), "Measurement of Neutrino Flux from Neutrino-Electron Elastic Scattering", Phys. Rev. vol. D93 (11) p. 112007 (2016), doi:10.1103/PhysRevD.93.112007, 1512.07699

[94] Z. Wang et al. (MINERvA), "First evidence of coherent K^+ meson production in neutrino-nucleus scattering", Phys. Rev. Lett. vol. 117 (6) p. 061802 (2016), doi:10.1103/PhysRevLett.117.061802, 1606.08890

[95] D.G. Michael et al., "The magnetized steel and scintillator calorimeters of the MINOS experiment", Nuclear Instruments and Methods in Physics Research Section A: Accelerators, Spectrometers, Detectors and Associated Equipment vol. 596 (2) pp. 190 – 228 (2008), doi:https://doi.org/10.1016/j.nima.2008.08.003, URL http://www.sciencedirect.com/science/article/pii/S0168900208011613

[96] Patrick Jussel, "Neutrino-Oszillationen in Japan", http://www.fnal.gov/pub/science/particle-accelerators/ (2010)

[97] P. Adamson et al., "The NuMI Neutrino Beam", Nucl. Instrum. Meth. vol. A806 pp. 279–306 (2016), doi:10.1016/j.nima.2015.08.063, 1507.06690

[98] Sacha E. Kopp, "The NuMI neutrino beam at Fermilab", AIP Conf. Proc. vol. 773 pp. 276–278 (2005), doi:10.1063/1.1949545, [,276(2004)], hep-ex/0412052

[99] Cheryl Patrick, Measurement of the Antineutrino Double-Differential Charged-Current Quasi-Elastic Scattering Cross Section at MINERvA, Ph.D. thesis, Northwestern U. (2016), doi:10.1007/978-3-319-69087-2, URL http://lss.fnal.gov/archive/thesis/2000/fermilab-thesis-2016-04.pdf

[100] K. Abe et al. (T2K), "Characterization of nuclear effects in muon-neutrino scattering on hydrocarbon with a measurement of final-state kinematics and correlations in charged-current pionless interactions at T2K", Phys. Rev. vol. D98 (3) p. 032003 (2018), doi:10.1103/PhysRevD.98.032003, 1802.05078

[101] Ozgur Altinok, Measurement of Muon Neutrino Charged Current Single π^0 Production on Hydrocarbon using MINERvA, Ph.D. thesis, Tufts Uni-

versity (2017), doi:10.2172/1352001, URL http://lss.fnal.gov/archive/thesis/2000/fermilab-thesis-2017-08.pdf

[102] Leonidas Aliaga et al., "A brief documentation of the flux", Tech. rep., MINERvA Collaboration (2015)

[103] Brandon Eberly, "Pion Production – Analysis Update", Tech. rep., MINERvA Collaboration (2014)

[104] B. Eberly et al. (MINERvA Collaboration), "Charged pion production in ν_μ interactions on hydrocarbon at $\langle E_\nu \rangle = 4.0$ GeV", Phys. Rev. D vol. 92 p. 092008 (2015), doi:10.1103/PhysRevD.92.092008, URL https://link.aps.org/doi/10.1103/PhysRevD.92.092008

[105] Philip Rodrigues, Callum Wilkinson, and Kevin McFarland, "Constraining the GENIE model of neutrino-induced single pion production using reanalyzed bubble chamber data", Eur. Phys. J. vol. C76 (8) p. 474 (2016), doi:10.1140/epjc/s10052-016-4314-3, 1601.01888

[106] Brandon M. Eberly, Characterization of Final State Interaction Strength in Plastic Scintillator by Muon-Neutrino Charged Current Charged Pion Production, Ph.D. thesis, Pittsburgh U. (2014), doi:10.2172/1156544, URL http://d-scholarship.pitt.edu/20853/

[107] Minerba Betancourt, "Internal Note, DocDB-11367-v8", Tech. rep., MINERνA Collaboration, Fermilab (2015)

[108] C. McGivern, "Internal Note, DocDB-10367", Tech. rep., MINERνA Collaboration, Fermilab (2014)

[109] DONALD E. GROOM, NIKOLAI V. MOKHOV, and SERGEI I. STRIGANOV, "MUON STOPPING POWER AND RANGE TABLES 10 MeV–100 TeV", Atomic Data and Nuclear Data Tables vol. 78 (2) pp.

183 – 356 (2001), doi:https://doi.org/10.1006/adnd.2001.0861, URL http://www.sciencedirect.com/science/article/pii/S0092640X01908617

[110] Ron Ransome, "Internal Note DocDB-6016-v7", Tech. rep., MINERvA Collaboration (2012)

[111] Tammy Walton, A Measurement of the Muon Neutrino Charged Current Quasielastic-like Cross Section on a Hydrocarbon Target and Final State Interaction Effects, Ph.D. thesis, Hampton U. (2014), doi:10.2172/1155872, URL http://lss.fnal.gov/archive/thesis/2000/fermilab-thesis-2014-11.shtml

[112] A. R. Mislivec, "Internal Note DocDB-7571-v3", Tech. rep., MINERvA Collaboration (2012)

[113] J B Birks, "Scintillations from Organic Crystals: Specific Fluorescence and Relative Response to Different Radiations", Proceedings of the Physical Society. Section A vol. 64 (10) p. 874 (1951), URL http://stacks.iop.org/0370-1298/64/i=10/a=303

[114] D Zhang, "Internal Note DocDB-11443", Tech. rep., MINERvA Collaboration (2015)

[115] D. Ashery et al., "True absorption and scattering of pions on nuclei", Phys. Rev. C vol. 23 pp. 2173–2185 (1981), doi:10.1103/PhysRevC.23.2173, URL https://link.aps.org/doi/10.1103/PhysRevC.23.2173

[116] Trung Le, "Internal Note DocDB-10423-v2", Tech. rep., MINERvA Collaboration (2014)

[117] G. D'Agostini, "A Multidimensional unfolding method based on Bayes' theorem", Nucl. Instrum. Meth. vol. A362 pp. 487–498 (1995), doi:10.1016/0168-9002(95)00274-X

[118] X.-G. Lu et al. (MINERvA Collaboration), "Measurement of Final-State Correlations in Neutrino Muon-Proton Mesonless Production on Hydrocarbon at $\langle E_\nu \rangle = 3$GeV", Phys. Rev. Lett. vol. 121 p. 022504 (2018), doi:10.1103/PhysRevLett.121.022504, URL https://link.aps.org/doi/10.1103/PhysRevLett.121.022504

[119] K. Abe et al. (T2K), "T2K ND280 Upgrade - Technical Design Report", (2019), 1901.03750

[120] A. Blondel et al., "A fully active fine grained detector with three readout views", JINST vol. 13 (02) p. P02006 (2018), doi:10.1088/1748-0221/13/02/P02006, 1707.01785